

**Automated Deformable Mapping Methods to Relate Corresponding Lesions in
3D X-ray and 3D Ultrasound Breast Images**

by

Crystal Ann Green

A dissertation submitted in partial fulfillment
of the requirements for the degree of
Doctor of Philosophy
(Nuclear Engineering and Radiological Sciences)
in the University of Michigan
2019

Doctoral Committee:

Professor Alex Bielajew, Co-Chair
Professor Mitchell Goodsitt, Co-Chair
Associate Professor Kristy K. Brock
Professor Emeritus Paul L. Carson
Assistant Professor Martha Matuszak

Crystal A. Green

canngree@umich.edu

ORCID iD: [0000-0003-3278-7568](https://orcid.org/0000-0003-3278-7568)

© Crystal Ann Green 2019

Dedication

For my aunt Claudean Freemon and my God-mother Ann Bryant.

Acknowledgements

I would first like to express my sincerest gratitude to my research advisor, Dr. Mitchell Goodsitt, for the considerable amount of time and patience he has provided me through comments, suggestions, and revisions of my research. I would also like to thank my academic advisor, Prof. Alex Bielajew, for all of his support and feedback, as well as his mentorship while I was his graduate student assistant for the Radiation Dosimetry course. I thank you both for taking me on as a student. The feedback and mentorship you have provided me will be invaluable as I continue to pursue my career in medical physics. I am grateful for my other three committee members, Dr. Paul Carson, Dr. Kristy Brock and Dr. Martha Matuszak for their hard work and dedication to train, mentor and share their experiences with young medical physicists like myself. I appreciate all of the feedback and guidance you have provided me, personally and professionally, throughout the course of my thesis and my time at Michigan.

There are countless people with whom I've interacted with during my tenure at Michigan who have helped me get thus far and therefore have indirectly contributed to my thesis work. I would like to thank our industry collaborator, Dr. Cynthia Davis, for all her feedback and involvement in allowing the use and loan of the Invenia system for this work. I'd like to thank Dr. Marilyn Roubidoux for all the time she has spent with me to view images, recruit patients, and answer all the clinical questions I had in regard to the patient study as our lead collaborative

radiologist. I would like to thank the ultrasound and mammography technologists within the University of Michigan Medicine's Breast Imaging department for all of their hard work and efforts in recruitment, study logistics, and imaging of patient volunteers as part of the patient study. I would like to thank Dr. Sandra Larson, for her help in testing fabrics for the ultrasound camisole. I would like to thank Dr. Manos Christodoulou, for his assistance in scanning the phantoms as well as his assistance in retrieving image datasets from PACS. I would like to thank Dr. Heang-Ping Chang and the University of Michigan CAD laboratory for allowing the use of the MiViewer software for this thesis. I would also like to thank Dr. William Johnson for being an excellent mentor to me throughout my summer internships and for exposing me to my first clinical experience in imaging medical physics. I have learned immensely about clinical work through working with all of you and hope my future endeavors remain in research that is translatable for clinical use.

I am grateful for my research group the Basic Radiological Science (BRS) Division of the Radiology department lead by Dr. J. Brian Fowlkes. Within this group I would also especially like to thank Dr. Mario Fabiilli and Dr. Oliver Kripfgans for allowing me to use lab space and equipment. I am so blessed to have worked with such an amazing group of people in BRS and I know if I had not been in this lab environment the success of this dissertation would not have been possible. I pray that the next group of people I work with emulate the bond and family we have in BRS. I extend my gratitude to the wonderful administrators Sandra Crump from BRS and Mary Burton of Radiology for their support and assistance in the patient study related to this thesis. I would also like to thank Jasmine Lau for her efforts in creating a graphical user interface for the registration platform.

I am extremely thankful to my home department, Nuclear Engineering and Radiological Sciences (NERS), and specifically to Prof. John Foster and Prof. Ronald Gilgenbach. Prof. Foster, thank you for being an amazing mentor to me and motivating me to remain tenacious even through difficult times in my PhD journey. I pray that wherever my journey leads me next, that I am able to be half the mentor to someone else as you have been for me. Prof. Gilgenbach, I am immensely thankful for the support you provided to me for the research project, conference presentations, and recruitment back at my undergraduate institution. Also, I extend my deepest gratitude to the administrators in NERS (Cherilyn Davis, Peggy Jo Gramer, Jennifer Melms, Amber French, Caroline Joaquin, Trisha Fountains and Garnette Roberts) for all of their assistance and administrative support.

I would like to thank my parents, Rev. Dr. Timothy and Beatrice Green, and my loving family for their overwhelming love and support. I specifically want to thank my aunt Claudean Freemon and my God-Mother Ann Bryant for being amazing women that I have always admired. As they are the breast cancer survivors closest to my heart, I dedicate this dissertation to them.

I am blessed to have made lifelong friends through this journey who have become part of my extended family. Many of which I met during the Summer Institute provided by the Rackham Graduate School for Rackham Merit fellows or as part of student organizations. I thank all my friends here at Michigan for their love and mutual support. My experiences at Michigan would not have been as meaningful without you all being here and I definitely will cherish the memories.

I would like to thank the funding sources that supported me financially to conduct the research described within this dissertation. My fellowships the Science, Mathematics and Research for Transformation (SMART) Scholarship for Service Program (HQ0034-16-C-0008)

and the Rackham Merit Fellowship. This thesis work was funded in-part by a research grant (15-PAF04328) from GE Global Research, a Rackham Student Research Grant, and the Glenn Knoll Chairman's Fund from the Nuclear Engineering and Radiological Sciences Department.

Last but not least, I would like to thank God and my savior Jesus Christ for extending grace and mercy throughout this journey. I am so grateful for all of the individuals God has placed in my path to get me to this point in my career. Throughout my PhD, I have constantly been reminded of the importance of staying grounded in Christ and to look to God during difficult times for strength. I pray that this dissertation and all my future endeavors reflect, honor and glorify God's name through Jesus Christ.

Table of Contents

Dedication	ii
Acknowledgements.....	iii
List of Tables	x
List of Figures	xv
Abstract.....	xxiii
Chapter 1 Introduction	1
1.1 Significance of Work.....	1
1.2 Dissertation Outline	6
Chapter 2 Breast Imaging Acquisition and Finite Element Methodology.....	9
2.1 Breast Anatomy and Density	9
2.2 Digital Breast Tomosynthesis.....	12
2.3 Dedicated Breast Computed Tomography.....	14
2.4 Automated Breast Ultrasound.....	16
2.5 Breast Camisole for ABUS Imaging	19
2.6 External Fiducial Markers	29
2.7 Finite Element Method and Analysis	30

Chapter 3 Deformable Mapping Technique to Correlate Lesions in Digital Breast Tomosynthesis and Automated Breast Ultrasound Images	41
3.1 Abstract.....	41
3.2 Introduction.....	43
3.3 Materials and Methods	46
3.4 Results.....	64
3.5 Discussion.....	71
3.6 Conclusions.....	78
3.7 Acknowledgements.....	78
Chapter 4 Deformable Mapping Technique for lesion registration for Multiple Digital Breast Tomosynthesis views to Automated Breast Ultrasound Images.....	79
4.1 Abstract.....	79
4.2 Introduction.....	80
4.3 Materials and Methods	82
4.4 Results.....	90
4.5 Discussion.....	101
4.6 Conclusions.....	104
4.7 Acknowledgements.....	104
Chapter 5 Deformable Mapping Method to Relate Lesions in Dedicated Breast CT Images to those in Automated Breast Ultrasound and Digital Breast Tomosynthesis	105
5.1 Abstract.....	105
5.2 Introduction.....	106
5.3 Materials and Methods	110
5.4 Results.....	123
5.5 Conclusions.....	132
5.6 Discussion.....	133
5.7 Acknowledgements.....	138
Chapter 6 Proof-of-Concept patient validation study of Deformable Mapping Technique to relate lesions between DBT and ABUS images	139

6.1	Abstract.....	139
6.2	Introduction.....	140
6.3	Materials and Methods	143
6.4	Calculations	153
6.5	Results.....	161
6.6	Discussion.....	168
6.7	Conclusions.....	174
6.8	Acknowledgements.....	175
Chapter 7 Conclusions and Future Works		176
7.1	Summary of Contributions	176
7.2	Conclusions and Limitations	177
7.3	Future Works	184
7.4	Final Thoughts.....	188
Appendix.....		189
Bibliography		202

List of Tables

Table 2.1 Comparisons of DOP between various testing combinations. P= Phantom Only. Inv= Invenia Mesh fabric. Mat 1=108” Nylon Chiffon Tricot, Mat2= 108” 40 Denier Tricot, Mat3= Power Mesh, Mat 4, Mat5= Telio Matte Chiffon	26
Table 3.1 Phantom material properties	47
Table 3.2 Criteria for lesion correlation between ABUS and DBT model	62
Table 3.3 Average DSC and average COM distance (d_{COM}) results between readers for corresponding lesions in all DBT and ABUS data sets for Phantoms A and B.....	64
Table 3.4 Average COM distance (d_{COM}) between external markers among readers in DBT and ABUS data sets for Phantoms A and B	65
Table 3.5 Reproducibility for each reader’s lesion segmentations in DBT and ABUS data sets for Phantoms A and B using DSC coefficients and average COM distance (d_{COM}).	65
Table 3.6 Lesion correlation for Phantom A when no external markers are used for the deformation (left) vs. three external markers used for the deformation (right).	69
Table 3.7 Lesion correlation for Phantom B when no external markers are used for the deformation and with the use of 3 and 2 marker analysis. Note: Lesion Overlap is defined by the resultant of at least 2 out of 3 readers’ data showing overlap for that specific lesion between ABUS and DBT set. +Indicates that lesion 3 in no marker analysis showed overlap for 2 out of 3	

readers' datasets. * Indicates that lesion 7 was out of correlation bounds for one reader set and therefore the values are averaged based for two readers' data and not all three..... 71

Table 4.1 Material Properties of CIRS phantom 83

Table 4.2: Lesion correlation criteria between DBT (CC or MLO) and ABUS models 89

Table 4.3: Lesion correlation summary for DBT (CC) registered to ABUS. A maximum of 18 lesions could be matched between image sets. 91

Table 4.4: Lesion correlation summary for 8 matched lesions between without marker analysis and with marker analysis cases for DBT (CC) registered to ABUS..... 92

Table 4.5: Effect of d_{COM} based on lesion COM distance to nearest external marker (d_{COM-M}).. 93

Table 4.6: Lesion correlation results for each lesion with and without marker analysis for DBT (CC) registered to ABUS. Location for breast margins abbreviations include I=Inferior S=Superior C=Central A=Anterior P=Posterior M=Medial L=Lateral..... 96

Table 4.7: Lesion correlation summary for DBT (MLO) registered to ABUS. A maximum of 18 lesions could be matched between image sets. 97

Table 4.8: Lesion correlation summary of 8 matched lesions between without marker analysis and with marker analysis cases for DBT (MLO) registered to ABUS 98

Table 4.9: Effect of d_{COM} based on lesion COM distance to nearest external marker (d_{COM-M})... 99

Table 4.10: Lesion correlation results for each lesion with and without marker analysis for DBT (MLO) registered to ABUS. Location for breast margins abbreviations include I=Inferior S=Superior C=Central A=Anterior P=Posterior M=Medial L=Lateral 101

Table 5.1: Phantom Material Properties 111

Table 5.2: Lesion Correlation summary for bCT registered to ABUS. A maximum of 20 lesions could be matched between image sets. (d_{COM} = distance between centers of masses of

corresponding lesions in the two modalities, d_o = minimum distance for overlap of corresponding lesions, d_M = distance between external fiducial markers). 124

Table 5.3: Lesion correlation summary of 14 matched lesions between without marker analysis and with marker analysis cases for bCT registered to ABUS (d_{COM} = distance between centers of masses of corresponding lesions in the two modalities, d_o = minimum distance 125

Table 5.4: Lesion matching results for each lesion with and without marker analysis for bCT registered to ABUS 126

Table 5.5: Lesion Correlation summary for bCT registered to DBT (CC). A maximum of 18 lesions could be matched between image sets (d_{COM} = distance between centers of masses of corresponding lesions in the two modalities, d_o = minimum distance for overlap of corresponding lesions, d_M = distance between external fiducial markers). 127

Table 5.6: Lesion correlation summary of 9 matched lesions between without marker analysis and with marker analysis cases for bCT registered to DBT (CC). (d_{COM} = distance between centers of masses of corresponding lesions in the two modalities, d_o = minimum distance for overlap of corresponding lesions, d_M = distance between external fiducial markers). 127

Table 5.7: Lesion matching results for each lesion with and without marker analysis for bCT registered to DBT (CC)..... 129

Table 5.8: Lesion Correlation summary for bCT registered to DBT (MLO). A maximum of 18 lesions could be matched between image sets. (d_{COM} = distance between centers of masses of corresponding lesions in the two modalities, d_o = minimum distance for overlap of corresponding lesions, d_M = distance between external fiducial markers). 130

Table 5.9: Lesion correlation summary of 9 matched lesions between without marker analysis and with marker analysis cases for bCT registered to DBT (MLO). (d_{COM} = distance between

centers of masses of corresponding lesions in the two modalities, d_o = minimum distance for overlap of corresponding lesions, d_M = distance between external fiducial markers). 131

Table 5.10: Lesion matching results for each lesion with and without marker analysis for bCT registered to DBT (MLO) 132

Table 6.1: Mechanical properties used for biomechanical modeling. By default, a lesion is assigned the properties of benign lesion. 155

Table 6.2: Minimum and Maximum Young’s Moduli of adipose, glandular and lesion tissue for sensitivity analysis 155

Table 6.3: Coefficients for Equation 1 based on different lengths, L, as described in Figure 6.2. SA= Superior Anterior. SP= Superior Posterior. IA= Interior Anterior. IP=Interior Posterior.. 157

Table 6.4: Subject and lesion demographics. Compressed thickness is based on the DBT (CC view) RA=Retroareolar, LOQ= Lower Outer Quadrant, UOQ= Upper Outer Quadrant, LIQ= Lower Inner Quadrant, UIQ= Upper Inner Quadrant. A=Anterior depth P=Posterior depth M=Middle MP=Middle to Posterior depth *Indicates a mass has components of fibrocystic change, stromal fibrosis, and usual ductal hyperplasia..... 162

Table 6.5: Deformable registration results compared to rigid registration for various marker combinations based on resulting d_{COM} values for DBT (CC view) mapped to ABUS. For Lesion ID #4, the lateral marker “G” (see Figure 6.1(b)) was not seen in resulting ABUS views due to ABUS view misalignment therefore cases using 4 and 7 markers were not evaluated. For retroareolar lesions marker analysis using 1 marker is not evaluated. Best d_{COM} values are reported in bold. 163

Table 6.6: Deformable registration results compared to rigid registration for various marker combinations based off resulting d_{COM} values for DBT (MLO view) mapped to ABUS. For

Lesion ID #4, the lateral marker “G” (see Figure 6.1 (a) Ultrasound camisole for ABUS imaging (b) External fiducial marker locations (denoted by A-G) denoted on a breast for marker placement on the left breast(b)) was not seen in resulting ABUS views due to ABUS view misalignment therefore cases using 4 and 7 markers could not be evaluated. For Lesion ID 7, was not seen in reconstructed DBT (MLO view) and therefore could not be registered due to lack on anterior compression. 164

Table 6.7: Variation in d_{COM} and FEA run time varying meshing parameters in Case 1 and resampling rates in Case 2 in comparison to the base values 168

Table A.1: Parameter setting used to Run MiViewer program on DBT and ABUS images.....194

List of Figures

Figure 2.1 Schematic of adult female breast anatomy (figure used with permission from GE Healthcare ³⁷)	9
Figure 2.2 BI-RADS breast density category examples from mammography (figure used with permission from GE Healthcare ³⁸).....	11
Figure 2.3 Examples of mammographic compression types of a breast mimicking test device for (a) cranio-caudal compression and (b) medial lateral oblique compression Note: The sheer fabric is typically not used on the detector plate during breast imaging	13
Figure 2.4 Schematic of image acquisition of a digital breast tomosynthesis imaging system (figure used with permission from Rodríguez-Ruiz et al. ⁴⁴).....	14
Figure 2.5 Schematic of image acquisition for dedicated breast CT imaging system (figure used with permission from Lindfors et al. ⁴⁹).....	15
Figure 2.6 Invenia ABUS imaging system a. shown from operator view b. shown imaging a patient (figure used with permission from GE Healthcare ⁶⁶)	18
Figure 2.7 Illustration of the three different ABUS scans performed on the right breast for an ABUS exam (figure used with permission from GE Healthcare ⁶⁶).....	19
Figure 2.8 Camisole used for ABUS imaging	20
Figure 2.9 ROI of image profile used to average pixel values of full cine-loop independent images	23

Figure 2.10 Signal and Noise pixel profiles used to determine system sensitivity using the tissue-mimicking water phantom in a water medium measuring the Invenia mesh. $S+N = \text{Averaged Image Signal}$. $N = \text{Electronic Noise (acquired from air-only acquisition)}$ 24

Figure 2.11 Resulting SNR_{IEC} values plotted as a function of imaging depth 25

Figure 2.12 Talled Evaluation for efficacy of ABUS Camisole 28

Figure 2.13 Edge artifact of external fiducial marker in ABUS imaging 30

Figure 2.14: Surface meshes of the skin (brown), inner gel (yellow), multiple lesions (pink, red, green and blue) from a breast phantom for (a) surface meshes created from segmented DICOM (Notice surface meshes are hollow on the interior and not filled or connected to one another) (b) tetrameshed model of breast fully connected..... 34

Figure 3.1: Load-strain curve comparing elastic properties of Phantom A and Phantom B. Note: Phantom B a similar phantom made of same material properties were used for these points as the Phantom had ruptured due to the amount of time that had passed as these measurements took place 48

Figure 3.2 Phantom A with external fiducial marker locations indicated by A-F 49

Figure 3.3 DBT and ABUS acquired images. The red arrows indicate the locations of external fiducial markers in:(a) DBT image of Phantom A, (b) DBT image of Phantom B, (c) ABUS image of Phantom A, and (d) ABUS image of Phantom B 50

Figure 3.4 Reader 1’s manual segmentation of a slice in (a) Phantom A – DBT, (b) Phantom B- DBT, (c) Phantom A - ABUS (d) Phantom B - ABUS 52

Figure 3.5 The automated deformable mapping process. Software’s used shown in red 54

Figure 3.6: Periphery uncertainty from skin segmentation for a slice in ABUS for (a) Phantom A (b) Phantom B. 55

Figure 3.7: Mesh transformation for external DBT breast surface mesh to match shape of ABUS surface mesh. Brown: ABUS (unchanged) Yellow:Blue (deformed): (a) COM translation and rotation of DBT to ABUS COM (b) Coronal handle manipulation of DBT breast surface mesh (along y axis) (c) Axial handle manipulation of DBT breast surface mesh (along z axis)..... 58

Figure 3.8 Pseudo-code for lesion correlation used within deformable mapping algorithm 62

Figure 3.9 Lesion correlation metrics for COM distance (dCOM) and minimum distance to overlap (dO) for (a) non-overlapping lesions and (b) overlapping lesions. (Blue = ABUS, Yellow = DBT)..... 63

Figure 3.10 Average distances between COMs of corresponding lesions in ABUS and DBT images (dCOM) for all 3 readers, as well as minimum distance to overlap (do), and overall lesion overlap ratio (the number of lesions that overlapped between DBT and ABUS sets divided by the total number of lesions that were imaged) for Phantom A with various number of external fiducial markers. (a) All marker distances were within a distance ($d_M \leq 1$ mm) between readers' data sets. (b) All marker distances were within a distance ($d_M \leq 5$ mm) between readers' data sets. Marker combinations from Figure 3.2:6 markers (A-F), 5 Markers (A, B, C, E, and F), 4 markers (F, B, E, and C), 3 markers (A, B, and F) and two markers (F and B). 67

Figure 3.11 Phantom A lesion correlation for Reader 1 (a) without marker analysis coronal view (b) with marker analysis coronal view (c) without marker analysis axial view (d) with marker analysis axial view. All numeric values correspond with Lesion ID's in Table 3.6. (Blue = ABUS, Yellow = DBT)..... 68

Figure 3.12 Phantom B lesion correlation for Reader 1 (a) without marker analysis in the coronial view (b) with three marker analyses in the coronial view (c) without marker analysis in the axial view (d) with three marker analyses in the axial view. All numeric values correspond

with Lesion ID's in Table 3.7. Note that for the without marker analysis lesions 5, 6, and 7 did not meet the correlation criteria of being within 15 mm of each other (See Table 3.7). (Blue = ABUS, Yellow = DBT)..... 70

Figure 3.13 Relating corresponding lesion in DBT and ABUS original datasets for Phantom A based on use of deformable mapping algorithm results..... 72

Figure 4.1 CIRS Multi-modality phantom with 8 external markers attached..... 83

Figure 4.2: Reconstructed slice indicating external fiducial marker (red arrow) for a slice of (a) DBT (CC view) (b) DBT (MLO view) (c) ABUS transverse view (d) ABUS coronal view..... 84

Figure 4.3: Segmentation of lesions within an image slice of (a) DBT CC (b) DBT MLO (c) ABUS 85

Figure 4.4 The automated deformable mapping process for DBT to ABUS registration. Software's used are shown in red. 86

Figure 4.5 Skin Mesh transformation for base DBT-MLO model (blue) to ABUS model (brown) (a) translation and rotation of DBT-MLO model to COM of ABUS model (b) decompression of skin model along the y-axis to match ABUS shape (c) compression in the z direction of the DBT-MLO model 88

Figure 4.6 Lesion correlation for DBT-CC (blue) registered to ABUS (yellow) for selected lesions in the coronal plane (a) without marker analysis (b) with marker analysis. Note: All lesions could not be shown due to superposition..... 92

Figure 4.7: Plot of d_{COM} (COM distance between corresponding lesions) vs d_{COM-M} (distance between COM of lesion to nearest external marker) for DBT (CC view) to ABUS 94

Figure 4.8: GUI representation for marked corresponding lesion (Lesion ID=1 see Table 4.5) in the DBT (CC) to ABUS original DICOM image views. From the view in the ABUS image the

suspicious mass can be interpreted as a dense solid lesion. Detailed corresponding lesion values are shown in Table 4.5. 95

Figure 4.9: Lesion correlation for DBT (MLO view) (red) registered to ABUS (yellow) for selected lesions in the coronal plane (a) without marker analysis (b) with marker analysis. Note: All lesions could not be shown due to superposition. 98

Figure 4.10: Plot of d_{COM} (COM distance between corresponding lesions) vs d_{COM-M} (distance between COM of lesion to nearest external marker) for DBT (MLO view) to ABUS 100

Figure 4.11: GUI representation from original DICOM images for a lesion (Lesion ID=11 see) left shows a slice from DBT (MLO) data, upper right shows the ABUS coronal view, and lower right shows the ABUS transverse view 100

Figure 5.1: Load Strain curve showing elastic nature of breast phantom. 112

Figure 5.2: (a) CIRS Multi-modality breast phantom with external fiducial markers attached. Segmented lesion Images acquired with (b) DBT (c) simulated bCT, and (d) ABUS. Red arrow shows external fiducial marker locations 113

Figure 5.3: ABUS image acquisition setup on uncompressed phantom 115

Figure 5.4: The automated deformable mapping process. Software's used shown in red. 117

Figure 5.5: Plate deformation (a). bCT in DBT (CC) setup no compression applied (b) resulting CC compression to bCT model (c) bCT to ABUS setup no compression applied (d) resulting ABUS compression to bCT model 119

Figure 5.6: Matching corresponding lesions showing a. overlapping lesions b. non-overlapping lesions. d_{COM} is restricted to 15 mm ($d_{COM} \leq 15$ mm) for both and dO is restricted to 7.5 mm ($dO \leq 7.5$ mm) for non-overlapping corresponding lesions. 123

Figure 5.7: Lesion correlation for bCT (blue) registered to ABUS (yellow) (a) coronal view without marker analysis (b) coronal view with marker analysis (c) GUI representation from a lesion in original DICOM images of bCT (left), coronal view ABUS (upper-right), and transverse ABUS (lower-right) for a lesion (Lesion ID= 8). Numbers correspond to lesion ID's and correlation values in Table 5.4)..... 125

Figure 5.8: Lesion correlation bCT (blue) registered to DBT (CC view) (red) (a) axial view without marker analysis (b) axial view with marker analysis (c) GUI representation from original DICOM images for lesion (Lesion ID= 8). Numbers correspond to lesion ID's and correlation values in Table 5.7. Note: All lesions are not visually represented in this figure due to superposition of the 2D representation 128

Figure 5.9: Lesion correlation bCT (blue) registered to DBT (MLO view) (green) (a) axial view without marker analysis (b) axial view with marker analysis (c) GUI representation from original DICOM images for a lesion. Numbers correspond to lesion ID's and correlation values in Table 5.10. Note: All lesions are not visually represented in this figure due to superposition of the 2D representation. 131

Figure 5.10: Measurement of lateral compression difference from Invenia Reverse curve transducer during ABUS imaging..... 135

Figure 6.1 (a) Ultrasound camisole for ABUS imaging (b) External fiducial marker locations (denoted by A-G) shown for marker placements on the left breast 145

Figure 6.2: Red Arrow indicates glass bead of an external fiducial marker in (a) DBT (CC view) (b) DBT (MLO view) and (c) ABUS AP view. Yellow arrow shows length x for (a) the medial to lateral breast margins in DBT (CC view) needed for DBT surface skin transformation (b) nipple to posterior breast length in DBT (MLO view) 146

Figure 6.3: MiViewer lesion segmentation for (a) DBT (CC view) image slice (b) DBT (MLO view) image slice (c) ABUS (AP view) image slice (sagittal) (d) 3D Slicer skin segmentation of ABUS (AP view) (coronal)..... 149

Figure 6.4: (a) Original DBT DICOM slice (b) LIBRA-generated color map of dense breast regions (c) Breast mask segmentation (red) and dense mask segmentation (green) of DBT slice 151

Figure 6.5: Overview of the Automated Deformable Mapping Process. Software’s used are shown in red..... 154

Figure 6.6: Handle manipulation for external skin DBT mesh. Blue=ABUS (unchanged). Brown= deformed DBT (CC view) (a) original DBT mesh registered to COM of ABUS (b) morphed DBT mesh following parabolic deformation for nodes along x-axis (c) resulting morphed DBT model after compression along z-axis. The handles (red and yellow spheres) are used to manipulate the DBT mesh model to match similar shape of the ABUS model. 157

Figure 6.7: Handle manipulation for external skin DBT mesh. Blue=ABUS (unchanged). Brown= deformed DBT (MLO view) (a) original DBT mesh registered to COM of ABUS (b) original DBT mesh registered to the nipple of the ABUS model (c) skin morphing performed by handle perturbations to allow DBT MLO model to match similar shape of ABUS model. The handles (red and yellow spheres) are used to manipulate the DBT mesh model to match similar shape of the ABUS model..... 159

Figure 6.8: Sensitivity Analysis of variations in Young's Moduli, E, for registered d_{COM} for DBT (CC view) mapped to ABUS using the deformable mapping technique without marker analysis. Base values for E for lesion (benign), glandular tissue, and adipose tissue are shown in Table 6.1. The minimum and maximum E values for these tissues are shown in Table 6.2. 166

Figure 6.9: Sensitivity Analysis of variations in Young's Moduli, E, for registered d_{COM} for DBT (CC view) mapped to ABUS using the deformable mapping technique without marker analysis. Base values for E for lesion (malignant), glandular tissue, and adipose tissue are shown in Table 6.1. The minimum and maximum E values for these tissues are shown in Table 6.2. 167

Figure 6.10: Registration results for Subject ID=2 Lesion ID=2 extremely dense breast tissue with presence of dilated ducts (a) registered lesion in DBT (CC view) (b) registered lesion in DBT (MLO view) (c) registered lesion in an ABUS image slice (d) presence of dilated ducts seen in a ABUS slice; These dilated ducts extended from ABUS Slices 180-215 169

Figure 6.11: Corresponding lesions of multiple breast masses based on deformable registration results (a) a DBT (CC view) image slice showing Lesion ID=5 (b) a DBT (CC view) image slice showing Lesion ID=6 (red arrow) and Lesion ID=7 (yellow arrow) (c) the corresponding ABUS slice for Lesion ID=5 (d) the corresponding ABUS slice for Lesion ID=6 (e) the corresponding ABUS slice for Lesion ID=7..... 170

Figure A.1: Example of parent directory that houses all segmentation folders and base DICOM folder for base FE model generation..... 195

Figure A.2: Pseudo-code describing base FE model generation used within the deformable mapping algorithm..... 196

Figure A.3: Selection Menu for GUI interface..... 197

Figure A.4 GUI Viewer results for a corresponding mass between the DBT (CC view) and ABUS view indicated by the red cross hair..... 198

Abstract

Mammography is the current standard imaging method for detecting breast cancer by using x-rays to produce 2D images of the breast. However, with mammography alone there is difficulty determining whether a lesion is benign or malignant and reduced sensitivity to detecting lesions in dense breasts. Ultrasound imaging used in conjunction with mammography has shown valuable contributions for lesion characterization by differentiating between solid and cystic lesions. Conventional breast ultrasound has high false positive rates; however, it has shown improved abilities to detect lesions in dense breasts. Breast ultrasound is typically performed freehand to produce anterior-to-posterior 2D images in a different geometry (supine) than mammography (upright). This difference in geometries is likely responsible for the finding that at least 10% of the time lesions found in the ultrasound images do not correspond with lesions found in mammograms. To solve this problem additional imaging techniques must be investigated to aid a radiologist in identifying corresponding lesions in the two modalities to ensure early detection of a potential cancer.

This dissertation describes and validates automated deformable mapping methods to register and relate corresponding lesions between multi-modality images acquired using 3D mammography (Digital Breast Tomosynthesis (DBT) and dedicated breast Computed Tomography (bCT)) and 3D ultrasound (Automated Breast Ultrasound (ABUS)). The methodology involves the use of finite element modeling and analysis to simulate the differences

in compression and breast orientation to better align lesions acquired from images from these modalities. Preliminary studies were performed using several multimodality compressible breast phantoms to determine breast lesion registrations between: i) cranio-caudal (CC) and mediolateral oblique (MLO) DBT views and ABUS, ii) simulated bCT and DBT (CC and MLO views), and iii) simulated bCT and ABUS. Distances between the centers of masses, d_{COM} , of corresponding lesions were used to assess the deformable mapping method.

These phantom studies showed the potential to apply this technique for real breast lesions with mean d_{COM} registration values as low as 4.9 ± 2.4 mm for DBT (CC view) mapped to ABUS, 9.3 ± 2.8 mm for DBT (MLO view) mapped to ABUS, 4.8 ± 2.4 mm for bCT mapped to ABUS, 5.0 ± 2.2 mm for bCT mapped to DBT (CC view), and 4.7 ± 2.5 mm for bCT mapped to DBT (MLO view). All of the phantom studies showed that using external fiducial markers helped improve the registration capability of the deformable mapping algorithm. An IRB-approved proof-of-concept study was performed with patient volunteers to validate the deformable registration method on 5 patient datasets with a total of up to 7 lesions for DBT (CC and MLO views) to ABUS registration. Resulting d_{COM} 's using the deformable method showed statistically significant improvements over rigid registration techniques with a mean d_{COM} of 11.6 ± 5.3 mm for DBT (CC view) mapped to ABUS and a mean d_{COM} of 12.3 ± 4.8 mm for DBT (MLO view) mapped to ABUS.

The present work demonstrates the potential for using deformable registration techniques to relate corresponding lesions in 3D x-ray and 3D ultrasound images. This methodology should improve a radiologists' characterization of breast lesions which can reduce patient callbacks, misdiagnoses, additional patient dose and unnecessary biopsies. Additionally, this technique can

save a radiologist time in navigating 3D image volumes and the one-to-one lesion correspondence between modalities can aid in the early detection of breast malignancies.

Chapter 1

Introduction

1.1 Significance of Work

According to the most recent statistics, breast cancer accounts for 30% of all new cancer diagnoses in women and 1 in 8 women in the United States will develop breast cancer during their lifetime.¹ Breast cancer incidence rose in the 1980s. This is largely attributed to the increase in breast cancers detected with the increase in mammography screening.¹ A decline in breast cancer incidence was observed in the early 2000s. This is attributed to the reduction in the use of menopausal hormonal therapy, which was associated with an increase in breast cancer risks.² Breast cancer incidence has remained stable in the United States over the last decade.¹ However, breast cancer has the second highest mortality rate behind lung cancer for women in the United States. Early detection and screening initiatives have been strongly encouraged in order to detect breast cancer while it is localized within the breast and therefore is the most treatable. Based on the National Cancer Institute's Surveillance, Epidemiology and End Results (SEER) programs localized cancers that have not spread beyond the breast have a 99% 5-year relative breast cancer survival.³ This relative 5-year survival rate decreases to 85% if the cancer has spread to the neighboring lymph nodes. The 5-year relative survival rate decreases to 27% if the cancer cells have spread to other parts of the body by metastasis³. Therefore, in an effort to reduce breast

cancer mortality it is important to have effective medical diagnostic equipment available to aid in early diagnosis.

Mammography is the current standard imaging method for breast cancer screening and diagnosis. However, the benefits of screening mammography vary by age. Women between the ages of 50-69 have the greatest overall benefit of screening mammography for breast cancer detection and it was concluded by the U.S. Preventative Services Task Force (USPSTF) that mammography every 2 years has approximately the same benefit as mammography every year while reducing the associated risk.⁴ The USPSTF recommends mammography every two years for women between the ages of 50-69.⁵ For women between the ages of 40-49, the overall benefit is less than older women as various study findings vary.^{4,6} Women ages 40-49 have a lower overall risk for breast cancer and tend to have dense breast tissue which leads to a rise in false positive screening results in comparison to older women.⁷ For this reason, the USPSTF does not recommend routine mammography for women ages 40-49.⁵ Instead, the USPSTF and the American College of Physicians recommend that women within this age group discuss the benefits and risks with their health care providers to make an informed decision regarding the start and frequency of mammography screening.^{5,8} For women over the age of 70, there are few studies and no randomized control trials to evaluate the benefits of mammography screening. The USPSTF recommends mammography for every 2 years for women between the ages of 70-74. Currently, there isn't enough evidence to recommend for or against routine mammography above the age of 75.⁵ Most major health organization, recommend that women over the age of 70 continue to get screening mammograms on a regular basis as long as they are in good health.^{5,9}

However, several studies have raised questions against the recommendations of the USPSTF as their recommendations neglect scientific evidence in regard to the mortality benefit of

mammography screening.^{10,11} A study by Hendricks and Helvie examined the evidence considered by the USPSTF and their results support mortality benefit to annual screening mammography for women over the age of 40, as the potential harms in screening are minor in comparison.¹⁰ Their study shows a 36.9% mortality reduction from using the annual screening of women between the ages of 40-84 which would save 71% more lives than the USPSTF recommendation which only had a 23.2% mortality reduction.¹⁰ A more recent study by Hendricks et al. further supports that screening mammography reduces the mortality rate by showing between 284,000-615,500 breast cancer deaths have been averted through the use of screening mammography since 1989.¹² A study by Kopans also disagrees with the USPSTF guidelines and states there is no biological or scientific reason to delay mammography screening for women to the age of 50.¹¹

Ultrasound imaging does not use ionizing radiation like mammography. Instead ultrasound imaging uses sound waves in order to produce images of the breast. Conventional ultrasound imaging is performed freehand in a different geometry (supine) than mammography (upright), which makes it difficult to relate corresponding images between the two modalities. False positive results are a problem when searching for secondary masses and the detection in high risk or screening populations with the use of conventional ultrasound.^{13,14} A study by Conway found that at least 10% of the time, lesions found in ultrasound images do not correspond to those in mammography.¹⁵

Ultrasound imaging used in conjunction with mammography in diagnosis has improved the characterization of breast lesions because of its ability to differentiate between solid and cystic (fluid-filled) lesions.¹⁶⁻¹⁸ A study by Wilczek et al. found that adding 3D automated breast ultrasound (ABUS) imaging as an adjunct to screening mammography has shown an increase in

cancer detection for women with extremely dense or heterogeneously dense breast tissue.¹⁹ A study by V. Giuliano and C. Giuliano found that mammography followed by ABUS in breast cancer screening resulted in increased sensitivity (76.0% to 97.7%) and increased specificity (98.2% to 99.7%) over screening using mammography alone.²⁰

One solution to the problem of lesions found in ultrasound images not corresponding to those in mammograms is the development of a combined x-ray/ultrasound system that would image the breast in the same mammographic geometry using special modality compression paddles. A combined system addresses these problems by first taking a 3D digital x-ray image of the breast in the compressed mammography state and then to image using ultrasound by using the same compression with the use of high-frequency ultrasonic transducers (ranging from 9 – 15 MHz) across a specialty dual- modality compression paddle. A dual x-ray/ultrasound system creates co-registered 3D x-ray and 3D ultrasound images in the same geometry and allows the potential for the use for advanced x-ray and ultrasound modes which provide additional information about breast tissues that are not currently available using conventional mammography and ultrasound.^{21–31}

A study by Padilla et al. showed improved discrimination of malignant lesions when adding the 3D ultrasound to 3D x-ray images in an initial reader study using a dual system.²⁶ However, there are challenges for automated ultrasound scanning in the mammographic geometry in a dual-modality breast imaging systems. These challenges include limited penetration depth and difficulty achieving good transducer coupling around the peripheral breast margins. A study by Sinha et al. found that an adhesive spray that preserves image quality worked best for coupling the breast to a solid TPX plastic compression paddle. This study also showed that this adhesive spray minimized motion and that a highly viscous ultrasound gel was most effective for

transducer coupling along the breast peripheral margins.²¹ A study by Li. et al., showed enhanced breast to paddle contact and a reduction in gaps along the breast peripheral margins using a gel detainment dam with the dual-modality breast imaging system.²⁸ Lecarpentier et al. evaluated the ultrasound transmission properties of two dual modality mesh compression paddles.³² They found that by all measures, polyester mesh fabrics of 1 and 2 mm spacing outperformed the original solid TPX paddle. A study by Larson et al., compared the use of single-sided and dual-sided ultrasound in the mammographic setup using a breast phantom and reported improvement using dual-sided ultrasound in image quality from a mean contrast-to-noise ratio of 57% (single-sided ultrasound) to 79% (dual-sided ultrasound) and breast volume coverage from 59% (single-sided ultrasound) to 89% (dual-sided ultrasound).³³

The disadvantage to the previous methods described above is that all studies to date have not completely addressed issues of poor ultrasound transducer coupling along the breast periphery in the mammographic geometry. Additionally, a combined 3D x-ray/ultrasound system is not yet FDA approved or commercially available. An alternative to the combined system is to image the breast using a 3D x-ray modality (e.g. DBT or dedicated breast CT (bCT)) and then image the breast using an ABUS modality in their own respective geometries and then use a deformable mapping technique to relate corresponding lesions. This has the advantage of better acoustic coupling and improved breast coverage with ultrasound. However, this method has greater technical difficulty in relating corresponding lesions due to the differences in patient positioning and compression during image acquisition.

This thesis describes and validates novel automated deformable mapping methods to register lesions between 3D mammography (DBT and bCT) and 3D ultrasound (ABUS) breast image datasets. This method involves the use of finite element modeling and analysis to simulate the

differences in compression and breast orientation to better relate corresponding lesions between these modalities. This utilizes imaging equipment that is often already commercially available with small changes in current imaging protocols. Such a method should help simplify the time it takes a radiologist to review breast images and improve radiologist's characterizations of breast lesions, which in turn should reduce patient callbacks, misdiagnoses, and negative biopsies. This method can also be especially beneficial for women with dense breasts or multiple breast lesions.

1.2 Dissertation Outline

This dissertation serves as a detailed investigation of novel deformable mapping techniques to relate corresponding lesions between 3D x-ray (DBT, and simulated bCT) and 3D automated breast ultrasound images to address issues related to multimodality breast registration. These investigations have allowed the development of deformable mapping algorithms using breast test objects (phantoms) through extensive simulation using biomechanical modeling. Additionally, for DBT to ABUS registration, these algorithms are tested with clinical datasets. The body of this dissertational text is organized as follows:

Chapter 2: This chapter will provide background information of topics that provide a framework to this thesis. It will begin with a discussion of the breast anatomy and understanding the importance of breast density. Next, the imaging modalities that are used are further described, specifically looking at their differences in patient positioning and the use of compression during image acquisition. This chapter also looks at a preliminary study of an ultrasound camisole that was designed and tested to be used in ABUS imaging for the patient study discussed in Chapter 6. Lastly, this chapter will go over the fundamental principles of the FEM which is used as the primary tool for registration between lesions in modalities.

Chapter 3: This chapter describes the development of a deformable mapping algorithm that uses the FEM to relate corresponding lesions between the DBT cranio-caudal (CC) view and a single ABUS view using two breast phantoms (test objects). This chapter provides the framework for all the deformable registration cases analyzed within this thesis. It compares the validity of this method using locational information from external fiducial markers to aid in the registration process. The results show up to 28% improvement in lesion registration with the use of external fiducial markers during registration analysis.³⁴

Chapter 4: This chapter extends upon the work in Chapter 3, by showing results of registering CC and medial lateral oblique (MLO) DBT views to an ABUS volume using the automated deformable registration algorithm. One compressible breast phantom with 20 simulated lesions was used for this analysis. The results show improvements in registering 14 to 17 corresponding lesions from the DBT (CC view) to ABUS and 9 to 17 registered lesions for the DBT (MLO view) to ABUS when external fiducial markers were employed in the analysis.³⁵

Chapter 5: This chapter describes the development of an automated deformable mapping algorithm to register bCT images to DBT (CC and MLO views) and to register bCT images to ABUS images. This study uses the same compressible phantom from Chapter 4 that contains 20 simulated lesions. The algorithm uses FEM to simulate plates that compress the bCT model to register to DBT (CC and MLO views) and ABUS views. Using external fiducial markers there was improvement up to 49% in the reduction in d_{COM} for bCT to ABUS registration, 57% improvement in the reduction in d_{COM} for bCT to DBT (CC) registration, and 40% improvement in the reduction in d_{COM} for bCT to DBT (MLO) registration.³⁶

Chapter 6: This chapter describes an IRB-approved proof-of-concept validation study with patient image datasets containing known masses using the deformable registration techniques

described in Chapters 3 and 4. The deformable mapping algorithm is tested on 5 clinical data sets for DBT (CC and MLO) registration to ABUS. This study compares the deformable FEM-based registration using none or various external marker combinations (specific quantities and locations). The deformable results are compared to results from using a rigid registration. Results show up to 5 times improvement using the deformable method over rigid registration based on 5 subjects with 13 total registrations. This study shows the superiority of the deformable registration technique to rigid registration and displays how the deformable registration algorithm can be translated for clinical use.

Chapter 7: This chapter summarizes the major findings, conclusions, and limitations of this dissertation. It discusses future works that include registration and stitching of multiple ABUS views for improvement in the deformable registration to ABUS images and the potential use of ultrasound tomography to DBT lesion registration.

Chapter 2

Breast Imaging Acquisition and Finite Element Methodology

This chapter will give an overview of the breast imaging techniques and registration methods used within this thesis.

2.1 Breast Anatomy and Density

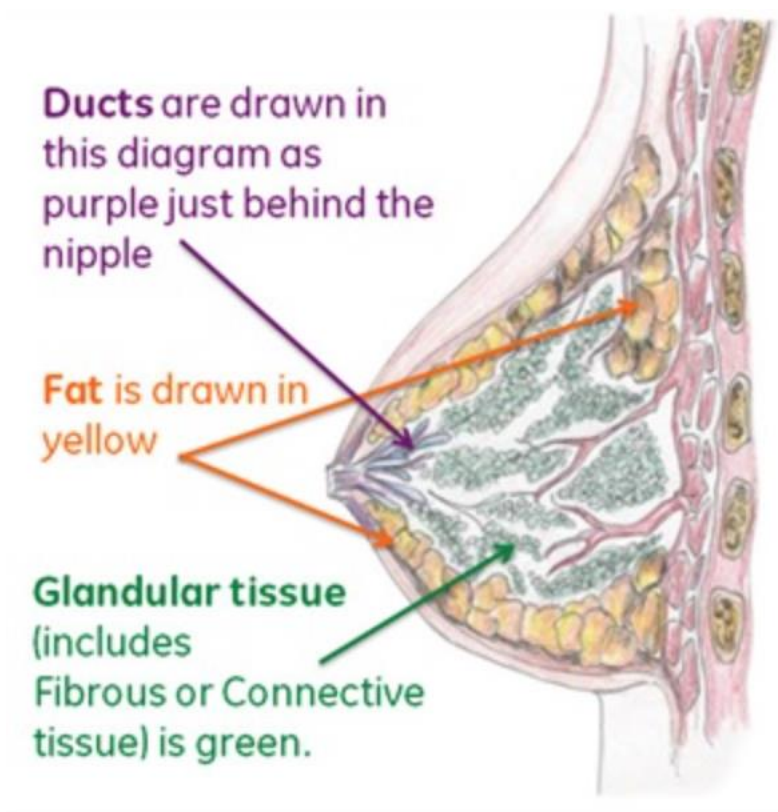


Figure 2.1 Schematic of adult female breast anatomy (figure used with permission from GE Healthcare³⁷)

Familiarity with breast anatomy is important to understand how the breasts' various structural components (e.g. glands, skin, ligaments, fat and ducts) can affect the breasts' shape during imaging positioning and while the breast is under compression. The breasts are located on the anterior portion of the chest (over the pectoralis major muscle) and are scientifically known as the mammary glands. The female breast is predominately composed of skin, lobules, ducts, adipose, and the connective tissue matrix. The glandular lobules and ducts used for milk secretion are surrounded by connective tissues. Each breast consists of 15-20 lobes that are separated by adipose (fatty) tissue. Each lobe contains smaller compartments known as lobules. The lobules are composed of clusters of milk secretion glands known as alveoli within the connective tissue. Milk ducts attach to the glandular lobules. Milk ducts and the glandular lobules are typically referred to as fibroglandular tissue. Each breast has a nipple that is a pigmented projection on the exterior breast where milk is excreted from the body. The suspensory ligaments of the breasts (Cooper's ligaments) run between the skin and breast fascia to add support for each breast. These ligaments tend to become looser as a woman ages. A schematic of the breast's anatomy is shown in Figure 2.1³⁷.

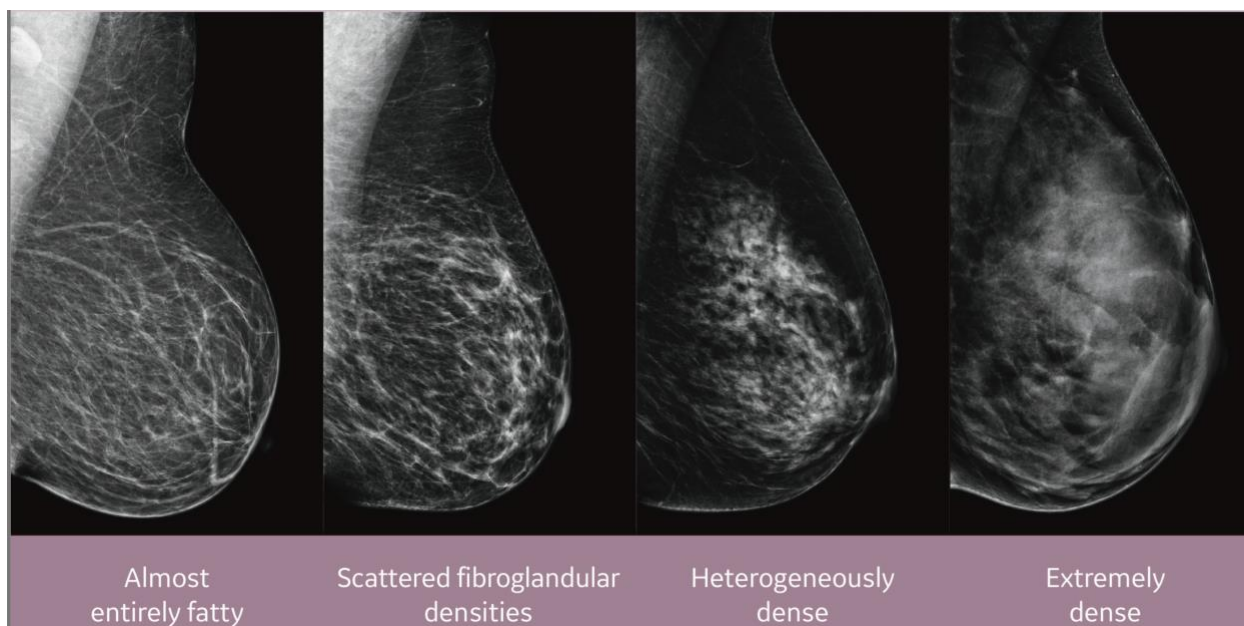


Figure 2.2 BI-RADS breast density category examples from mammography (figure used with permission from GE Healthcare³⁸)

Breast density is a measure of the amount of dense (glandular and fibrous) tissue volume to the total breast volume as seen on a mammogram.³⁹ To have a higher concentration of fibroglandular tissues constitutes a dense breast. Currently, radiologists use the Breast Imaging Reporting and Data System, or BI-RADS⁴⁰, to classify breast density into 4 major categories that go from breasts that are almost entirely comprised of fatty tissue to extremely dense breast tissue. Examples are shown in Figure 2.2.³⁸ For women with extremely dense breast the sensitivity of mammography is lowest for which an ultrasound examination provides higher sensitivity.

Breast density is one of the strongest predictors of breast cancer risk. Research now suggests that women with high breast density are 4-5 times more likely to develop breast cancer than women with low breast density.^{41,42} Although the sensitivity of mammography for detecting breast cancer is 85%, a study by Kolb et al. showed that for women with dense breast tissue mammography sensitivity is reduced to 47.8-64.6%.¹⁴ High breast density is very common and accounts for 40-50 percent of women in the U.S. population between ages 40-74.⁴³ Dense breasts

are more common for younger women and higher breast density is higher among women of healthy weight than women who are obese.⁴³ Additionally, cancer developed in women with dense breasts are typically associated with more aggressive tumor characteristics such as being larger in size, higher in grade, and estrogen receptor negative over breast masses found in fatty breasts.⁴²

Unfortunately, to date, there is not a consensus as to whether a specific modality or supplementary screening should be used for women with dense breasts. However, a medical provider may suggest additional types of breast imaging to be done from a suspicion in a screening mammogram. For women with dense breasts, supplementary screening can be beneficial for the diagnosis of breast cancer and usually involves using ultrasound. Therefore, a method would be needed to relate lesions between the x-ray and ultrasound modalities.

2.2 Digital Breast Tomosynthesis

Digital breast tomosynthesis, DBT, is an advanced form of breast imaging and known as a 3D form of digital mammography. In mammography, typically two 2D breast images, or mammograms, are taken of the breast during a screening exam. The breast is compressed between a plastic compression paddle and an imaging detector. There are several compression types, the two types that this thesis focuses on are known as the cranial-caudal (CC) and the medial lateral oblique (MLO) compressions. For CC compression, the detector and compression paddle are parallel to the floor and the compression paddle compresses the breast downward to the detector to produce a top-to-bottom view of the breast also known as the CC view. CC compression is shown in Figure 2.3(a). For MLO compression, the detector and compression paddle are angled to approximately 45° from the vertical and compresses the breast from the

medial to lateral breast margins. The MLO view incorporates imaging of the axillary and shoulder regions, and the pectoral muscle. MLO compression is shown in Figure 2.3(b).

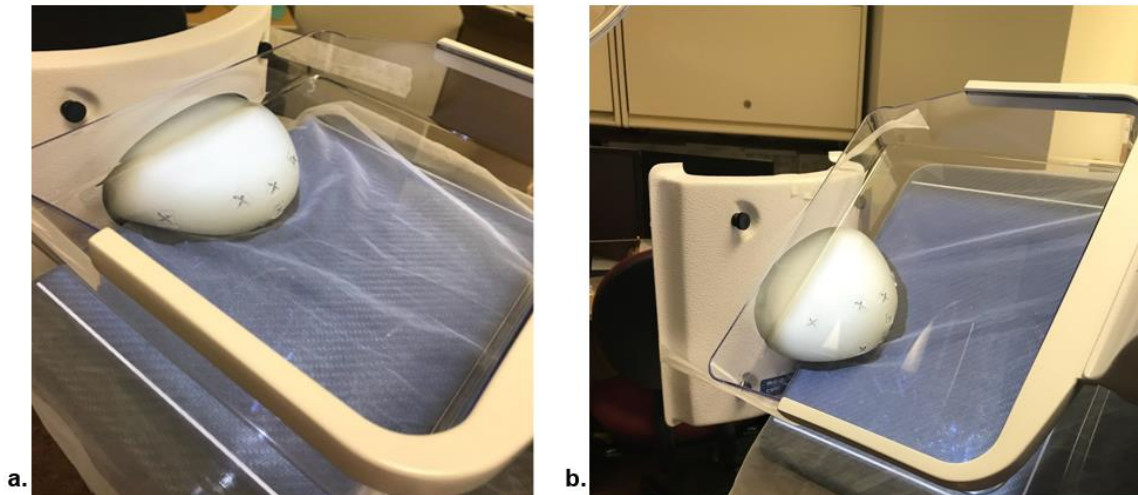


Figure 2.3 Examples of mammographic compression types of a breast mimicking test device for (a) cranio-caudal compression and (b) medial lateral oblique compression Note: The sheer fabric is typically not used on the detector plate during breast imaging

Breast compression is necessary to produce improved image quality and reduce the dose to the patient. However, since in mammography a single 2D image which can cause abnormal tissue to be hidden due to the superposition of tissues. In DBT imaging, the x-ray tube takes multiple projections while moving across a limited angled arc while the breast is compressed in the mammographic geometry. This allows multiple images of each breast to be taken at various angles as shown in Figure 2.4⁴⁴. These digital projections are reconstructed using computer algorithms to create quasi-3D images of the breast. These projections can help minimize tissue superposition and make it easier to distinguish lesions within images. Each reconstructed image slice shows a different depth within the breast which will show some breast structures in and out of focus. Due to the limited tomographic angle and the limited number of projections, structures that are out of focus typically generate artifacts in the axial direction in their neighboring reconstructed slices.

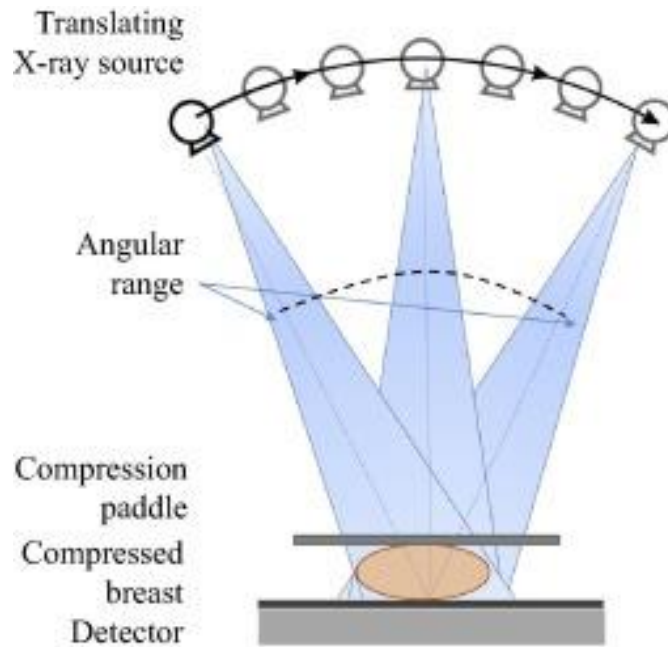


Figure 2.4 Schematic of image acquisition of a digital breast tomosynthesis imaging system (figure used with permission from Rodríguez-Ruiz et al.⁴⁴)

DBT is able to locate cancers that are masked by the digital mammogram. Studies have shown a general decrease in recall rate and an increase in cancer detection with the addition of DBT to digital mammography.⁴⁵⁻⁴⁷ Additionally, DBT imaging has been shown to reduce recall rates and increase cancer detection rates over mammography in both screening and diagnostic uses for imaging women with dense breasts.⁴⁸

2.3 Dedicated Breast Computed Tomography

Dedicated breast computed tomography, bCT, is a new and emerging technology that unlike DBT provides complete 360° angle acquisition of the breast using cone-beam CT. In bCT, the patient lies prone (face-down on her stomach). One breast is placed through an opening of the table and the CT scanner and detector combination rotate 360° around the breast. Each breast is scanned separately in the pendant position without compression as shown in Figure 2.5⁴⁹. By

using a cone-beam CT, x-rays are taken for many angles and provide a true 3D image using the same amount of radiation as mammography.

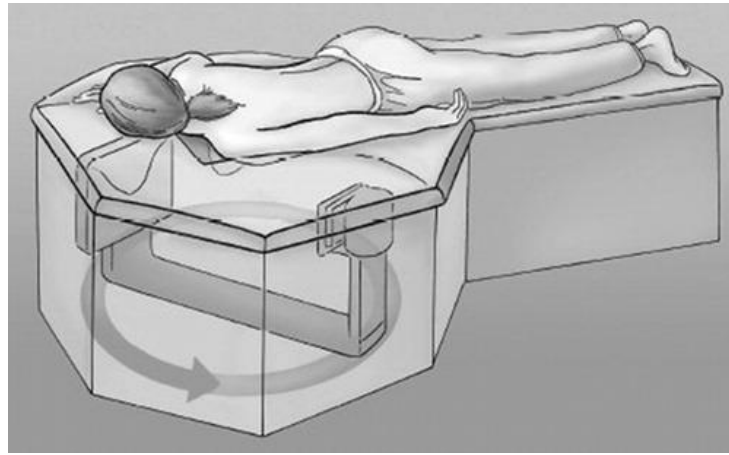


Figure 2.5 Schematic of image acquisition for dedicated breast CT imaging system (figure used with permission from Lindfors et al.⁴⁹)

In comparison to mammography, bCT is only proposed to be utilized for diagnostic purposes unlike mammography which is used for screening and diagnostic breast imaging. bCT is superior to mammography in several ways. By providing 3D images, bCT eliminates image artifacts due to the superposition of tissue due to the overlaying of normal breast structures in comparison to 2D mammographic images. By eliminating superposition this could potentially be helpful for women with dense breasts where breast tissue often masks suspicious lesions. Imaging with bCT also eliminates the need for compression with the use of cone-beam CT. In a study comparing the visualization of 180 lesions with non-contrast bCT vs. mammography, Lindfors et al. found that the conspicuity of masses was superior for bCT, but the conspicuity of calcifications was inferior.⁵⁰ Similarly, in a study of 24 breast lesions, Kuzmiak et al. found that the reader visualization confidence scores for the shape and margins of masses were statistically significantly greater for bCT compared to digital mammography.⁵¹ Also, the reader visualization confidence scores for the morphology and distribution of microcalcifications were statistically significantly worse for bCT compared to digital mammography.⁵¹

bCT has several advantages over DBT. bCT imaging has demonstrated an improved and constant slice sensitivity profile which for DBT imaging worsens with increasing object size and as a result of a limited tomographic angle.⁵² Additionally, bCT provides imaging of the breast at any desired plane with near isotropic resolution, whereas DBT imaging suffers from poor resolution in the axial plane. bCT is superior in the reduction of superposition by imaging with a higher number of projections over a complete 360° angle whereas DBT images have artifacts due to the limited acquisition angle and a lower number of projections.⁵³ Lastly, bCT imaging does not use compression of the breast which increases patient comfort during image acquisition.

2.4 Automated Breast Ultrasound

Conventional ultrasound imaging uses sound waves to produce real-time 2D images of the breasts' internal structures. While a patient lies supine the patient is imaged by ultrasound with a transducer probe and ultrasound gel or lotion that is applied directly to the skin. Ultrasound gel or lotion is used as a coupling agent to ensure the high-frequency non-ionizing sound waves transmitted from the transducer into the breast. The sound signals are reflected and scattered back to the transducer and an algorithm uses the returning sound waves to generate a real-time 2D image of the breast.

Ultrasound breast imaging used in complement with mammography has shown large improvement in the characterization of breast lesions,¹⁶⁻¹⁸ particularly in women with dense breasts⁵⁴. Ultrasound imaging used in combination with mammography has been shown to improve the radiologists' overall characterization of breast lesions by aiding in the determination of whether a lesion is solid or cystic.¹⁶⁻¹⁸ Ultrasound imaging has also aided in finding breast lesions that were not seen in mammography due to dense breast tissue.⁵⁴ DBT imaging improves lesion detection in comparison to mammography alone. However, DBT imaging can still miss

cancers that ultrasound can identify based on lesion similarities located within dense tissue structures of the breast.⁵⁵ A recent study by Chouldhery et al. concluded that 98% of DBT screen-detected masses can be properly assessed with a diagnostic ultrasound alone without the need for diagnostic mammography. This study indicates the potential for avoiding a diagnostic mammogram for the evaluation of majority of DBT screening-detected masses.⁵⁶ A solid lesion may be a non-cancerous lesion (e.g. fibroadenomas) or a cancerous tumor. A fluid-filled lesion (e.g. cysts) are also non-cancerous and very common.

Conventional breast ultrasound imaging is performed freehand and therefore these 2D images are often difficult to reproduce due to high operator dependence. Automated breast ultrasound, ABUS, visualizes the breast as a 3D image volume by allowing automated 3D ultrasound imaging for the entire breast. ABUS technologies have advantages over conventional breast ultrasound in terms of reproducibility, operator independence, and acquisition speed.³⁻⁵ Several studies have also shown the addition of ABUS imaging used in conjunction with mammography screening for women with dense breasts (ACR3 or ACR4) has significantly improved the breast cancer detection rate with an acceptable recall increase.^{19,57,58}

However, ABUS has several disadvantages in comparison to conventional handheld ultrasound in relation to breast coverage and lesion diameter.⁵⁹ A study by An et al. showed that conventional handheld ultrasound is superior for the conspicuity of lesions over ABUS for lesions in the peripheral breast margins, irregular in shape, non-circumscribed margins, and BI-RADS category 4 or 5.⁶⁰ Studies by Chang et al.⁶¹ and Jeh et al.⁶² show the mean diameter of a lesion is important for lesion detectability in ABUS, as smaller lesions are often missed and the rate of lesion detectability increases with size. Some potential rolls for ABUS are follow-up analysis for benign lesions, breast density assessment, and potentially molecular subtypes of

breast cancer.⁵⁹ A study by Padilla et al. indicated increased reader confidence using DBT imaging for breast screening with automated breast ultrasound as a complement.⁶³ A study by Choi et al., shows comparable diagnostic ability between ABUS and conventional ultrasound and reports diagnostic accuracies of 96.5% for conventional ultrasound and 97.7% using ABUS.⁶⁴ A study by Kim et al. shows considerable agreement between masses classified using the BI-RADS categories 4 and 5 between ABUS and conventional handheld ultrasound.⁶⁵

The work in this thesis uses the GE Invenia ABUS (GE Healthcare, Milwaukee, WI) system for all automated 3D ultrasound imaging. When imaged using ABUS, the patient is positioned supine and light anterior to posterior compression is applied by the ABUS transducer panel. This system is FDA approved and uses a curved 153 mm long motor-driven ultrasound transducer that scans the superior to inferior margins of the breast over a mesh compression paddle that is positioned over the breast as shown in Figure 2.6⁶⁶.

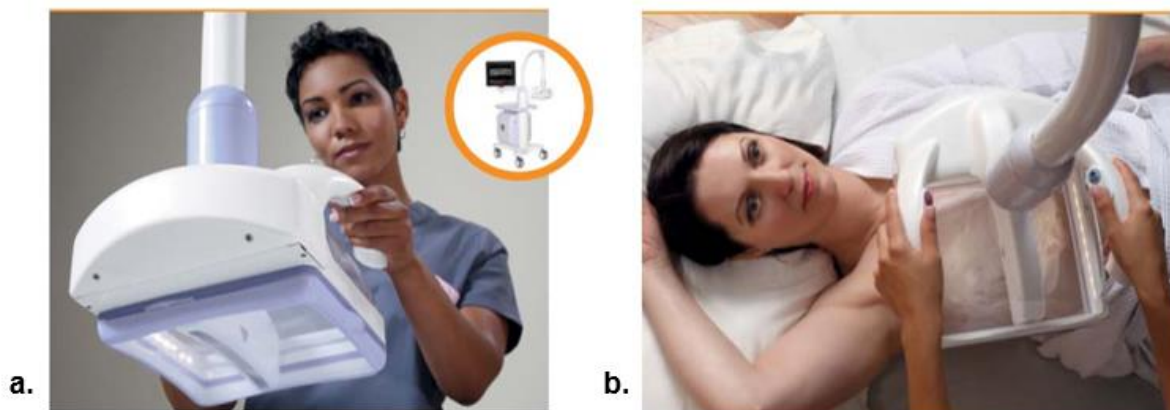


Figure 2.6 Invenia ABUS imaging system a. shown from operator view b. shown imaging a patient (figure used with permission from GE Healthcare⁶⁶)

There are three settings on the Invenia ABUS system (high, medium, and low) based on imaging depth, which changes the frequency setting of the transducer. Depending on breast size, three or more breast image volumes can be acquired to ensure adequate breast coverage during

ABUS imaging. The additional views vary the tilt of the transducer device by imaging the medial and lateral extents of the breast to ensure complete breast coverage as shown in Figure 2.7⁶⁶. It should be noted that additional views not shown in Figure 2.7⁶⁶ can be performed, however, this thesis will not consider those other views. The Invenia ABUS reverse curved transducer has a bandwidth of 6 to 15 MHz and can image up to a 50 mm depth. The transducer travels up to 170 mm across the mesh compression paddle for each scan or view.



Figure 2.7 Illustration of the three different ABUS scans performed on the right breast for an ABUS exam (figure used with permission from GE Healthcare⁶⁶)

2.5 Breast Camisole for ABUS Imaging

An ultrasound camisole was designed (in collaboration with a local seamstress, see Chapter 6 Section 6.8) and evaluated to ensure sufficient image quality, restriction in breast motion, and feasibility with external fiducial markers. Since the breast does not contain any muscles and is comprised of mostly adipose and glandular fascia, it moves relatively freely when various forces act on it. The extent of this can be magnified based on a woman's breast density and age. Since ABUS scanning requires taking multiple projections/views of the breast (as shown in Figure 2.7⁶⁶); a camisole that helps restricts breast motion would be helpful to better relate breast anatomy between ABUS views. This camisole material should not impede in ultrasound depth of penetration, DOP, and also should not obstruct the use of ultrasound coupling gel or lotion. We found that using an ultrasound camisole was helpful in the deformable registration for DBT and

ABUS images which will be further discussed in Chapter 6. A picture of this camisole is shown in Figure 2.8. The front of the camisole is made of a nylon stretchable mesh material and the back of the camisole is made of a cotton-based fabric.



Figure 2.8 Camisole used for ABUS imaging

The camisole is sized based off a woman's band size. A band measurement (underneath the breasts and around the woman's torso to include her back) is taken to determine the adequate camisole size. An elastic band is used in the design in order to provide flexibility in fitting women with various chest diameters. The camisole should be fitted to the breast similar to a sports bra, additional binding clips^a can be used to improve the camisole fit. Other camisoles are currently being used in industry to reduce breast motion during breast imaging and radiation therapy treatments. The company SonoCine (Reno, NV)^b uses an ultrasound camisole to reduce breast motion for 3D ultrasound imaging of the breast using their 3D whole breast ultrasound

^a https://www.staples.com/Staples-Binder-Clips-Medium-1-1-4-Width-5-8-Capacity-Black/product_103549?cid=PS:GooglePLAs:103549&ci_src=17588969&ci_sku=103549&KPID=103549&gclid=EAIaIQobChMI6c-Ch8Pm3wIViANpCh0Zxg4LEAQYBCABEgIjSPD_BwE&akamai-feo=off

^b <http://www.sonocine.com/how-it-works/>

system. In breast radiation therapy treatments, the Chabner XRT Radiation bra^c is used to provide breast support and reproducibility during radiation therapy treatments.

2.5.1 Depth of Penetration Measurements for Breast Camisole

Since this study involves the use of the Invenia ABUS system this camisole material has to be tested with the Invenia mesh panel material to ensure it can be effectively used in conjunction with the Invenia system. Systematic measurements of DOP are among the tests used for ultrasound scanners quality control and can be affected by many factors, including attenuation by materials/fabrics. In order to reduce operator dependence on these parameters automated methods have been used to determine DOP in ultrasound devices. A study by Gorny et al. concluded that measurements based on signal-to-noise (SNR) phantom-images is best suited for routine QC for the clinically important DOP and tested three automated methods for its measurement.⁶⁷

Software developed by Sandra Larson, Ph.D. of the University of Michigan Department of Radiology was used to compute the DOP via minor adaptations of the IEC 61391-2.⁶⁸ Modifications used in this measurement include the setting of the transmit energy at the ultrasound systems highest setting, the positioning of transmit focal distance at the maximum relative to the DOP displayed on the screen, and lastly the setting of the overall system gain and time gain control (TGC) to a level high enough that electronic noise is easily displayed on the ultrasound imaging monitors. In order to calculate the DOP, the uniform section of a tissue-mimicking ultrasound phantom was employed using the GE Logic ML6-15-D linear ultrasound transducer in a water medium. The Invenia ABUS transducer was not used since it is so large in comparison to the phantom; the GE Logic ML6-15-D transducer is often used for breast

^c <http://civcort.com/ro/breast-positioning/treatment-brassiere/Chabner-XRT-Radiation-Bra1.htm>

examinations and operates at a similar frequency range as the Invenia. The maximum DOP is determined from the image SNR ratio vs. depth. The phantom used for this study was the ATS Multipurpose Ultrasound Phantom Model 539^d and is suitable over most clinical frequencies (between 2-20 MHz) for DOP measurements. It has a speed of sound of 1450 m/s and an attenuation coefficient of 0.5 dB/cm/MHz.

This method first requires collecting a cine loop of ultrasound noise, N . This acquisition is taken “in air” therefore showing the ultrasound systemic noise. The “in air” acquisition was taken using the same gain and processing settings described previously. Second, a cine loop of ultrasound images is acquired using the phantom in a water medium to determine baseline values for DOP using the same gain and processing settings. This is repeated several times. First by adding the Invenia mesh material wrapped against the transducer. Then with the Invenia Mesh material still in use, five commercially available fabrics (nylon or polyester based) were tested with the Invenia mesh in the water medium by performing a cine loop with the uniform phantom. A region of interest, ROI, which extends from the bottom of the image to transducer face is used to average the pixel values over the cine loop, $S+N$, as shown in Figure 2.9 for all acquired images.

^d <http://www.atslaboratories-phantoms.com/resources/Model-539-Data.pdf>

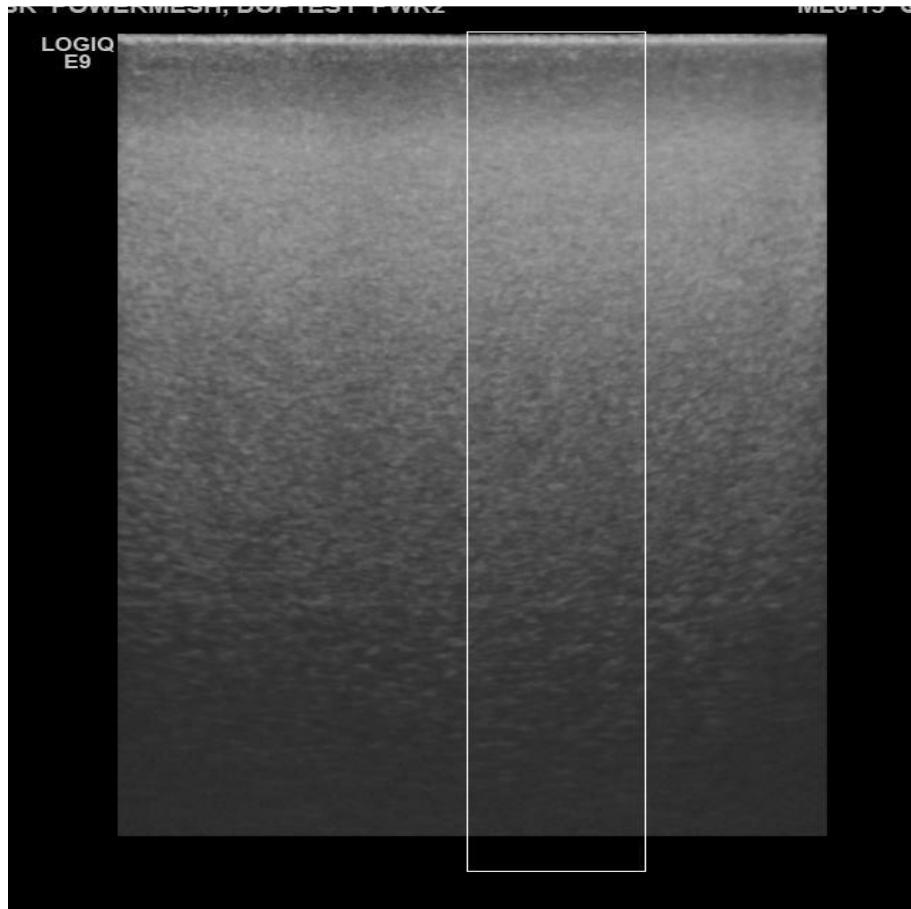


Figure 2.9 ROI of image profile used to average pixel values of full cine-loop independent images

The digitized pixel values from the image data formed in the rectangular ROI shows the mean value, $S+N$. The relative DOP at an imaging depth, d , which is the distance from the transducer face can be determined by plotting the mean pixel value vs the imaging depth. Figure 2.10, illustrates the comparison of $S+N$ and detector noise, N , for the acquired images using the Invenia mesh. The $S+N$ and N are computed horizontally line by line within the ROI (Figure 2.9) progressing from the top to bottom of the image to determine the mean pixel value as shown in Figure 2.10.

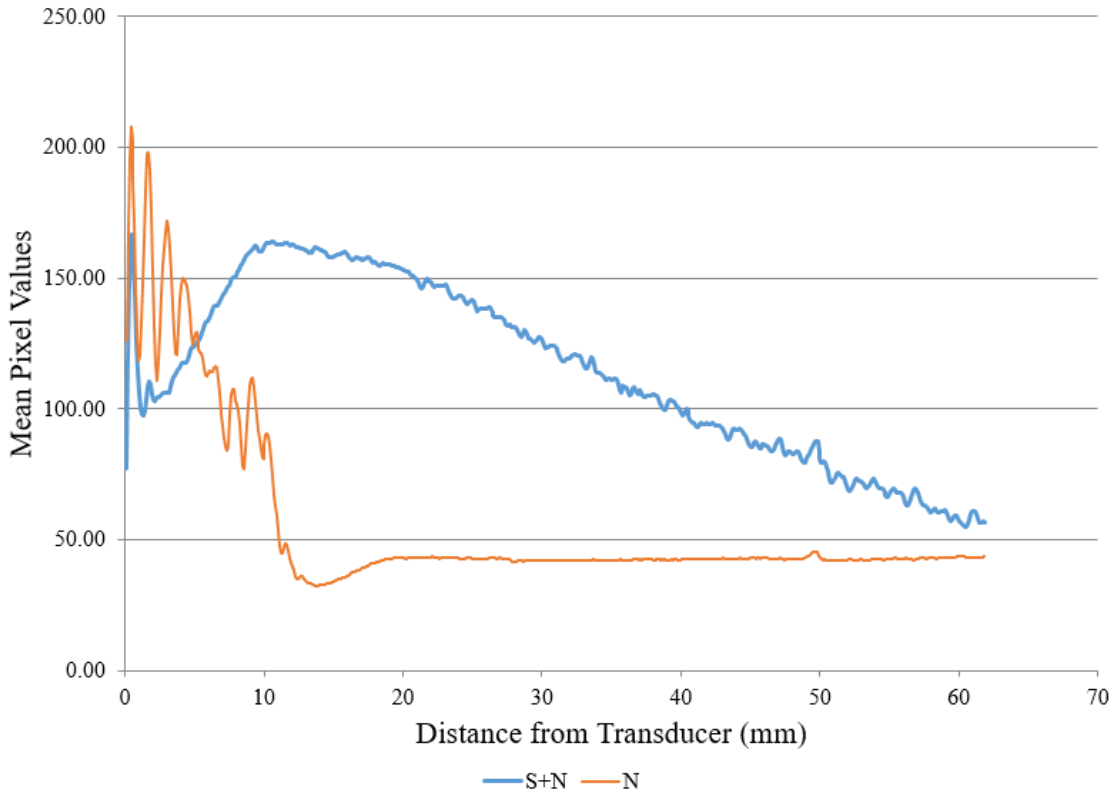


Figure 2.10 Signal and Noise pixel profiles used to determine system sensitivity using the tissue-mimicking water phantom in a water medium measuring the Invenia mesh. $S+N$ = Averaged Image Signal. N = Electronic Noise (acquired from air-only acquisition)

From the above plots the SNR_{IEC}^{68} can be calculated from the graphs shown above for distance, d , values where the $S+N$ values are greater than the N values in Eq.(1).

$$SNR_{IEC}(d) = \sqrt{\frac{SN(d)^2}{N(d)^2} - 1} \quad (1)$$

The corresponding $SNR_{IEC}(d)$ is shown in Figure 2.11.

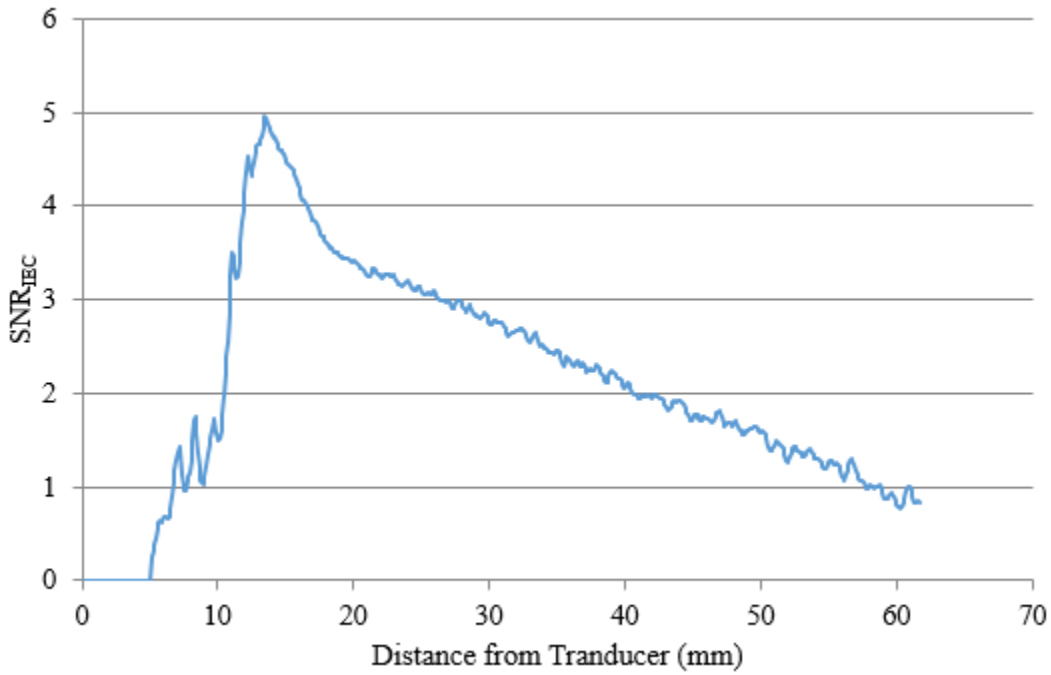


Figure 2.11 Resulting SNR_{IEC} values plotted as a function of imaging depth

The maximum DOP resulting from the SNR_{IEC} is calculated using Eq. 2.

$$SNR_{IEC}(DOP) = 1 \quad (2)$$

This is done by determining a line of best fit for the descending area after the peak in Figure 2.11. The equation that determined the best fit is shown in Eq. 3; this equation is only useful for the specific transducer used in this study. The coefficients a , b , and c are determined by fitting the raw data from Figure 2.11. Once the fit coefficients are determined the substitutions of Eq. 2 is used to solve for the DOP which is taken at the distance, d , to satisfy Eq. 3.

$$SNR_{IEC}(d) = a + b \cdot \ln(d - c) \quad (3)$$

Several potential camisole materials were tested and two were superior. Material 1, *Mat1*, was the 108” Nylon Chiffon Tricot white^e and material 2, *Mat2*, is the 108” 40 Denier Tricot white^f. The DOP-values are recorded in Table 2.1. Other materials tested were Power Mesh^g and Telio Matte Chiffon^h. All the tested materials were a nylon base similar to the Invenia mesh panel and had 10% or greater stretch across the grain in order to better conform to the mold of a woman’s breast.

Table 2.1 Comparisons of DOP between various testing combinations. P= Phantom Only. Inv= Invenia Mesh fabric. Mat 1=108” Nylon Chiffon Tricot, Mat2= 108” 40 Denier Tricot, Mat3= Power Mesh, Mat 4, Mat5= Telio Matte Chiffon

Case ID	Testing Combination	R ² of fit	DOP (mm)	DOP _{Case ID 1} / DOP _{Case ID 2}
1	P only	0.997	58.6	99%
2	P+Inv	0.996	59.4	100%
3	P+Inv+Mat1	0.996	58.3	98%
4	P+Inv+Mat2	0.997	58.9	99%
5	P+Inv+Mat3	0.997	55.6	94%
6	P+Inv+Mat4	0.996	54.3	91%

With the use of the phantom and Invenia mesh only, the DOP increases. This is likely due to uncertainty in measurements. It is also possible that the increased penetration with the Invenia paddle was due to an incidental reduction in air bubbles and improved impedance matching between the transducer and the phantom through the Invenia mesh fabric. Adding the Mat.1 the DOP was maintained by 99% and Mat. 2 maintained the DOP by 98%. Due to cost effectiveness, Mat1 was chosen as the fabric to use for the camisoles for ABUS imaging.

^e <https://www.fabric.com/buy/uf-737/nylon-chiffon-tricot-white>

^f <https://www.fabric.com/buy/uf-733/108-40-denier-tricot-white>

^g <https://www.fabric.com/buy/0450610/power-mesh-white>

^h <https://www.fabric.com/buy/0455281/telio-matte-chiffon-mesh-white>

2.5.2 Efficacy of Breast Camisole for ABUS imaging

The breast camisole is designed to include the nylon material in the front and a cotton based material in the back similar to a sports bra. The breast imaging camisole is shown in Figure 2.8. The camisoles are designed to fit women between dress sizes 0 - 26. An IRB-approved patient study was performed on 10 patient volunteers of different ages (25-51) and breast sizes (breast cup size B-DDD) to evaluate the efficacy of the breast camisole. The purpose of this study was to ensure that the designed camisole was sufficient in restricting breast motion between the multiple views acquired in ABUS imaging and ensure that external markers stayed in place during ABUS imaging. After ABUS imaging was completed the ultrasound technologist evaluated the camisole performance based on completing a check list shown in Figure 2.12.

The protocol for this study and the ABUS camisole form is listed in the Appendix. An overview of the results for all 10 patient volunteers based on the ABUS camisole evaluation form is shown in Figure 2.12. This form is also provided in the Appendix.

ABUS Camisole Form

Patient ID _____

Date _____

Ultrasound Technologist/ Observer Initials _____

	Yes	No	Additional Comments
Were all external markers glued to breast before ABUS imaging?	10		
Did the glued external markers move when ultrasound gel/lotion is added over breast?		10	
Did the glued external markers move when patient puts on ABUS camisole?	4	6	
Was the camisole fitted to the breast?	9	1	1- Needed clips for improved fitting
Does the camisole help restrict breast motion in comparison to if no camisole were not used?	10		
Do the external markers remain in the same position in between ABUS scans?	10		
Did the external fiducial markers have to be repositioned at any time during ABUS exam		10	
Once breast camisole is removed were the external markers still in place?	8	2	

Additional Comments:

Figure 2.12 Tallied Evaluation for efficacy of ABUS Camisole

Based on these results, we can conclude that the ultrasound camisole is sufficient for reducing patient motion. We can also conclude that the external fiducial markers locations that are underneath the material are not compromised during ultrasound imaging. Clips can be used to further improve the fit of the camisole and were needed for one patient in order to ensure proper camisole fit. However, these results also indicate that marker positioning can be compromised when the patient initially puts on the ABUS camisole. This can be minimized by assisting the patient in putting on the camisole, ensuring that enough time (at least 5 minutes) has passed before putting on the camisole after markers are glued, and by marking breast locations (e.g. by using a washable marker) prior to attaching the external markers.

2.6 External Fiducial Markers

External fiducial markers are markers attached to the skin that can be easily recognizable in reconstructed image views. These markers should not obscure much, if any, of the breast tissue images if they are to be used clinically. This study investigates the use of external fiducial markers to help improve the registration between corresponding lesions between 3D x-ray and 3D ultrasound breast images. Several studies have used external fiducial markers and have found improved registration results for MRI/PET breast registration^{69,70}, compressed and uncompressed prone breast MRI⁷¹, and breast MRI to conventional ultrasound⁷². For ultrasound imaging, this marker cannot cause refraction or other distortion artifacts below the skin in ultrasound imaging and should not cause artifacts in 3D x-ray imaging.

A study by Cloutier et al., found that glass bead fiducial markers were useful when imaging a multimodality vascular phantom with digital subtraction angiography, CT angiography and ultrasound.⁷³ We decided to investigate the use of small beads between 0.79 mm - 2 mm in size composed of different material (acrylic, polystyrene, nylon, Teflon, and glass). These are common materials used in x-ray and ultrasound quality control. A thermoplastic elastomer, TPE, gel was melted and degassed in a vacuum oven over each echogenic and x-ray absorbing bead in order to create the external fiducial marker. This clear degassed gel allows for the bead target to be clearly seen in ultrasound imaging in the absence of voids.

Of the bead target combinations, we found that a 1 mm diameter glass bead target within the TPE gel worked best in reducing ultrasound artifacts and not being too attenuating in x-ray imaging. A detailed procedure of how to make this marker is available in the Appendix.

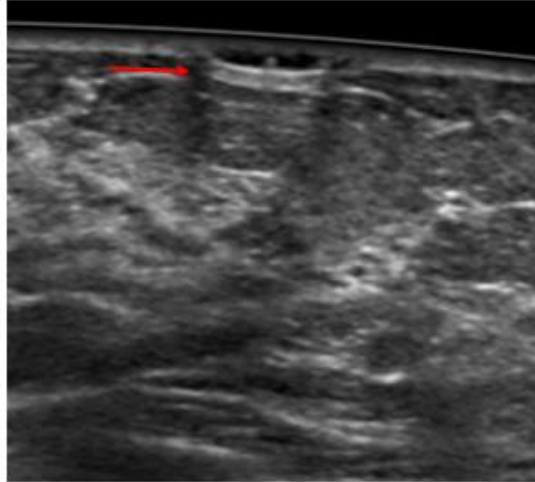


Figure 2.13 Edge artifact of external fiducial marker in ABUS imaging

These markers are glued to the breast and ultrasound gel or lotion is placed over the marker when the breast is imaged. Although the glass bead combination is easily seen in reconstructed ABUS images, we found that edge artifacts are present with these external fiducial markers as shown in Figure 2.13. Depending on marker width and thickness these artifacts can be more pronounced. To reduce the effect of edge artifacts we recommend that the markers are ≤ 3 mm thick and about 3 mm – 5 mm radial diameter surrounding the bead. Adequate ultrasound lotion or coupling gel can also reduce these effects. However, these effects may not be eliminated entirely due to the impedance and speed of sound differences between the marker and the skin and subcutaneous fat.

2.7 Finite Element Method and Analysis

Once images are acquired within this research, the finite element method (FEM) is used to model breast deformation from one image modality in order to register lesions to another breast imaging modality. FEM was used to simulate the difference in breast compression and shape as an effect of the various imaging schemes with this thesis. FEM is a numerical discretization method used to compute approximations for physics laws (e.g. law of conservation of energy,

law of conservation of mass and law of conservation of momentum) for space and time-dependent problems that are typically expressed using partial differential equations (PDEs). For most geometries and engineering problems, these PDEs are complicated and cannot be solved analytically to compute relevant mechanical properties (e.g. stress and strain) to estimate the corresponding behavior (e.g. deformation) of a component under specified loading conditions. Therefore, FEM is used to compute such approximations for various engineering applications such as thermomechanical, biomechanical, electromagnetics etc. Finite element analysis, FEA, is the simulation of any physical phenomenon using the FEM to predict how a structure behaves under specified conditions.

FEM approximates a continuous structure into a mesh of smaller finite elements using simple geometric shapes (e.g. triangles or quadrilaterals for surfaces and tetrahedrons or hexahedrons for volumes). Any point within the finite element structure can be expressed within an element through interpolation of the surrounding mesh nodes through the interpolation of shape functions. Any force/load applied to the structure can be approximated as a function on the interpolated finite mesh. This results in a finite system of equations based on nodal coordinates to approximate the result of the problem. For a more in-depth explanation of the application of continuum mechanics and the theory of FEM discretization involved for biomechanical models see the text from Maurel et al.⁷⁴

FEA for medical application has become increasingly popular and universal for the advancement of biomedical engineering, biomechanics, and clinical research.⁷⁵ There are many studies that have been proposed to model the female breast to simulate deformation for image registration. One of the pioneering efforts for using FEM in modeling and analysis for modeling breast deformations was performed by Samani et al.⁷⁶ This group developed a biomechanical

model for the breast from MRI data.⁷⁶ Shortly after, studies by Azar et al., used 3D hexahedral FE meshes to estimate the location of a tumor during mammographic compression for needle biopsies for three sampled patients.^{77,78} The FEA can be broken into three main sections:

1. Description of the Physical Model. 2. FEA Preprocessing 3. FEA Solution and Post-Processing. Each is described below.

2.7.1 Description of the Physical Model

Before the FEA process can begin a description of the problem must be defined and simplified in order to be solved using FEMs. For this application, it requires that 3D image data must be acquired and segmented (i.e. a breast mass segmented from glandular and fatty tissue). Ensuring accurate geometry is key to successful modeling using FEM and should be defined with sufficient detail in spatial resolution in order to differentiate between the various tissue structures needed for FEA to simulate deformation.

Tissue composition directly contributes to the breast's mechanical behavior and is important to have accurate biomechanical properties of the breast anatomy. As the breast contains a variety of anatomical structures (e.g. blood vessels, ducts, ligaments etc.) the segmentation must be simplified for FEA. Several experimental studies have measured the mechanical properties of breast tissues to determine elasticity, specifically with measurements of fibroglandular and adipose tissues.^{71,79-83} Therefore, biomechanical studies simplify the breast anatomical model to include the skin, fibroglandular, adipose, and lesion (if applicable) for FEA.

Segmentation of each tissue in the acquired image is the process of identifying tissues and differentiating their boundaries from other tissues. Studies have used manual^{71,76}, semi-automated^{84,85}, and automated⁸⁶⁻⁸⁸ segmentation in FE-based breast deformation modeling techniques based on MRI data sets. Within this thesis, large 3D image sets (e.g. ABUS and bCT)

are used and can be laborious and time-consuming. Automated and semi-automated methods should be investigated in order to minimize the time associated with this task. The specific methods used in this text will be discussed in the subsequent chapters but deals with a combination of manual and semi-automated techniques. Once segmentation of all necessary tissues from the 3D imaging data is completed, the corresponding base FE model can be generated.

2.7.2 Finite Element Analysis Preprocessing

Once the simplified physical anatomical structures have been identified and segmented from the acquired image data, the next step involves the discretization and mesh creation of the base FE model for the image data set. Within this text, each tissue is segmented into separate DICOM binary files from which a surface mesh is created of each segmentation. A mesh is a network model body that is formed by many elements (discretized smaller units) that are interconnected at nodes (FE XYZ-coordinate points that serve as boundaries of the mesh). This provides a simulated representation of the outline of the tissue structure in 3D. Surface meshes create up to millions of small elements and their corresponding nodes to generate the 3D shape of the tissue structure from the segmented DICOM files. There are many meshing schemes (e.g. quadrilateral, triangular, pentagonal etc.) that can be used to create the separate elements that discretize the surface mesh. These meshes only show the outline of the segmented DICOM files and are therefore hollow on the inside. Triangular meshing schemes are used within this thesis and examples of the surface meshes or different tissue types are shown in Figure 2.14.

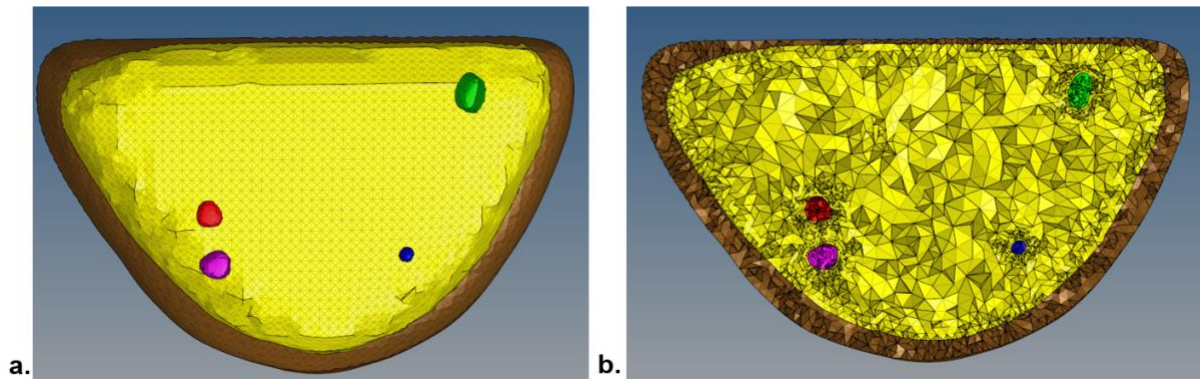


Figure 2.14: Surface meshes of the skin (brown), inner gel (yellow), multiple lesions (pink, red, green and blue) from a breast phantom for (a) surface meshes created from segmented DICOM (Notice surface meshes are hollow on the interior and not filled or connected to one another) (b) tetrahedral meshed model of breast fully connected

For breast FEA literature, there has been a plethora of mesh node density values and it is an ongoing area of research. No experimental study has concluded an optimal value.⁸⁹ Breast plate compression studies have varied the number of elements by hundreds^{86,90} to thousands³⁴, and even tens of thousands^{76,84,91}.

After surface contours are meshed, volumetric meshing is needed to provide a fully connected breast FEA model. For volumetric meshing, tetrahedral and hexagonal meshes are typically used to mesh within a surface mesh volume and allow connectivity between surface components. Most breast studies using FEA have used tetrahedral meshes⁹², however hexahedral meshes have been used in studies by Lee et al.⁶⁰, and Ruitter et al.⁶⁵ The majority of breast FEA has been used on tetrahedral meshes⁸⁹, however there is not a consensus as to which (hexahedral or tetrahedral) meshing scheme is superior. These methods rely on a subdivision algorithm of the volume. A volumetric mesh is built by triangulating each of the cells of the volumes and may slightly change the coordinates of the vertices of the exterior nodes in order to improve mesh quality. Tetrahedral meshing schemes are used within this thesis and examples of the surface meshes or different tissue types are shown in Figure 2.14b.

Material properties (e.g. Young's Modulus, Poisson's Ratio) are assigned to each meshed component in the model. The modulus of elasticity, Young's Modulus (E), is a measure of a material's stiffness and is often calculated from tensile stress (σ) /strain (ε) curves and formulates Eq. 4.

$$E = \frac{\sigma}{\varepsilon} \quad (4)$$

Stress can be defined as the force applied to a specific cross-sectional area of an object. Strain is a dimensionless parameter that is defined as the amount of deformation of a material along the applied force direction divided by the initial length of an object. The Poisson's ratio (ν) is a dimensionless parameter that is defined as the ratio of the transverse strain to longitudinal strain in the direction of the stretching force as shown in Eq. 5. Breast tissues are modelled as incompressible materials having Poisson's ratio nearly 0.50.

$$\nu = -\frac{\varepsilon_{transverse}}{\varepsilon_{longitudinal}} \quad (5)$$

For the phantom studies within this thesis, the manufacturer provided information for the material properties as described in Chapters 3-5. For real breasts, there is high variability in the moduli of elasticity, Young's Modulus, as this is still a current area of research. Studies by Kruse et al.⁸³, Sinkus et al.^{80,94}, and McKnight et al.⁹⁵ used in vivo magnetic resonance elastography in order to quantify the elastic modulus for adipose, glandular, and carcinoma breast tumors. A study by Gefen et al. showed the Young's modulus for glandular tissue ranges from 7.5 kPa - 66 kPa and adipose tissue ranges from 0.5 kPa – 25 kPa.⁸² A study by Athanasiou et al. used supersonic shear wave imaging on 46 women with 48 breast lesions where the mean elasticity

values was 146.6 ± 40.05 kPa for malignant lesions and a mean elasticity value of 45.3 ± 41.1 kPa for benign breast lesions.⁹⁶ A study by Kellner et al., determined the skin, fat and glandular elastic moduli for FEA simulations for bCT plate compressions based on a combination of published results.⁹⁷

The physical constraints (or boundary conditions) are defined to approximate the loading of the model. These prescribed boundary conditions define the force or nodal displacement needed to determine the resulting stress-strain deformation on types of breast tissues based on set material characteristics. For example, for a bCT FE model that is compressed to the DBT (CC view) imaging model, this involves applying loading on compression plates to simulate CC plate compression on an uncompressed bCT breast. For DBT FE deformed to ABUS this involves nodal loading displacements that will be described in greater detail in Chapters 3, 4 and 6.

Once boundary conditions are defined, specifications of analysis types need to be determined as an indicator to the FEA solver as to which types of equations need to be used in order to approximate the result of the model. There are many analysis types that can be used within FEA (e.g. heat transfer, fatigue, linear buckling). For breast deformation static or quasi-static (quasi-Newtonian) stress analysis is most commonly used. The difference between static and quasi-static is that static analysis neglects a time dependent material response. Both analysis types include linear elastic or nonlinear elastic analysis and neglects inertial effects. An elastic material is defined a material whose stress is dependent on the materials' strain.

Studies by Tanner et al.⁸⁴ and Alonzo-Proulx et al.⁹⁸ used linear elastic models when modeling large breast deformation. However, non-linear model analysis is considered more accurate for large breast deformations.⁸⁹ Work involved in this thesis also found non-linear

elastic quasi-static analysis yielded more precise results for the applications due to large deformation involved in the various modality registration.

For linear solutions the basic FEM equation to be solved is Eq. 6⁹⁹

$$[K]\{u\} = \{F\} \quad (6)$$

Where K is the elastic stiffness matrix, u is displacement vector and F is the vectors or loads applied to the structure. Eq. 6 is solved for the displacement vector. Thus, creating a set of simultaneous algebraic equations at each node within the FE model. Since all elements are interconnected through their nodes FEM uses piecewise polynomial interpolation to resolve a set of simultaneous equations at each node within the model. Linear solutions assume a homogenous deformation and neglect the interdependency of stress and strain.

For non-linear solutions Eq. 6 is modified to in Eq. 7.¹⁰⁰

$$[K(u)]\{u\} = \{F\} \quad (7)$$

Where, $K(u)$ is the nonlinear stiffness response matrix of the nodal system reactions which is a function of u , u is the displacement vector, and F is the total force/loading vector. Non-linear solutions are generally history dependent as the solution is obtained in a series of small increments. Therefore, the model equilibrium equation is solved for each increment using Newton's method.

2.7.3 Finite Element Analysis Solutions & Post-Processing

Once all these considerations are performed an input file can be generated and a FEA solver is used in order to simulate the deformation of the input breast model using FEM. The FEA solver solves the set millions of differential equations which approximates the resulting stress,

strain, and nodal displacements of the models based off the loading scheme. Implicit FEA is used using non-linear quasi-Newton analysis and large displacement theory to determine the deformation of the breast within this dissertation.

Nonlinear analysis using quasi-Newtonian techniques, by satisfying the equilibrium equation at each step while ignoring inertial and momentum effects, allows a dynamic problem to be solved as a static problem by simplifying the problem into incremental load steps.¹⁰¹ After each increment, the FE breast model geometry changes and therefore the stiffness matrix needs to be updated for the sequential increment. For explicit analysis, the incremental procedure is done such that the increments are small enough for the results to be accurate. The problem with using explicit analysis is that many small increments are needed for accuracy and analysis convergence which is time consuming and this method does not enforce equilibrium.¹⁰² Implicit analysis uses the same incremental procedure however, equilibrium is enforced using Newton's methods. Implicit analysis can handle more sophisticated problems. However, implicit analysis can be even more time consuming because the stiffness matrix must be updated and equilibrium is checked at the end of each increment.¹⁰² All studies in this dissertation used implicit analysis with quasi-Newtonian techniques for the non-linear analysis and large displacement theory.

The quasi-Newton method is then applied to enforce equilibrium of the internal structures of within the simulated breast model based on the external loads being applied to it.

Eq. 7 can be rewritten to show the application of the Newton method for a typical iteration, i , as follows^{100,102}:

$$[K_i(u_i)]\{\Delta u\} = \{F\} - \{F_i\} \quad (8)$$

Where, $K_i(u_i)$, is the Jacobian nonlinear stiffness response matrix (the structural stiffness for computing element displacements within the model) for current iteration, Δu is the change in the DOF displacement vector between the previous and current iteration, and F_i is the vector of internal force vector determined from elemental stresses in the current iteration. For each iteration $K_i(u_i)$ and F_i is evaluated from u_i . The next approximation is then made, u_{i+1} , as shown in Eq. 9¹⁰⁰.

$$\{u_{i+1}\} = \{\Delta u\} + \{u_i\} \quad (9)$$

The process repeats until the right hand side of Eq. 8 converges or $\{F\} - \{F_i\} = 0$.^{100,102}

Quasi-Newton analysis modifies the above equations when the regular Newton method is too difficult or time-consuming to evaluate for $K_i(u_i)$. Instead of obtaining the $K_i(u_i)$ at a single point, quasi-Newton methods gradually build up an approximate $K_i(u_i)$ by using gradient information from the previous iterations of $K_i(u_i)$. Various quasi-Newton techniques can be used depending on the FEA solver system. Quasi-Newton methods were first introduced by Charles Broyden¹⁰³ and he extended upon this works to include a more detail analysis of minimization algorithm of the DFP (David- Fletcher- Powell formula) method¹⁰⁴ and the Davidson formula in 1970.¹⁰⁵ The work in this thesis incorporates the use of commercial software packages for FEA specifically Optistruct (Altair Engineering, Troy, MI) and ABAQUS (Dassault Systèmes Americas Corp., Waltham, MA). ABAQUS implements the BFGS (Broyden-Fletcher-Goldfarb-Shanno) stiffness update that was shown by Matthies and Strang to help simplify systems of equations in nonlinear applications where the Jacobian is symmetric and not highly variable from one iteration to the next.¹⁰⁶ More information about the quasi-Newton methods can be found in

the ABAQUS documentation.ⁱ Similar information for Optistruct can be found in its documentation.^j

Commercial, open-source, and in-house codes can be used to solve these systems of equations. Commercial FEA solvers typically provide complete tools for FEA through the pre-processing, post-processing, and visualizations for the model generation and results. Studies by Hopp et al.^{88,107} and Samani et al.⁷⁶ have used ABAQUS to simulate breast deformations. Likewise, studies by Tanner et al.^{71,84,108}, Ruiter et al.⁹⁰, Unlu et al.⁷⁰ used the commercial FEM package ANSYS for simulating breast deformation. Once the FEA is completed, the deformation results can be applied to the base FE model for registration considerations.

This thesis shows the implementation of this software by using FEM for breast deformation for different registration schemes. Unlike in the previous studies mentioned, nodal displacement is used to relate breast lesions from DBT to ABUS views instead of solving for the plate compression and decompression between these modalities. The use of nodal displacement in FEA for the two compressed states allows for the method to be more transferrable for use in the clinic in comparison to modeling plate compression. Nodal displacement was used because without uncompressed image data of the breast (e.g. as done in MRI or bCT) there is no way to verify a breast in its uncompressed state after DBT compression in the upright geometry and before ABUS compression in the supine geometry. These specifics will be further discussed in Chapter 3, 4 and 6. For bCT to DBT and bCT to ABUS registration the use of plates was used to model the breast deformation and will be further discussed in Chapter 5.

ⁱ<https://www.sharenet.ca/Software/Abaqus610/Documentation/docs/v6.10/books/stm/default.htm?startat=ch02s02at h15.html>

^jhttps://altairhyperworks.com/hwhelp/Altair/2017/help/os/topics/solvers/analysis_nonlinear_quasi_static_c.htm

Chapter 3

Deformable Mapping Technique to Correlate Lesions in Digital Breast Tomosynthesis and Automated Breast Ultrasound Images^k

3.1 Abstract

Purpose: To develop a deformable mapping technique to match corresponding lesions between digital breast tomosynthesis (DBT) and automated breast ultrasound (ABUS) images.

Methods: External fiducial markers were attached to the surface of two CIRS multi-modality compressible breast phantoms (A and B) containing multiple simulated lesions. Both phantoms were imaged with DBT (upright positioning with cranial-caudal compression) and ABUS (supine positioning with anterior-to-chest wall compression). The lesions and markers were manually segmented by three different readers. Reader segmentation similarity and reader reproducibility were assessed using Dice similarity coefficients (DSC) and distances between centers of mass (dCOM). For deformable mapping between the modalities each reader's segmented dataset was processed with an automated deformable mapping algorithm as follows: First, Morfeus, a finite element (FE) based multi-organ deformable image registration platform,

^k This work is published in the *Medical Physics Journal*: Green CA, Goodsitt MM, Brock KK, et al. Deformable mapping technique to correlate lesions in digital breast tomosynthesis and automated breast ultrasound images. *Med Phys.* 2018;45(10):4402-4417. doi:10.1002/mp.13113. Note: Italicized text in this chapter was not included in the original publication and is used to provide supplementary information.

converted segmentations into triangular surface meshes. Second, Altair HyperMesh, a FE pre-processor, created base FE models for the ABUS and DBT data sets. All deformation is performed on the DBT image data; the ABUS image sets remain fixed throughout the process. Deformation was performed on the external skin contour (DBT image set) to match the external skin contour on the ABUS set, and the locations of the external markers were used to morph the skin contours to be within a user-defined distance. Third, the base DBT-FE model was deformed with the FE analysis solver, Optistruct. Deformed DBT lesions were correlated to matching lesions in the base ABUS FE model. Performance (lesion correlation) was assessed with d_{COM} for all corresponding lesions and lesion overlap. Analysis was performed to determine the minimum number of external fiducial markers needed to create the desired correlation and the improvement of correlation with the use of external markers.

Results: Average DSC for reader similarity ranged from 0.88 to 0.91 (ABUS) and 0.57 to 0.83 (DBT). Corresponding d_{COM} ranged from 0.20 to 0.36 mm (ABUS) and 0.11 to 1.16 mm (DBT). Lesion correlation is maximized when all corresponding markers are within a maximum distance of 5 mm. For deformable mapping of phantom A, without the use of external markers, only 2 out of 6 correlated lesions showed overlap with an average lesion d_{COM} of 6.8 ± 2.8 mm. With use of 3 external fiducial markers, 5 out of 6 lesions overlapped and average d_{COM} improved to 4.9 ± 2.4 mm. For deformable mapping of Phantom B without external markers analysis, 4 lesions were correlated out of 7 with overlap between only 1 of 7 lesions, and an average lesion d_{COM} of 9.7 ± 3.5 mm. With 3 external markers, all 7 possible lesions were correlated with overlap between 4 out of 7 lesions. The average d_{COM} was 8.5 ± 4.0 mm.

Conclusion: This work demonstrates the potential for a deformable mapping technique to relate corresponding lesions in DBT and ABUS images by showing improved lesion correspondence

and reduced lesion registration errors with the use of external fiducial markers. The technique should improve radiologists' characterization of breast lesions which can reduce patient callbacks, misdiagnoses and unnecessary biopsies.

3.2 Introduction

Ultrasound imaging used in conjunction with mammography has been shown to improve characterization of breast lesions.^{16–18} Conventional ultrasound imaging is performed freehand in a different geometry (supine) than mammography (upright). Since the acquisition is freehand, the 2D ultrasound images are difficult to reproduce. Automated breast ultrasound, ABUS, visualizes the breast as a 3D image volume and has advantages in terms of reproducibility, acquisition speed and operator independence over conventional breast ultrasound.^{18,19,57} Likewise, studies have also shown the addition of ABUS imaging used in conjunction with mammography screening for women with dense breasts (ACR3 or ACR4) has significantly improved the breast cancer detection rate with an acceptable recall increase.^{19,57,58} Digital breast tomosynthesis, DBT, provides better detection and characterization of breast lesions over mammography through the reduction of tissue superposition. However, DBT has not completely eliminated the need for the use of ultrasound.^{109,110} One problem with the use of ultrasound in conjunction with mammography/DBT is that at least 10% of the time, the lesions found in the ultrasound images do not correspond to those found in mammograms/DBT.¹⁵

One solution to this problem is to develop a combined x-ray/ultrasound system that images the breast in the same upright geometry using a special dual-modality compression paddles.^{21,22,24–30} However, the simpler single-sided combined systems are limited in ultrasound depth of penetration, and all studies to date have not completely addressed issues of poor ultrasound transducer coupling at the periphery of the breast in the mammographic geometry.

Some improvements such as dual sided ultrasound¹¹¹ for better coverage and resolution have been explored but have not yet been implemented into a single combined system. An alternative to the combined system is to image the breast with the DBT and ABUS modalities in their own separate geometries and then use a deformable mapping technique to relate corresponding lesions. This has the advantage of better acoustic coupling and possibly better coverage of the breast with ultrasound. It utilizes DBT and ABUS systems that are already commercially available and does not require the extra expense of purchasing a special combined system. However, a deformable mapping method has the disadvantage of greater technical difficulty in relating corresponding lesions.

To date, there are no deformable registration techniques for detecting corresponding lesions between ABUS and DBT breast images. The purpose of the present study is to investigate the viability of a deformable mapping method to relate corresponding lesions between DBT and ABUS breast images. Such a method should simplify and improve radiologist's characterizations of breast lesions which can reduce patient callbacks, misdiagnoses, and negative biopsies. Using finite element analysis, FEA, a biomechanical algorithm can be used to relate regions of interest between modalities, so a radiologist can directly verify that a lesion seen in a DBT view is solid or cystic as determined from the ABUS image set.

To produce FE based biomechanical models, segmentation of the entire breast volume is required for creation of surface and volumetric meshes. Defining the boundary between breast tissue and the pectoral muscle and distinguishing between glandular, connective, and adipose tissues poses difficulty for segmentation of breast images. Studies have used manual^{71,76}, semi-automated^{84,85}, and automated⁸⁶⁻⁸⁸ segmentation in FE-based breast deformation modeling. For

large deformations due to breast compressions non-linear models have proven to be more effective than linear elastic models.⁹²

Relating breast images across modalities is a challenging task since the breast is a highly deformable entity. Patient positioning in various modalities can change from upright (mammography/DBT), prone (MRI, transmission US, and dedicated breast CT), and supine (ultrasound/ABUS). Immobilization of the breast with compression plates and paddles adds an additional challenge when relating areas of the breast between modalities. A recent study has proposed FE based non-linear biomechanical models for correlating breast structures between two compressed states for cranio-caudal, CC, to medial lateral oblique, MLO, mammography views.¹¹² Several studies, have found favorable results in using FE modeling between MRI to x-ray registration for CC and/or MLO mammograms.^{85,86,88,90} A recent study has found favorable results in relating lesions in supine breast ultrasound to prone MRI.¹¹³ Another correlation study showed favorable agreement between ultrasound computed tomography and mammography registration. That research group also used ultrasound to determine the distribution in the breast of Young's Modulus from the speed of sound. This distribution was directly used in FE deformation modeling.¹⁰⁷

Due to high deformation fields of the breast between modalities and even over time in a single modality¹¹⁴ the use of external fiducial markers could provide an added benefit for lesion correlation. Several studies have used external fiducial markers and found improved registration results. In 2 studies of MRI/PET breast registration, ink was used to mark locations on the breast (up to nine in total). MRI visible markers were placed at those locations prior to MR imaging, and PET-visible markers were placed at the same locations prior to PET imaging.^{69,70} In a study of registration between compressed and uncompressed prone MRI, four external markers were

placed around the breast and on the nipple.⁷¹ Finally, using a volume navigation technique a study of breast MRI and ultrasound registration, 3 external markers (soft-gel capsules contain vitamin E in lipid solution) were used.⁷² In the present study, we investigate the use of external fiducial markers to improve the registration of breast lesions in upright DBT to supine ABUS images.

3.3 Materials and Methods

3.3.1 Phantoms

Two CIRS Multi-Modality Breast Biopsy and Sonographic phantoms¹ were used in this study. The first, Phantom A, contains a total of 7 lesions: 3 cystic masses and 4 dense masses. This phantom also contains 3 calcifications. The lesions were randomly positioned in a Zerdine-based background gel emulsion and wrapped by a Z-skin membrane material. Z-skin is a proprietary self-healing skin-like membrane that reduces phantom desiccation and simulates the texture and properties of skin during imaging and biopsy. Zerdine is a patented solid elastic water based polyacrylamide tissue mimicking material that's formulation can be adjusted to correspond to a variety of soft-tissue acoustic properties for ultrasound imaging.¹¹⁵ For some time, similar polyacrylamides have been described for ultrasound imaging and therapy phantoms.^{116,117} Since it is a water-based material and the density can be controlled it can be used for CT and MR imaging as well.^{115,118}

The second phantom, Phantom B, contains a total of 12 lesions: 6 cystic masses and 6 dense masses. These lesions were randomly positioned in a Zerdine-based background gel, without the Z-skin outer membrane. CT images of both phantoms were acquired with a GE Discovery

¹ Computerized Imaging Reference Systems, Inc., 2428 Alameda Ave, Suite 316 Norfolk, Virginia 23513, <http://www.cirsinc.com/file/Products/073/073%20DS%20032316.pdf>

CT750 CT scanner. These images were used solely to identify lesion type and quantity; the CT scans have no bearing on the deformation algorithm. Material properties for the phantoms were provided by the manufacturer. (See Table 3.1.)

Table 3.1 Phantom material properties

	<i>Young's Modulus (E)</i>	<i>Poisson's Ratio (ν)</i>
Z-skin Membrane	10 kPa	0.50
Zerdine background gel	10 kPa	0.50
Dense lesions	60 kPa	0.50
Cystic lesions	0 kPa	0.50

HyperMesh, the finite element pre-processor, cannot utilize the Poisson's Ratio of 0.50 for the materials in Table 3.1 therefore, a Poisson's ratio of 0.49 was assumed for all materials. For this study, based on visual inspection of the phantom before and after DBT and ABUS imaging there were no external indications that the phantoms did not fully recover to their original states. To better quantify the differences in phantom deformations, measured load-strain curves are shown in Figure 3.1. Based on these curves, the elasticities of the phantoms are linear, and phantom A is a factor of 1.9 times stiffer than phantom B.

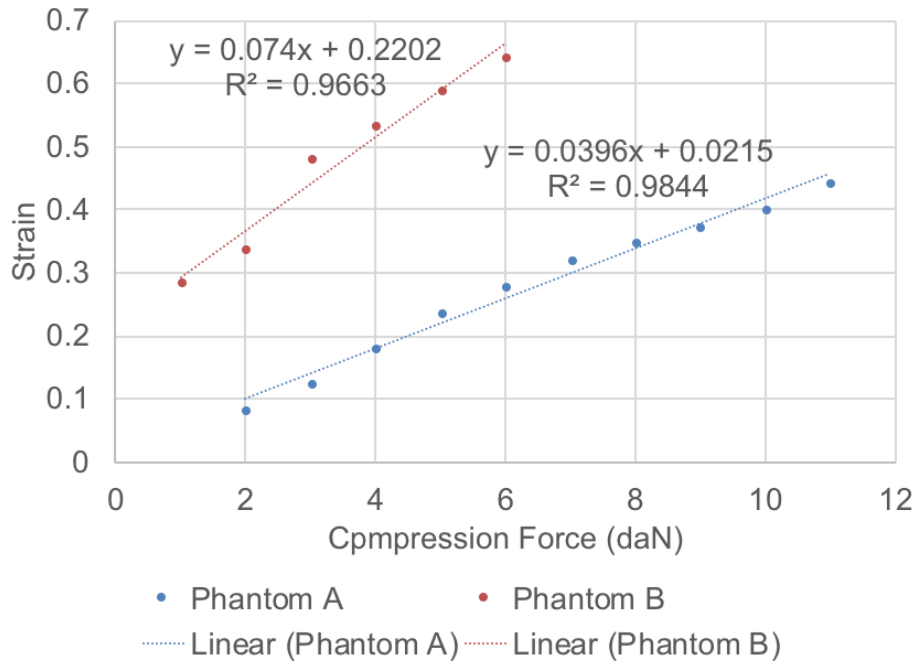


Figure 3.1: Load-strain curve comparing elastic properties of Phantom A and Phantom B. Note: Phantom B a similar phantom made of same material properties were used for these points as the Phantom had ruptured due to the amount of time that had passed as these measurements took place

3.3.2 External Fiducial Markers

The present application requires an external marker that does not cause refraction or other distortion below the skin in ultrasound imaging and does not cause artifacts in mammography/DBT imaging. In previous work, Cloutier et al, found glass bead fiducial markers were useful when imaging a multimodality vascular phantom with DSA, CTA, MRA and ultrasound.⁷³ We investigated various targets within different background materials as candidates for external fiducial markers. The fiducial marker that we found worked best for both DBT and ABUS was a 1 mm diameter glass bead target within a clear bubble-free thermoplastic elastomer (TPE) gel. To make this marker, thin samples of TPE were placed on top of the 1 mm glass beads on a cupcake baking sheet and melted at 130° C in a vacuum oven. The vacuum was

applied to the TPE as it cooled to eliminate air pockets/bubbles, which can be mistaken for the markers in ultrasound images. The fiducial markers have a thickness of approximately 3 mm.

The markers were placed around the breast, using Nu-Hope Liquid Waterproof Adhesive^m. A waterproof adhesive is recommended to ensure maintenance of fiducial marker placement with use of ultrasound coupling gel or lotion. Six external markers were applied to phantom A as show in in Figure 3.2. Results were obtained using all 6 markers as well as using 5 markers (positions F, A, B, C, and E), 4 markers (positions F, E, B, and C), 3 markers (position F, A, B), and two markers (positions F and B). Results for Phantom A, indicated no statistical difference in lesion correlation when using 6 markers and when using a maximum of three markers at locations F, A, and B. Therefore, for Phantom B, only 3 markers at those approximate locations were used when imaged.

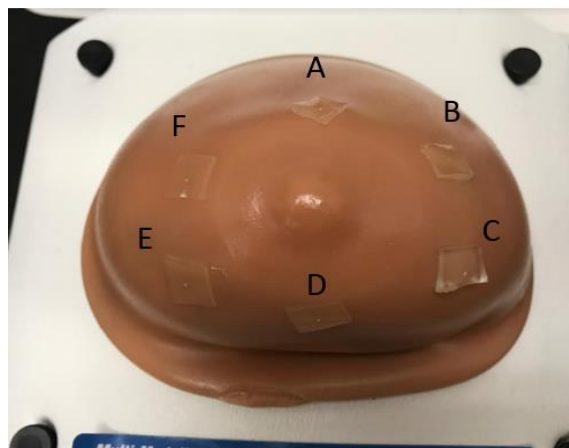


Figure 3.2 Phantom A with external fiducial marker locations indicated by A-F

3.3.3 Data Collection

A GE-SenoClaire DBT system (GE Healthcare, Milwaukee, WI) was used to image Phantom A in the CC view with a compressive force of 6 daN and compressed breast thickness of 48 mm. The maximum uncompressed breast phantom thickness measured 98 mm from reconstructed CT

^m (Nu-Hope Laboratories, Inc., P.O. Box 331150 Pacoima, CA 91333-1150, <http://nu-hope.com/products.php>).

images. Thus, phantom A was compressed 51% for this study. 6 out of the 7 lesions in this phantom were identified in the reconstructed DBT images. A GE Senographe Pristina DBT system (GE Healthcare, Milwaukee, WI) was used to image Phantom B in the CC view with a compressive force of 3 daN and compressed breast thickness of 31 mm. For Phantom B, 7 of the 12 lesions were identified in the reconstructed DBT images. The maximum uncompressed breast phantom thickness measured 97 mm from reconstructed CT images. Thus, phantom B was compressed 68% for this study. The reason 1 lesion in Phantom A and 5 lesions in Phantom B were not seen in the reconstructed DBT images is that the plastic backing on both phantoms restricted the ability to image close to the “chest wall” where those lesions were located.

Figure 3.3 (a) and Figure 3.3 (b), show DBT images of both phantoms including some of the lesions and an external fiducial marker (red arrow).

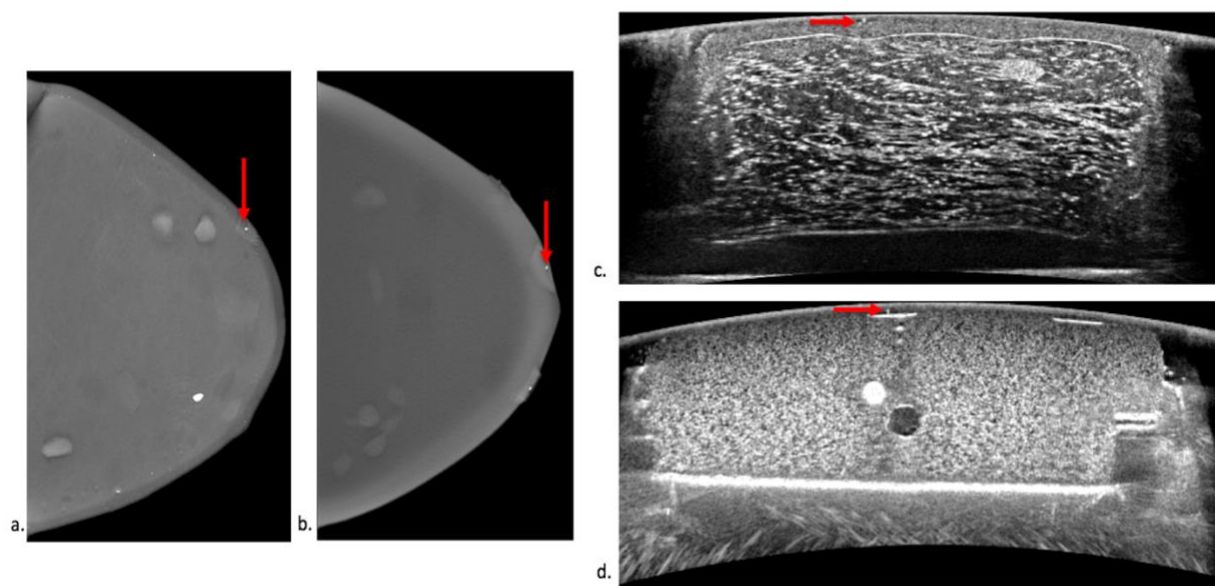


Figure 3.3 DBT and ABUS acquired images. The red arrows indicate the locations of external fiducial markers in: (a) DBT image of Phantom A, (b) DBT image of Phantom B, (c) ABUS image of Phantom A, and (d) ABUS image of Phantom B

Both phantoms were imaged with a GE Invenia ABUS system¹¹⁹ (GE Healthcare, Milwaukee, WI) immediately after DBT imaging. Light AP compression is applied to the phantoms when

they are imaged with the Invenia ABUS system. There are three settings on the system (high, medium, and low) based on imaging depth. The high setting was used for imaging Phantom A and the medium setting was used for imaging Phantom B. The system has a safety stop at 20lbs (8 daN) which is lower than the compression used in most mammography exams today. The Invenia ABUS reverse curve transducer has a bandwidth of 6 to 15 MHz and can image up to 50 mm in depth. The transducer has a width of 153 mm and automatically travels approximately 170 mm across a mesh compression paddle. The breast/phantom was positioned supine with anterior-posterior compression applied by the mesh paddle. One ultrasound volume of each phantom was taken in the anterior posterior view. Clinical procedures typically include acquisitions of three separate volumes per breast to ensure full coverage of the breast and axillary region. Raw data from the Invenia ABUS system does not include correction for the curved transducer. Therefore, an algorithm was developed and used to correct for transducer curvature in ABUS images. Figure 3.3 (c) and Figure 3.3 (d), indicate marker positioning under the ABUS imaging for Phantoms A and B with the correction for the transducer curvature. In Phantom A, the 3 calcifications were not seen in the reconstructed ABUS images. A disadvantage of ultrasound imaging is that microcalcifications are often not seen and even larger calcium macrocalcifications deposits can be missed.¹²⁰ All 12 lesions were seen in the ABUS scans of Phantom B.

3.3.4 Manual segmentation

All lesions and external markers from the acquired image sets from both modalities were manually segmented using a free-hand drawing tool within 3D Slicer¹²¹ by three readers (CAG, MMG and JHL) using the same window-level settings on the same work station. Readers viewed the images together and agreed upon a window-level setting to be used for each image set in

order to eliminate window-leveling as a variable in inter-reader concordance of lesion segmentation. Since DBT images have poor axial resolution, the lesions were segmented until the superior and inferior extents of the lesions exhibited significant blur along the edges. These decision points are very subjective so the axial extents of the lesion segmentations in DBT can vary significantly between readers.

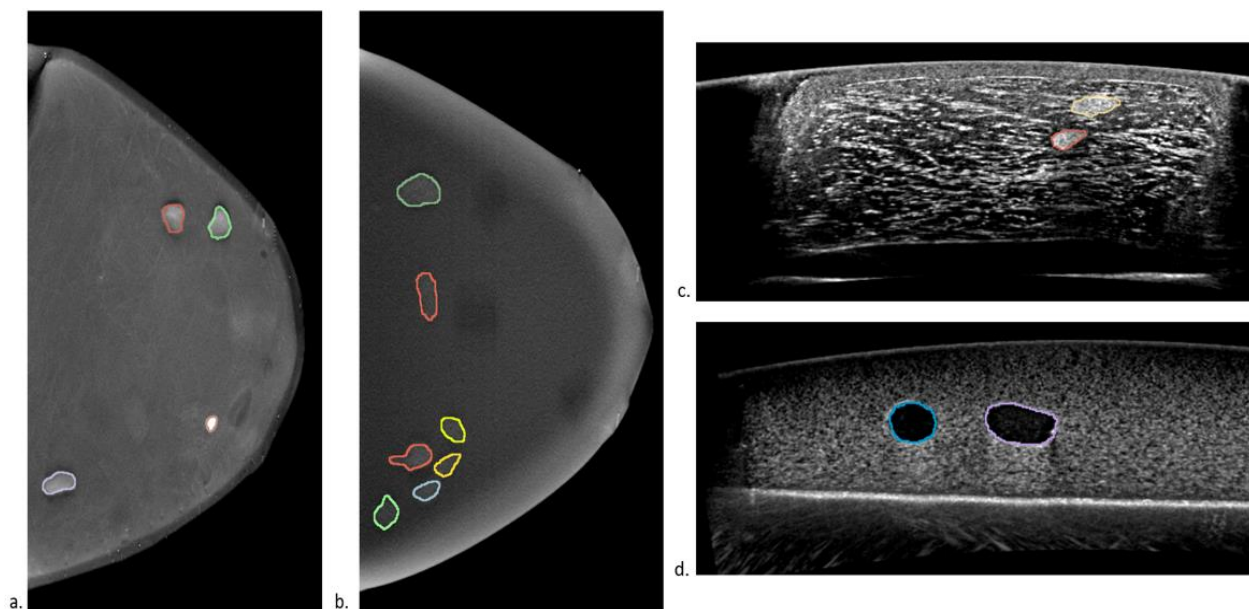


Figure 3.4 Reader 1's manual segmentation of a slice in (a) Phantom A – DBT, (b) Phantom B- DBT, (c) Phantom A - ABUS (d) Phantom B - ABUS

Figure 3.4, shows examples of lesion segmentation for Phantom A and B in both DBT and ABUS image sets. Dice similarity coefficients (DSC) (twice the overlap of corresponding segmented volumes/sum of those volumes) were used to evaluate similarities between lesion and marker contours between readers.¹²² For the DBT and ABUS data sets, one reader manually segmented the outer skin layer from the air and the body of breast phantom A and segmented the body of breast phantom B from the air. For the ABUS images, that same reader performed these same segmentations manually. There was no correction in the segmentations for DBT reconstruction artifacts. After segmentations were completed, resampling was used to decrease

runtime when converting segmentations into triangular surface meshes. The DBT images were resampled from a native voxel size of 0.1 mm width, 0.1 mm length, and 1.0 mm depth to 0.2 mm width, 0.2 mm length, and 1.0 mm depth. The ABUS images were resampled from a native voxel size of 0.082 mm width, 0.2 mm depth, and 0.506 mm length (distance between adjacent slices), to 0.2 mm width, 0.2 mm depth, and 0.506 mm length. *Image resampling is done using the MATLAB `imresize`ⁿ command.*

3.3.5 Deformable mapping algorithm

The deformable mapping algorithm is an automated process that integrates the use of Morfeus, a commercial FE pre-processor (HyperMesh 2017, Altair Engineering, Troy, MI) and a finite element analysis (FEA) solver processor (Optistruct 2017, Altair Engineering, Troy, MI). An overview of the process is shown in Figure 3.5.

ⁿ <https://www.mathworks.com/help/images/ref/imresize.html>

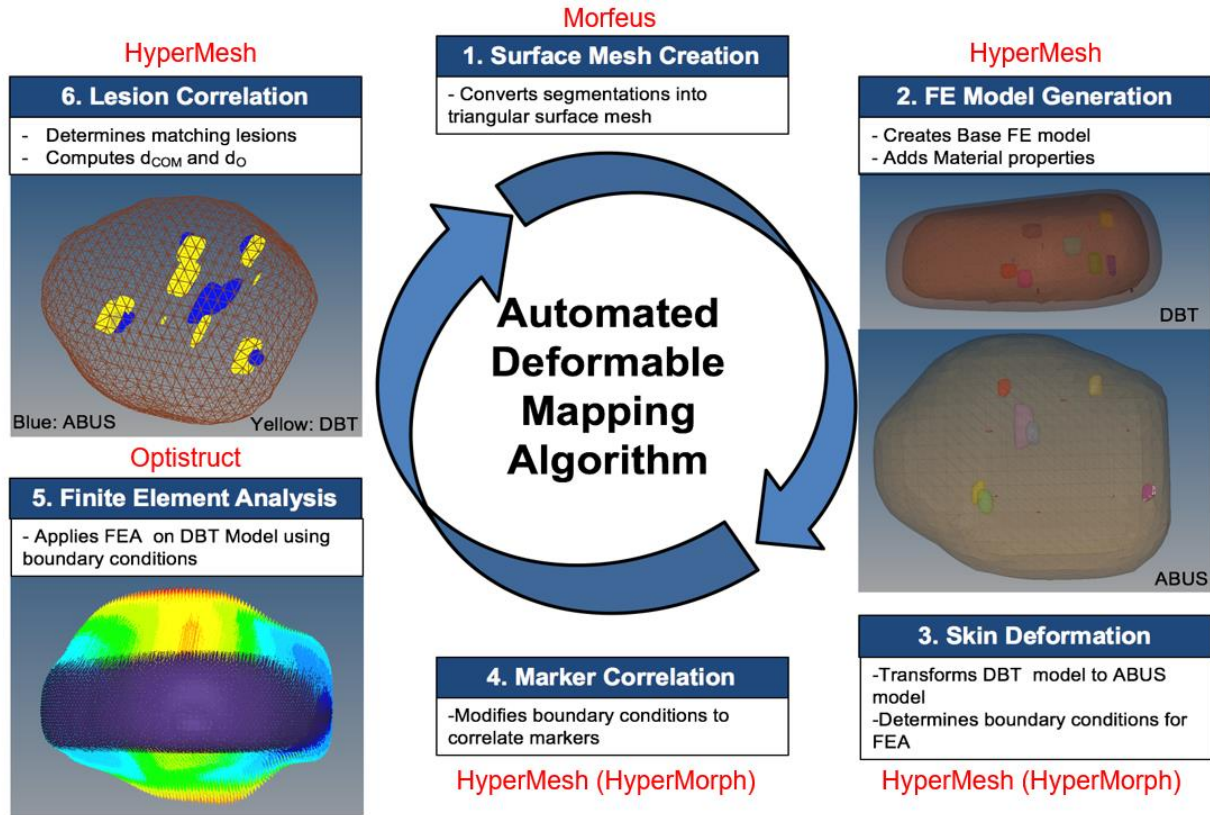


Figure 3.5 The automated deformable mapping process. Software's used shown in red.

The entire deformable mapping algorithm takes up to approximately 40 minutes to complete from start to finish on a Windows 7 Intel® Core™ i7 CPU with a speed of 2500 MHz and 4GB RAM. In ABUS imaging, poor acoustic contact with the transducer often occurs around the periphery of the breast causing artifacts as shown on the right and left sides of Figure 3.3 © and Figure 3.3 (d). These artifacts cause the actual breast size and shape in ABUS imaging to be not as well defined in comparison to DBT. An example of the segmentation of the skin layer for both phantoms is shown in Figure 3.6.

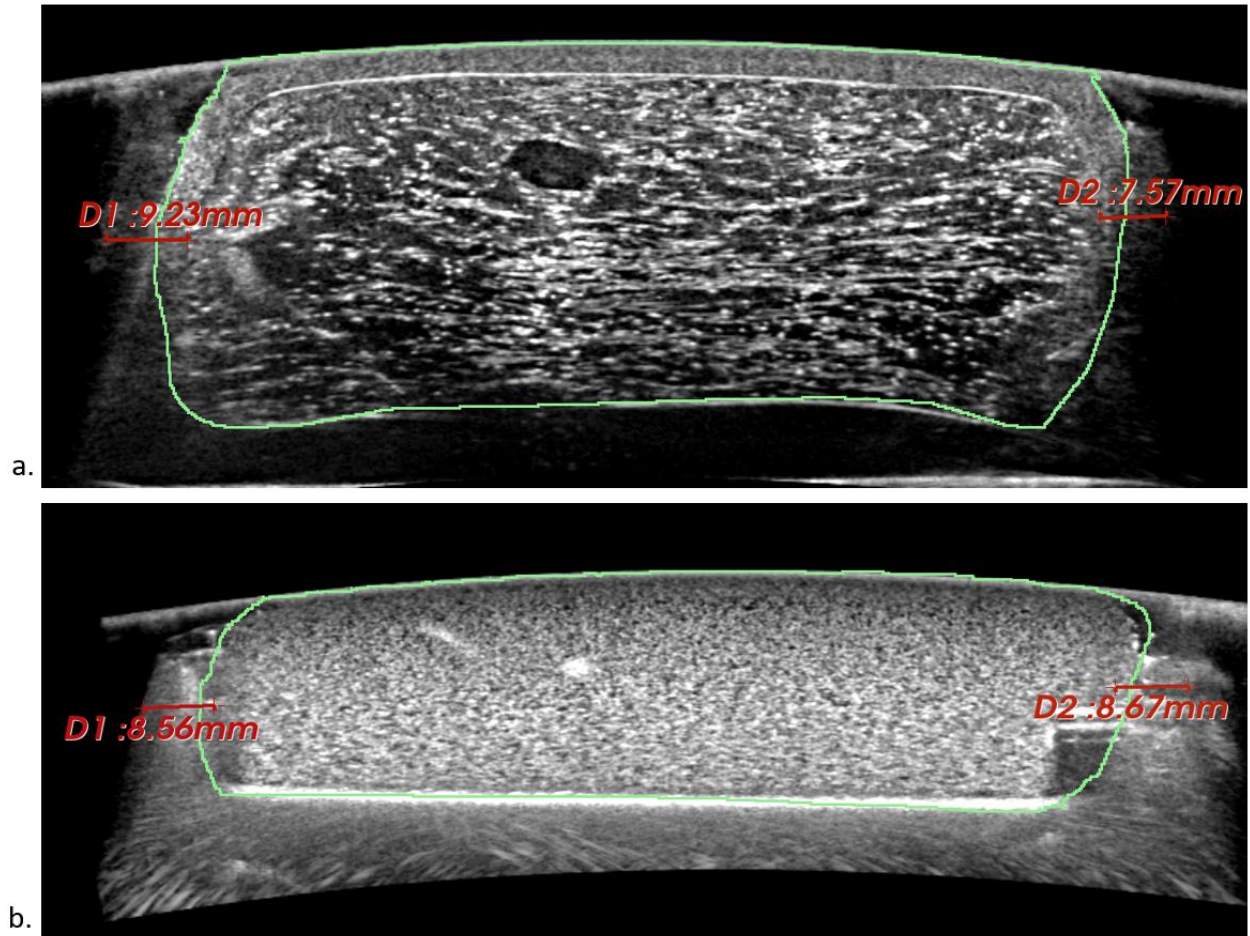


Figure 3.6: Periphery uncertainty from skin segmentation for a slice in ABUS for (a) Phantom A (b) Phantom B.

Reader bias can affect the segmentation in the periphery boundary. The use of external markers for registration should help to reduce and correct for these differences in lesion registration. On the other hand, the breast shape and size are better defined in the DBT images as shown in Figure 3.3 (a) and Figure 3.3 (b). Therefore, we chose to have the deformable mapping algorithm perform deformation only to the DBT FE model and register the resulting deformation to the ABUS image set. The external fiducial markers allow for adjustments to be made since all markers observed in the ABUS images had potentially corresponding points in the DBT images. More sophisticated registration rules are required if that is not the case.

3.3.5.1 Conversion of DICOM segmented images to triangular surface mesh

Morfeus, a FE based multi-organ deformable image registration platform, converts all DICOM segmented contours into individual triangular surface mesh for use in the FE model pre-processor.⁴⁷ Morfeus converts the DICOM image data into mask files for image analysis using Interactive Data Language (IDL, Research Systems Inc.). Each mask file is then converted into a triangular surface mesh file. Within HyperMesh, the shrinkwrap function is used on the Morfeus generated triangular surface element mesh in order to create a triangular “trias” surface mesh for further processing and FEA. Prior to FEA, an element quality check is performed to ensure all elements in the model are within various specifications (e.g., aspect ratio, Jacobian, warpage etc.) in order for the analysis to commence. Therefore, Morfeus uses Laplacian smoothing and a decimate function to better ensure the triangular mesh is within element quality specifications by smoothing rough or sharp elements to ensure viable mesh integrity while maintain a reasonable mesh size to maintain structural features.

3.3.5.2 Finite element model generation

The algorithm uses the FE model pre-processing software, HyperMesh, to build the base FE model for the DBT and ABUS image set from the individual mesh triangular surface contours. 3D four-point tetrahedral FE models are created using the trias surface meshing algorithm within HyperMesh from all 3D-triangular surface mesh contours for each modality model which results in fully connected tetrameshed base FE ABUS and DBT models. The algorithm takes into account the shape of the triangular surface being meshed and uses a defined library of element patterns to map them to triangular surfaces for tetrahedral mesh generation. Each reader’s segmented dataset includes the resulting base DBT and ABUS models for both phantoms. The material properties that were assigned to the 3D tetrahedral model volumes are as noted in Table

3.1. Surface interfaces are defined, and boundary conditions are determined using a mesh morphing module named HyperMorph. The base DBT model is deformed to match the ABUS model since there is higher certainty in the overall breast shape in the DBT model. Since the simulated dense and cystic lesions cannot be distinguished in the DBT images, all lesions are assumed to have the material property of the dense lesions from Table 3.1. For Phantom A, the average number of elements/nodes are 366,000/65,800 for the base DBT model and 102,000/20,300 for the base ABUS model. For Phantom B the average number of nodes/elements are 192,000/35,600 for the base DBT model and 137,000/24,200 for the base ABUS model. The DBT model has a larger number of elements/nodes due to smaller element size since it is used for FEA and the ABUS model is used as the reference model.

3.3.5.3 Skin surface transformation of DBT model to match ABUS skin surface

The base DBT FE model (Figure 3.7 (a), blue) is translated and rotated to the center of mass, COM, of the base ABUS FE model (Figure 3.7 (b), brown). Nodal locations, (x, y, z-coordinate locations that define elements in FE model) from the skin surface of the base DBT-FE model are automatically moved to best match the outer surface of ABUS FE model along the axial and coronal planes by morphing the original mesh, which results in Figure 3.7 (c). This transformation reshapes the skin surface mesh and does not use any breast phantom material properties. For this transformation, the entire skin surface as the volume is encased in a six-sided hexahedron to encompass the entire skin volume. The handles, (68 in total, yellow and red spheres shown around the DBT skin mesh in Figure 3.7) are created and encompass the outer contour of the DBT skin model at seven equidistant locations along each planar axis. The red spheres indicate global handles, which are 8 in total and are generated at the eight corners of the hexahedron box surround the skin mesh. Global handles are used for making large scale changes

to the mesh. The yellow spheres indicate local handles which make smaller scale changes to localized areas of the. There are 60 yellow spheres in total and are used to manipulate a small region of the skin mesh by influencing external nodal locations. Influence functions, using the HyperMorph feature within the HyperMesh software, relate the movement of the handles to the nodes within. There are a number of non-linear algorithms used depending on the size and shape of the domains and the number of nodes within. The algorithm enforces symmetry or constrain nodal movements in many different patterns to modify the relationship between handle movement and node manipulation. The external nodes of the DBT skin model are then related along the axial and coronal anatomical planes to the nearest node in the ABUS model based on the axes of interest. The external nodes of the DBT skin model are then related along the axial and coronal anatomical planes to the nearest node in the ABUS model based on the axes of interest.

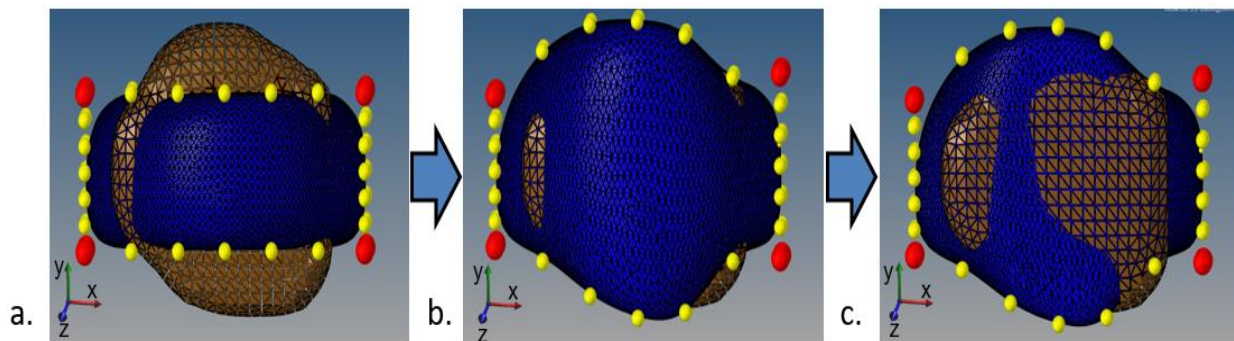


Figure 3.7: Mesh transformation for external DBT breast surface mesh to match shape of ABUS surface mesh. Brown: ABUS (unchanged) Yellow:Blue (deformed): (a) COM translation and rotation of DBT to ABUS COM (b) Coronal handle manipulation of DBT breast surface mesh (along y axis) (c) Axial handle manipulation of DBT breast surface mesh (along z axis)

The algorithm computes the differences and manipulates the handles so the DBT volume can match the external ABUS shape. Manipulating handles along the coronal plane (Figure 3.7 (b)) simulates the decompression of the DBT surface mesh. Manipulating handles along the axial

plane (Figure 3.7 (c)), simulates AP compression of the DBT surface mesh to match the ABUS surface mesh. In other words, the original DBT surface mesh is morphed by changing nodal locations to better align with the overall shape of the ABUS surface mesh. The sagittal plane (the plane the ultrasound transducer is scanned) is not considered due to poor coupling along the right and left sides of the breast during ABUS image acquisition.

3.3.5.4 External Marker Correlation

After surface deformation is completed using the outer skin contours between models, the algorithm computes COM positions of the external fiducial markers from the morphed DBT model and reference ABUS model. The DBT surface mesh is further deformed based off external marker correlation as follows: External fiducial markers in the DBT model are matched with the base ABUS external fiducial markers by determining the minimum distance between the COMs of corresponding markers. This distance will be used to align markers closer together and allows for mesh corrections along all anatomical planes (includes correction along the scanning plane of the ultrasound transducer).

Once external markers are matched between the two sets and the resulting distances between COMs is determined, the algorithm determines which local handle (yellow spheres shown in Figure 3.7 (c)) is needed to adjust nodes within the mesh domain. This handle is determined by proximity to handle locations along the x-axis. Once the local handle is determined, the local handle is manipulated by half the distances between the COMs of correlated markers for each planar axis. This is repeated for all corresponding markers. After all handle manipulation is completed the algorithm recalculates the COM distances between markers. If all markers are within a user-defined distance, d_M (between 1 and 10 mm), the algorithm will begin FEA. If not, the algorithm identifies which markers are not within d_M and iterates again to manipulate the

handles for markers that are not satisfying the d_M boundary condition. The algorithm will iterate until all markers satisfy the d_M boundary condition. Each iteration will only perform handle corrections based off the total number of matched markers (i.e. 6 matched markers corresponds to a maximum of 6 handle corrections for that iteration).

To maintain mesh integrity, the DBT FE model is deformed by half the distance between correlated markers to ensure that mesh quality is not compromised due to large changes to the skin mesh which can halt processing by the FEA solver. Skin deformation per iteration occurs only for corresponding markers that are greater than d_M . For those markers, deformation by further manipulation of the handles, as described in Sec. 3.3.5.3 is performed in that area of the DBT model of the breast. A lower bound of 1 mm is used as it is approximately equal to the ultrasound point spread function expected for the fiducial markers. If there are no markers inferior to the nipple, mesh deformation is assumed symmetric superior and inferior to the nipple. The displacement for each node from the surface mesh of the DBT translated model (Figure 3.7 (a)) and the deformed DBT surface mesh (Figure 3.7 (c) with the addition of external marker corrections) are stored and applied as boundary conditions for FEA deformation to begin on the base DBT model. Skin surface deformation is used for the sole purpose of creating the boundary conditions needed to begin the FEA.

3.3.5.5 Finite Element Analysis

The constraints or boundary conditions for each external DBT surface mesh are applied to the translated base DBT FE model. These boundary conditions are used as input to the FEA solver program, Optistruct, to generate and solve the differential equations to describe the model deformation based off the defined constraints. The FEA uses the material properties and boundary conditions to find the resultant stress and strain of the deformation of the entire breast

volume. Due to the high deformation that is needed to match the DBT and ABUS volumes, the FEA is performed as a non-linear quasi-static analysis in a single step. Linear static deformation would compromise mesh integrity and result in faulty output or inability of FEA to run.

Therefore, this study does not recommend the use of linear static deformation analysis between DBT and ABUS compressions. The FEA was performed on a Windows 7 Intel® Core™ i7 CPU speed of 2500 MHz with 4GB RAM with analysis complete in approximately twenty minutes.

The analysis time will be longer for models with greater complexity.

3.3.5.6 Lesion correlation

After FEA is performed, the COM of all lesions from the FEA-DBT model and the base FE ABUS model are determined. A correlation algorithm determines which lesions correspond to lesions in the other set with the constraint that the difference in COM is within 15 mm. Previous studies, for deformable registration from breast MR to mammography CC views have shown mean registration errors of 10 - 20 mm.⁹² Therefore, since those studies were based on real breast data these bounds were used loosely as correlation criteria for registration measurement. All external nodal locations of each lesion are analyzed to determine overlap of correlated lesions. Corresponding lesions from DBT and ABUS sets that have a minimum distance between the COMs, d_{COM} are considered to match. For two lesions in DBT that have the same d_{COM} with a lesion in ABUS, the code checks the d_{COM} of those two DBT lesions with other ABUS lesions to minimize all d_{COM} and thereby determines the correct lesion matches. The matching process is described in pseudo-code in Figure 3.8.

```

READ COMs for DBT Lesions
READ COMs for ABUS Lesions
FOR i=1 to number of DBT Lesions
  COMPUTE dCOM between each ABUS lesion and each DBT lesion
  IF minimum dCOM < 1.5 cm
    DETERMINE ABUS Lesion of minimum dCOM and SET as Match[i]
    STORE minimum dCOM in dCOM[i]
    IF second minimum dCOM < 1.5 cm
      DETERMINE ABUS Lesion of minimum dCOM and SET as Match2[i]
      STORE second minimum dCOM in dCOM2[i]
    END IF
  END IF
END FOR LOOP
IF values in Match are not discrete
  DETERMINE Positions of the same values in Match and STORE as SameLesion(i, k)
  WHILE number of SameLesion > 0
    IF SameLesion(i,1) is in the Match2 list & dCOM2[SameLesion (1, k)] <
      dCOM[SameLesion(i,1)]
      SET dCOM[SameLesion (1, k)] == dCOM2[SameLesion(i,1)]
      SET Match [SameLesion (1, k)] == Match2[SameLesion(i,1)]
    END IF
    DETERMINE Positions of the same values in Match and STORE as SameLesion (i, k)
  END WHILE LOOP
END IF
PRINT Match and dCOM

```

Figure 3.8 Pseudo-code for lesion correlation used within deformable mapping algorithm

All corresponding lesions are considered matched between the two modality sets based on the criteria in Table 3.2. Since our studies use uniform background phantoms with large numbers of lesions, stricter lesion correlation guidelines were employed to reduce the likelihood of mismatch.

Table 3.2 Criteria for lesion correlation between ABUS and DBT model

	d_{COM}	d_O
Overlapping Lesions	$d_{COM} \leq 10 \text{ mm}$	n/a
Non-overlapping Lesions	$d_{COM} \leq 15 \text{ mm}$	$d_O \leq 7.5 \text{ mm}$

Therefore, if two corresponding lesions overlap, they are considered a match if d_{COM} is within 10 mm. If lesions correspond but do not overlap the minimum distance to overlap, d_O, is calculated as shown in Figure 3.9. If the two corresponding lesions are within a d_{COM} of 15 mm and d_O is within 7.5 mm, the lesions are matched. The d_O is restricted to 7.5 mm to ensure a match discrepancy is not made. The results are output into a table and can be used to relate

positions from the original ABUS and DBT DICOM data. Calcifications from Phantom A are not considered during lesion matching.

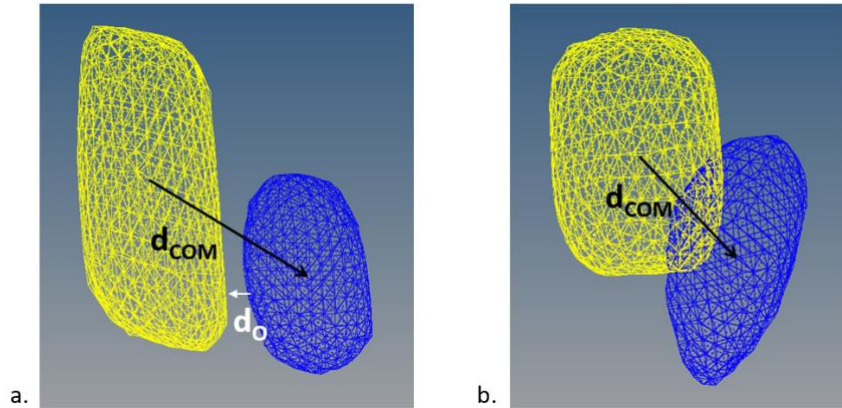


Figure 3.9 Lesion correlation metrics for COM distance (d_{COM}) and minimum distance to overlap (d_O) for (a) non-overlapping lesions and (b) overlapping lesions. (Blue = ABUS, Yellow = DBT)

3.3.5.7 Studies performed

The following studies were performed:

- *Inter-reader concordance of segmented lesions*: Inter-reader concordance of all segmented lesions was evaluated using DSC and distances between the COM's of corresponding lesions.
- *Inter-reader concordance of locations of fiducial markers*: Inter-reader concordance of the locations of the fiducial markers was evaluated by measuring the distances between the COM's of each segmented marker for each image set.
- *Reader reproducibility*: After segmentation was performed for all lesions, three lesions were selected from each image set of each phantom for a study of reader segmentation reproducibility. Each reader segmented those three lesions in the DBT and ABUS images several days after completing their original segmentations.
- *Accuracy of deformable mapping technique*: For Phantom A, results were compared for

cases when sufficient iterations were performed to achieve corresponding marker separations of ≤ 1 mm vs. ≤ 5 mm This comparison included results when different numbers of markers were used. In addition, results were compared with and without the use of the markers. For all comparisons, the statistical significance of any differences between the average d_{COM} values for corresponding lesions were determined with paired t-tests. The numbers of lesions that overlapped and d_O were also compared.

3.4 Results

3.4.1 Analysis of inter-reader concordance of segmented lesions in both phantoms

Table 3.3 compares the segmentation results between readers for all lesions in both phantoms. The DSC for the ABUS data for both phantoms is approximately 0.90. For DBT data for both phantoms DSC results are lower, likely due to differences in reader determination of the vertical extents of the lesions. The smallest DSC is 0.57 for R2 to R3 for Phantom 2. For this same reader correlation, the average distance between COM (d_{COM}) is 0.81 mm thus illustrating that even though the DSC values are low, the central positions of the lesions segmented by the different readers are still very close to one another.

Table 3.3 Average DSC and average COM distance (d_{COM}) results between readers for corresponding lesions in all DBT and ABUS data sets for Phantoms A and B.

Reader correlation	Phantom A				Phantom B			
	ABUS		DBT		ABUS		DBT	
	DSC	d_{COM} (mm)	DSC	d_{COM} (mm)	DSC	d_{COM} (mm)	DSC	d_{COM} (mm)
R1 to R2	0.89 ±	0.20 ±	0.70 ±	1.06 ±	0.90 ±	0.31 ±	0.62 ±	0.78 ±
	0.07	0.03	0.19	0.27	0.05	0.06	0.24	0.08
R2 to R3	0.88 ±	0.29 ±	0.73 ±	0.59 ±	0.88 ±	0.30 ±	0.57 ±	0.81 ±
	0.08	0.01	0.11	0.12	0.09	0.05	0.25	0.17
R3 to R1	0.89 ±	0.36 ±	0.72 ±	1.16 ±	0.91 ±	0.21 ±	0.83 ±	0.11 ±
	0.03	0.01	0.21	0.23	0.04	0.03	0.04	0.02

3.4.2 Analysis of inter-reader concordance of fiducial markers locations

Table 3.4 illustrates the average distances between the COM's of the fiducial markers segmented by the three readers. The largest differences between the COM's for both DBT and ABUS are approximately 2 mm.

Table 3.4 Average COM distance (d_{COM}) between external markers among readers in DBT and ABUS data sets for Phantoms A and B

	d_{COM} (mm)			
	Phantom A		Phantom B	
	ABUS	DBT	ABUS	DBT
R1 to R2	1.31 ± 0.37	1.37 ± 0.26	0.45 ± 0.27	1.18 ± 0.26
R2 to R3	1.33 ± 0.40	0.69 ± 0.08	0.74 ± 0.23	1.38 ± 0.34
R3 to R1	1.77 ± 0.61	0.97 ± 0.32	0.48 ± 0.27	2.24 ± 0.72

3.4.3 Reader reproducibility analysis

Table 3.5 illustrates the reproducibility of the segmentation results for each individual reader for three lesions in Phantom A and Phantom B. The reproducibilities of the DSC for the individual readers are in general higher for the lesions in the ABUS images and lower in the DBT images. The latter is likely due to differences in reader determination of the vertical extents of the lesions in DBT images when the readers repeat the segmentations themselves. However, the d_{COM} values in Table 3.5 are less than 2 mm for both modality images indicating good reproducibility of the positions of the lesions.

Table 3.5 Reproducibility for each reader's lesion segmentations in DBT and ABUS data sets for Phantoms A and B using DSC coefficients and average COM distance (d_{COM}).

Reader ID	Phantom A				Phantom B			
	ABUS		DBT		ABUS		DBT	
	DSC	d_{COM} (mm)	DSC	d_{COM} (mm)	DSC	d_{COM} (mm)	DSC	d_{COM} (mm)
R1	0.85 ± 0.04	0.50 ± 0.27	0.78 ± 0.09	1.88 ± 1.34	0.89 ± 0.02	0.19 ± 0.03	0.68 ± 0.19	0.59 ± 0.05
R2	0.86 ± 0.03	0.47 ± 0.34	0.85 ± 0.05	0.60 ± 0.45	0.86 ± 0.01	0.23 ± 0.13	0.66 ± 0.16	0.69 ± 0.05
R3	0.86 ± 0.01	0.29 ± 0.26	0.78 ± 0.07	1.19 ± 0.92	0.87 ± 0.05	0.16 ± 0.04	0.69 ± 0.07	0.42 ± 0.38

For segmentations by each reader, deformation was successfully performed on the base DBT

FE model and correlated to the corresponding ABUS datasets between reader segmented data. In every iteration of the algorithm, the average distances between the COMs between the readers of the correlated markers decreased as shown in Figure 3.10. After 6 iterations, the average correlated difference between all markers is 3.0 mm which corresponds to a $d_M \leq 5$ mm.

3.4.4 Accuracy of deformable mapping for different numbers of fiducial markers for Phantom A

Phantom A has 7 lesions, all of which were viewed with ABUS. However, only 6 of the lesions were viewed in the DBT images because 1 lesion was too close to the chest wall and moved outside the image field of view when the phantom was compressed. Figure 3.10 (a), illustrates the resulting lesion d_{COM} , d_o , and overall lesion overlap where no marker analysis was used and compares it to various marker combinations described in Sec. 3.3.1 when markers within a 1-mm distance ($d_M \leq 1$ mm). Figure 3.10 (b), illustrates the resulting lesion d_{COM} , d_o , and overall lesion overlap fraction that were obtained when no fiducial marker analysis was used and compares it to various marker combinations described in Sec. 3.3.1 when all corresponding markers were within a 5-mm distance ($d_M \leq 5$ mm).

For the 6 marker case, 6 iterations were needed for all of the corresponding external markers to be within a 5-mm distance of each other. For all corresponding external markers to be within a 1-mm distance of each other required 17 iterations. Each iteration can have runtimes of up to 3 minutes depending on the number of markers used in the analysis. Therefore, a difference of 10 iterations can increase runtime by about 30 minutes. Although as shown in Figure 3.10, the d_{COM} are slightly greater for markers being within 1 mm vs. 5 mm (likely due to the greater number of iterations and corrections made to get all of the markers within the 1 mm distance), the p-value for a paired t-test was 0.12. Thus, there was no statistical difference in d_{COM} when markers were

within 1-mm versus a 5-mm distance. Hence a d_M of 5 mm is regarded as an acceptable distance between correlated markers to ensure acceptable algorithm run time, with the employed, simple processor, while maintaining desired lesion correlation. Without the use of markers only 2 out of 6 lesions overlapped. For both d_M cases analyzed, overlap improved to 6 out of 6 lesions with 4 - 6 marker analysis combinations and improved to 5 out of 6 lesions overlapped for 2 and 3 marker analyses. The largest improvement in d_{COM} is shown for 2 and 3 markers vs. 0 markers.

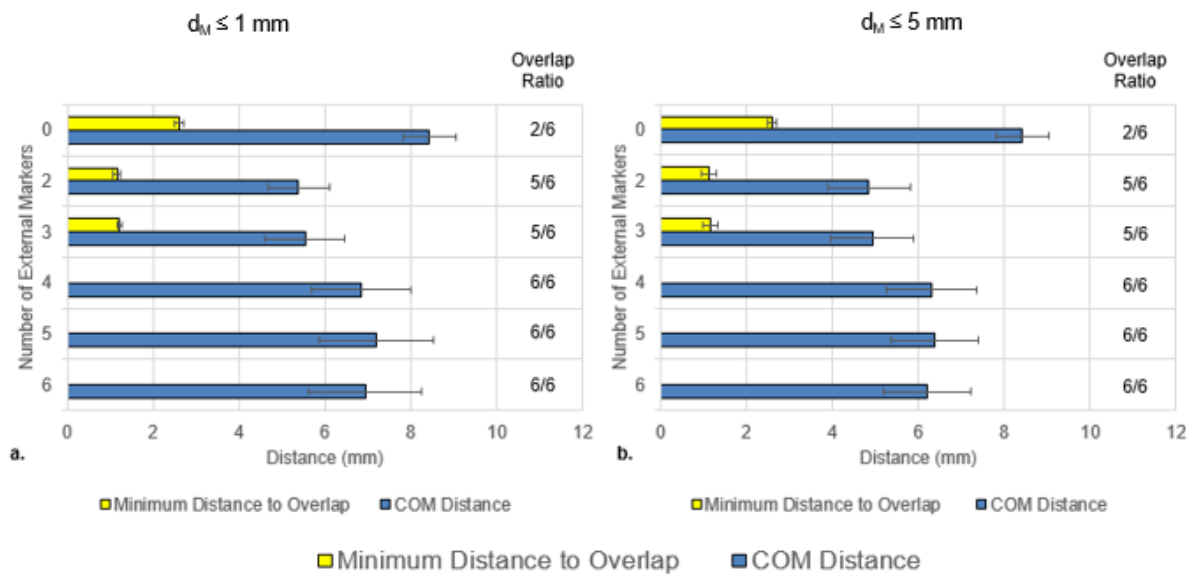


Figure 3.10 Average distances between COMs of corresponding lesions in ABUS and DBT images (d_{COM}) for all 3 readers, as well as minimum distance to overlap (d_O), and overall lesion overlap ratio (the number of lesions that overlapped between DBT and ABUS sets divided by the total number of lesions that were imaged) for Phantom A with various number of external fiducial markers. (a) All marker distances were within a distance ($d_M \leq 1$ mm) between readers' data sets. (b) All marker distances were within a distance ($d_M \leq 5$ mm) between readers' data sets. Marker combinations from Figure 3.2: 6 markers (A-F), 5 Markers (A, B, C, E, and F), 4 markers (F, B, E, and C), 3 markers (A, B, and F) and two markers (F and B).

Figure 3.11 displays the improvement from no marker analysis to that with three marker analyses in Phantom A for all correlated lesions for Reader 1 segmented datasets.

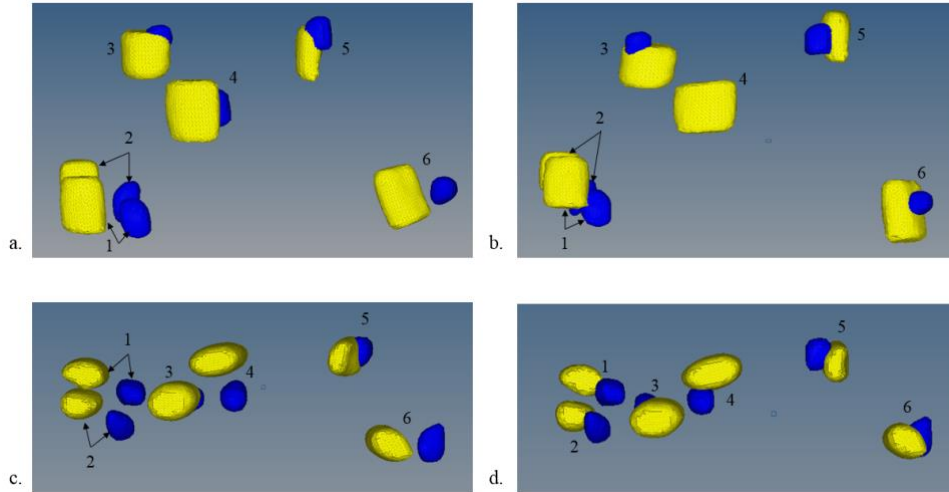


Figure 3.11 Phantom A lesion correlation for Reader 1 (a) without marker analysis coronal view (b) with marker analysis coronal view (c) without marker analysis axial view (d) with marker analysis axial view. All numeric values correspond with Lesion ID's in Table 3.6. (Blue = ABUS, Yellow = DBT)

Table 3.6, compares the average distances between the COMs of corresponding individual lesions \pm the standard deviations of those distances in the deformed DBT and base ABUS images for the combined data for all 3 readers for phantom A, without the use of markers and with the use of three external markers for lesion correlation. The mean difference in lesion d_{COM} was 1.9 mm with 3 marker analyses vs. without. A paired t-test of the mean d_{COM} values was performed and resulted with an overall p-value of 0.01 for the averaged dataset. Therefore, the use of 3 external markers showed statistically significant improvements in lesion d_{COM} in comparison to the use of no external markers.

Table 3.6 Lesion correlation for Phantom A when no external markers are used for the deformation (left) vs. three external markers used for the deformation (right).

Without Marker Analysis				With 3 Marker Analysis ($d_M \leq 0.5$ mm)			
Lesion ID	d_{COM} (mm)	d_o (mm)	Overlap	Lesion ID	d_{COM} (mm)	d_o (mm)	Overlap
1	8.2 ± 0.3	3.4 ± 0.4	no	1	4.5 ± 0.2	n/a	yes
2	10.2 ± 0.7	3.6 ± 0.3	no	2	7.1 ± 1.1	n/a	yes
3	5.0 ± 0.3	n/a	yes	3	3.9 ± 0.5	n/a	yes
4	8.5 ± 0.1	1.9 ± 0.1	no	4	8.4 ± 0.5	1.1 ± 0.0	no
5	4.7 ± 0.5	n/a	yes	5	2.0 ± 0.5	n/a	yes
6	4.5 ± 0.1	1.5 ± 0.6	no	6	3.6 ± 1.4	n/a	yes
Average	6.8	2.6	Overlap	Average	4.9	1.1	Overlap
σ	2.4	1.1	2/6	σ	2.4	0.0	5/6

3.4.5 Accuracy of deformable mapping technique for phantom B

Based on the results for Phantom A, Phantom B was only imaged with three markers in the positions F, A, and B as illustrated in Figure 3.2. Phantom B has 12 lesions, all of which were viewed with ABUS. However, only 7 of the lesions were viewed in the DBT images because 5 lesions were too close to the chest wall and moved outside the image field of view when the phantom was compressed. Without the use of markers analysis, 4 lesions were correlated (within 15 mm of each other) with only 1 overlapped. As shown in Table 3.7, the average d_{COM} between corresponding ABUS and DBT lesions for the 3 readers was 9.7 ± 3.5 mm and the average lesion d_o was 2.9 ± 1.8 mm. For the segmented data without marker analysis only one lesion showed overlap. These results are tabulated in Table 3.7.

Table 3.7, also includes a comparison between the deformable mapping method without marker analysis with that for 2 and 3 external markers. Using 2 and 3 marker analyses, the average d_{COM} between corresponding lesions improved by 18% and 27%, respectively, relative to the no markers case. For the 4 lesions correlated without marker analysis a paired t-test of the

mean d_{COM} values was performed with the results for 2 and 3 marker analysis combinations and both resulted in p-values of 0.01 respectively. Therefore, these 4 lesions on average show statistically significant improvement in lesion d_{COM} with the use of external markers. Figure 3.12 displays the improvement from no marker analysis to that with three marker analyses in Phantom B for all correlated lesions for Reader 1 segmented datasets.

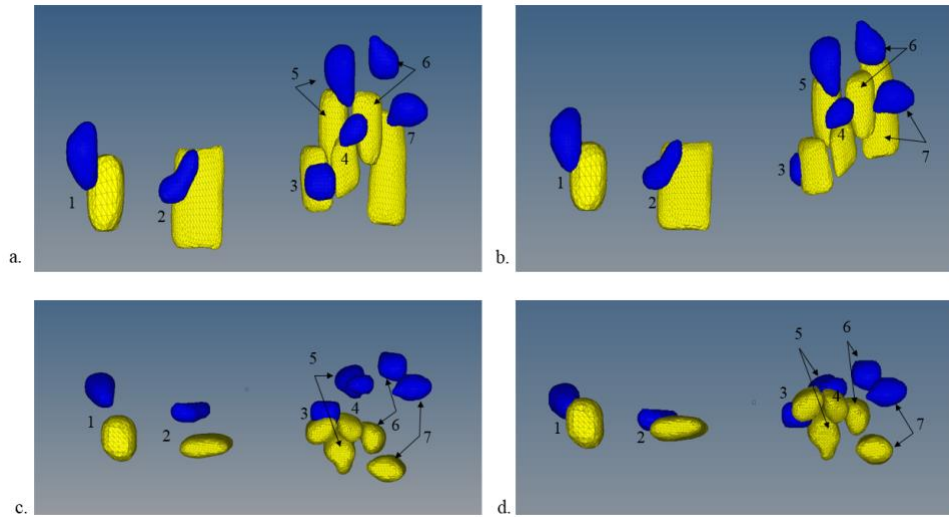


Figure 3.12 Phantom B lesion correlation for Reader 1 (a) without marker analysis in the coronial view (b) with three marker analyses in the coronial view (c) without marker analysis in the axial view (d) with three marker analyses in the axial view. All numeric values correspond with Lesion ID's in Table 3.7. Note that for the without marker analysis lesions 5, 6, and 7 did not meet the correlation criteria of being within 15 mm of each other (See Table 3.7). (Blue = ABUS, Yellow = DBT)

Table 3.7, shows a comparison between the deformable mapping method without marker analysis and with 2 and 3 external markers. The mean d_{COM} values for 2 and 3 marker analyses are 7.6 ± 3.6 mm and 8.5 ± 4.0 mm, respectively. A paired two-sample t-test for means was performed on the average d_{COM} values. The p-value was 0.053 and supports that the difference between using 2 markers and 3 markers is not statistically significant. Lesion ID=7 values were calculated for only two readers, as that specific lesion was not within bounds for correlation for one of the readers as defined in Table 3.2.

Table 3.7 Lesion correlation for Phantom B when no external markers are used for the deformation and with the use of 3 and 2 marker analysis. Note: Lesion Overlap is defined by the resultant of at least 2 out of 3 readers' data showing overlap for that specific lesion between ABUS and DBT set. +Indicates that lesion 3 in no marker analysis showed overlap for 2 out of 3 readers' datasets. * Indicates that lesion 7 was out of correlation bounds for one reader set and therefore the values are averaged based for two readers' data and not all three.

Without Marker Analysis				With 2 Marker Analysis ($d_M \leq 0.5$ mm)				With 3 Marker Analysis ($d_M \leq 0.5$ mm)			
Lesion ID	d_{COM} (mm)	d_O (mm)	Overlap	Lesion ID	d_{COM} (mm)	d_O (mm)	Overlap	Lesion ID	d_{COM} (mm)	d_O (mm)	Overlap
1	13.8 ± 0.4	2.7 ± 0.2	No	1	5.8 ± 2.0	n/a	Yes	1	9.1 ± 0.9	n/a	Yes
2	8.1 ± 0.5	2.9 ± 0.4	No	2	3.4 ± 0.9	n/a	Yes	2	2.9 ± 1.5	n/a	Yes
3 ⁺	5.8 ± 2.4	0.8 ± 0.0	Yes	3	3.4 ± 0.7	n/a	Yes	3	3.3 ± 2.0	n/a	Yes
4	11.1 ± 2.0	5.2 ± 1.3	No	4	6.7 ± 1.5	n/a	Yes	4	8.3 ± 1.6	1.1 ± 1.3	No
5	n/a	n/a	n/a	5	10.1 ± 1.2	1.0 ± 0.9	No	5	11.5 ± 0.8	1.6 ± 0.5	No
6	n/a	n/a	n/a	6	11.1 ± 2.7	4.0 ± 0.4	No	6	11.8 ± 3.7	5.1 ± 1.6	No
7	n/a	n/a	n/a	7*	12.7 ± 0.7	5.8 ± 0.1	No	7*	12.8 ± 0.2	6.6 ± 0.8	No
Average	9.7	2.9	Overlap	Average	7.6	3.6	Overlap	Average	8.5	3.6	Overlap
σ	3.5	1.8	1/4	σ	3.6	2.5	4/7	σ	4	2.6	3/7

3.5 Discussion

A novel automated deformable mapping algorithm has been described and assessed between upright DBT and supine ABUS images. Although this method uses commercially-available biomechanical modeling and FEA software, the techniques described can be applied to other commercially available software or research algorithms. This study demonstrates that with the use of 2-3 external fiducial markers for the deformation results in up to 28% improvement in lesion correlation (d_{COM}) in comparison with not using external markers. An expansion of this work will incorporate an interface on a radiologist work station for displaying corresponding lesions in the original ABUS and DBT slices as shown Figure 3.13.

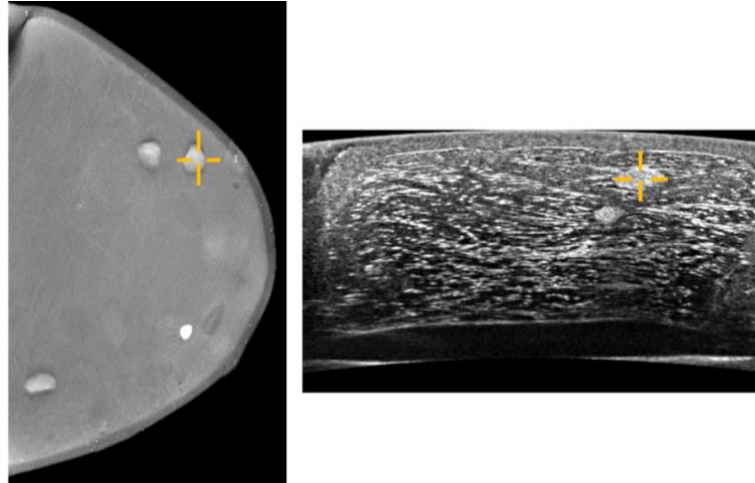


Figure 3.13 Relating corresponding lesion in DBT and ABUS original datasets for Phantom A based on use of deformable mapping algorithm results

Figure 3.10 demonstrates that for Phantom A, as the number of external fiducial markers that are used for deformable mapping increase from 4 to 6, the overlap fraction remains the same and the average d_{COM} remains approximately the same. This effect is probably a result of Phantom A being a stiff phantom. It should be noted that although, in this study, two different compression forces were used, and the phantoms represented two different breast densities, the automated deformable mapping algorithm was successful in identifying the majority of the corresponding lesions within the two phantom data sets. This supports translation of the deformable mapping method to actual patient data where there will be a wide range of compressions used as well as differences in breast density and size.

For Phantom B, without marker analysis only 4 lesions were correlated. Comparative t-tests of the means of the d_{COM} of those lesions without marker analysis to those with 2 and 3 marker combinations indicated statistical significance. With the use of 2 and 3 markers all 7 lesions came within correlation parameters. However, a statistically insignificant t-test of d_{COM} between the use of 2 and 3 markers indicates no greater improvement in correlation with the use of 3 markers over 2 in the indicated geometry. Nevertheless, additional markers in the axillary region,

which was not simulated in the phantoms for this study could potentially allow better registration in patient imaging. This will be investigated in future studies.

It is difficult to directly compare the results between Phantom A and Phantom B for the following reasons: Phantom A used more external markers than Phantom B. Phantom B did not contain the Z-skin membrane and all lesions were near the chest wall. Phantom B was easily compressed simulating a fatty breast and Phantom A represented a breast with higher glandular tissue content. Using only 3 external markers for Phantom B vs. 6 markers for phantom A may have biased the results. Using the same number of external markers for both phantoms would have allowed for a better direct comparison between the two data sets.

Overall, the phantoms were easily segmented by readers. The largest differences between readers and variance in reader reproducibility were evident in the DBT data sets. Due to poor axial resolution in DBT imaging, determining where lesions were blurred or out of focus at the superior and inferior extents of the lesions was difficult. Therefore, the use of an automated segmentation method would be useful and will be investigated for future work. Drawing the top and bottom of the lesions at a distance from the central plane equal to the mean circumference in the central plane might prove most effective. After lesions are correlated, their borders in DBT might be drawn better based on the ABUS contours.

When deforming the DBT model to the base ABUS model this study assumes that all lesions are homogenous and have the material properties of dense lesions. After correlation has taken place, for lesions that correlated to cystic lesions in the ABUS set the algorithm could be rerun with the correct cystic material properties. In actual patient data, there will be heterogeneity in breast tissue. An expansion of this study could investigate the significance of this heterogeneity in the FEA-based registration.

The use of 2 or 3 markers for deformable mapping with Phantom A showed improvements for d_{COM} results over the use of 4-6 markers. Based on marker placement in this study, markers located inferior to the nipple have direct contact with the breast support plate during DBT compression. The inferior part of the phantom flattens initially when the phantom is placed in contact with the breast support plate. It is believed that this contact restricts the movement of the markers resulting in small displacements of the markers in this region. The contact could also cause the markers to stick to the breast support plate during compression and fall off the breast eliminating their use in the subsequent ABUS scans and therefore in the deformable registration.

Conversely, markers located superior to the nipple (Figure 3.2 Positions A, B, and F) did not have initial contact with the DBT compression paddle and the marker displacements were not as easily compromised between DBT and ABUS imaging. Results from both phantoms indicate that a minimum of two or three external markers at the indicated positions provide significant improvement in lesion registration. However, we intend to directly quantify the number of markers and their respective locations that are the most helpful in an IRB approved proof-of-concept study with patients. Likewise, an MRI to US breast study also used three external markers at those approximate locations and found improvement in lesion registration.⁷²

Intuitively, one would suspect that more external markers would allow for better correlation. However, this study indicates that when modeling large breast compressions, external deformation may not be completely indicative of internal breast deformation. The degree to which this holds true for real breasts is yet to be determined. We believe that determination of optimal external marker positions on the breast could yield better results in lesion correlation, which could allow the use of fewer markers. A recent study using external fiducial markers to register MR breast images with microwave images found that fewer better placed fiducial

markers reduced the effect of skin translation that is associated with movement of internal structures in the breast.¹²³

The multimodality phantoms used in this work have limitations with respect to simulating real breasts. Some of these limitations include: 1) they are made of materials that follow a linear elastic behavior while under compression; whereas, real breast tissue follows hyperelastic behavior^{20,38,39}, 2) they have a homogeneous background; whereas, real breasts have a heterogeneous background and 3) they do not simulate attachment to the pectoral structure which could also contribute to the linear elastic behavior. Our planned human subject study will determine the degree to which these limitations affect the results in patients. To reduce these effects, we will use automatic segmentation of the DBT images into glandular and adipose tissues and include the elasticity properties of those tissues in our model. Further developments are needed to produce physical breast phantoms with materials that better model patient specific breast tissue properties and can model the axillary region of the breast. Other deformable breast registration studies have proposed the use of patient-specific in vivo parameters to determine biomechanical properties.^{71,85}

During ABUS imaging, up to 3 scans are rendered to image the breast in its entirety. The Invenia system scans from the superior to inferior margins of the breast producing axial images. The scans are performed in an AP view. For different views of the breast, this process can be repeated with parasagittal imaging planes. Multiple ABUS scans allow the ability to estimate the patient-specific distribution of elastic properties in the breast. Inclusion of ABUS-based elastography or pulse echo segmentation¹²⁴ could offer great benefits for the deformable mapping algorithm and other biomechanical techniques for use in FEA. With more ABUS scans, the need for an additional marker near the axilla region of the breast could be helpful in relating

ABUS projections. The present study only considers one ABUS volume; whereas, up to three volumes can be taken during an ABUS exam of a patient. Stitching or overlaying ABUS views into one volume would be helpful and provide better coverage for deformation of the DBT FE base algorithm. ABUS stitching or overlay could also allow this technique to deform the base ABUS model into the DBT base model. This would allow the correct cystic and dense lesion material properties to be assigned before FEA to their respective lesions. A future goal is to include correlation between DBT and ABUS sets in the axilla region of the breast.

When translating this technique to patients, we intend to use more external markers placed at better breast locations and have the patient wear a special camisole for the ABUS acquisitions. Currently, this study shows satisfactory results with the use of just three external markers for both phantoms. The use of more external markers will allow for full coverage of the breast including the axillary region and we can better determine what number of markers and their locations render the best results. As shown for the results of Phantom B, it would be better to directly determine which marker locations are best for all patient data by using the same number of markers at the same locations and then using the algorithm to determine the minimum needed for a desired registration result.

We expect that with the use of a breast ultrasound camisole, breast movement between various scans can be restricted. This restriction should reduce the effect of varying the compression between ABUS views. The use of the camisole can also address an additional potential problem with the external markers becoming attached to the ultrasound mesh paddle between multiple ABUS compressions. This camisole would need to be made of sheer material similar to the Invenia mesh membrane that does not affect the ultrasound depth of penetration and also does not interfere with coupling to the ultrasound transducer. Ultrasound penetration

and coupling of the Invenia mesh material is well understood and in some cases the use of this material improves coupling as it holds ultrasound gel in place. The SonoCiné AWBUS system (SonoCiné, Inc., Reno, NV)¹²⁵ is a commercially available system that uses an ultrasound camisole that fits similar to a sports bra to reduce breast movement during scanning. By restricting breast motion, a breast camisole should allow for improvement in lesion registration for the deformable mapping algorithm.

Specifically, even if some markers become detached there will still be a sufficient number remaining that can be used for registration. This study uses a tight 15 mm bound when determining a match between corresponding lesions since the phantoms have a uniform background. When translated to real breasts, this bound will likely increase due to breast heterogeneity and breast structures (i.e. Cooper's ligaments) that will not be modeled in the FE process. Additionally, we expect to segment glandular tissue from the background adipose tissue in the breast of the ABUS⁴³ and DBT images. Several studies, have found successful results in determining breast density from DBT breast images.⁴⁴⁻⁴⁶ Although, the poor spatial resolution of DBT in the z (depth) direction reduces the accuracy of the dense tissue segmentation in that direction, the overall coarse volumetric segmentation should still be of value in providing information about the spatial distribution of the glandular and adipose tissues within the breast for the deformable mapping. This should assist with the lesion correlation when the method is translated to patient images.

The process that took the most time in this study was the manual segmentation. In order for this technique to be effective in a clinical platform semi-automated and automated segmentation techniques will be needed and explored. Once all images are segmented the automated deformable mapping algorithm takes about 40 minutes to run on a Windows 7 Intel® Core™ i7

CPU with a speed of 2500 MHz and 4GB RAM. The runtime could be improved greatly with a computer with more memory and a capable GPU.

3.6 Conclusions

This work demonstrates the potential use of deformable mapping techniques to relate lesions between DBT and ABUS breast images. The utilization of external fiducial markers has been shown to improve the accuracy of this approach. The resulting one-to-one correlation between lesions in DBT and ABUS could help improve radiologists' characterization of breast lesions, which can reduce patient callbacks, negative biopsies and false negative biopsies. Future work will expand this platform to include an IRB approved study for patient volunteers, and an expansion of the deformable mapping technique for use in relating lesions in other breast modalities such as MRI, dedicated breast CT and transmission US.

3.7 Acknowledgements

This work was supported in-part by a research grant (15-PAF04328) from GE Global Research. Crystal A. Green is supported by the Science, Mathematics and Research for Transformation (SMART) Scholarship for Service Program (HQ0034-16-C-0008). The authors would like to thank Ted Lynch, Ph.D., of CIRS, Inc. for his assistance in phantom development and characterization. The authors would like to thank Darius Fadanelli, Eamon Whalen, and John P. Kytasty of Altair Engineering Inc. for their assistance in FE modeling and processing.

Chapter 4

Deformable Mapping Technique for lesion registration for Multiple Digital Breast Tomosynthesis views to Automated Breast Ultrasound Images^o

4.1 Abstract

Purpose: To test an automated deformable mapping method for registering corresponding lesions in the craniocaudal (CC) and mediolateral oblique (MLO) digital breast tomosynthesis (DBT) views to automated breast ultrasound (ABUS) images with and without the use of external fiducial markers.

Methods: A Computerized Imaging Reference Systems Inc. (CIRS) multi-modality breast phantom containing 20 lesions was employed and imaged with DBT (upright positioning with CC compression and MLO compression), and ABUS (supine positioning with anterior-to-chest wall compression). Eight external fiducial markers (gel pads containing 1-mm glass beads) were attached to the surface of the breast phantom prior to the imaging. The reconstructed images were segmented using manual (ABUS) and semi-automated (DBT) techniques. An automated

^o This chapter is published in the Radiological society of North America 2018 Scientific Assembly and Annual Meeting: Green CA, Goodsitt MM, Lau JH, Brock KK, Davis CL, Carson PL. Evaluation of an Automated Deformable Mapping Technique with and Without External Fiducial Markers to Relate Corresponding Lesions in Digital Breast Tomosynthesis and Automated Breast Ultrasound Images.itle. In: *Radiological Society of North America 2018 Scientific Assembly and Annual Meeting, November 25 - November 30, 2018, Chicago IL.* ; 2018. archive.rsna.org/2018/18005292.html.

mapping method generates, deforms, and relates the resulting models of the breast for registration of lesions between the DBT (CC or MLO) and ABUS image sets. Performance was assessed by the number of matched paired lesions and measures of the distances between the centers of mass (d_{COM}) of corresponding lesions.

Results: The maximum number of lesions that could be matched was 18 because 2 of the 20 lesions were too close to the chest wall to be visible in the reconstructed DBT images. For mapping of DBT (CC) to ABUS without markers, 14 of the 18 lesions were matched and the mean d_{COM} was 13.6 ± 6.3 mm. With markers, 17 of the 18 lesions were matched and the mean d_{COM} was 12.8 ± 6.0 mm. For mapping of DBT (MLO) to ABUS without markers, 8 of the 18 lesions were matched and the mean d_{COM} was 9.3 ± 2.8 mm. With markers, 17 of the 18 lesions were matched and the mean d_{COM} was 12.3 ± 5.8 mm.

Conclusion: This work demonstrates the potential for using this deformable mapping technique to identify related lesions between two DBT views and ABUS images. This method shows improved lesion correlation with the use of external fiducial markers and extends upon our previous work by incorporating registration from the DBT MLO to the ABUS view. This method should improve radiologists' characterization of breast lesions which should reduce patient callbacks and unnecessary biopsies. Future work will include an IRB-approved proof of concept study with patient data for registration between DBT and ABUS images.

4.2 Introduction

Ultrasound imaging used in adjunct with mammography has been shown to improve the characterization of breast lesions.¹⁶⁻¹⁸ However, at least 10% of the time lesions found in ultrasound images do not correspond to those in mammograms.¹⁵ This discrepancy is due to several factors. Mammography images the entire breast as a 2D projection which results in the

superposition of breast structures. Conventional ultrasound uses sound reflection imaging, typically from linear or convex linear arrays, that creates 2D planar images of the specified breast area in depth and along the length of the array. Most ultrasound imaging is controlled and operated by hand and therefore has high operator dependence. This can cause difficulty in reproducing ultrasound images. There is also a difference in patient positioning and a major difference in compression applied to the breast between the two modalities. Conventional ultrasound imaging is performed in the supine geometry where typically anterior-to-posterior (AP) compression is applied by a sonographer using an ultrasound transducer. Mammography imaging is performed with the woman upright and with typically, CC or MLO compression being applied to the breast between a compression plate and detector panel.

Three dimensional forms for ultrasound and mammographic technologies ultrasound exist and could be beneficial in relating lesions between these 3D imaging modalities. A 2D mammogram only allows localization of a mass to a line through the thickness of the breast. Automated breast ultrasound, ABUS, has advantages over conventional breast ultrasound in terms of reproducibility and operator independence by visualizing the breast as a 3D image volume. Studies have shown the addition of ABUS images with mammography screening have significantly improved breast cancer detection rate for women with dense breasts.^{19,57,58} Digital breast tomosynthesis, DBT, is a quasi-3D form of mammography that provides better detection and characterization of breast lesions over mammography through the reduction of tissue superposition. However, even with these improvements, DBT has not completely eliminated the need for the use of ultrasound as a complement to DBT/mammography.^{109,110}

In our previous work³⁴, a deformable mapping method was developed to relate corresponding lesions between the DBT (CC view) to ABUS where a significant improvement

($p=0.01$) was shown using external fiducial markers to aid in the methodology. The purpose of the present study is to extend upon this work by evaluating the deformable mapping technique using both the CC and MLO DBT views to relate corresponding masses to ABUS. This is significant as the MLO view is important for imaging close to the axillary regions of the breast which encompasses the upper outer breast quadrant where most cancers are located.¹²⁶ A study by Duffy et al. suggests that using breast density as an indicator of breast cancer risk is enhanced by interactive software that uses the CC and MLO view vs a single view.⁵⁸ Additionally, this work also incorporates the use of semi-automated segmentation of the lesions in the DBT images; whereas only manual segmentation was used for all modalities in our previous work³⁴.

4.3 Materials and Methods

4.3.1 Phantom

A CIRS Multi-Modality Breast Biopsy and Sonographic phantom (Computerized Imaging Reference Systems, Inc., Norfolk, Virginia)^p was used in this study. The phantom contains a total of 20 lesions: 10 spherical cystic lesions, 5 spherical dense lesions, and 5 spiculated dense lesions. The lesions are randomly located in a background gel, Zerdine, and wrapped in a Z-skin membrane material. The lesions are made of the similar Zerdine-based materials; however, the cystic lesions have anechoic properties and the dense lesions have hyperechoic properties under ultrasound. Material properties phantom components were provided by the manufacturer in Table 4.1. For use in the finite element analysis (FEA) solver, a Poisson's ratio of 0.49 was used for convergence stability since the FEA solver cannot run using a Poisson's ratio of 0.50.

^p [http://www.cirsinc.com/file/Products/073/073%20DS%20110617\(3\).pdf](http://www.cirsinc.com/file/Products/073/073%20DS%20110617(3).pdf)

Table 4.1 Material Properties of CIRS phantom

	Young's Modulus (E)	Poisson's Ratio (ν)
Z-skin Membrane	10 kPa	0.50
Zerdine background gel	10 kPa	0.50
Lesions	60 kPa	0.50

4.3.2 External Fiducial Markers

The breast phantom was marked with a magic marker to differentiate marker locations. Eight external fiducial markers were attached using Jobst “It-Stays” Roll-On Adhesive (BSN Medical, Charlotte, NC)^q to the breast phantom at the indicated locations as shown in Figure 4.1. Each marker contains a solid 1 mm diameter glass bead within a thermoplastic elastomer gel. The 1 mm glass bead within the gel can be clearly seen in the reconstructed images and are used to aid in the deformable mapping process. A detailed explanation of how these markers are created can be found in our previous study³⁴ and in the Appendix.

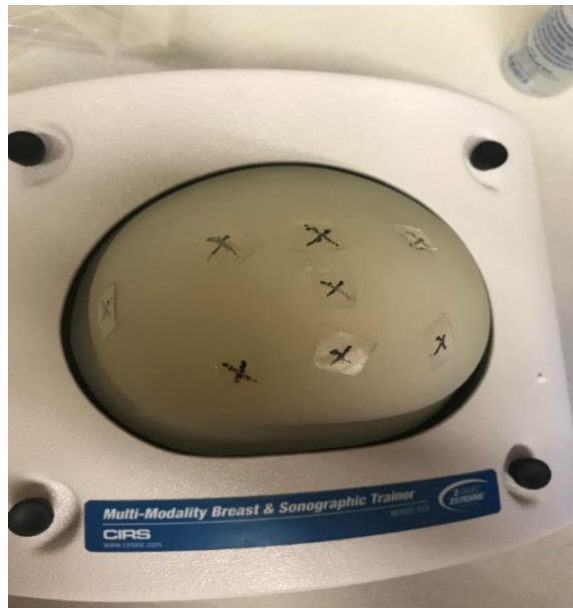


Figure 4.1 CIRS Multi-modality phantom with 8 external markers attached

^q <http://www.jobst-usa.com/product/it-stays-roll-on-adhesive/>

This phantom was imaged using DBT and ABUS techniques, the external fiducial markers can be clearly seen in reconstructed DBT and ABUS images as shown by the red arrow in Figure 4.2.

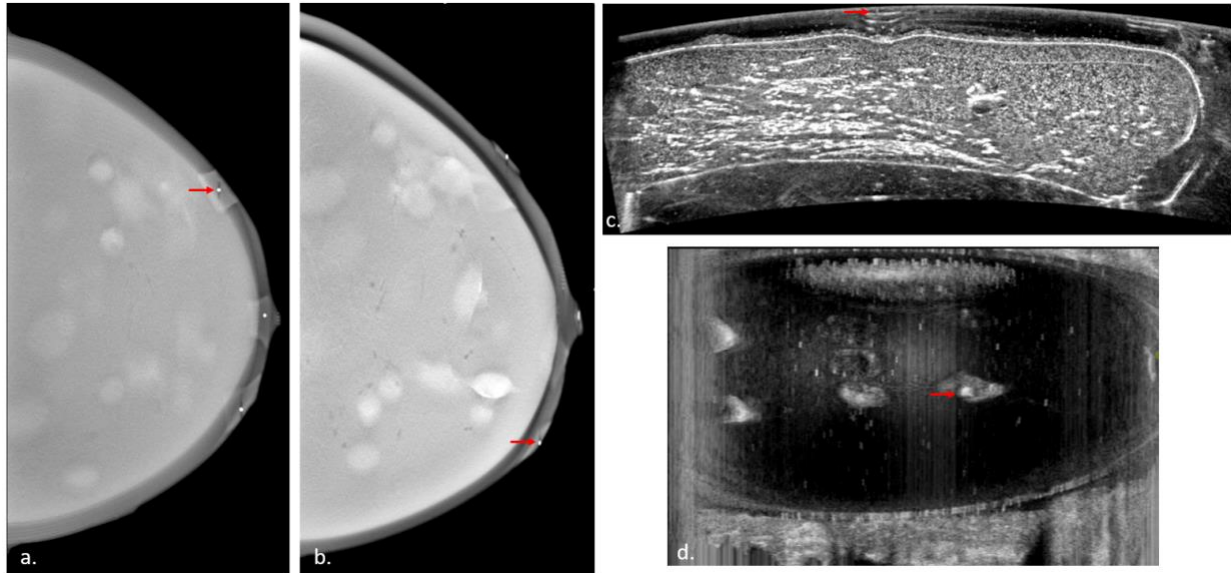


Figure 4.2: Reconstructed slice indicating external fiducial marker (red arrow) for a slice of (a) DBT (CC view) (b) DBT (MLO view) (c) ABUS transverse view (d) ABUS coronal view

4.3.3 Image Acquisition

The GE Senographe Pristina DBT system (GE Healthcare, Milwaukee, WI) was used to image the phantom in CC and MLO view. For the CC view, a compressive force of 3 daN (decanewton) was used and the phantom was compressed to a thickness of 44.2 mm. For the MLO view, a compressive force of 2.5 daN was used and the phantom was compressed to a thickness of 48.5 mm. For both image views, only 18 lesions were shown in reconstructed DBT images. Two lesions were not seen because they are close to the phantom “chest wall”. The phantom backing restricts the ability to image close to that area.

Lastly, the phantom was imaged with the GE Invenia ABUS system (GE Healthcare, Milwaukee, WI). Light anterior-to-posterior (AP) compression is applied when imaged with the Invenia and the medium imaging setting was used. The Invenia ABUS operates between 6-15

MHz and can image up to a 50 mm depth. The system contains three settings based on imaging depth (high, medium and low). For this study, the medium setting was used which images up to 40 mm. Clinical procedures can include up to three image sweeps of the breast depending on breast size to ensure coverage of the breast and axillary region in its entirety. Due to the absence of the axillary region, only one image sweep using ABUS was acquired. All 20 lesions were shown in reconstructed ABUS images.

4.3.4 Segmentation Techniques

Lesions in the DBT acquired images were segmented using a semi-automated segmentation program called MiViewer.¹²⁷ For the ABUS images, all dense lesions were segmented using the MiViewer program. The 10 cystic lesions in ABUS images were segmented using automated nonlinear filtering and segmentation approach by Elawady et al.¹²⁸ Figure 4.3 shows a representation of segmentations of the phantoms.

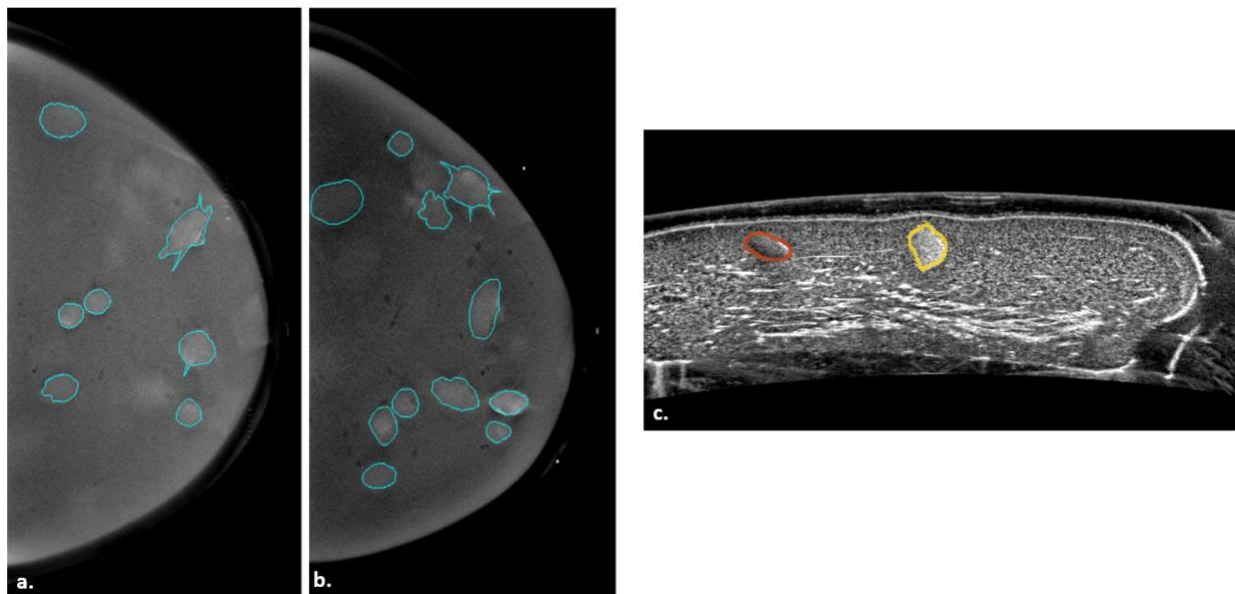


Figure 4.3: Segmentation of lesions within an image slice of (a) DBT CC (b) DBT MLO (c) ABUS

4.3.5 Automated deformable mapping algorithm

The deformable mapping algorithm is an automated process that integrates the use of Morfeus, a commercial FE pre-processor (HyperMesh 2017, Altair Engineering, Troy, MI) and a finite element analysis (FEA) solver processor (Optistruct 2017, Altair Engineering, Troy, MI). An overview of the process is shown in Figure 4.4. The entire algorithm takes up to approximately 60 minutes to complete from start to finish on a Windows 7 Intel® Core™ i7 CPU with a speed of 2500 MHz and 4GB RAM.

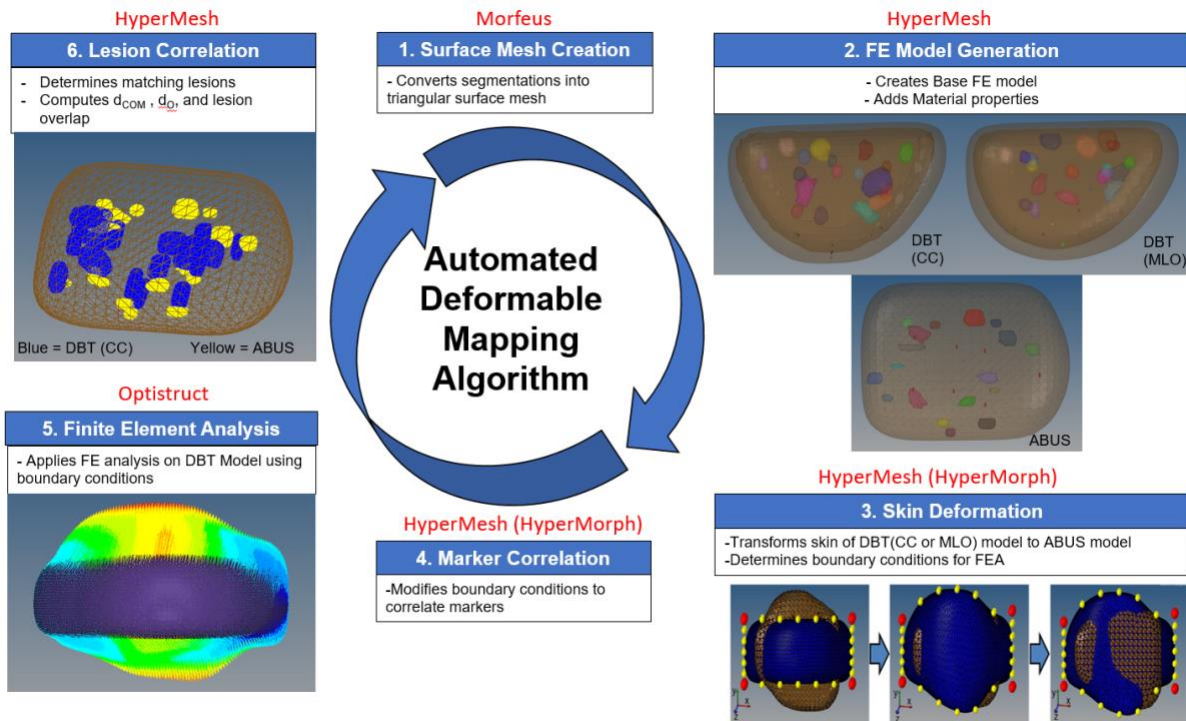


Figure 4.4 The automated deformable mapping process for DBT to ABUS registration. Software's used are shown in red.

In ABUS imaging, poor acoustic contact with the transducer often occurs around the periphery of the breast causing artifacts as shown on the right and left sides of Figure 4.2 (c). These artifacts cause the actual breast size and shape in ABUS imaging to be unknown. In comparison, the breast shape and size are better defined in the DBT (CC or MLO) images as shown in Figure 4.2 (a) and Figure 4.2 (b). Therefore, the deformable mapping algorithm

performs deformation only to the DBT FE model and registers the resulting deformation to the reference ABUS image set.

The algorithm begins with a conversion of DICOM segmented images to a triangular surface mesh using Morfeus, a finite element based multi-organ deformable image registration platform. Morfeus converts the DICOM image data into mask files for image analysis using Interactive Data Language (IDL, Research Systems Inc.). A surface mesh is created for each individual contour. Morfeus uses Laplacian smoothing and a decimate^r function in order to maintain a reasonable mesh size while maintaining structure features for each mesh.

Next, the algorithm uses the FE pre-processing software, HyperMesh, to build the base FE models for the DBT (CC and MLO) image sets from the associated mesh surface contours. From these contours, 3D four-point tetrahedral FE models are generated for each modality which results in fully connected meshed FE base DBT and ABUS models. Material properties are assigned to the different models as noted in Table 4.1. The number of elements/nodes is 577,295/99,684 for the base DBT (MLO) model, 547,426/94,408 for the base DBT (CC) model and 231,990/38,021 for the base ABUS model.

Skin deformation for the DBT (CC) model to ABUS is explained in Sec. 3.3.5.3. Skin deformation for the DBT (MLO) model is slightly different and will be described as follows. For the base DBT-MLO model the ABUS, the ABUS model is rotated -45° (Figure 4.5, brown) for the left breast and 45° for the right breast. Then the DBT-MLO base model (Figure 4.5 (a), blue) is translated and rotated to the COM of the rotated ABUS model as shown in Figure 4.5 (a). Skin deformation then performs exactly as described in Sec. 3.3.5.3 by manipulating the handles (red and yellow spheres shown in Figure 4.5). First corrections along the axial plane of the breast are

^r A decimate function is used to decrease the sampling rate of a signal sequence or continuous function by an integer factor

made along the y-axis as shown in Figure 4.5 (b) and then corrections along the coronal plane as shown in Figure 4.5 (c). Again, there are no corrections along the sagittal axis (x-plane) due to poor transducer coupling on the right and left sides of the breasts as shown in Figure 4.2 (c).

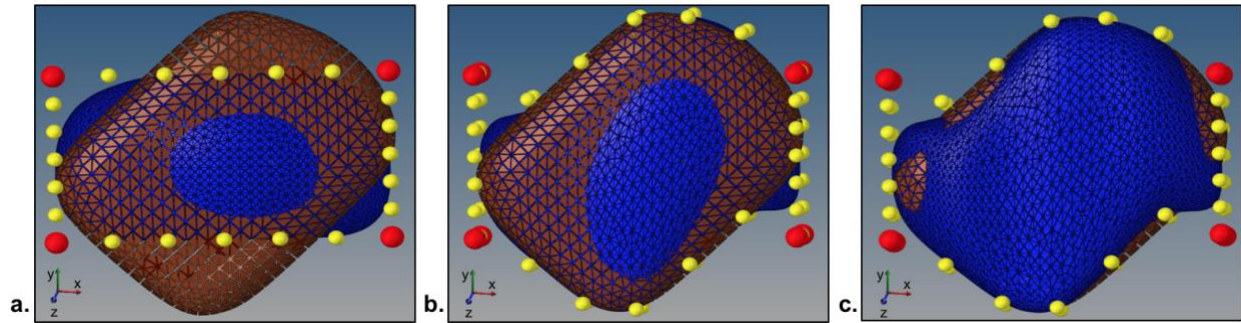


Figure 4.5 Skin Mesh transformation for base DBT-MLO model (blue) to ABUS model (brown) (a) translation and rotation of DBT-MLO model to COM of ABUS model (b) decompression of skin model along the y-axis to match ABUS shape (c) compression in the z direction of the DBT-MLO model

Once skin surface deformation is completed, the algorithm computes the COM positions of the external marker locations between the two models as described in Chapter 3 Sec. 3.3.5.4. Once the marker locations are matched the handles shown in Figure 4.5 are manipulated again so that the DBT-MLO model is more aligned with the external markers of the reference ABUS model within a user-defined distance, d_M . The resulting changes in the displacement of each node of the original surface mesh (Figure 4.5 (a)) are applied as boundary conditions for FEA deformation. The boundary conditions are applied to the translated base DBT model (Figure 4.5 (a) for MLO case) that incorporates changes for skin deformation and external marker correlation. These boundary conditions are used as input for the FEA solver, Optistruct. Optistruct generates and solves the differential equations that describe the model deformation and returns the resulting stress and strain due to the deformation of the entire breast volume. The FEA was performed on a Windows 10 Intel® Core™ i7 CPU speed of 2500 MHz with 4GB RAM with analysis complete in approximately twenty minutes.

After FEA is performed the COM of all lesions between the resultant DBT model and the reference ABUS model are calculated. The COM of each lesion is computed by exporting the nodal (x, y, and z coordinates) from HyperMesh of the lesion exterior surface mesh and taking an average of those coordinate values. The algorithm then determines which lesions correspond by determining the minimum distance between COMs and ensuring the lesions are within correlation guidelines as described in Table 4.2. The d_{COM} value for this study increased due to the softness of this phantom in comparison to the previous study in Chapter 3 Sec. 3.3.5.6. The minimum distance to overlap, d_o , for non-overlapping lesions is restricted by half of tolerable d_{COM} distance in order to reduce the likelihood of a match discrepancy. The results are exported as a table and are used to relate the original position from the ABUS and DBT DICOM data.

Table 4.2: Lesion correlation criteria between DBT (CC or MLO) and ABUS models

	d_{COM}	d_o
Overlapping Lesions	$d_{COM} \leq 25$ mm	n/a
Non-overlapping Lesions	$d_{COM} \leq 25$ mm	$d_o \leq 12.5$ mm

4.3.6 Studies Performed

Studies were undertaken to evaluate the performance of the deformable mapping technique for DBT (CC view) to ABUS and DBT (MLO view) to ABUS and are described as follows:

- *Accuracy of the deformable mapping technique for DBT (CC) to ABUS registration:*

Results (d_{COM}) are compared between using the deformable mapping algorithm (with and without marker analysis). T-test and signed Wilcoxon rank tests are used to provide the null hypothesis, that there is no improvement using the deformable method with using external marker locations in comparison to using the deformable method without external marker analysis included. Based off d_{COM} results further analysis is performed to

determine how the d_{COM} results vary based off lesion locations within the breast (e.g. quadrants and depths) and the effect lesion proximity to external markers.

- *Validation of deformable registration of DBT (MLO view) mapped to ABUS images:* This study was performed just as described previously for the DBT (CC view).

4.4 Results

4.4.1 Accuracy of deformable mapping technique for DBT (CC) to ABUS registration

An overview of results for lesion registration of the DBT (CC) model to ABUS is illustrated in Table 4.3. A maximum of 18 lesions can be related in the reconstructed DBT (CC) images since 2 lesions were located too close to the phantom “chest wall” and pushed outside of the detector field of view. Without the use of marker analysis (Step 4 is skipped in Figure 4.3), 14 lesions were matched with an average d_{COM} of 13.6 ± 6.3 mm. With the use of external markers this improves to 17 matched lesions with a mean d_{COM} was 12.8 ± 6.0 mm. With the use of external markers, the total number of matched lesions improved to 17 out of 18. When all external markers were within 1-mm distances ($d_M \leq 1$ mm) the average d_{COM} was 12.93 ± 6.28 mm. When the external markers were within 5-mm ($d_M \leq 5$ mm) the average d_{COM} was 12.83 ± 6.03 mm. The mean difference in lesion d_{COM} was 0.10 mm. A paired t-test was performed on the mean d_{COM} values when markers are within a 1 mm distance ($d_M \leq 1$ mm) and a 5 mm distance ($d_M \leq 5$ mm) and resulted in a p-value of 0.64. Using a Wilcoxon signed-rank test the p-value was calculated to be 0.49. Thus, both statistical tests show that the null hypothesis cannot be rejected.

Table 4.3: Lesion correlation summary for DBT (CC) registered to ABUS. A maximum of 18 lesions could be matched between image sets.

	Without Marker Analysis	With Marker Analysis ($d_M \leq 1$ mm)	With Marker Analysis ($d_M \leq 5$ mm)
Total Matched Lesions	14	17	17
Mean d_{COM} (mm)	13.6 ± 6.3	12.9 ± 6.3	12.8 ± 6.0
Mean d_O (mm)	5.3 ± 3.6	5.4 ± 3.3	4.9 ± 3.3
Total Overlapping Lesions	4	6	6

To assess the effect of deformable mapping with external fiducial marker vs. without external fiducial marker analysis, a paired t-test of the d_{COM} 's was performed for the 14 lesions that were matched without marker analysis to the same 14 lesions that were matched with marker analysis with $d_M \leq 1$ mm and $d_M \leq 5$ mm. A summary of the values used for this calculation is shown in Table 4.4. Using a paired t-test the resulting p-value for $d_M \leq 1$ mm and $d_M \leq 5$ mm was 0.19 and 0.04. Thus, for those 14 lesions using a $d_M \leq 5$ mm for the deformable registration indicates significant improvement in lesion d_{COM} with the use of external fiducial markers. Using a Wilcoxon signed-rank test the resulting p-value for $d_M \leq 1$ mm and $d_M \leq 5$ mm was 0.21 and 0.06. Thus, both statistical tests show that the null hypothesis cannot be rejected.

There were 4 lesions whose correlated d_{COM} 's worsened using marker analysis (Lesion ID's 4, 8, 9, and 10 in Table 4.6) and three of those lesions were in the superior lateral breast margins. There were 3 lesions that were not within correlation bounds without using marker analysis but became within correlation bounds using marker analysis (Lesion ID's 6, 11, and 12 in Table 4.6) which two of these are in the central lateral breast margin, one is located in central medial breast margins and all lesions were posterior in depth. Lesions that showed the greatest improvements (d_{COM} (without markers analysis) - d_{COM} (with markers analysis) ≥ 1.12 mm based on the 95% confidence interval) are along the medial breast margins (Lesion ID's 2,3,14 and 17 in Table 4.6) and inferior breast margins (Lesion ID's 3, 5, and 13 in Table 4.6).

Table 4.4: Lesion correlation summary for 8 matched lesions between without marker analysis and with marker analysis cases for DBT (CC) registered to ABUS.

	Without Marker Analysis	With Marker Analysis ($d_M \leq 1$ mm)	With Marker Analysis ($d_M \leq 5$ mm)
Total Matched Lesions	14	14	14
Mean d_{COM} (mm)	13.6 ± 6.3	12.7 ± 5.9	12.5 ± 5.8
Total Overlapping Lesions	4	5	5

Figure 4.6 visually displays the improvement in lesion correlation between the DBT (CC) to ABUS models for several lesions.

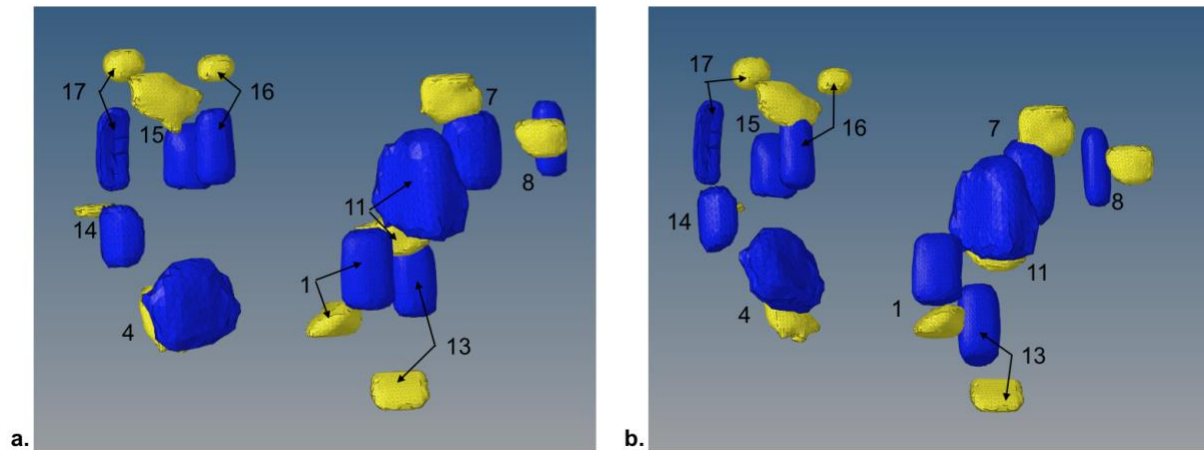


Figure 4.6 Lesion correlation for DBT-CC (blue) registered to ABUS (yellow) for selected lesions in the coronal plane (a) without marker analysis (b) with marker analysis. Note: All lesions could not be shown due to superposition.

A study was performed to show how d_{COM} results varied with the distance of the lesions to the nearest matched external fiducial marker. This study also was performed to quantify the amount of improvement in d_{COM} when a lesion is closer to the nearest ABUS external marker. The distance between the lesion COM and the nearest ABUS external marker is denoted as the d_{COM-M} . Results for this study are shown in Table 4.5. From this table we see that markers that had most improvements (negative difference in d_{COM} using marker analysis vs. no markers used) were Lesion ID's 3, 5 and 13. These lesions were at least 26 mm away from the nearest external marker (d_{COM-M}). The lesions that were closest to an external marker ($d_{COM-M} \leq 10$ mm) were Lesion

ID's 1 and 4. From these two lesions one shows improvement in d_{COM} while the other does not. Lesion ID 8 was the furthest away from the nearest marker and had a corresponding d_{COM} of 6.2 mm using marker analysis. Visually, as shown in Figure 4.7, we see that lesions proximity to external markers is independent of corresponding d_{COM} .

Table 4.5: Effect of d_{COM} based on lesion COM distance to nearest external marker (d_{COM-M})

Lesion ID	Without Marker Analysis	With Marker Analysis ($d_M \leq 5$ mm)		Difference in d_{COM} (mm)
	d_{COM} (mm)	d_{COM} (mm)	d_{COM-M} (mm)	
1	12.5	11.5	8.8	-1.0
2	4.6	3.2	23.0	-1.4
3	8.0	3.5	33.1	-4.5
4	8.0	9.3	6.4	1.3
5	23.3	19.5	26.5	-3.8
6	n/a	23.9	27.0	n/a
7	11.3	10.9	29.6	-0.4
8	5.0	6.2	37.0	1.2
9	21.2	21.6	23.5	0.4
10	14.4	15.0	21.2	0.6
11	n/a	9.5	15.7	n/a
12	n/a	10.1	18.8	n/a
13	23.6	19.2	25.5	-4.4
14	11.1	8.9	21.6	-2.1
15	14.3	14.1	23.8	-0.2
16	16.5	15.9	16.7	-0.6
17	17.3	15.7	32.4	-1.6
18	n/a	n/a	22.8	n/a
Average	13.6	12.8	23.0	-1.2
σ	6.3	6.0	7.9	2.0

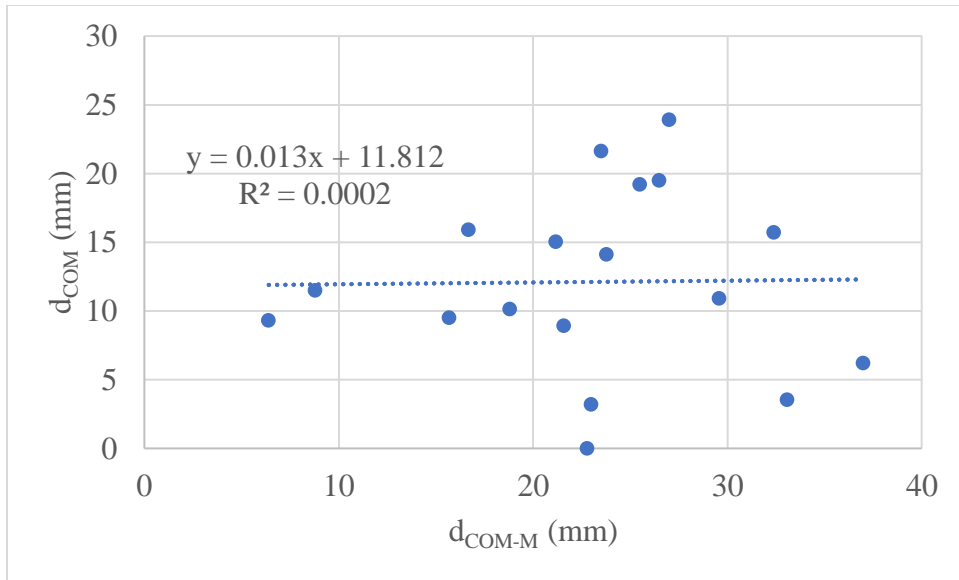


Figure 4.7: Plot of d_{COM} (COM distance between corresponding lesions) vs d_{COM-M} (distance between COM of lesion to nearest external marker) for DBT (CC view) to ABUS

Figure 4.8 shows a GUI-Viewer for a marked corresponding lesion in the DBT (CC view) to ABUS original DICOM image sets. From the view in the ABUS image the suspicious mass can be interpreted as a dense spiculated solid lesion. Detailed lesion correlation values are shown in Table 4.6. Further information on the GUI viewer can be found in the Appendix.

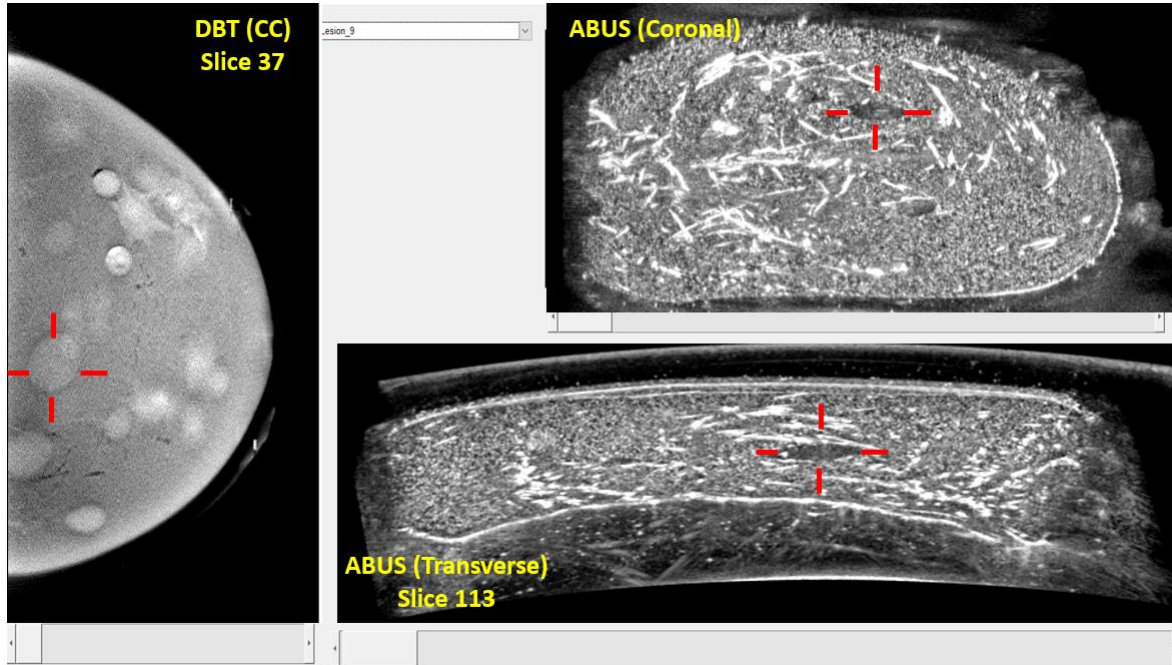


Figure 4.8: GUI representation for marked corresponding lesion (Lesion ID=1 see Table 4.5) in the DBT (CC) to ABUS original DICOM image views. From the view in the ABUS image the suspicious mass can be interpreted as a dense solid lesion. Detailed corresponding lesion values are shown in Table 4.6.

Table 4.6: Lesion correlation results for each lesion with and without marker analysis for DBT (CC) registered to ABUS. Location for breast margins abbreviations include I=Inferior S=Superior C=Central A=Anterior P=Posterior M=Medial L=Lateral

Lesion ID	Lesion Type & (Location)	Without Marker Analysis			With Marker Analysis ($d_M \leq 5$ mm)		
		d_{COM} (mm)	d_o (mm)	Overlap	d_{COM} (mm)	d_o (mm)	Overlap
1	Dense (UOQ-A)	12.5	1.2	no	11.5	0.0	yes
2	Dense (LIQ-A)	4.6	0.0	yes	3.2	0.0	yes
3	Dense (UIQ-P)	8.0	0.0	yes	3.5	0.0	yes
4	Dense (UIQ-A)	8.0	1.3	no	9.3	0.0	yes
5	Dense (UIQ-P)	23.3	10.4	no	19.5	5.8	no
6	Dense (UOQ-P)	n/a	n/a	n/a	23.9	10.7	no
7	Cystic (LOQ-P)	11.3	0.0	yes	10.9	0.0	yes
8	Dense (LOQ-A)	5.0	0.0	yes	6.2	0.3	no
9	Dense (LOQ-P)	21.2	8.2	no	21.6	8.1	no
10	Dense (LOQ-P)	14.4	3.2	no	15.0	3.3	no
11	Cystic (UOQ-P)	n/a	n/a	n/a	9.5	0.0	yes
12	Cystic (UOQ-P)	n/a	n/a	n/a	10.1	0.7	no
13	Cystic (UOQ-P)	23.6	11.6	no	19.2	7.4	no
14	Cystic (UIQ-P)	11.1	4.0	no	8.9	2.7	no
15	Cystic (LIQ-A)	14.3	2.6	no	14.1	3.8	no
16	Cystic (LIQ-A)	16.5	5.4	no	15.9	6.2	no
17	Cystic (LIQ-A)	17.3	5.1	no	15.7	5.4	no
18	Dense (UIQ-P)	n/a	n/a	n/a	n/a	n/a	n/a
Mean		13.6	5.3	Overlap	12.8	4.9	Overlap
σ		6.3	3.6	4/14	6.0	3.3	6/17

4.4.2 Accuracy of deformable mapping technique for DBT (MLO) to ABUS registration

An overview of results for lesion registration of the DBT (MLO) model to ABUS is illustrated in Table 4.7. A maximum of 18 lesions can be related in the reconstructed DBT (MLO) images since 2 lesions were located too close to the phantom “chest wall” and pushed outside of the detector field of view. Without the use of marker analysis, only 8 out of 18 lesions were matched with an average d_{COM} of 9.3 ± 2.8 mm. When all external markers were within 1-mm distances ($d_M \leq 1$ mm) the number of matched lesions improved to 16 and the average d_{COM} was 12.7 ± 6.4 mm. When the external markers were within 5-mm ($d_M \leq 5$ mm) the number of

matched lesions improved to 17 and the average d_{COM} was 12.3 ± 5.8 mm. A paired t-test was performed on the mean d_{COM} values of the 16 shared lesions when markers are within a 1 mm distance ($d_M \leq 1$ mm) and a 5 mm distance ($d_M \leq 5$ mm) and resulted in a p-value of 0.30. Using the Wilcoxon-signed rank test for when markers are within a 1 mm distance ($d_M \leq 1$ mm) and a 5 mm distance ($d_M \leq 5$ mm) both resulted in a p-value of 0.60. Thus, both statistical tests show that the hypothesis claim cannot be rejected.

Table 4.7: Lesion correlation summary for DBT (MLO) registered to ABUS. A maximum of 18 lesions could be matched between image sets.

	Without Marker Analysis	With Marker Analysis ($d_M \leq 1$ mm)	With Marker Analysis ($d_M \leq 5$ mm)
Total Matched Lesions	8	16	17
Mean d_{COM} (mm)	9.3 ± 2.8	12.7 ± 6.4	12.3 ± 5.8
Mean d_O (mm)	1.9 ± 1.3	6.0 ± 3.7	5.3 ± 3.8
Total Overlapping Lesions	3	6	8

To assess the effect of deformable mapping with external fiducial marker vs. without external fiducial marker analysis, a paired t-test of the d_{COM} 's was performed for the 8 lesions that were matched without marker analysis to the same 8 lesions that were matched with marker analysis with $d_M \leq 1$ mm and $d_M \leq 5$ mm. A summary of the values used for this calculation is shown in Table 4.8. The resulting p-value was 0.65 using a paired t-test and the p-value was 0.95 using a Wilcoxon signed-rank test. This indicates that the hypothesis claim cannot be rejected. However, with the use of markers the number of matching lesions increased from 8 to 17, therefore showing improvement in lesion correlation.

There were 9 lesions that were not within correlation bounds without using marker analysis but became within correlation bounds using marker analysis (Lesion ID's 2, 5, 6, 7, 9, 10, 12, 13, and 15 in Table 4.10). These lesions are within various breast locations and depth of the breast. However, there were 4 lesions whose correlated d_{COM} 's worsened using marker analysis (Lesion

ID's 4, 8, 11, and 18 in Table 4.10) and two of those lesions were within the upper outer quadrants (Lesion ID 8) and central lateral breast region (Lesion ID 11 see Table 4.10) The other two lesions were along the lower inner breast quadrants (Lesion ID 4 and 18 see Table 4.10). All of these lesions are posterior in depth and were either the most medial or most lateral lesions within the breast. Lesions that showed an improvement in registration using marker analysis were located in the upper inner quadrants (Lesion ID's 14, 16 and 17 see Table 4.10) and one lesions was in the lower central breast region (Lesion ID 1 see Table 4.10).

Table 4.8: Lesion correlation summary of 8 matched lesions between without marker analysis and with marker analysis cases for DBT (MLO) registered to ABUS

	Without Marker Analysis	With Marker Analysis ($d_M \leq 1$ mm)	With Marker Analysis ($d_M \leq 5$ mm)
Total Matched Lesions	8	8	8
Mean d_{COM} (mm)	9.3 ± 2.8	9.8 ± 4.2	9.8 ± 3.6
Total Overlapping Lesions	3	4	4

Figure 4.9 visually displays the improvement in lesion correlation between the DBT (CC) to ABUS models for several lesions.

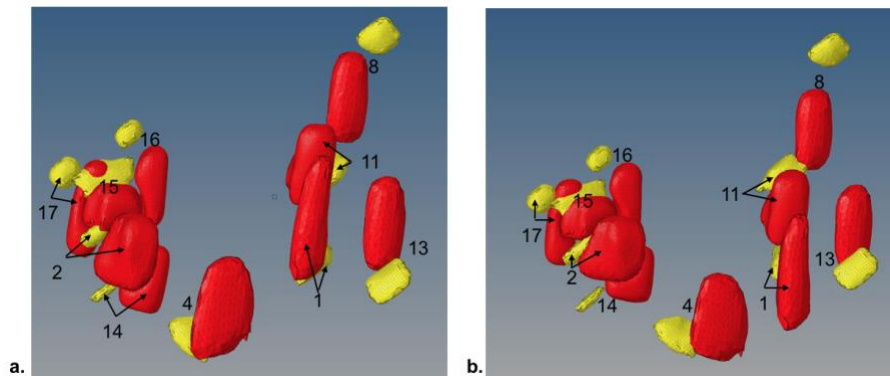


Figure 4.9: Lesion correlation for DBT (MLO view) (red) registered to ABUS (yellow) for selected lesions in the coronal plane (a) without marker analysis (b) with marker analysis. Note: All lesions could not be shown due to superposition.

A study was performed to show how d_{COM} results varied with the distance of the lesions to the nearest matched external fiducial markers. This study also was performed to quantify the

amount of improvement in d_{COM} when a lesion is closer to an external marker. Results for this study are shown in Table 4.9. The markers observed to have the most improvements (negative difference in d_{COM} using marker analysis vs. no markers used) were Lesion ID's 1, 16 and 17. These lesions were at least 14 mm away from the nearest external marker (d_{COM-M}). The lesions that were closest to an external marker ($d_{COM-M} \leq 15$ mm) were Lesion ID's 11, 12 and 16. From these two lesions two showed improvement in d_{COM} while the other does not. Lesion ID 8 was the furthest away from the nearest marker and had a corresponding d_{COM} of 10.3 mm using marker analysis and without marker analysis was not within correlation bounds. Visually as shown in Figure 4.10, we see that lesions proximity to external markers is independent of corresponding d_{COM} .

Table 4.9: Effect of d_{COM} based on lesion COM distance to nearest external marker (d_{COM-M})

Lesion ID	Without Marker Analysis	With Marker Analysis ($d_M \leq 5$ mm)		Difference in d_{COM} (mm)
	d_{COM} (mm)	d_{COM} (mm)	d_{COM-M} (mm)	
1	11.3	8.9	20.2	-2.4
2	n/a	7.9	17.1	n/a
3	n/a	n/a	22.7	n/a
4	5.9	6.1	17.7	0.2
5	n/a	11.4	22.4	n/a
6	n/a	19.5	26.8	n/a
7	n/a	21.9	23.2	n/a
8	11.1	16.9	28.1	5.8
9	n/a	21.9	14.8	n/a
10	n/a	21.3	22.8	n/a
11	7.9	9.9	14.4	2
12	n/a	9.9	11.7	n/a
13	n/a	10.3	30.9	n/a
14	6.4	5.9	16.2	-0.5
15	n/a	6.1	19.5	n/a
16	13.9	12.5	14.0	-1.4
17	10.5	8.6	27.0	-1.9
18	7.5	9.2	25.9	1.7
Average	9.3	12.3	20.9	0.4
σ	2.8	8.9	5.6	2.7

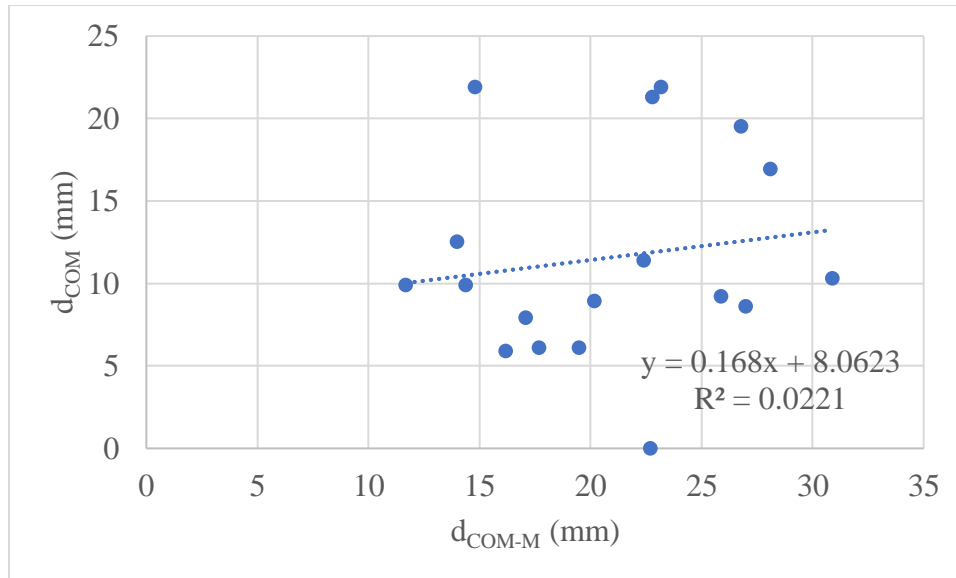


Figure 4.10: Plot of d_{COM} (COM distance between corresponding lesions) vs d_{COM-M} (distance between COM of lesion to nearest external marker) for DBT (MLO view) to ABUS

Figure 4.11 shows a GUI-Viewer for a marked corresponding lesion in the DBT (MLO view) to ABUS original DICOM image sets. From the view in the ABUS image, the suspicious mass can be interpreted as a dense spiculated solid lesion. Detailed lesion correlation values are shown in Table 4.11. Further information on the GUI viewer can be found in the Appendix.

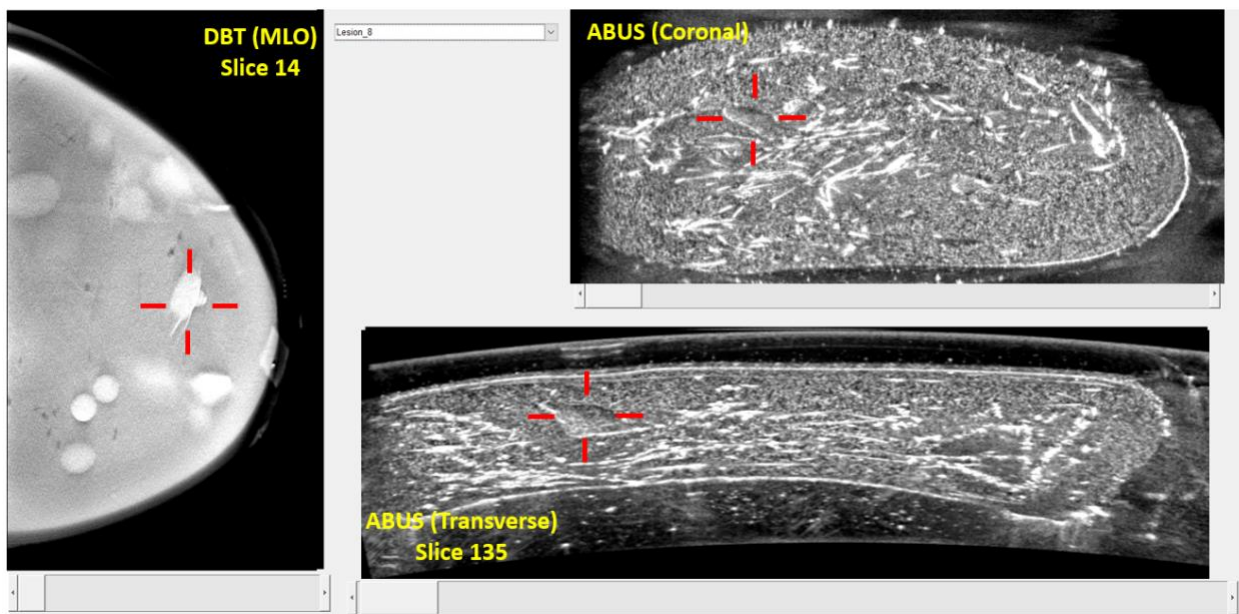


Figure 4.11: GUI representation from original DICOM images for a lesion (Lesion ID=11 see) left shows a slice from DBT (MLO) data, upper right shows the ABUS coronal view, and lower right shows the ABUS transverse view

Table 4.10: Lesion correlation results for each lesion with and without marker analysis for DBT (MLO) registered to ABUS. Location for breast margins abbreviations include I=Inferior S=Superior C=Central A=Anterior P=Posterior M=Medial L=Lateral

Lesion ID	Lesion Type & (Location)	Without Marker Analysis			With Marker Analysis ($d_M \leq 5$ mm)		
		d_{COM} (mm)	d_O (mm)	Overlap	d_{COM} (mm)	d_O (mm)	Overlap
1	Dense (UOQ-A)	11.3	0.00	yes	8.9	0.0	yes
2	Dense (LIQ-A)	n/a	n/a	n/a	7.9	0.0	yes
3	Dense (UIQ-P)	n/a	n/a	n/a	n/a	n/a	n/a
4	Dense (UIQ-A)	5.9	0.00	yes	6.1	0.0	yes
5	Dense (UIQ-P)	n/a	n/a	n/a	11.4	1.5	no
6	Dense (UOQ-P)	n/a	n/a	n/a	19.5	7.2	no
7	Cystic (LOQ-P)	n/a	n/a	n/a	21.9	11.6	no
8	Dense (LOQ-A)	11.1	3.3	no	16.9	7.3	no
9	Dense (LOQ-P)	n/a	n/a	n/a	21.9	0.0	yes
10	Dense (LOQ-P)	n/a	n/a	n/a	21.3	10.0	no
11	Cystic (UOQ-P)	7.9	1.2	no	9.9	0.0	yes
12	Cystic (UOQ-P)	n/a	n/a	n/a	9.9	2.3	no
13	Cystic (UOQ-P)	n/a	n/a	n/a	10.3	0.0	yes
14	Cystic (UIQ-P)	6.4	1.6	no	5.9	1.9	no
15	Cystic (LIQ-A)	n/a	n/a	n/a	6.1	0.0	yes
16	Cystic (LIQ-A)	13.9	3.1	no	12.5	2.2	no
17	Cystic (LIQ-A)	10.5	0.4	no	8.6	0.0	yes
18	Dense (UIQ-P)	7.5	0.00	yes	9.2	3.3	no
	Mean	9.3	1.9	Overlap	12.3	5.3	Overlap
	σ	2.8	1.3	3/8	5.8	3.8	8/17

4.5 Discussion

A novel deformable registration method has been described and assessed for identifying corresponding lesions between two common DBT views (CC and MLO) to ABUS images. For both analyzed cases there was improvement in the number of matched lesions with the use of external fiducial markers. This study extends upon previous work by expanding this technique to relate corresponding lesions in the DBT-MLO view and ABUS and by the use of semi-automated segmentation techniques for the lesions in DBT and ABUS images. The use of automated segmentation techniques will allow this technique to quickly translate to the clinic.

Similar to our previous work, this study also showed improvement in lesion correlation when all corresponding markers for ABUS registration are within a 5-mm vs 1-mm distance. This is likely because larger mesh corrections take place to get all markers closer in distance and can also indicate that external deformation is not entirely indicative of internal deformation. For the deformable mapping of DBT (CC view) to ABUS, for the 14 lesions that were within the defined correlation bounds with and without using marker analysis cases there was a statistical improvement in lesion d_{COM} using a paired t-test. For the deformable mapping of DBT (MLO view) to ABUS, for the 8 lesions that were within the defined correlation bounds with and without using marker analysis there was no statistical improvement in lesion d_{COM} . However, in the MLO view the number of matched lesions increased from 8 to 17 as set by our correlation bounds. The correlation criteria described in this chapter is larger range than shown in our previous work in Chapter 3. This may be an effect of using automated segmentation where the method segments to higher and lower extents of a lesion that may be viewed out-of-focus due to DBT's limited angle acquisition and poor axial resolution.

Lesion location was also analyzed in regard to its effect on improvement in d_{COM} when using external markers vs. not using external markers in the deformable registration algorithm. For DBT (CC) to ABUS registration we see the largest improvement for lesions along the medial and inferior breast margins. Lesion registration seems to worsen for lesions in the upper outer breast quadrant using marker analysis. However, the resulting d_{COM} correlation is still within the specified correlation bounds. However, since this phantom does not have a pectoral/axillary attachment the deformable registration algorithm cannot thoroughly assess improvements in lesion registration for lesions in the superior lateral breast margins. Additionally, in Table 4.5 and Table 4.9 we see that resulting improvement d_{COM} is independent of lesion proximity to

external markers. In one case we actually see that using marker analysis causes the d_{COM} to worsen (Lesion ID 4) for a lesion that is very close in proximity to an external fiducial marker. Therefore, a proof-of-concept study will need to be performed with patient volunteers to better quantify if there are improvements using the technique with markers.

For DBT (MLO view) to ABUS registration we see a decrease in lesion registration using marker analysis for those lesions that are on the lateral or medial most margins of the breast which is likely a direct result of the MLO compression. However, using marker analysis for lesions in all areas of the breast there seems to be a significant improvement as the number of matched markers improved from 8 to 17. This will also have to be further analyzed with a patient study since there is no axillary attachment on the breast phantom.

Lesions in this study are given the material property of dense lesion during FEA since in all x-ray based breast imaging solid and cystic lesions are not differentiable. This study also assumes that all lesions are homogenous in material. In actual patient data, there will be heterogeneity in breast tissue and a study could be performed to determine the differences in registration that makes in FE-based techniques. Unlike our previous study, this phantom contains simulated dense and cystic lesions that use the same Zerdine- based material. This material exhibits different ultrasound properties (anechoic for cystic lesions and if dense have hyperechoic). Therefore, when applied to patients, it is expected to see a larger difference in d_{COM} for cystic masses. After correlation has taken place, for lesions that correlated to cystic lesions in the ABUS set the algorithm could be rerun with the correct cystic material properties. However, this could lead to an increase in algorithm runtime.

A large limitation to this study is the fact that this is a phantom study that uses very homogenous materials. In a real breast there will be much heterogeneity within tissues and a real

breast will contain structures that will not be modeled during FEA. Breast studies that using FE-based registration techniques typically only segment the breast skin, adipose, glandular tissue, and breast mass for modeling breast deformation.⁸⁹ When translating this technique to patients segmentation of these structures will be given. However, due to DBT poor axial resolution there will still be high variability in determining the slices for these structures and high variability in the elastic properties to be used.

4.6 Conclusions

This work demonstrates the potential to use this deformable mapping technique to relate lesions between DBT (CC and MLO views) and ABUS breast images. This study extended upon previous works by incorporating the MLO view for relating corresponding lesions between DBT and ABUS modalities. This is significant as the MLO view is important for imaging close to the axillary regions of the breast where most cancers are located. The utilization of external fiducial markers has been shown to improve the accuracy of this approach. The resulting one-to-one correlation between lesions in DBT and ABUS could help improve radiologists' characterization of breast lesions, which can reduce patient callbacks, negative biopsies, and false negative biopsies. Future work will expand this platform to include an IRB approved study for patient volunteers to test the viability of this technique with real breast lesions.

4.7 Acknowledgements

The authors would like to thank Ted Lynch of CIRS, Inc. for providing the TPE that is used to create the external fiducial markers within this study and also for providing the dual-modality breast phantom used within this study.

Chapter 5

Deformable Mapping Method to Relate Lesions in Dedicated Breast CT Images to those in Automated Breast Ultrasound and Digital Breast Tomosynthesis^s

5.1 Abstract

This work demonstrates potential for using a deformable mapping method to register lesions between dedicated breast CT (bCT) and both automated breast ultrasound (ABUS) and digital breast tomosynthesis (DBT craniocaudal, CC, and mediolateral oblique, MLO, views) images. A multi-modality breast phantom with external fiducial markers attached was imaged by the three modalities. Then the automated deformable mapping algorithm uses biomechanical modeling to determine corresponding lesions based on distances between their centers of mass (d_{COM}) in the deformed bCT model and the reference model (DBT or ABUS). For bCT to ABUS, the mean d_{COM} was 4.8 ± 2.4 mm. For bCT to DBT (CC), the mean d_{COM} was 5.0 ± 2.2 mm. For bCT to DBT (MLO), the mean d_{COM} was 4.7 ± 2.5 mm. This application could help improve a radiologist's efficiency and accuracy in characterization of breast lesions when imaged with multiple modalities.

^s This chapter has been submitted to a journal for publication

5.2 Introduction

Mammography is currently the gold standard for early breast cancer detection during screenings. One limitation of mammography is reduced sensitivity and increased false-negative examinations for women with dense breasts due to reduced lesion conspicuity as a result of superposition of breast tissue. Digital breast tomosynthesis, DBT, which uses limited angle tomography with breast compression in the mammographic geometry is one approach used to improve performance due to the reduction of tissue superposition. The addition of DBT for screenings and diagnostic purposes has shown increased cancer detection rate and reduction in the recall rate in comparison to digital mammography⁴⁸. These gains are largely seen for women with heterogeneously dense breasts¹²⁹. Mammography and DBT have the advantage of superior resolution in the x-y dimensions compared to dedicated breast CT (bCT). However, DBT imaging has poor axial resolution, which is due to the limited angle of the tomographic acquisition.

Breast CT is an emerging technology that, unlike DBT, provides complete 360° angle acquisition of the breast using cone-beam CT. In bCT, the patient lies prone and each breast is scanned separately in the pendant position without compression. Currently, the Koning breast CT (KBCT) system is the only FDA approved and commercially available system in the United States¹³⁰. In a study comparing visualization of 180 lesions with non-contrast bCT vs. mammography, Lindfors et al.⁵⁰ found that the conspicuity of masses was superior for bCT, but the conspicuity of calcifications was inferior. Similarly, in a study of 24 breast lesions, Kuzmiak et al. (2016) found that the reader visualization confidence scores for the shape and margins of masses were statistically significantly greater for bCT compared to digital mammography. However, the reader visualization confidence scores for the morphology and distribution of

microcalcifications were statistically significantly worse for bCT compared to digital mammography.

Breast CT has major advantages over DBT. For angular acquisitions of 180° and above in bCT, the slice sensitivity profile (SSP) axial line spread function approaches an ideal delta function. On the other hand for DBT with its limited angle acquisition the SSP is considerably worse than that of bCT and it worsens with increasing lateral object size, which is not observed with bCT for 180° and above acquisitions⁵². As a result of the wider acquisition angle and greater number of projection views, the resolution of bCT is nearly isotropic. This reduces superposition artifacts and volume averaging compared to DBT⁵³. Lastly, bCT imaging does not use compression of the breast which increases patient comfort. This last advantage, however, requires a longer path length through the breast for bCT. The maximum path length in a breast is typically approximately 10-18 cm in bCT and 2-8 cm in DBT. Thus, higher x-ray energies are required for bCT, with reduced differences in tissue attenuation coefficients. For microcalcifications, this loss in contrast is probably not compensated by the increase resulting from fully-sampled projections over 360°.

Similar to mammography and DBT, there is still difficulty in differentiating between malignant and benign lesions in bCT images^{49,53}. Ultrasound imaging used in combination with mammography has been shown to improve the radiologists' overall characterization of breast lesions by aiding in the determination of whether a lesion is solid or cystic¹⁶⁻¹⁸. Therefore, bCT imaging in conjunction with ultrasound would likely improve lesion characterization and this may especially be significant for women with dense breasts. 2D ultrasound images are often difficult to reproduce due to freehand acquisition and operator dependence. Automated breast ultrasound systems (ABUS) images the breast as a 3D volume and has advantages in terms of

reproducibility and operator independence over conventional breast ultrasound. Studies have also shown a significant improvement in breast cancer detection rate with an accompanying acceptable recall increase for ABUS imaging used in conjunction with mammography for women with dense breasts ^{19,57,58}.

With the promise shown by bCT as an imaging modality it will become important to relate lesions found with bCT to those in other widely used breast imaging modalities. Several studies have used finite element modeling, FEM, modeling on bCT data to measure breast density ⁹⁸, peripheral breast thickness ¹³¹, and simulate the effect of gravity and compression (craniocaudal, CC, or mediolateral oblique, MLO) to generate simulated mammograms for multi-modality applications ¹³². A non-rigid registration technique was used to relate bCT and PET/CT images that does not involve FEM ¹³³. FEM or biomechanical modeling has also been used to validate conventional registration methods as shown by Tanner et al. (2007) and Hill et al. (2009) for dynamic contrast-enhanced MR breast images however these studies do not involve high deformation. FEM has proven to be useful for lesion registration when modeling large deformations that can occur due to the changes of the direction of gravity and compression plate deformation in comparison to conventional registration method (i.e. intensity-based, with B-splines) ⁹². A study by Dmitriev et al. (2013) used a conventional B-splines method for registration of MRI and PET-CT tumor registration and indicated that the lack of biomechanical modeling was a limitation to their approach. To date there has not been a study dedicated to registering lesions from bCT to other breast imaging modalities and this study will help address that using FEM techniques.

Breast MR and transmission US tomography (Delphinus Medical Technologies, Inc., Plymouth, MI and QT Ultrasound, Novato, CA) images are acquired in the same prone geometry

as bCT, with the modest exception that the breast is suspended in water, rather than air, for transmission US tomography. While registration of bCT to breast MR, or even transmission US tomography, will be much simpler, there will remain considerable need for registration between imaging modes without and with various compressions. Several studies have used FE models of breast MRI to simulate breast compression¹³⁷ and register breast MRI to CC and/or MLO mammograms^{81,85,86,88,90}. Likewise, other breast MR studies have shown external fiducial markers could be beneficial for registration and lesion correlation in breast MRI and PET^{69,70}, compressed and uncompressed prone breast MRI⁷¹, and breast MRI and ultrasound⁷².

In our previous work, we developed a novel deformable mapping method to relate corresponding lesions in DBT (CC-view only) and ABUS with and without the use of external fiducial markers³⁴. This method did not simulate the compression plates involved in DBT and ABUS imaging. Instead it used a mesh morphing feature to morph the DBT model to match the ABUS and used nodal displacement for the finite element analysis, FEA. Here, we extend this work to the problems of relating lesions in bCT to ABUS and DBT. To distort the bCT image volume of the freely-dependent breast into the shape predicted for a DBT or ABUS view, compression plates were added to the bCT biomechanical model to simulate DBT plate compression (CC and MLO with compression paddle and breast support plate) and ABUS mesh plate compression (supine anterior to posterior). The resulting bCT biomechanical models were then registered to the DBT or ABUS image volumes, respectively. We also used semi-automatic segmentation of all lesions in all modalities for this work; whereas, only manual segmentation was used for all modalities in our previous work.

This study incorporates the use of commercial FE-processing and FEA packages to match lesions between bCT to DBT and bCT to ABUS modalities. This is done by using semi-

automated software in order to segment all phantom components. A commercial FE pre-processor is used to create base FE models for the bCT and reference modalities (i.e. ABUS or DBT). Plate deformation is performed on the bCT FE model to simulate DBT or ABUS compression using a commercial FEA solver. Next, the deformed bCT data is registered to the center of mass (COM) of the reference modality data set (DBT or ABUS) and modifies the resulting deformed data mesh set to align external markers between the bCT and the reference modality model (DBT or ABUS). Lastly, the algorithm determines corresponding matching lesions between the image sets using measures of distances between COMs (d_{COM}) and lesion overlap. Although commercial software is incorporated into this work, the automated algorithm shows a novel use of the commercial technology by relating corresponding lesions between breast imaging modalities with very different geometries and degrees of breast compression.

Identifying corresponding lesions between modalities does not pose as large a difficulty for lesions that are easily identifiable. A benefit to this technique is that for women with dense breasts, a radiologist could indicate a region of interest, ROI, within the bCT image set and this technique can help a radiologist determine with higher confidence if that is the same region within the corresponding ABUS or DBT data set. This can directly influence lesion characterization and reduce negative biopsies. Using a deformable registration algorithm can decrease review time so that a radiologist can quickly determine corresponding regions especially for large datasets in these 3D modalities.

5.3 Materials and Methods

5.3.1 Phantom Information

A CIRS Multi-Modality Breast Biopsy and Sonographic phantom ¹³⁸ was used in this study. The phantom contains a total of 20 lesions: 10 spherical cystic lesions, 5 spherical dense lesions,

and 5 spiculated dense lesions. The lesions are randomly located in a background gel, Zerdine, and wrapped in a Z-skin membrane material. The self-healing Z-skin membrane simulates the texture and properties of skin during imaging and biopsy. Zerdine is a patented solid elastic water based polyacrylamide tissue mimicking material the formulation of which can be adjusted to correspond to a variety of soft-tissue acoustic properties for ultrasound imaging ¹¹⁵. Since it is a water-based material and the density can be controlled it can be used for CT and MR imaging as well ^{115,118}. All lesions in the phantom are made of Zerdine formulations and are 5-10 mm in diameter. They have average CT numbers at 80 kVp ranging from 337-430 HU on a GE Discovery CT750 HD CT scanner (GE Healthcare, Milwaukee, WI); however, the cystic lesions have anechoic properties and the dense lesions have hyperechoic properties in ultrasound images. Elastic material properties of the substances in our phantoms provided by the manufacturer are listed in Table 5.1.

Table 5.1: Phantom Material Properties

	<i>Young's Modulus (E)</i>	<i>Poisson's Ratio (ν)</i>
Z-skin Membrane	10 kPa	0.50
Zerdine background gel	10 kPa	0.50
Dense lesions	60 kPa	0.50

For use in the finite element analysis solver, a Poisson's ratio of 0.49 was used since a ratio of 0.50 will not allow the FEA solver to converge. Measurements of the phantom uncompressed thickness were taken before and after compression to ensure that the phantoms recovered to their original state before imaging with a different modality. A measured load-strain curve for this phantom is shown in Figure 5.1. Based on this curve, the elastic modulus of the phantom appears to be linear.

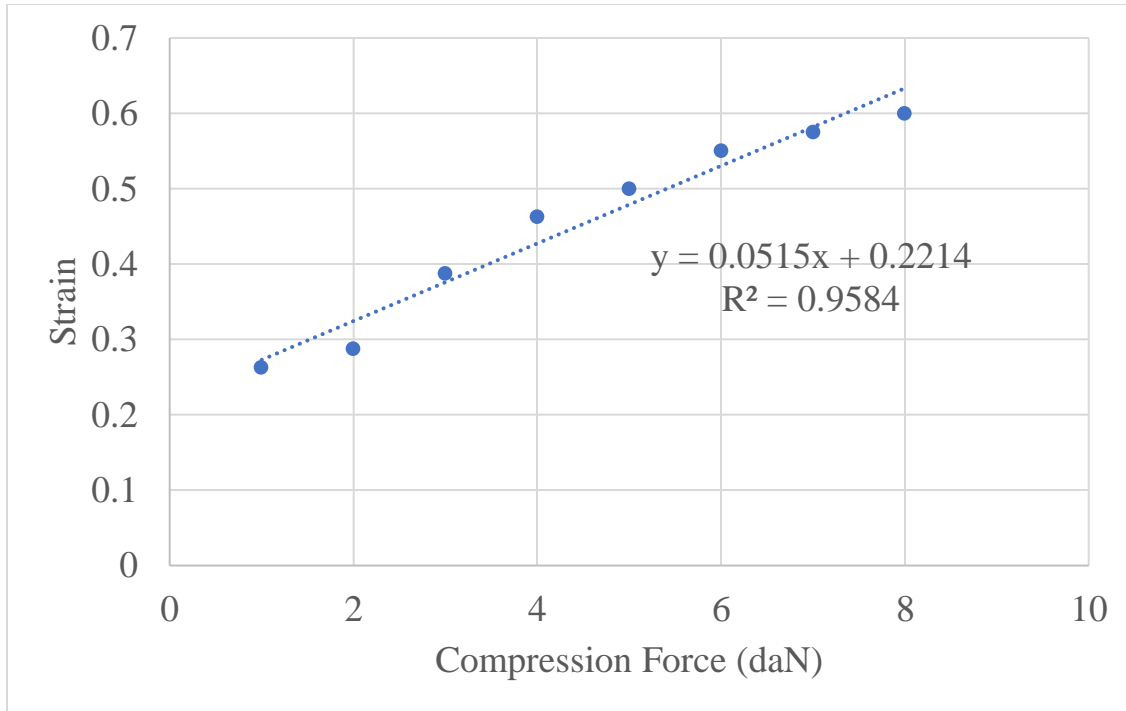


Figure 5.1: Load Strain curve showing elastic nature of breast phantom.

5.3.2 External fiducial markers

In our previous work, we found that the use of external markers were helpful in relating corresponding lesions between DBT and ABUS modalities and the manufacturing method is discussed in our previous paper³⁴. The same markers were created and used in this study. Each marker contains a 1 mm diameter solid glass bead within a thermoplastic elastomer (TPE) gel and is about 3 mm thick.

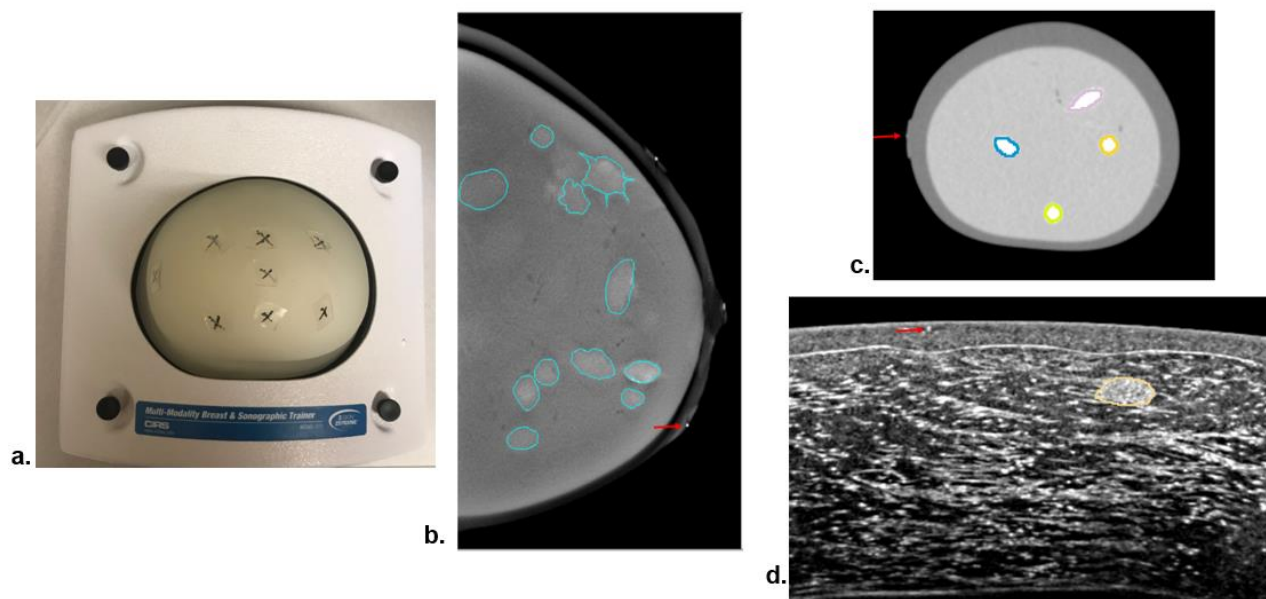


Figure 5.2: (a) CIRS Multi-modality breast phantom with external fiducial markers attached. Segmented lesion Images acquired with (b) DBT (c) simulated bCT, and (d) ABUS. Red arrow shows external fiducial marker locations

The multi-modality breast phantom was marked with a magic marker with an ‘x’ at eight locations. Eight external markers were attached to the phantom, using Jobst “It-Stays” Roll-On Adhesive (BSN Medical, Charlotte, NC). (See Figure 5.2). The red arrows in Figure 5.2 show the location of a fiducial marker in simulated bCT, DBT, and ABUS reconstructed images.

5.3.3 Imaging Methods

Conventional CT images of the phantom were acquired with a GE Discovery CT750 HD scanner (GE Healthcare, Milwaukee, WI). The phantom placed supine within the scanner. Due to the softness of the phantom material and the weight of the phantom backing we found we could not support the phantom in the upright position to simulate the coronal slice acquisition that is performed with dedicated breast CT scanners. The CT settings were 80 kVp, 200 mA, 1 second, helical acquisition, 0.969:1 pitch, 20 cm field of view, 30% ASiR, 0.625 mm slice, 0.625 mm

slice increment. The voxel dimensions were 0.39 mm x 0.39 mm x 0.625 mm. All 20 lesions were seen in the reconstructed simulated bCT images. The maximum uncompressed breast phantom thickness (superior to inferior breast margins) measured 106 mm from reconstructed simulated bCT images.

DBT images were acquired in both CC and MLO views with a GE Senographe Pristina DBT system (GE Healthcare, Milwaukee, WI). For the CC view, a compressive force of 3 daN was used and the phantom was compressed to a thickness of 44.2 mm. Thus, the phantom was compressed by 58%. For the MLO view, a compressive force of 2.5 daN was used and the phantom was compressed 54% to a thickness of 48.5 mm. The standard automatic optimization parameter (AOP) mode was used in each case and the resulting technique factors were CC: Rh target, Ag filter, 34 kVp, 29.7 mAs with a displayed summed average glandular dose of 1.11 mGy; and MLO: Rh target, Ag filter, 34 kVp, 36.9 mAs, with a displayed average glandular dose of 1.29 mGy. The (x, y, depth) voxel dimensions were 0.1 mm x 0.1 mm x 1 mm. Forward pressure on the back detector plate was maintained by tightly taping the phantom casing to the detector plate while under compression. However, for both image views only 18 lesions were shown in reconstructed DBT images. Two lesions were not imaged because they were close to

the phantom “chest wall” and moved back outside the imaging field-of-view when the phantom was compressed.



Figure 5.3: ABUS image acquisition setup on uncompressed phantom

Lastly, the phantom was imaged with the GE Invenia ABUS system (GE Healthcare, Milwaukee, WI). This system consists of a curved 153 mm long ultrasound transducer that scans over a mesh compression paddle that is positioned over the breast. The breast is covered with an acoustic coupling lotion or gel prior to application of the paddle to the breast. A picture of the uncompressed phantom ABUS setup is shown in Figure 5.3. The paddle is lightly pressed down for good contact between the paddle/transducer and the breast, and the transducer scans across the breast to generate the 3D ABUS image volume. The Invenia ABUS reversed-curve transducer operates between 6-15 MHz and can image up to a 50 mm depth. When imaged the phantom is placed supine and the transducer travels approximately 170 mm across a mesh compression paddle from the superior to inferior margins of the breast. The system contains

three settings based on desired imaging depth (high, medium and low). The medium setting was used which images acquired to a depth of 40 mm. Clinical procedures typically include several transducer sweeps of the breast depending on breast size to ensure coverage of the breast and axillary region. Due to the absence of an axillary area of the phantom only one image sweep was acquired. Correction for the reverse-curve of the transducer is not included in the raw DICOM images, therefore an algorithm was used to correct for transducer curvature. The ABUS images were resampled from a native voxel size of 0.082 mm width, 0.2 mm depth, and 0.506 mm length (distance between adjacent slices), to 0.2 mm width, 0.2 mm depth, and 0.506 mm length. *Image resampling is done using the MATLAB imresize^t command.* Resampling is needed to increase speed in surface mesh creation since ABUS images contain 330 image slices with small voxel size for the skin and body phantom layers. All 20 lesions were seen in reconstructed ABUS images.

5.3.4 Segmentation Methods

Lesions in the DBT acquired images were segmented using a semi-automatic segmentation program MiViewer. MiViewer is an in-house interface used for computer aided diagnosis for the detection and segmentation of breast masses in breast tomosynthesis^{139–141}. For the ABUS images, all dense lesions were segmented using the MiViewer program. The 10 cystic lesions in ABUS images were segmented using automated nonlinear filtering and segmentation approach by Elawady et al.¹²⁸. The external fiducial markers were manually segmented using 3D Slicer for ABUS and DBT images. Thresholding techniques were used within 3D Slicer to segment the lesions, external markers, background gel material, and skin layer for the bCT image set¹⁴².

^t <https://www.mathworks.com/help/images/ref/imresize.html>

Examples of the segmentations of the lesions in the images of each modality are shown in Figure 5.2.

5.3.5 Automated deformable mapping algorithm

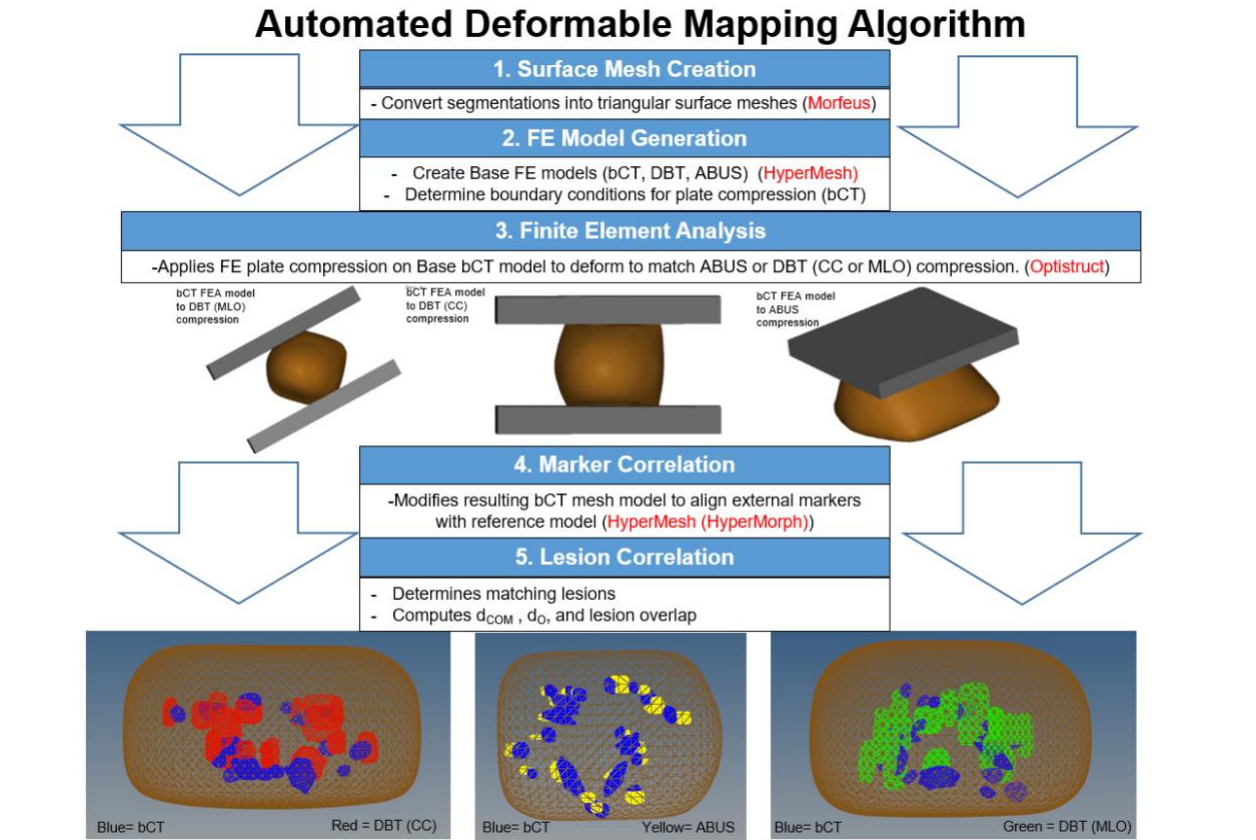


Figure 5.4: The automated deformable mapping process. Software's used shown in red.

The deformable mapping algorithm leverages the model creation capabilities in Morfeus, a FE based multi-organ deformable image registration platform¹⁴³, which utilizes a commercial pre-processor (HyperMesh version 2017.2, Altair Engineering, Troy, MI) with a commercial finite element analysis (FEA) solver (ABAQUS version 2017x, Dassault Systèmes Americas Corp., Waltham, MA). In this process the base bCT model is deformed to register the lesions in bCT to those in each of the two views in DBT and to the lesions in ultrasound. For registration the voxel sizing of the reference model data set (either DBT or ABUS) is used for lesion

correlation. An overview of the process is shown in Figure 5.4. Since the breast is in an uncompressed state when imaged in bCT, the bCT base model is being deformed to match the reference models for DBT and ABUS imaging.

5.3.5.1 Surface Mesh Creation

All segmented contours are converted into triangular surface meshes using the shrinkwrap tool in the FE pre-processor, HyperMesh. The compilation of surface meshes are used to build the base model. A 1 mm element size was used for all lesions and 5 to 10 mm element sizes were used for the other phantom areas (phantom skin and background gel) due to the larger volume in comparison to the lesions. Each surface mesh is based off the original voxel sizes. The HyperMesh FE pre-processor uses a widely accepted proprietary meshing technology that ensures to high accuracy that created elements have a proper aspect ratio suitable for FEA. If the elements are outside the aspect ratio the user is notified of a mesh error.

5.3.5.2 Finite element model generation

Once all segmentations are converted into surface mesh files. The deformable mapping algorithm uses the FE pre-processing software, HyperMesh, to generate the base FE model for the bCT image set and the reference image sets (e.g. base DBT (CC), base DBT (MLO), and base ABUS). 3D four point fully meshed tetrahedral models are created from the mesh contours for each modality model being used for registration. The material properties are assigned for the various model volumes as described in Table 5.1. Two plates are added to the bCT model to simulate DBT compression (top compression plate and bottom breast support plate) and one compression plate is added to the bCT model for the case of ABUS compression as shown in Figure 5.5. For simulating DBT compression the model assumes no flexure in the compression plate. The plate used in ABUS compression is flat, representing the ABUS mesh paddle. The

curvature of the transducer is not modeled for the simulation of ABUS compression. Contact interfaces are defined between the face of the plate model in contact with the skin of the phantom and the skin of the base bCT model. A study by Han et al. (2012) used frictionless contact to simulate plate compression. Additionally, a study by Mertzaniidou et al. (2014) found negligible difference when introducing friction into a model vs. using a frictionless plate model for lesion registration. Other studies, have used a friction coefficient of 0.1 between breast skin and compression plates^{98,144,145}. As a compromise, we chose to use a coefficient of friction between the skin and plate contact interfaces of 0.05, which is the median between the 0.1 and frictionless coefficients. Each plate is initially positioned to clear 1 mm from the breast surface. For DBT compression the bottom plate is fixed, and compression is only performed with the top plate. For DBT-MLO compression the plates are rotated 45°. The back of the phantom or “chest wall” region restricts motion along the x-axis for DBT compression as shown in Figure 5.5(a) and (b), and this “chest wall” restricts motion in the along the y-axis for ABUS compression as shown in Figure 5.5(c) and (d). In bCT it is often difficult to distinguish between solid and cystic lesions^{49,53}, which is even more true from this phantom since all lesions are made of the same material they just have difference in ultrasound properties. Therefore, all lesions in the bCT model has the material properties of dense lesions as shown in Table 5.1.

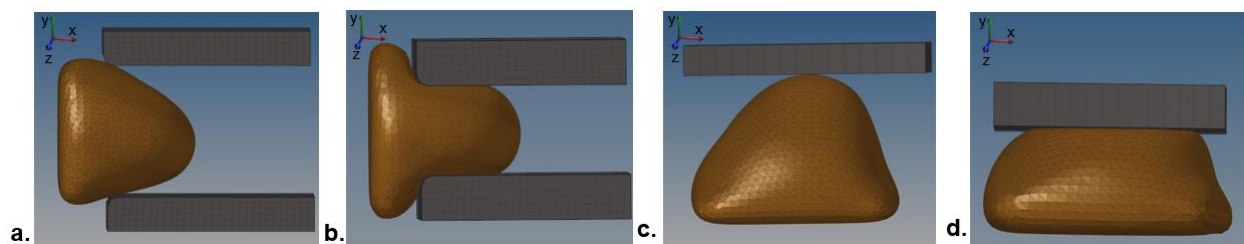


Figure 5.5: Plate deformation (a) bCT in DBT (CC) setup no compression applied (b) resulting CC compression to bCT model (c) bCT to ABUS setup no compression applied (d) resulting ABUS compression to bCT model

Correction for gravity was not made in this model as it is a minor effect in comparison to the high deformation induced by the compression plates in both DBT and ABUS. The effect of gravity is likely accounted for with the use of the external fiducial marker corrections involved in this study. Other research groups have ignored the initial stress present from gravity with the breast in the prone geometry and believe its effect would not be significant in most cases^{132,146}. However, other studies have found the effect of gravity loading significant for biomechanical models for prone and supine MRI^{147,148} and directly relating prone to supine breast MRI¹⁴⁹. For those studies' gravity needed to be modeled as there are no other external or compressive forces acting on the breast unlike in ABUS and DBT imaging.

The amount of plate compression is determined by the difference between the face of the compression plate and the compressed thickness of the reference model. For the DBT (CC view), to match the experimental conditions, the compressed thickness that was used was 44.2 mm and for the MLO view it was 48.5 mm. For ABUS imaging, the imaging depth 40 mm was used as the compressed thickness. The number of elements/nodes are 698,768/118,730 for the base bCT model, 577,295/99,684 for the base DBT (MLO) model, 547,426/94,408 for the base DBT (CC) model and 231,990/38,021 for the base ABUS model.

5.3.5.3 Finite Element Analysis

The FEA solver, ABAQUS, is used to implement FE methodologies to solve the partial differential equations to simulate the plate compression and outputs the resulting stress and strain of the deformation applied to the bCT breast volume. The resultant breast compression by the plate, as shown in Figure 5.5(b) and (d), to the breast is performed using a non-linear quasi-static analysis and large displacement theory in two steps. The first step is to ensure adequate contact between the breast surface and plates. In the first step the breast is compressed to half the total

compression distance. The second step continues the compression until the boundary condition is satisfied by compressing the plate on the bCT model to ensure an axial compression depth of approximately 40 mm for ABUS compression (ABUS imaging depth), 44 mm for DBT-CC compression and 49 mm for DBT-MLO compression (compressed breast thicknesses from the DICOM headers).

5.3.5.4 External fiducial marker correlation

After the FEA is completed, the deformed bCT model is loaded back into HyperMesh and the model is translated and rotated to the COM of the reference DBT or ABUS breast model. Then the algorithm determines the COM locations of all the corresponding external fiducial markers between the two models. Using HyperMorph, a mesh-morphing feature within HyperMesh, handles are generated at seven equidistant locations along each coordinate axis that encompasses the entire deformed bCT volume. Global handles (8 in total) are generated at the 8 corners surrounding the skin mesh, they are used to make large scale changes to the mesh. Local handles (60 in total) are positioned on each plane between the global handles which can make smaller scale manipulations to skin nodes of that region. This allows modifications to be made to the deformed bCT model so that markers can be registered to the markers in the reference model (DBT or ABUS) within a user-defined distance, d_M . The algorithm determines which local handle from the deformed bCT model is needed in order to be better aligned with the corresponding marker from the reference model (DBT or ABUS). To create the changes to the nodes within the morphed volume, HyperMorph, takes the handle information to create proprietary non-linear influence functions that relate the movement of the handles to the morphed volume. The algorithm only manipulates handles in areas of the breast where the distances between the corresponding external fiducial markers are greater than d_M . Once all

marker corrections take place, the algorithm determines if there are still marker distances greater than d_M . If so, the algorithm will iterate until all markers satisfy the d_M boundary condition only performing handle corrections for the markers that do not satisfy the d_M boundary condition. The maximum number of handle corrections for each iteration is the same as the total number of matched markers. More information on this process can be found in our previous paper.³⁴

5.3.5.5 Matching Corresponding Lesions

Once all external fiducial markers are within d_M the COMs of all lesions from the external markers, the FEA deformed bCT model and the reference model are determined. A matching algorithm is then used to determine the lesion matches between the two models by finding the minimum distances, d_{COM} , between each possible pair of COMs. Two corresponding lesions are considered matched if the minimum d_{COM} between the FEA bCT lesion and the reference model is ≤ 15 mm and the lesions overlap as shown in Figure 5.6 (a). If the lesions do not overlap the minimum d_{COM} is still restricted to being ≤ 15 mm. A second parameter known as the minimum distance to overlap, d_O , is calculated and is restricted to 7.5 mm to ensure a match discrepancy is not created. Figure 5.6 (b) shows two corresponding lesions that are considered matched but do not show overlap. The results are output into a table and are used to relate corresponding lesions in the original sets of DICOM images in a graphical-user-interface (GUI) viewer application.

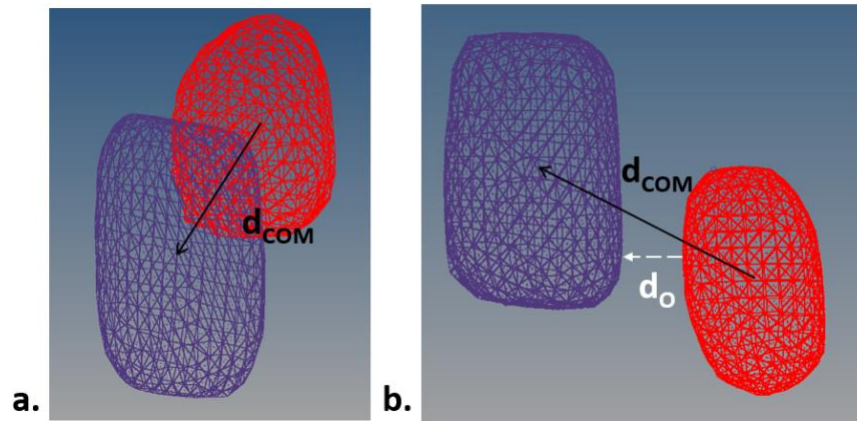


Figure 5.6: Matching corresponding lesions showing a. overlapping lesions b. non-overlapping lesions. d_{COM} is restricted to 15 mm ($d_{COM} \leq 15$ mm) for both and d_O is restricted to 7.5 mm ($d_O \leq 7.5$ mm) for non-overlapping corresponding lesions.

5.3.6 Studies Performed

Studies were undertaken to evaluate the performance of the deformable mapping technique for bCT registered to ABUS, bCT registered to DBT (CC) and bCT registered to DBT (MLO). Lesion correlation results (total matched lesions, d_{COM} , number of lesions that overlap, and d_O) were compared with and without the use of external fiducial marker correlation and the statistical significance ($p < 0.05$) of the differences were quantified using paired t-test of the average d_{COM} values. For each registered set, results also included comparisons of lesion correlation results when external fiducial markers were within $d_M \leq 5$ mm vs. within $d_M \leq 1$ mm.

5.4 Results

5.4.1 Performance of deformable mapping technique for bCT registered to ABUS

An overview of the results for registration of the bCT model to ABUS is illustrated in Table 5.2. All 20 lesions were visible in the bCT and ABUS reconstructed images. Without the use of marker analysis 13 out of 20 lesions were matched with an average d_{COM} of 8.6 ± 3.0 mm. With the use of external markers, the total number of matched lesions improved to 20 out of 20. When

all external markers were within 1-mm distances ($d_M \leq 1$ mm) the average d_{COM} was 5.3 ± 1.8 mm. When the external markers were within 5-mm ($d_M \leq 5$ mm) the average d_{COM} was 4.8 ± 2.4 mm. The mean difference in lesion d_{COM} for $d_M \leq 1$ mm vs. $d_M \leq 5$ mm was 0.41 mm and resulted with a p-value of 0.02. Thus, there is a statistically significant improvement in lesion d_{COM} when the markers are within a $d_M \leq 5$ mm.

Table 5.2: Lesion Correlation summary for bCT registered to ABUS. A maximum of 20 lesions could be matched between image sets. (d_{COM} = distance between centers of masses of corresponding lesions in the two modalities, d_o = minimum distance for overlap of corresponding lesions, d_M = distance between external fiducial markers).

	Without Marker Analysis	With Marker Analysis ($d_M \leq 1$ mm)	With Marker Analysis ($d_M \leq 5$ mm)
Total Matched Lesions	13	20	20
Mean d_{COM} (mm)	8.6 ± 3.0	5.3 ± 1.8	4.8 ± 2.4
Mean d_o (mm)	5.2 ± 4.1	3.0 ± 2.8	2.4 ± 2.0
Total Overlapping Lesions	5	14	14

A paired t-test of the d_{COM} 's was performed for the 13 lesions that were matched in the without marker analysis case to the same 13 lesions that were matched with marker analysis cases with $d_M \leq 1$ mm and $d_M \leq 5$ mm, a summary of the values used for this calculation are shown in Table 5.3. For $d_M \leq 1$ mm and $d_M \leq 5$ mm, the resulting differences in the average d_{COM} between without marker vs. with marker analysis were 5.3 mm and 4.8 mm, respectively, with p-values of 0.01 and 0.005, indicating significant improvement in average lesion d_{COM} with the use of external fiducial markers.

Table 5.3: Lesion correlation summary of 14 matched lesions between without marker analysis and with marker analysis cases for bCT registered to ABUS (d_{COM} = distance between centers of masses of corresponding lesions in the two modalities, d_O = minimum distance

	Without Marker Analysis	With Marker Analysis ($d_M \leq 1$ mm)	With Marker Analysis ($d_M \leq 5$ mm)
Total Matched Lesions	13	13	13
Mean d_{COM} (mm)	8.6 ± 3.0	5.3 ± 1.8	4.8 ± 1.9
Mean d_O (mm)	5.2 ± 4.1	2.3 ± 1.5	2.5 ± 1.3
Total Overlapping Lesions	5	9	10

Figure 5.7 (a) and Figure 5.7 (b) display the improvement in lesion correlation between the bCT and ABUS models for all 20 lesions. Figure 5.7 (c) shows a GUI-Viewer display of corresponding marked lesions in the original bCT and ABUS images. The d_{COM} values for each pair of corresponding lesions are listed in Table 5.4.

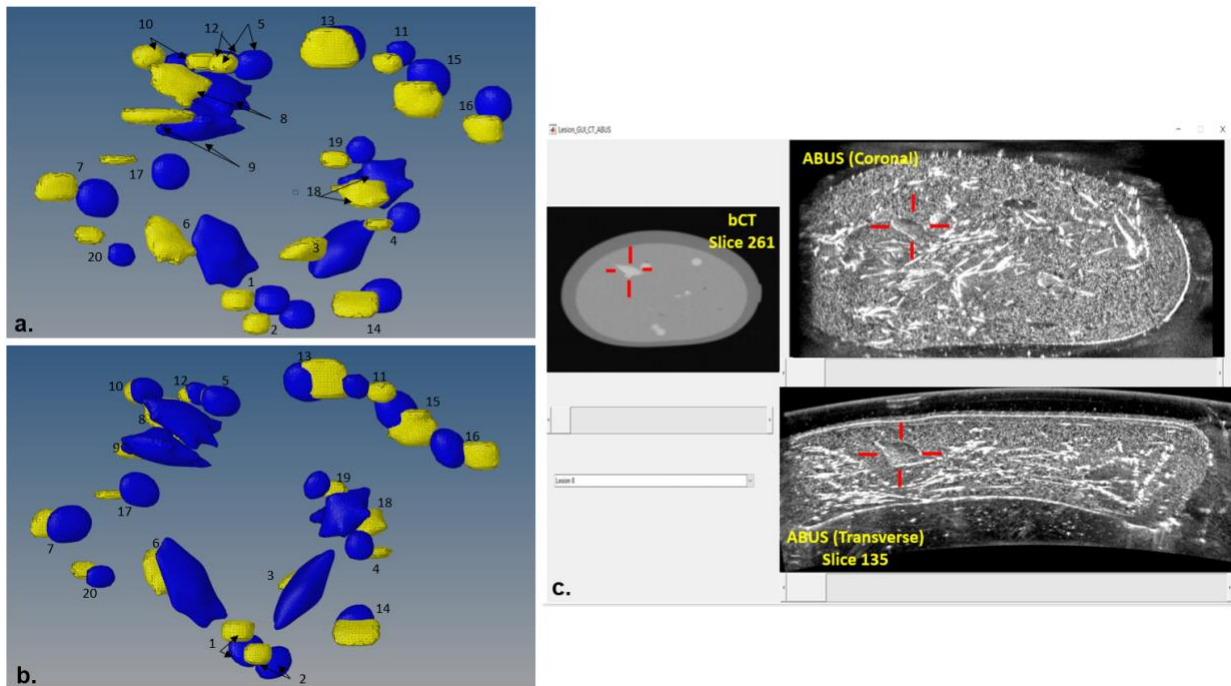


Figure 5.7: Lesion correlation for bCT (blue) registered to ABUS (yellow) (a) coronal view without marker analysis (b) coronal view with marker analysis (c) GUI representation from a lesion in original DICOM images of bCT (left), coronal view ABUS (upper-right), and transverse ABUS (lower-right) for a lesion (Lesion ID= 8). Numbers correspond to lesion ID's and correlation values in Table 5.4).

Table 5.4: Lesion matching results for each lesion with and without marker analysis for bCT registered to ABUS

Lesion ID	Lesion type	Without Marker Analysis			With Marker Analysis ($d_M \leq 5$ mm)		
		d_{COM} (mm)	d_o (mm)	Overlap	d_{COM} (mm)	d_o (mm)	Overlap
1	dense	n/a	n/a	no	11.1	5.6	no
2	dense	n/a	n/a	n/a	3.3	0.0	yes
3	dense	5.6	0.0	yes	6.9	0.0	yes
4	dense	4.5	0.0	yes	7.0	1.8	no
5	dense	8.9	3.5	no	2.3	0.00	yes
6	dense	7.4	0.00	yes	7.6	0.9	no
7	cystic	n/a	n/a	n/a	6.1	0.0	yes
8	dense	n/a	n/a	n/a	3.6	0.0	yes
9	dense	6.8	0.00	yes	5.1	0.0	yes
10	dense	n/a	n/a	n/a	2.7	0.0	yes
11	cystic	9.8	6.1	no	2.9	0.0	yes
12	cystic	n/a	n/a	n/a	0.5	0.0	yes
13	cystic	11.5	5.5	no	2.2	0.0	yes
14	cystic	13.7	7.8	no	4.0	0.0	yes
15	cystic	11.1	5.2	no	5.1	0.0	yes
16	cystic	12.3	5.5	no	3.7	0.0	yes
17	cystic	9.0	6.3	no	4.7	1.7	no
18	dense	6.4	0.00	yes	5.2	0.0	yes
19	cystic	4.5	0.8	no	7.4	4.0	no
20	cystic	n/a	n/a	n/a	4.3	0.4	no
Mean		9.00	5.51	Overlap*	4.8	2.4	Overlap*
σ		3.12	1.97	5/14	2.4	1.2	14/20

5.4.2 Performance of deformable mapping technique for bCT registered to DBT (CC)

An overview of the results for registration of the bCT model to DBT-CC is illustrated in Table 5.5. As explained previously, only 18 lesions were viewed in the reconstructed DBT-CC images because 2 lesions were too close to the chest wall. Therefore, the maximum number of possible lesion matches is 18. Without the use of external fiducial marker analysis only 9 out of 18 lesions were matched with an average d_{COM} of 11.6 ± 2.0 mm. With the use of external markers, the total number of matched improved to 18 out of 18. When all external markers were

within 1 mm ($d_M \leq 1$ mm) the average d_{COM} was 5.0 ± 2.2 mm. When the external markers were within 5 mm ($d_M \leq 5$ mm) the average d_{COM} was 5.1 ± 2.2 mm. The mean difference in lesion d_{COM} for $d_M \leq 1$ mm vs. $d_M \leq 5$ mm was 0.12 mm with a p-value of 0.11 indicating no statistical difference in lesion d_{COM} when the external fiducial markers are closer in distance.

Table 5.5: Lesion Correlation summary for bCT registered to DBT (CC). A maximum of 18 lesions could be matched between image sets (d_{COM} = distance between centers of masses of corresponding lesions in the two modalities, d_O = minimum distance for overlap of corresponding lesions, d_M = distance between external fiducial markers).

	Without Marker Analysis	With Marker Analysis ($d_M \leq 1$ mm)	With Marker Analysis ($d_M \leq 5$ mm)
Total Matched Lesions	9	18	18
Mean d_{COM} (mm)	11.6 ± 2.0	5.0 ± 2.2	5.1 ± 2.2
Mean d_O (mm)	2.7 ± 1.9	0.5 ± 0.3	0.3 ± 0.1
Total Overlapping Lesions	2	16	16

A paired t-test of the d_{COM} 's was performed for the 9 lesions that were matched in the without marker analysis case to the same 9 lesions that were matched with marker analysis cases with $d_M \leq 1$ mm and $d_M \leq 5$ mm, a summary of the values used for this calculation are shown in Table 5.6. For $d_M \leq 1$ mm, and $d_M \leq 5$ mm the resulting differences in the average d_{COM} were 8.1 mm and 8.2 mm, respectively, with p-values of 0.00001 and 0.000008 indicating significant improvement in average lesion d_{COM} with the use of external fiducial markers.

Table 5.6: Lesion correlation summary of 9 matched lesions between without marker analysis and with marker analysis cases for bCT registered to DBT (CC). (d_{COM} = distance between centers of masses of corresponding lesions in the two modalities, d_O = minimum distance for overlap of corresponding lesions, d_M = distance between external fiducial markers).

	Without Marker Analysis	With Marker Analysis ($d_M \leq 1$ mm)	With Marker Analysis ($d_M \leq 5$ mm)
Total Matched Lesions	9	9	9
Mean d_{COM} (mm)	11.6 ± 2.0	3.5 ± 1.6	3.4 ± 1.4
Mean d_O (mm)	2.7 ± 1.9	0.0 ± 0.0	0.0 ± 0.0
Total Overlapping Lesions	2	9	9

Figure 5.8 (a) and Figure 5.8 (b) visually display the improvement in lesion correlation between the bCT and DBT (CC) models for several lesions. Figure 5.8 (c) shows a GUI-Viewer for a marked corresponding lesion in the bCT and DBT (CC) original image sets. The d_{COM} and do values for each pair of corresponding lesions are listed in Table 5.7.

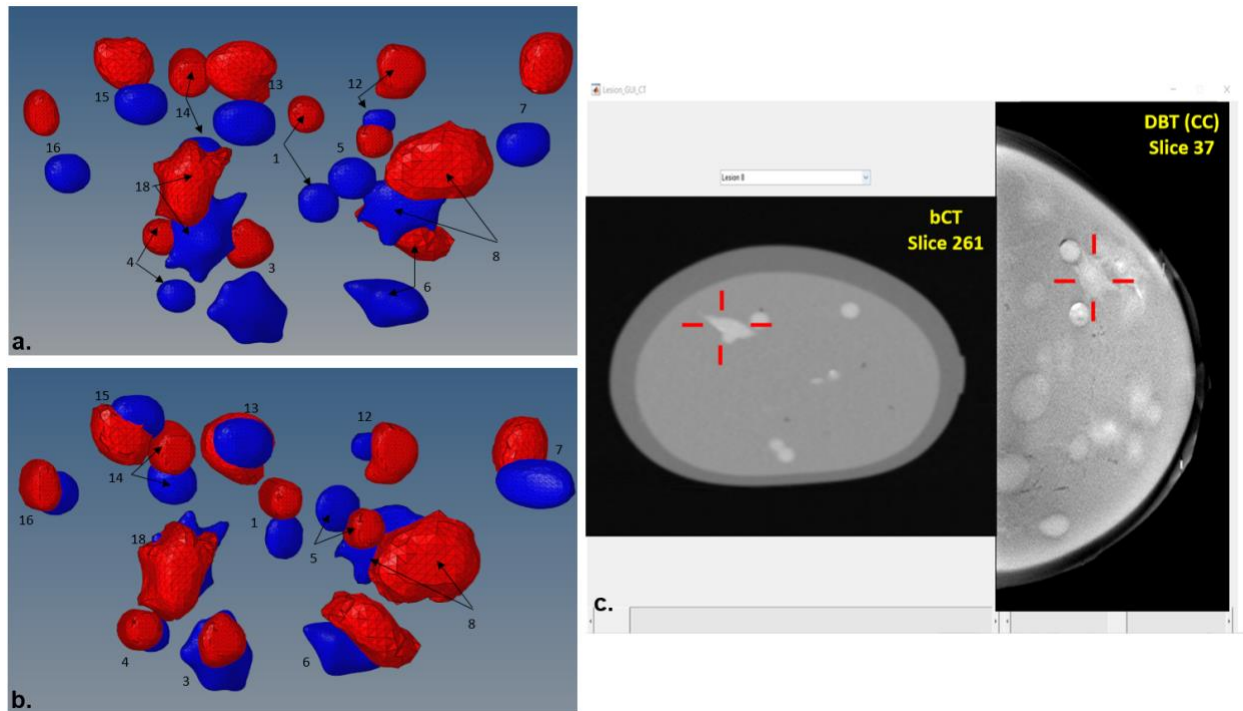


Figure 5.8: Lesion correlation bCT (blue) registered to DBT (CC view) (red) (a) axial view without marker analysis (b) axial view with marker analysis (c) GUI representation from original DICOM images for lesion (Lesion ID= 8). Numbers correspond to lesion ID's and correlation values in Table 5.7. Note: All lesions are not visually represented in this figure due to superposition of the 2D representation

Table 5.7: Lesion matching results for each lesion with and without marker analysis for bCT registered to DBT (CC)

Lesion ID	Lesion type	Without Marker Analysis			With Marker Analysis ($d_M \leq 1$ mm)		
		d_{COM} (mm)	d_O (mm)	Overlap	d_{COM} (mm)	d_O (mm)	Overlap
1	dense	n/a	n/a	n/a	8.2	0.0	yes
2	dense	n/a	n/a	n/a	8.4	0.3	no
3	dense	14.6	1.1	no	2.7	0.0	yes
4	dense	13.2	5.4	no	3.5	0.0	yes
5	dense	9.4	1.2	no	6.4	0.0	yes
6	dense	n/a	n/a	n/a	5.5	0.0	yes
7	cystic	n/a	n/a	n/a	6.0	0.0	yes
8	dense	n/a	n/a	n/a	8.0	0.0	yes
9	dense	n/a	n/a	n/a	5.4	0.0	yes
10	dense	n/a	n/a	n/a	5.2	0.0	yes
11	cystic	10.1	2.1	no	2.2	0.0	yes
12	cystic	11.6	3.7	no	5.0	0.0	yes
13	cystic	11.0	0.7	no	1.0	0.0	yes
14	cystic	n/a	n/a	n/a	7.4	0.7	no
15	cystic	9.3	0.0	yes	4.2	0.0	yes
16	cystic	14.1	4.6	no	3.7	0.0	yes
17	cystic	n/a	n/a	n/a	3.7	0.0	yes
18	dense	11.6	0.0	yes	2.9	0.0	yes
19	cystic	n/a	n/a	n/a	n/a	n/a	n/a
20	cystic	n/a	n/a	n/a	n/a	n/a	n/a
Mean		11.6	2.7	Overlap*	5.0	0.5	Overlap*
σ		2.0	1.9	2	2.2	0.3	16

5.4.3 Performance of deformable mapping technique for bCT registered to DBT (MLO)

An overview of the results for registration of the bCT model to DBT (MLO) is illustrated in Table 5.8. As with the CC view, only 18 lesions were viewed in the reconstructed DBT (MLO) images because 2 lesions were too close to the chest wall. Therefore, the maximum number of lesions matches for this set is 18. Without the use of marker analysis only 9 out of 18 lesions were matched with an average d_{COM} of 8.2 ± 3.1 mm. With the use of external markers, the total number of matches improved to 18 out of 18. When all external markers were within 1 mm the

average d_{COM} was 4.7 ± 2.5 mm. When the external markers were within 5 mm the average d_{COM} was 5.4 ± 2.9 mm. lesion d_{COM} for $d_M \leq 1$ mm vs. $d_M \leq 5$ mm was 0.6 mm with a p-value of 0.09, indicating no statistical difference in lesion d_{COM} when the external fiducial markers are closer in distance. However, more lesions overlapped when the markers were closer together.

Table 5.8: Lesion Correlation summary for bCT registered to DBT (MLO). A maximum of 18 lesions could be matched between image sets. (d_{COM} = distance between centers of masses of corresponding lesions in the two modalities, d_O = minimum distance for overlap of corresponding lesions, d_M = distance between external fiducial markers).

	Without Marker Analysis	With Marker Analysis ($d_M \leq 1$ mm)	With Marker Analysis ($d_M \leq 5$ mm)
Total Matched Lesions	9	18	18
Mean d_{COM} (mm)	8.2 ± 3.1	4.7 ± 2.5	5.4 ± 2.9
Mean d_O (mm)	1.9 ± 1.5	1.4 ± 1.6	1.2 ± 1.0
Total Overlapping Lesions	4	16	13

A paired t-test of the d_{COM} 's was performed for the 9 lesions that were matched in the without marker analysis case to the same 9 lesions that were matched with marker analysis cases with $d_M \leq 1$ mm and $d_M \leq 5$ mm, summary of the values used for this calculation are shown in Table 5.9. For $d_M \leq 1$ mm and $d_M \leq 5$ mm the resulting differences in the average d_{COM} were 4.7 mm and 4.3 mm, respectively with p-values of 0.002 and 0.001 indicating significant improvement in average lesion d_{COM} with the use of external fiducial markers.

Table 5.9: Lesion correlation summary of 9 matched lesions between without marker analysis and with marker analysis cases for bCT registered to DBT (MLO). (d_{COM} = distance between centers of masses of corresponding lesions in the two modalities, d_O = minimum distance for overlap of corresponding lesions, d_M = distance between external fiducial markers).

	Without Marker Analysis	With Marker Analysis ($d_M \leq 1$ mm)	With Marker Analysis ($d_M \leq 5$ mm)
Total Matched Lesions	9	9	9
Mean d_{COM} (mm)	8.2 ± 3.1	3.6 ± 1.6	4.0 ± 1.5
Mean d_O (mm)	1.9 ± 1.5	0.0 ± 0.0	0.0 ± 0.0
Total Overlapping Lesions	4	9	9

Figure 5.9 (a) and Figure 5.9 (b) display the improvement in lesion correlation between the bCT and DBT (MLO) models for several lesions. Figure 5.9 (c) shows a GUI-Viewer display for a marked corresponding lesion in the bCT and DBT (MLO) original image sets. The d_{COM} , lesion overlap, and d_O values for each pair of corresponding lesions are listed in Table 5.10.

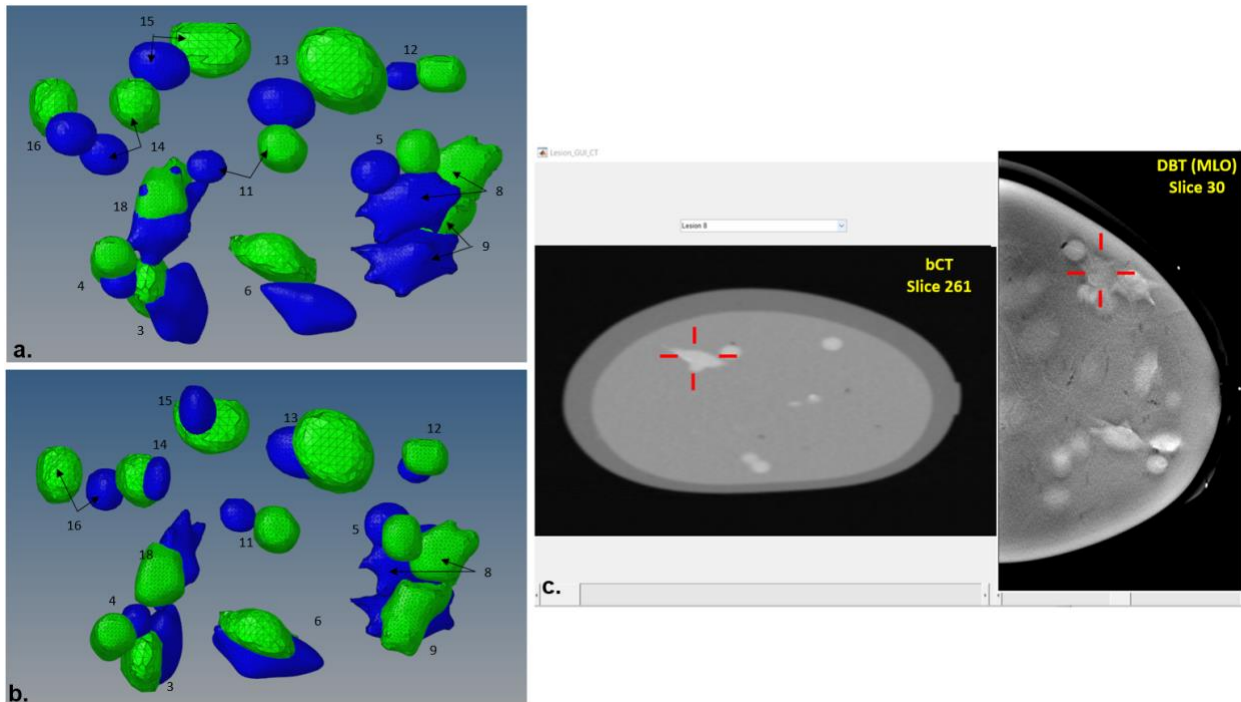


Figure 5.9: Lesion correlation bCT (blue) registered to DBT (MLO view) (green) (a) axial view without marker analysis (b) axial view with marker analysis (c) GUI representation from original DICOM images for a lesion. Numbers correspond to lesion ID's and correlation values in Table 5.10. Note: All lesions are not visually represented in this figure due to superposition of the 2D representation.

Table 5.10: Lesion matching results for each lesion with and without marker analysis for bCT registered to DBT (MLO)

Lesion ID	Lesion type	Without Marker Analysis			With Marker Analysis ($d_M \leq 1$ mm)		
		d_{COM} (mm)	d_o (mm)	Overlap	d_{COM} (mm)	d_o (mm)	Overlap
1	dense	n/a	n/a	n/a	7.5	0.2	no
2	dense	n/a	n/a	n/a	7.0	0.0	yes
3	dense	6.5	0.00	yes	4.0	0.0	yes
4	dense	4.0	0.00	yes	5.5	0.0	yes
5	dense	8.4	0.8	no	3.5	0.0	yes
6	dense	11.9	0.00	yes	3.25	0.0	yes
7	cystic	n/a	n/a	n/a	11.1	2.5	no
8	dense	12.0	1.4	no	6.0	0.0	yes
9	dense	7.3	0.00	yes	0.6	0.0	yes
10	dense	9.6	1.4	no	2.7	0.0	yes
11	cystic	0.00	n/a	n/a	8.0	0.0	yes
12	cystic	10.5	4.2	no	2.9	0.0	yes
13	cystic	0.00	n/a	n/a	6.0	0.0	yes
14	cystic	0.00	n/a	n/a	3.8	0.0	yes
15	cystic	0.00	n/a	n/a	3.8	0.0	yes
16	cystic	0.00	n/a	n/a	3.4	0.0	yes
17	cystic	0.00	n/a	n/a	2.7	0.0	yes
18	dense	3.9	0.00	yes	3.7	0.0	yes
19	cystic	n/a	n/a	n/a	n/a	n/a	n/a
20	cystic	n/a	n/a	n/a	n/a	n/a	n/a
Mean		8.2	1.9	Overlap*	4.7	1.4	Overlap*
σ		3.1	1.5	5/9	2.5	1.6	16/18

5.5 Conclusions

This work demonstrates and evaluates the potential for use of a deformable mapping technique to relate lesions in bCT images to ABUS images and to match lesions in bCT to DBT images. To our knowledge, this is the first study involving the use of deformable registration of bCT images to ABUS or DBT views. Segmentations for each model were used to create a 3D tetrahedral finite element breast model where plate deformations were performed on the bCT model to simulate DBT and ABUS compression. The rate of correlation between the lesions in

the two different modality images increased with the use of external fiducial markers with this method. With the use of external marker corrections, the mean d_{COM} values decreased by 49% for bCT to ABUS registration, 57% for bCT to DBT (CC) registration, and 40% for bCT to DBT (MLO) registration. Additionally, the maximum number of corresponding lesions was achieved with the use of external marker corrections, where the mean marker d_M values were within 1-mm and 5-mm distances for all analyzed cases. Thus, this study showed that external marker analysis could potentially correct for discrepancies that may be influenced by mesh density, friction, and elasticity properties of various tissue types. Implementation of this methodology could significantly improve radiologist's characterizations of breast lesions. In the case for dense breasts where a lesion is not easily identifiable, this method can allow a radiologist to indicate an ROI within the bCT image to determine with higher confidence the ROI location is a match to a better defined region in DBT or ABUS. However, some sort of optimization for patient specific material properties must be considered when applying this technique in the clinic. The results obtained in this work are preliminary and an expansion of this work is planned to quantify the effectiveness of this technique on actual patient data analyzed in an IRB-approved patient study.

5.6 Discussion

A novel deformable registration technique has been described and assessed for identifying related lesions in bCT and ABUS images and in bCT and CC and MLO DBT images. For all analyzed cases there was statistically significant improvement in lesion correlation with the use of external fiducial markers.

This study is to our knowledge the first to show lesion registration between bCT and ABUS breast images. The use of this technique with bCT in conjunction with ultrasound could likely lead to valuable contributions for breast characterizations as it has for mammography¹⁶⁻¹⁸. This

study does not show a significant variation in lesion d_{COM} for cystic lesions in comparison to dense lesions. All lesions in this study are given the material property of dense lesion during FEA since in all x-ray based breast imaging of this phantom, the solid and cystic lesions are not differentiable. The t-test results indicated no difference in lesion correlation based on lesion type. This result is expected since both the simulated dense and cystic lesions use the same Zerdine-based material and just exhibit different ultrasound properties (anechoic for cystic lesions and if dense have hyperechoic). Therefore, when applied to patients, there may be a difference in lesion correlation (d_{COM}) for cystic masses since the algorithm does not use cystic properties during FEA.

This study also indicated a significant difference lesion d_{COM} when the external markers were further apart ($d_M \leq 5$ mm) vs. ($d_M \leq 1$ mm) for the bCT to ABUS case. When all markers are aligned to be closer together larger iterations take place which may be over compensating for some areas of the breast. For instance, in one iteration a set of markers could have first been within correlation bounds and then fall outside the specified correlation bounds, due to shifts from movements of other neighboring corresponding markers within correlation bounds. Thus, this marker set must be readjusted in the next iteration. This over-correction feature may be the cause of the better results with a less strict marker distance ($d_M \leq 5$ mm). This effect was also noted in our previous work for DBT to ABUS registration³⁴. Additionally, this can be an indications that although the external fiducial markers are helpful in registration their use is not completely indicative of internal deformation caused by compression. Currently in ABUS imaging, there is not a distinct way to determine the compressive force used on the breast. In this study, the imaging depth was used to determine ultrasound compression. However, using the

imaging depth is not completely accurate since the transducer for the ABUS system has a reverse curvature so the depth varies with lateral position.

Additionally, this study did not model the reverse curvature of the ABUS transducer during FEA analysis. Due to this curvature, the lateral ends of the transducer can experience approximately an additional 6 mm of compression (See Figure 5.10). We believe the effect of the curvature is not very significant based on the high degree of lesion correlation found in our study. The degree to which this is true for real breasts can be better determined through an IRB-approved patient study. For translation of this technique to patients, the present limited depth of ultrasound penetration of 5 cm may make this technique unsuitable for patients with larger breasts. From our previous DBT to ABUS study, we found larger d_{COM} correlation values than with the present bCT to ABUS study. That is largely because the previous study did not simulate plate compression since the breast is compressed during the DBT and ABUS acquisitions.

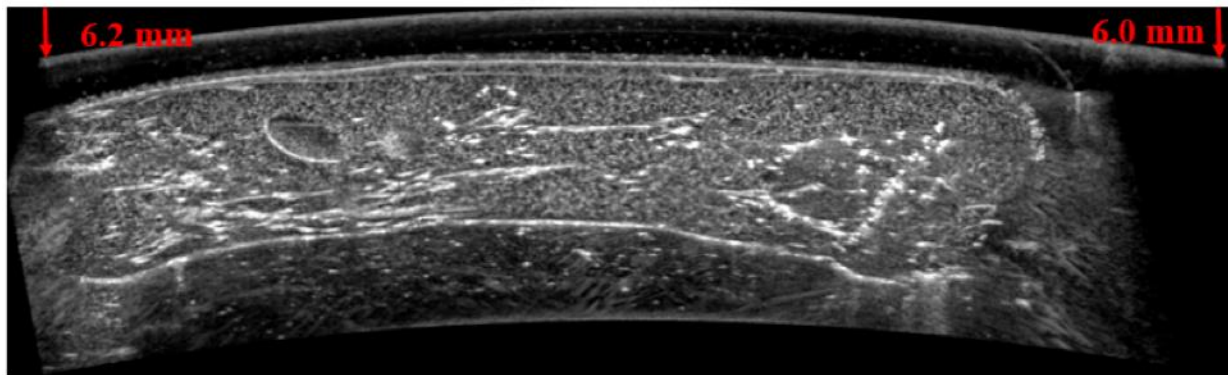


Figure 5.10: Measurement of lateral compression difference from Invenia Reverse curve transducer during ABUS imaging.

For the DBT studies analyzed, there was no statistical difference between results obtained with the use of different external fiducial marker spacing, at a distance of ≤ 5 mm vs. ≤ 1 mm apart. This is likely due to better compression modeling of the compression plates because of the knowledge of the compressive force and compressed breast thickness. However, for the MLO

case there was an increase in lesion overlap for 3 lesions when external markers were closer together ($d_M \leq 1$ mm). Two lesions were not visualized in reconstructed DBT images as they are too close to the phantom back plate or “chest wall” and were not imaged. In a real breast this would should not be an issue with proper technologist positioning.

We expect results for patients will likely be worse than those that were obtained in the phantom study. The phantom used in our study is made of viscoelastically homogenous material whereas there will be much more heterogeneity even within the same material in a real breast. A real breast also will include glandular tissue, adipose tissue, blood vessels, Cooper’s ligaments, ducts, etc. that can have an effect on the performance of the deformable registration. Breast studies that use FE-based techniques typically segment the breast skin, adipose tissue, fibroglandular tissue and the lesion (if applicable) for biomechanical modeling⁸⁹. These might or might not include the effects of ligaments with their primary function of shape control.

Another limitation to this study is that only one phantom was used. Further developments are still needed to produce physical multi-modal breast phantoms that show hyperelastic behaviors. The phantom used within this study exhibits linear elastic behavior, whereas real breast tissue follows hyperelastic behavior under compression^{76,150,151}. Although, other research groups such as Chung et al.¹⁵² have designed and used phantoms with non-linear properties for breast biomechanical modeling, these phantoms are not currently commercially available. There is a rigid posterior wall in the phantom. This causes extreme deformation at the posterior edge of the paddle (Figure 5.2 (b)). The gradient in the deformation might, in fact be greater than that in the human breast as there are ligaments in the breast that would tend to minimize that deformation by pulling down more skin and subcutaneous tissues than in the phantom. Therefore, when translating this technique to patients, segmentation of the dense fibroglandular breast tissue from

adipose tissue in bCT images and the use of corresponding elastic properties of those tissues will be critical. A proof of concept study would be needed to determine the effect these limitations have on lesion registration results in patients.

There is still high variability in the moduli of elasticity for breast tissues. A study by Gefen and Dilmoney⁸² the Young's modulus for glandular tissue ranges from 7.5 kPa- 66 kPa and adipose tissue ranges from 0.5 kPa – 25 kPa. A study by Athanasiou et al.⁹⁶ used supersonic shear wave imaging on 46 women with 48 breast lesions where the mean elasticity values was 146.6 ± 40.05 kPa for malignant lesions and a mean elasticity value of 45.3 ± 41.1 kPa for benign breast lesions. When applying this technique to patients consideration for what material properties will need to be used in order to make the model patient-specific. Kellner et al.⁹⁷ used average values found from several *in vitro* and *in vivo* elastic coefficients for the skin, fat and glandular breast tissue to arbitrarily assign to a model. Contrarily, Han et al.⁷¹ used a material property optimization algorithm to change the material property based on maximizing the similarity between the predicted deformed MR breast images. However, this type of technique could lead to huge runtimes with the use of commercial FE packages. Other differences between, the work of Han et al.⁷¹ and this work is that they used a GPU-based explicit dynamic FEA solver^{153,154} where in this work we use commercial non-linear quasi-static FEA. Due to the high runtimes observed in this study we will likely need to explore ways to optimize the results while decreasing runtime when applying this technique to patients.

When using FEA to simulate application of plate compression to breast models generated from bCT images of actual patients' breasts, a study by Hsu et al.¹⁴⁶ found that small alterations in the biomechanical properties of the tissues can result in significantly different representations of the resulting DBT breast models in the simulations. Hsu et al.¹⁴⁶ found that these differences

are largely influenced by mesh density, friction coefficient between plates and skin, and relative stiffness of the various tissue types which can change the breast tissue distribution during simulated compression up to 1 cm. However, other studies have shown the use of external fiducial markers can be very helpful and potentially could partially correct for these discrepancies and increase confidence in lesion registration ⁶⁹⁻⁷².

5.7 Acknowledgements

This work was supported in-part by a research grant (15-PAF04328) from GE Global Research. Crystal A. Green is supported by the Science, Mathematics and Research for Transformation (SMART) Scholarship for Service Program (HQ0034-16-C-0008). The authors would like to thank Ted Lynch, Ph.D. of CIRS, Inc. for his assistance in phantom development and characterization.

Chapter 6

Proof-of-Concept patient validation study of Deformable Mapping Technique to relate lesions between DBT and ABUS images

6.1 Abstract

Purpose: This work investigates the application of a deformable localization/mapping method to register lesions between the digital breast tomosynthesis (DBT) craniocaudal (CC) and mediolateral oblique (MLO) views and automated breast ultrasound (ABUS) images based on five patient data sets and up to 7 lesions. This method was initially validated using compressible breast phantoms.

Methods: The automated deformable mapping algorithm uses finite element modeling and analysis to determine corresponding lesions based on distances between centers of mass (d_{COM}) in the deformed DBT model and the reference ABUS model.

Results: This technique has found that using several combinations of external fiducial markers can be helpful to improve lesion registration. However, use of external markers are not required for deformable registration results described by this methodology. For DBT (CC view) mapped to ABUS, the mean d_{COM} was 11.0 ± 4.9 mm based on 7 lesions. For DBT (MLO view) mapped to ABUS, the mean d_{COM} was 12.3 ± 4.8 mm based on 6 lesions. Both DBT views registered to ABUS lesions showed statistically significant improvements ($p \leq 0.05$) in registration using

the deformable technique in comparison to a rigid registration.

Conclusion: Application of this methodology could help improve a radiologist's timing, efficiency, characterization and accuracy in relating corresponding lesions between DBT and ABUS image datasets, especially for cases of high breast densities and multiple masses.

6.2 Introduction

Conventional handheld ultrasound (HHUS) imaging is often used as a complement to mammography and has shown large improvements in the characterization of breast lesions by aiding in differentiating between solid and cystic lesions.¹⁶⁻¹⁸ HHUS has a higher sensitivity than mammography for lesions in women with dense breasts.⁵⁴ HHUS produces 2D images and is performed freehand in a different geometry (supine) than mammography (upright). In HHUS, the image acquisition is freehand and therefore there is difficulty in reproducing images due to high operator dependence. Automated breast ultrasound (ABUS) creates a 3D image volume and has advantages in terms of reproducibility, faster image acquisition speed, and operator independence over conventional HHUS for breast examinations.^{18,19,57} As demonstrated by D'Orsi et al.⁴⁰, using ABUS in conjunction with mammography screening for women with dense breasts (BI-RADS ACR3 or ACR4) increases the rate in breast cancer detection. Additionally, several other studies have shown that ABUS significantly improves the breast cancer detection rate with an acceptable recall increase.^{19,57,58} However, several studies concluded that HHUS is superior to ABUS for breast lesion that are smaller in size/diameter, irregular in shape, non-circumscribed margins, and for breast coverage in peripheral margins.⁵⁹⁻⁶²

Currently, mammography is the gold standard for detecting breast cancer and is the only screening test proven to reduce the breast cancer mortality rate in women.¹⁵⁵ However, mammography has reduced sensitivity and increased false-negative examinations for women

with dense breasts due to the superposition of breast tissues from the single 2D image projection. Digital breast tomosynthesis (DBT) mammography's quasi-3D counterpart, uses limited angle tomography in the mammographic geometry and can help locate breast masses that are masked in mammography due to superposition of breast tissues. Studies have shown DBT to have an increased cancer detection rate and reduced recall rate in comparison with digital mammography.⁴⁵⁻⁴⁷ Gains using DBT are largely seen for women with dense breasts, where DBT outperforms mammography in both screening and diagnostic uses.¹²⁹ However, like mammography, DBT still has difficulty in distinguishing between solid and cystic breast lesions. Thus, there remains a need for supplementary ultrasound imaging.^{109,110}

Considering that the breast is highly deformable, and the breast is imaged in different geometries and compression for mammography and ultrasound, it can be difficult to relate lesions between mammography and ultrasound images. Additionally, at least 10% of the time lesions found in ultrasound images do not correspond to those found in mammography/DBT.¹⁵ There are two potential solutions to this problem: (1) The development of a combined x-ray/ultrasound system that images the breast in the same mammographic geometry using special modality paddles or (2) The development of a deformable registration technique to detect and relate corresponding lesions between the x-ray and ultrasound modalities in their respective geometries. This study will investigate the latter proposed solution.

Several groups have evaluated the performance of a combined x-ray/ultrasound system that images the breast in the same mammographic geometry using special modality paddles.^{21,22,24,25,27-30,63} Since the images are acquired in the same geometry there is a direct localization for lesion registration between the 3D ultrasound to the DBT. However, the singled-sided ultrasound transducer combined systems have limitations in terms of ultrasound

penetration depth and poor ultrasound transducer coupling along the peripheral breast regions in the mammographic geometry. To address these issues, Larson et al.³³ explored using dual-sided ultrasound, however their work has not been implemented into a combined system using x-rays. Additionally, a combined x-ray ultrasound system is very expensive and not yet commercially available.

An alternative solution to using a combined system is to image the breast using DBT and ABUS modalities in their respective geometries and then use a deformable registration method to relate the corresponding lesions. Using a deformable registration method has advantages of improved transducer coupling while imaging with ABUS and it will utilize commercial systems that are likely already in the clinic. The main disadvantage of using a deformable registration method is that there is greater technical difficulty in relating corresponding masses due to the differences in patient positioning and compression between the DBT and ABUS modalities.

Our previous work involved the development of a deformable mapping method for lesions in DBT (CC-view) and ABUS on a breast phantom with increased improvement using external markers and finite element methods (FEM).³⁴ To our knowledge, that study was the first to show the direct registration of lesions between DBT and ABUS modalities. We extended that work to include registration of DBT (CC and MLO views) and ABUS using a compressible breast phantom with multiple lesions.³⁵ Additionally, we extended upon that work to include the registration of simulated dedicated breast CT to DBT (CC and MLO views) and ABUS using a compressible breast phantom with multiple lesions.³⁶ Like other studies, we found the use of FEM and external fiducial markers helpful in improving lesion registration.

Several studies have used FEM-based methods to register lesions between uncompressed MRI (prone positioning) to CC and/or MLO mammograms^{85,86,88,90} and between CC and MLO

views in mammography.¹¹² Segmentation of the entire breast is required to use FEM biomechanical breast models and studies have used manual^{71,76}, semi-automated^{84,85}, and automated^{86–88} segmentation techniques for the development of FEM breast models. Additionally, studies have found that using external fiducial markers were helpful to improve registration results for MRI/PET registration^{69,70}, compressed to uncompressed prone MRI registration⁷¹, and breast MRI to ultrasound registration⁷².

In this chapter, we present modifications and validate our automated deformable registration method to relate lesions between DBT (CC and MLO views) and ABUS using FEM. We evaluate the improvement in registration by using various numbers of external fiducial markers. This study validates the performance of a deformable mapping method based on 5 patient data sets to register up to 7 lesions. The validated algorithm can be used to relate regions of interests (ROIs) between these two modalities such that a radiologist can directly view corresponding lesions in DBT and ABUS images. Implementation of this method can save a radiologist time in navigating through the 3D image volumes. This will be especially beneficial for the more difficult cases such as women with dense breast tissue or women with multiple breast masses.

6.3 Materials and Methods

6.3.1 Experimental Procedures

In order to determine the efficacy of our deformable registration technique, we collected patient data as part of an IRB-approved study. Inclusion criteria for patient volunteers is defined as follows: 1) Women who were scheduled for a biopsy procedure within the Breast Imaging clinic at the University of Michigan Cancer Center and 2) have a breast mass 5 mm or greater in size that is visible on ultrasound and not located in the axillary breast region. A detailed description of the imaging procedures is provided in the Appendix.

In order to help restrict breast motion during ABUS imaging and between ABUS scans, the patient volunteer was first fitted by one of the research staff members for an ultrasound camisole. The camisole, shown in Figure 6.1 (a), fits on the patient similar to a sports bra. The camisole is made in various sizes (women's dress sizes 0-26). Each camisole is made of a sheer stretchable nylon mesh fabric in the front and a stiff cotton fabric in the back. This camisole was tested to ensure that penetration ability of ultrasound is not compromised. Additionally, the camisole was tested on 10 normal volunteers to ensure that breast motion was restricted, and the locations of the external fiducial markers located beneath the camisole were not compromised. The camisole was not worn during the x-ray portion of the exam. After being fitted for the camisole the patient takes off the camisole and then a research staff member denotes areas of the breast for placement of external fiducial markers with a washable magic marker (See Figure 6.1 (b)). Seven external fiducial markers were then attached to the breast at the indicated locations using Jobst "It-Stays" Roll-On Adhesive (BSN Medical, Charlotte, NC)^u.

^u <http://www.jobst-usa.com/product/it-stays-roll-on-adhesive/>

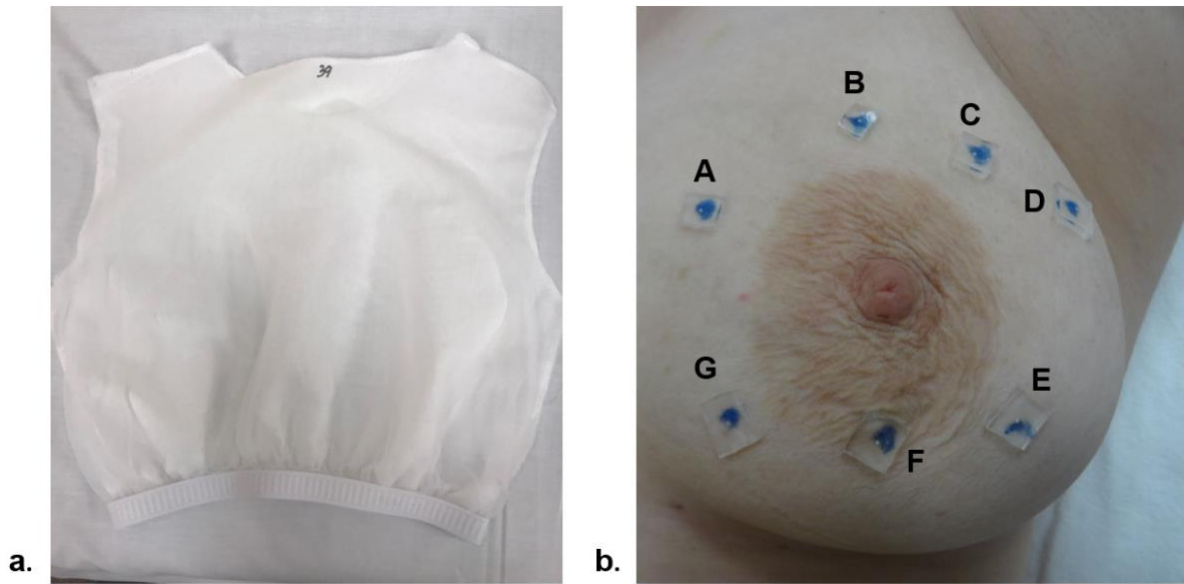


Figure 6.1 (a) Ultrasound camisole for ABUS imaging (b) External fiducial marker locations (denoted by A-G) shown for marker placements on the left breast

One marker was placed at the center of each breast quadrants (labeled as A, C, E and G in Figure 6.1 (b)), one marker was placed superior and one marker was placed inferior to the nipple (labeled as B and F Figure 6.1 (b)). An additional marker was placed more lateral in the upper outer quadrant due to this quadrant being the most common quadrant for breast malignancies (labeled as D in Figure 6.1 (b)). Various marker combinations can be analyzed using the deformable mapping algorithm. Results in this study are obtained using the following combinations with letter designation in Figure 6.1 (b): all 7 markers, 6 markers (located at positions A-C and E-G), 4 Markers (located at positions A-D), and 3 markers (positions A-C), and 1 marker analysis (dependent on the marker closest to the specified lesion). If a lesion is in the retroareolar region of the breast the 1 marker analysis is not run.

Each external fiducial marker contains a 1 mm glass bead in a bubble-free thermoplastic elastomer gel. The glass bead can be easily seen in the DBT and ABUS reconstructed images as shown in Figure 6.2. To ensure that the adhesive holding the fiducial markers to the breast has

enough time to cure, we waited a minimum of 5 minutes before initiating x-ray imaging. As a precaution TomoSpot bandages^v (with the x-ray target removed) were placed over each marker to ensure that the external markers remained in place during x-ray imaging.

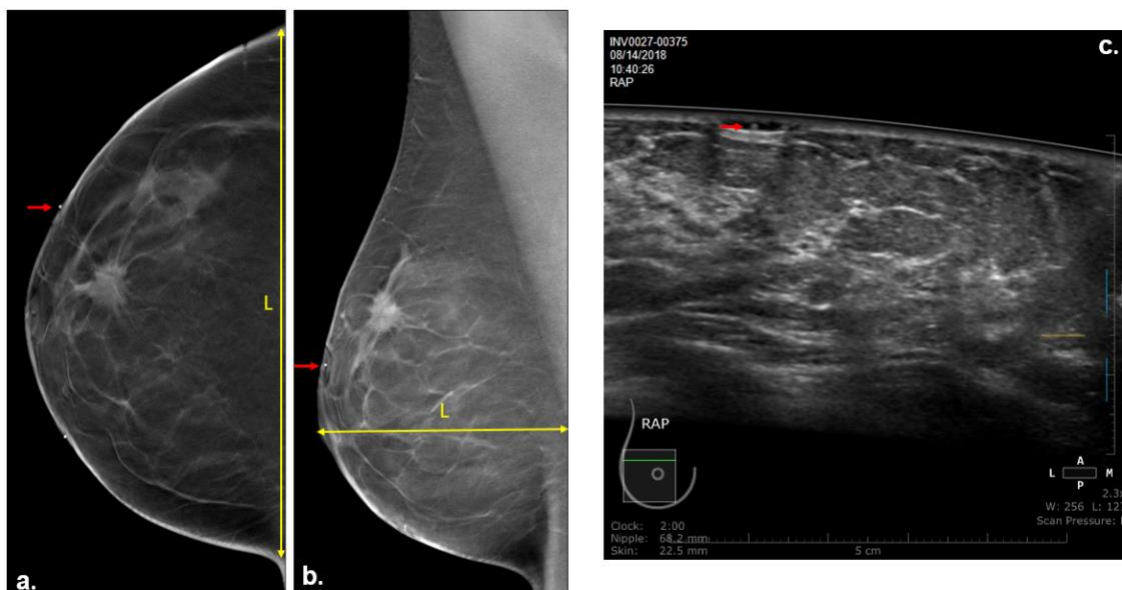


Figure 6.2: Red Arrow indicates glass bead of an external fiducial marker in (a) DBT (CC view) (b) DBT (MLO view) and (c) ABUS AP view. Yellow arrow shows length x for (a) the medial to lateral breast margins in DBT (CC view) needed for DBT surface skin transformation (b) nipple to posterior breast length in DBT (MLO view)

After patient preparation, DBT images were acquired in both CC and MLO (at 45° angles) views by x-ray technologists using the GE Senographe Pristina DBT system (GE Healthcare, Milwaukee, WI). The voxel width and length of the DBT images are 0.1 mm and the slice thickness (image depth) was 1 mm. Next, the patient was brought to an adjacent ultrasound room and positioned supine. The TomoSpot bandages were removed from the breast while the external markers remain attached. Prior to ABUS imaging, the patient puts on the ultrasound camisole with assistance from a research staff member. The markers may move in this process in which case the magic marker locations indicate where the markers need to be reapplied. Ultrasound lotion was then applied over the camisole and light AP compression was applied to the patients'

^v <https://www.beekley.com/product-details/tomospot-for-marking-nipples-781>

breast as she was imaged with the GE Invenia ABUS system (GE Healthcare, Milwaukee, WI). Three images were acquired during the ABUS exam (AP View, Lateral View, and Medial View) to ensure adequate breast coverage. Depending on patient breast size, the low, medium, or high setting could be used to image the desired depth. The 153 mm length reversed-curved transducer can image up to a 50 mm depth and scanned the breast through a mesh compression paddle. Correction for the reverse-curvature of the transducer is not included in the resulting DICOM images, therefore a MATLAB program was created to correct for the transducer curvature.

Within this curvature correction program, the ABUS images are resampled from a native voxel size of 0.082 mm in depth, 0.2 mm in width, and 0.506-0.511 mm in length (distance between adjacent slices dependent on exam setting), to 0.082 mm width, 0.082 mm depth, and 0.506-0.511 mm in length (depending on the imaging depth setting). This algorithm takes about 1 hour to complete the resampling and curvature corrections. Methods used within the Invenia ABUS workstation software could allow for this curvature processing to be done instantly.

The curvature-corrected ABUS images are then resampled from the 0.082 mm in depth, 0.082 mm in width, and 0.506-0.511 mm in length (distance between adjacent slices dependent on exam setting), to 0.2 mm in width, 0.2 mm in depth, and 0.506-0.511 mm length (dependent on imaging depth setting). Since each ABUS view generates 330 slices, resampling was needed to increase the speed of surface mesh creation for the base FE ABUS model generation. Image resampling is done using the MATLAB `imresizew` command.

6.3.2 Segmentation Methods

All lesions in the acquired patient-specific images in DBT and ABUS were segmented using MiViewer, a semi-automated segmentation program based on using 3D level set segmentations

^w <https://www.mathworks.com/help/images/ref/imresize.html>

from the University of Michigan CAD Laboratory^{140,141}. In the MiViewer, program the user specifies the best slice, the first slice, and the last slice that the lesion is seen in the 3D image set. Then the user places a small box to occupy the lesion in the best view of the image slice. We found using window level/width settings that provided more contrast and noise (as shown in Figure 3(a)-(c)) provided best visualization of the lesions for box placement to occupy the lesion in MiViewer. In the publication from Street et al., the MiViewer segmentation is described, “Our computer segmentation system consists of three stages. In the first stage, we apply preprocessing techniques to the original CT images in the 3D volume in order to obtain a set of smoothed images and a set of gradient images. In the second stage, an initial segmentation contour from the pre-processed images is extracted. In the last stage, a serial bank of level sets is propagated from the initial segmentation toward the final segmentation.”¹⁴⁰

MiViewer allows for adjusting many parameters in the level set segmentation. We found that two sets of parametric settings (e.g. level-set time sets, sample radius, blur kernel etc.) gave best segmentations with minimal adjustments needed. These are listed in the Appendix. Minor modifications can be made after segmentation. Further information of the MiViewer program can be found in the work by Street et al.¹⁴⁰ and Hadjiiski et al.¹⁴¹ If a lesion was unable to be sufficiently segmented using MiViewer then manual segmentation was performed. All lesion segmentations were checked and verified by a radiologist. Examples of a lesion segmented using MiViewer software are shown in Figure 6.3 (a) and Figure 6.3 (b) for DBT images and Figure 6.3 (c) for ABUS images.

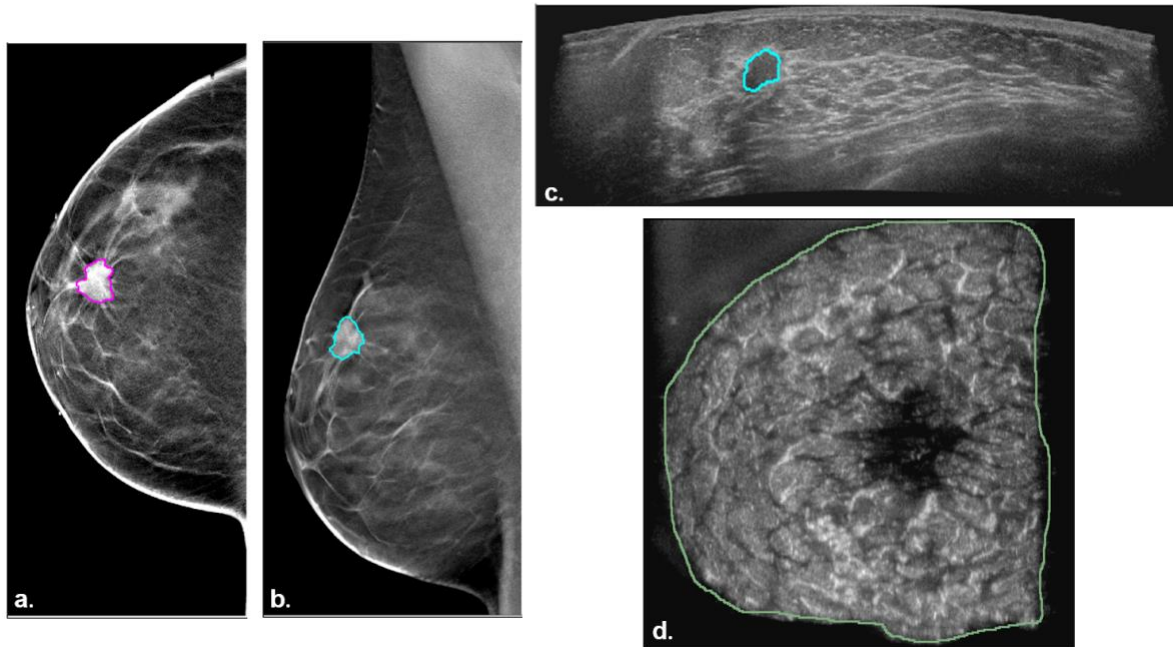


Figure 6.3: MiViewer lesion segmentation for (a) DBT (CC view) image slice (b) DBT (MLO view) image slice (c) ABUS (AP view) image slice (sagittal) (d) 3D Slicer skin segmentation of ABUS (AP view) (coronal)

Segmentation of the glandular/dense tissue from the breast mask of the DBT images was performed using LIBRA, an open-source software package developed by the Computational Breast Imaging Group at the University of Pennsylvania.¹⁵⁶ The LIBRA software was developed to quantitatively determine breast density of mammograms, by segmenting the dense breast regions from the breasts as shown in Figure 6.4. We found that it was sufficient for also segmenting the dense/breast masked from slices in DBT. Using the LIBRA executable, all DBT slices are housed in one directory. This is so that the executable is run using “Batch Processing” and also to save the additional intermediate files, which are produced for each image slice within the directory. The intermediate files contain the segmentations of the breast mask and the dense mask which are used for the patient-specific DBT FEM base model construction.

Since DBT has poor axial resolution the first 5 and last 5 image segmentation slices (which represents the top 5 and bottom 5 sections of the breast) for the glandular tissue are avoided during surface mesh creation. These are excluded from classification as dense tissue since the

voxels are likely skin. Five slices were used as it was the maximum number of slices that the 1 mm glass bead from the external fiducial markers is seen in reconstructed DBT views which is on the breast skin surface. An example of the resulting segmentation of the dense mask from a DBT image slice using the LIBRA executable is shown in green in Figure 6.4(c).

The breast was segmented from the background also using LIBRA to generate the breast (shown in red from an image slice in Figure 6.4(c)) mask for the skin. Breast skin thickness can range between 0.7 to 3.0 mm as reported by Huang et al.¹⁵⁷ from breast CT data. The breast mask segmentation (shown in red from an image slice in Figure 6.4(c)) is shrunk by 3 mm for each image slice in the x-y plane, to create the inner skin mask which accounts for skin thickness. This is done by using the MATLAB `bwmorphx` function. The inner skin mask rejects the first and last 3 image slices to account for the 3 mm skin thickness in the z-plane. The area between the glandular tissue and the inner skin mask is fatty/adipose tissue for FEM. An example of the resulting segmentation of the breast mask from a DBT image slice using the LIBRA executable is shown in red in Figure 6.4(c).

^x <https://www.mathworks.com/help/images/ref/bwmorph.html>

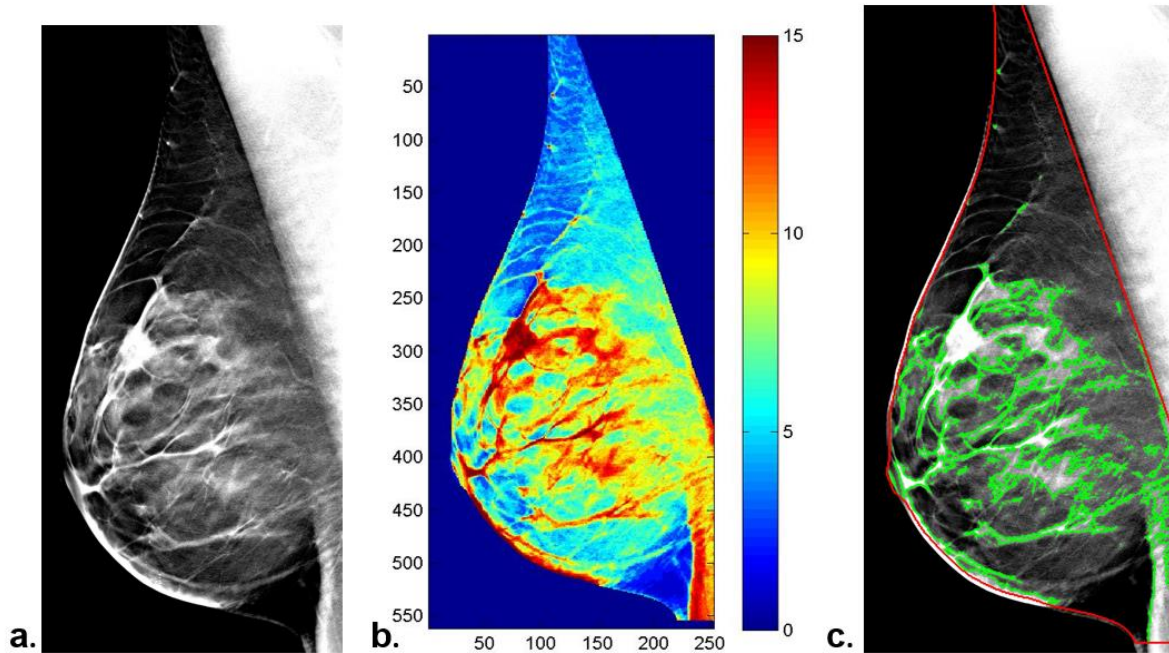


Figure 6.4: (a) Original DBT DICOM slice (b) LIBRA-generated color map of dense breast regions (c) Breast mask segmentation (red) and dense mask segmentation (green) of DBT slice

Since ABUS is the reference model, segmentations are only required for the markers, lesions, and outer skin layer. The skin layer is segmented using semi-automated techniques using 3D Slicer.¹⁴² This is done by manually segmenting various slices along the coronal ABUS view and using the “Fill between Slices” technique under the Segmentation module to segment the peripheral breast margins where there was not substantial scatter or signal drop out artifacts.¹⁴²

The first 4-6 slices in the coronal view (see Figure 6.3 (d)) were manually segmented by visual inspection. The last slice is segmented based on the manual segmentation of a slice before the ribs appear in the breast data. Several intermediate slices should also be segmented to achieve more improved results. A resulting segmentation of a slice of the breast image volume for the skin outline in ABUS is shown in Figure 6.3 (d).

6.3.3 Studies Performed

The studies undertaken to evaluate the performance of the deformable mapping technique for DBT (CC view) mapped to ABUS and DBT (MLO view) mapped to ABUS and are described as follows:

- *Validation of deformable registration of the DBT (CC view) mapped to ABUS images:* Results (d_{COM}) are compared using the deformable mapping algorithm (with and without marker analysis). Those results are then compared to a rigid registration of the DBT (CC view) and ABUS image volumes. Various marker combinations are also compared using the deformable mapping algorithm. T-test and signed Wilcoxon rank tests are used to provide the null hypothesis, that there is no improvement using the deformable method for lesion registration over that of rigid registration.
- *Validation of deformable registration of DBT (MLO view) mapped to ABUS images:* This study was performed similarly to the previous case for DBT (CC view) to ABUS registration.
- *Elastic Modulus Sensitivity Analysis:* Modifications to the Young's moduli for adipose, glandular and lesions tissues are run on all patient data sets using the deformable mapping algorithm without marker analysis. The minimum and maximum elastic moduli values that were used are described in Table 6.2. The resulting d_{COM} values are compared to the default d_{COM} results on all patient datasets using the default/base Young's moduli parameters (see Table 6.1) within the deformable mapping algorithm. The comparison is done in order to show the effect that varying the elastic parameters has on the registration results (d_{COM}) using the deformable mapping method.

- *Algorithm Optimization Study:* Results increasing the resampling size to 0.3 mm length, 0.3 mm width, and 1 mm depth are performed for the subject with the largest breast volume in order to determine the effect it on algorithm run time and d_{COM} . Additionally, reducing mesh coarseness of the skin, fat, and glandular tissues is performed for this same subject's image data in order to determine its effect in algorithm run time and overall resulting d_{COM} .

6.4 Calculations

The deformable mapping algorithm is an automated process that leverages a commercial pre-processor (HyperMesh version 2017.2, Altair Engineering, Troy, MI) for meshing model generation and a commercial FEA solver (HyperMesh version 2017.2, Altair Engineering, Troy, MI). An overview of this process is shown in Figure 6.5. This algorithm provides deformation results using, or without using, location information provided by external fiducial markers. The entire process can take between 30-60 minutes (depending on model/breast size) to complete using a Windows 10 Intel® Core™ i7 CPU with a speed of 2500 MHz and 8GB RAM.

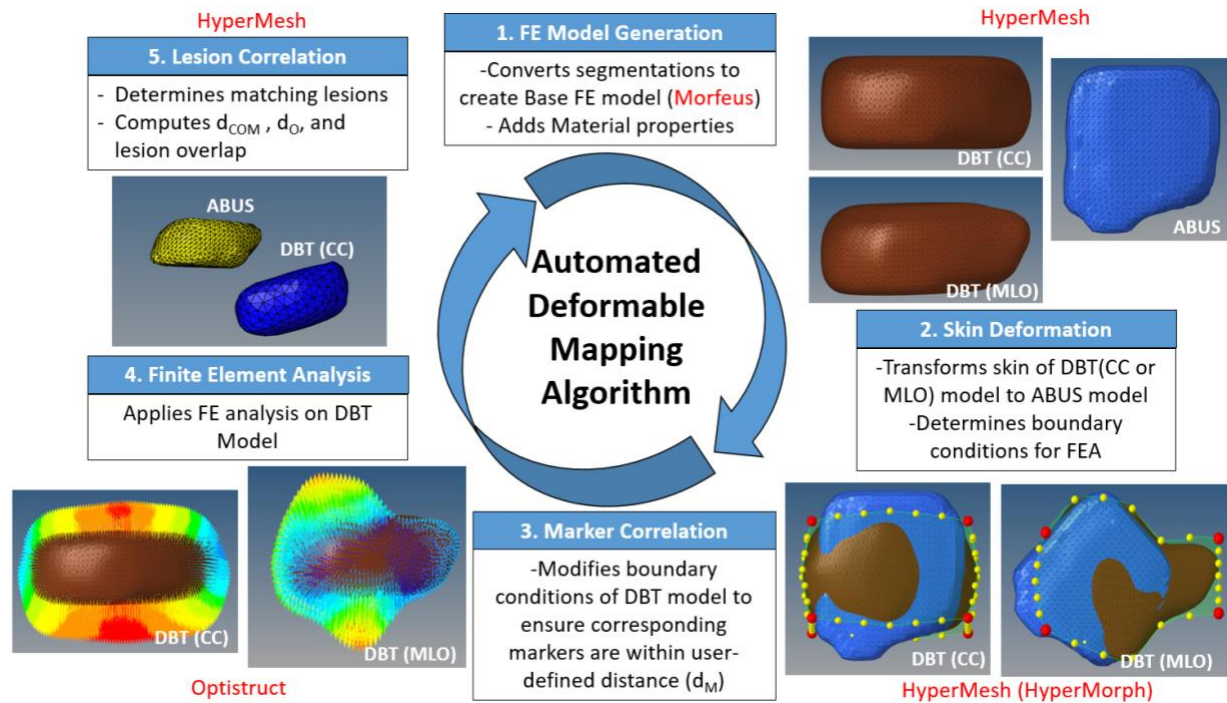


Figure 6.5: Overview of the Automated Deformable Mapping Process. Software's used are shown in red.

6.4.1 Base Finite Element Model Generation

The segmented contours are converted into triangular surface meshes using Morfeus, which uses the *shrinkwrap* tool in the finite element (FE) pre-processor, HyperMesh¹⁴³. The compilation of surface meshes are used to build each base model for the DBT (CC or MLO) and ABUS modality. More information on how to generate the base FE model can be found in the Appendix. A 1 mm element size was used for all lesions and 5 to 10 mm element sizes were used for the glandular, adipose, and skin volumes based on their larger volume and patient dependency. The triangular surface meshes are meshed using 3D four-point fully meshed tetrahedral models for each modality model being used for registration. This study employs the use of a four-compartment model (skin, adipose, glandular, and lesion). The material properties assigned for the various model volumes are described in Table 6.1. The skin, adipose, and glandular material properties were attributed from work by Kellner et al.¹⁵⁸ which has been used in other FEM-based breast models¹⁵⁹. Each lesion by default is given the property of a benign

lesion based on average reported values by Tozaki and Fukuma¹⁶⁰. If specified the algorithm can be run so that the mechanical properties of a malignant lesion are used (Tozaki and Fukuma¹⁶⁰).

Table 6.1: Mechanical properties used for biomechanical modeling. By default, a lesion is assigned the properties of benign lesion.

<i>Tissue Type</i>	<i>Young's Modulus (E)</i>	<i>Poisson's Ratio (ν)</i>
Skin	88 kPa	0.49
Adipose Tissue	1 kPa	0.49
Glandular Tissue	10 kPa	0.49
Lesion (Benign)	42 kPa	0.49
Lesion (Malignant)	146 kPa	0.49

Table 6.2 shows the range of the material properties tested for the sensitivity analysis study further discussed in the 6.5 Results section.

Table 6.2: Minimum and Maximum Young's Moduli of adipose, glandular and lesion tissue for sensitivity analysis

<i>Tissue Type</i>	<i>Young's Modulus (E)</i>	
	<i>Minimum (kPa)</i>	<i>Maximum (kPa)</i>
Adipose Tissue	0.5	1.5
Glandular Tissue	1	20
Lesion (Benign)	6.3	96
Lesion (Malignant)	7.1	299

6.4.2 DBT Skin Deformation

Once the base FEM models for the DBT and ABUS models are created the DBT model is registered to the center of mass (COM) of the ABUS model. Details of this registration will be addressed in the following text for DBT (CC view) to ABUS and DBT (MLO view) to ABUS.

6.4.2.1 DBT (CC view) mapped to ABUS

For DBT (CC view) mapped to ABUS, the base DBT model is rigidly registered to the COM of the ABUS base model, as shown in Figure 6.6(a). A check is performed to ensure that the nipple is within a 2 cm distance in both the x and y dimensions. If this is exceeded the model is rigidly registered to the nipple. This nipple registration check helps correct for proper alignment in the case where the nipple was not adequately positioned during ABUS image acquisition due to the shape or size of the breast, or improper positioning by a technologist. The

nipple correction only corrects in the x and y planes. Skin deformation is performed on the base DBT model using the HyperMorph feature, which creates local (yellow) and global (red) handles around the DBT FE volume. The handles are manipulated to morph the mesh to be a similar shape as the ABUS model in all anatomical directions. Our previous work described the detailed process of how skin deformation takes place.³⁴ This method was slightly modified in order to account for axillary attachment, breast size, and improper positioning during ABUS imaging. The modifications are explained below, and the process is summarized in Figure 6.6.

In our previous work, the skin deformation was based on a phantom that did not have an axillary attachment, therefore the method deformed the skin based on the shape of the phantom. This modification is necessary because real breasts are attached to the body. Since our previous method does not account for this attachment this could cause the breast to be deformed too great for smaller breasts in which the axillary and upper thoracic regions are included in the ABUS AP view. Similarly, it could cause for larger breasts to not be deformed enough, where the ABUS AP volume contains more breast tissue and not the upper thoracic and axillary breast regions. Therefore, this study employs the use of standardized parabolic shape corrections shown by Eq. (10) for skin deformation based on a measure of the medial to lateral breast skin length (denoted by L) in Figure 6.2 (a) indicated by the yellow arrow. The patient breast data was fit using the parabola equation to determine breast deformation based on L .

$$y = ax^2 + bx + c \quad (10)$$

Each handle controls deformation of the DBT breast volume based on influence functions that control those areas of the mesh model. There are 68 handles along the exterior of the breast in all planes. The handles along the x-plane are manipulated based on their location to the center of mass (COM) of the breast DBT FEM model (e.g. superior/inferior or anterior/posterior). Each

handle is equidistant, $L/6$, from the neighboring handle along the x-axis. The length from the left side of the breast to the handle is used as the variable “x” in Eq. (10) to calculate the proper y-distance needed for handle manipulation. The coefficients that were found to show the best fit based on location and the length L are defined in Table 6.3. Handle manipulations based on these parabolic dimensions are shown in Figure 6.6(b). All resulting R^2 values based on these fits were over 0.98.

Table 6.3: Coefficients for Equation 1 based on different lengths, L, as described in Figure 6.2. SA= Superior Anterior. SP= Superior Posterior. IA= Interior Anterior. IP=Interior Posterior.

Nodal Location	Coefficients for Equation 1								
	$L < 18.0$ cm			$18.0 \text{ cm} < L < 20$ cm			$L > 20$ cm		
	a	b	c	a	b	c	a	b	c
SA	-3.65	3.65	1.49	-7.31	7.31	1.48	-4.73	4.73	0.77
SP	-3.65	3.65	1.49	-7.31	7.31	3.48	-4.73	4.73	1.52
IA	2.57	-2.57	-1.46	2.57	-2.57	0.04	3.65	-3.65	-0.99
IP	2.57	-2.57	-2.96	2.57	-2.57	-1.46	3.65	-3.65	-1.99

After corrections are made along the y-axis, the anterior handles are then manipulated to show AP compression which results in Figure 6.6 (c).

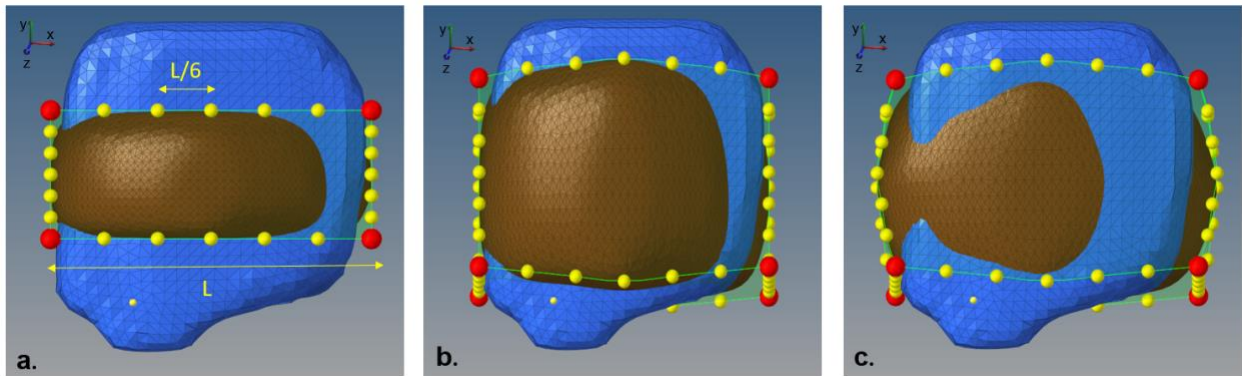


Figure 6.6: Handle manipulation for external skin DBT mesh. Blue=ABUS (unchanged). Brown= deformed DBT (CC view) (a) original DBT mesh registered to COM of ABUS (b) morphed DBT mesh following parabolic deformation for nodes along x-axis (c) resulting morphed DBT model after compression along z-axis. The handles (red and yellow spheres) are used to manipulate the DBT mesh model to match similar shape of the ABUS model.

6.4.2.2 DBT (MLO view to ABUS)

For MLO to ABUS registration, first the base ABUS model is rotated $\pm 45^\circ$ in the x-y plane (depending on breast laterality such that the lateral side of the DBT breast is superior and the medial side of the DBT breast is inferior as shown in Figure 6.7 (a) in comparison to its position in Figure 6.6 (a)). For the right breast the ABUS model is rotated 45° (shown in Figure 6.7) and for the left breast, the ABUS model is rotated -45° . It should be noted that all analyzed cases in this study were acquired at a 45° angle for the MLO view. DBT (MLO) base FEM model is then rigidly registered to the COM of the ABUS model shown in Figure 6.7 (a). A nipple correction is made by rigidly registering the nipple of base DBT model to the nipple of the ABUS model to ensure alignment across all planes, as shown in Figure 6.7 (b). Skin deformation is performed by manipulating the handles as similarly described in our previous works.^{34,35} The deformation is performed on the DBT (MLO) model to transform the DBT mesh volume to match the outer shape of the breast in the ABUS model. This is done by manipulating handles along the x and y planes as shown in Figure 6.7 (c). Posterior nodes are compressed in the positive z direction based on the length L (see Figure 6.2 (b)), subtracted from the depth of the ABUS 3D volume to correct for depth. Since the MLO view contains the axillary tail there is no correction for that area as shown in Figure 6.7(c). The axillary tail which is located on the right in the brown DBT MLO model does not correspond to any areas on the blue ABUS model; therefore, no skin deformation is made in that region.

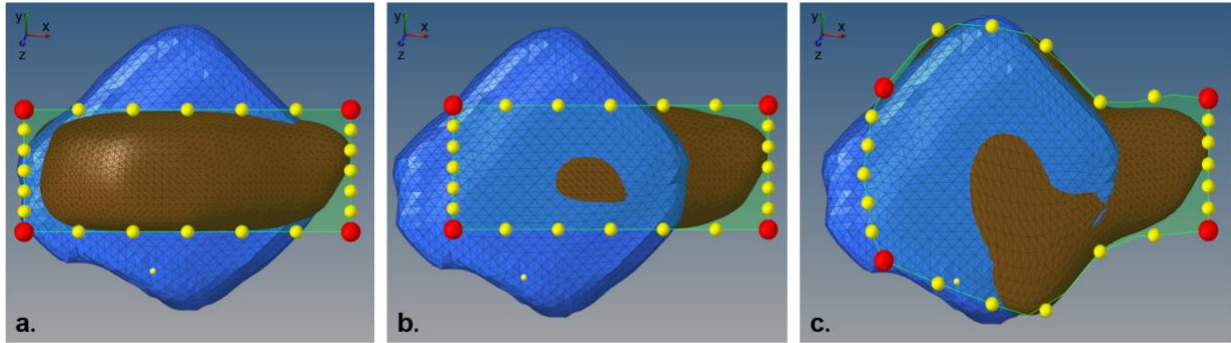


Figure 6.7: Handle manipulation for external skin DBT mesh. Blue=ABUS (unchanged). Brown= deformed DBT (MLO view) (a) original DBT mesh registered to COM of ABUS (b) original DBT mesh registered to the nipple of the ABUS model (c) skin morphing performed by handle perturbations to allow DBT MLO model to match similar shape of ABUS model. The handles (red and yellow spheres) are used to manipulate the DBT mesh model to match similar shape of the ABUS model.

6.4.3 External Marker Relation (Optional Step)

After skin deformation is completed, the algorithm computes the COM positions of the external fiducial markers between the morphed DBT and ABUS model. The external markers are matched using a matching algorithm that was described in greater detail in our previous work³⁴. We've found that allowing the algorithm to search for corresponding markers clockwise (right breast) and counter-clockwise (left breast) beginning with the marker located in the lower inner breast quadrant was the most helpful to ensure proper marker matching. Once the algorithm determines which external markers are matched between the two models and further manipulates the handles of the deformed DBT mesh as described in Figure 6.6 and Figure 6.7 to ensure are markers are within a 5 mm distance. We've found that high iterations (>10 iterations) of the algorithm can cause mesh distortions. Therefore, it is recommended that the external marker correlation does not iterate more than 10 iterations for both DBT (CC view) to ABUS registration and DBT (MLO view) to ABUS registration.

6.4.4 Finite Element Analysis

The constraints or boundary conditions for each external skin node are applied to the base DBT FE model. These boundary conditions are used as input to the FEA solver program, Optistruct, to generate and solve the differential equations to describe the model deformation based on the defined constraints. The boundary conditions are the nodal displacements of the external skin DBT mesh after skin deformation and marker corrections (if needed) subtracted from the nodal coordinates after being rigidly registered (or registered to the nipple when applicable) to the ABUS volume. The FEA is performed as a non-linear quasi-static analysis in a single step. The FEA was performed on a Windows 10 Intel® Core™ i7 CPU speed of 2.80 GHz with 8 GB RAM and it takes approximately 30-60 minutes (dependent on model size/complexity) to complete.

6.4.5 Lesion Registration

After FEA is performed, the COM of lesions from the FEA-DBT model and the base FE ABUS model are determined. A lesion correlation algorithm determines if lesions are matched based off distances between COM, d_{COM} , being within a 25 mm distance ($d_{COM} \leq 25$ mm). The lesion correlation algorithm also determines if lesions overlap and the distance between the overlap of corresponding lesions, d_o , if lesions do not overlap. In our previous study that dealt with phantoms with multiple simulated lesions, we restricted the value of the d_o and used it as part of corresponding lesion criteria. In this study, we do not use d_o as part of correlation criteria but as supplemental information for a radiologist to aid in validating the registration.

Previous studies, for deformable registration using FEM from breast MR to mammography CC views have shown mean registration errors between 10 - 20 mm⁹². Additionally, from consulting with a radiologist (Dr. Marilyn Roubidoux) on this study we determined that 25 mm

was an acceptable bound, considering that DBT lesions appear elongated due to poor axial resolution.

A radiologist verifies all results and views the original images from an in-house developed GUI software routine to show corresponding masses. The radiologist fills out a form to evaluate the performance of the algorithm, image quality using the external markers, segmentation quality of lesions, and any additional information that is necessary. This evaluation form can be found in the Appendix.

6.5 Results

There were up to 7 total masses to be evaluated out of 5 patient datasets that were imaged in both the DBT (CC and MLO views) followed by a complete ABUS exam. An overview of subject criteria and additional findings from the study is summarized in Table 6.4. There is up to 7 matched lesions as one patient dataset (Subject ID 7) was a case where 4 masses were seen in reconstructed DBT CC view. However, for this subject only 3 masses were found in reconstructed ABUS views and 2 in reconstructed DBT MLO views.

Table 6.4: Subject and lesion demographics. Compressed thickness is based on the DBT (CC view)
RA=Retroareolar, LOQ= Lower Outer Quadrant, UOQ= Upper Outer Quadrant, LIQ= Lower Inner Quadrant,
UIQ= Upper Inner Quadrant. A=Anterior depth P=Posterior depth M=Middle MP=Middle to Posterior depth
*Indicates a mass has components of fibrocystic change, stromal fibrosis, and usual ductal hyperplasia

Subject ID	Lesion ID	Compressed Thickness (mm)	Quadrant/Depth	BI-RADS Density (Suspicion)	Lesion Type (Size)	Additional Findings
1	1	59.9	RA/A	Extremely Dense (4A)	Fibroadenoma (13 mm)	Two additional fibroadenomas (ABUS)
2	2	48.1	LOQ/P	Extremely Dense (4A)	Papilloma (8 mm)	Dilated Ducts (ABUS)
3	3	52.2	UOQ/M	Scattered Areas (4C)	Invasive Ductal Carcinoma (16 mm)	n/a
4	4	65.3	LOQ/MP	Scattered Areas(4B)	Fibroadenoma (10 mm)	n/a
5	5	70.2	UIQ/MP	Scattered Areas (4)	Fibroadenoma (13 mm)	Four lesions shown in DBT (CC view) images only 3 found in ABUS, and 2 in DBT (MLO view)
	6		LIQ/M		Fibroadenoma (6 mm)	
	7		RA/A		Other* (4 mm)	

6.5.1 Validation of deformable registration of DBT (CC view) mapped to ABUS

For DBT (CC view) to ABUS registration, 5 patients were imaged, and 7 masses were identified between image sets. An overview of the results for deformable registration of the DBT (CC view) to ABUS is illustrated in Table 6.5, where the various marker combinations are compared to a rigid registration. Using the deformable mapping technique without marker analysis there is up to 2.6 times improvement over rigid registration. Using the deformable mapping technique with marker analysis there is up to 4.8 times improvement over rigid registration. Using the deformable mapping technique without external marker analysis, all 7 lesions were matched with a mean d_{COM} of 17.2 ± 4.3 mm. Using the deformable mapping technique with external marker analysis (best marker analysis cases), all 7 lesions were matched with a mean d_{COM} of 11.0 ± 4.9 mm.

Table 6.5: Deformable registration results compared to rigid registration for various marker combinations based on resulting d_{COM} values for DBT (CC view) mapped to ABUS. For Lesion ID #4, the lateral marker “G” (see Figure 6.1(b)) was not seen in resulting ABUS views due to ABUS view misalignment therefore cases using 4 and 7 markers were not evaluated. For retroareolar lesions marker analysis using 1 marker is not evaluated. Best d_{COM} values are reported in bold.

Lesion ID #	Rigid d_{COM} (mm)	Deformable Registration d_{COM} (mm)						
		Number of Markers used in Analysis						Best using Marker Analysis
		0	1	3	4	6	7	
1	14.7	11.9	n/a	7.2	18.5	3.2	5.5	3.2
2	21.1	19.6	21.9	18	20.9	20.1	21.2	18
3	37.4	14.3	15.5	20.9	n/a	12.5	n/a	12.5
4	11.1	14.7	13.6	8.4	8.3	10.9	11.4	8.3
5	31	20.2	13.4	20.4	17.6	21.8	18.8	13.4
6	30.8	23.3	16.8	19.1	16.9	14.9	13.6	13.6
7	37.6	16.7	n/a	24.5	23.1	7.9	8.22	7.9
Mean	26.2	17.2	16.20	16.9	17.6	13	13.1	11.0
σ	10.7	4.0	2.50	6.6	5.1	6.6	6.0	4.9

A paired t-test and a signed Wilcoxon ranks tests of the d_{COM} 's was performed to compare the best marker analysis cases to the rigid registration values and resulted in p-values of 0.004 and 0.016. Thus, indicating statistical improvement in lesion d_{COM} using the deformable method in comparison to a rigid registration. A paired t-test and a signed Wilcoxon ranks tests of the d_{COM} 's were performed to compare the deformable case without marker analysis to rigid registration and resulted in p-values of 0.06 and 0.08, indicating that the null hypothesis cannot be rejected. A paired t-test and a signed Wilcoxon ranks tests of the of d_{COM} 's were performed to compare the deformable case without marker analysis to the deformable case using marker analysis (best marker analysis cases) and resulted in p-values of 0.001 and 0.016; thus, showing a significant improvement in lesion d_{COM} using external fiducial markers within the deformable mapping method.

6.5.2 Validation of deformable registration of DBT (MLO view) mapped to ABUS

An overview of the results for registration of the DBT (MLO view) to ABUS is illustrated in Table 6.6 where they are compared to a rigid registration. Using the deformable mapping technique, we see up to 5 times improvement over rigid registration. Using the deformable mapping technique without external fiducial markers all 4 of the 6 lesions were matched within correlation bounds, a resulting mean d_{COM} of 19.6 ± 11.3 mm from all 6 lesions. Using the deformable mapping technique with the use of external fiducial markers (best marker analysis case), all 6 lesions were matched with a mean d_{COM} of 12.3 ± 4.8 mm.

Table 6.6: Deformable registration results compared to rigid registration for various marker combinations based off resulting d_{COM} values for DBT (MLO view) mapped to ABUS. For Lesion ID #4, the lateral marker ‘‘G’’ (see Figure 6.1 (a) Ultrasound camisole for ABUS imaging (b) External fiducial marker locations (denoted by A-G) shown for marker placements on the left breast(b)) was not seen in resulting ABUS views due to ABUS view misalignment therefore cases using 4 and 7 markers could not be evaluated. For Lesion ID 7, was not seen in reconstructed DBT (MLO view) and therefore could not be registered due to lack on anterior compression.

Lesion ID #	Rigid d_{COM} (mm)	Deformable Registration d_{COM} (mm)							Best using Marker Analysis
		Number of Markers used in Analysis							
		0	1	3	4	6	7		
1	7.8	3.9	n/a	12.7	16.1	8.6	11.2	8.6	
2	43.9	33.9	33.7	26.12	27.6	18.6	14.8	14.8	
3	31	26.7	10.8	21.5	n/a	9.04	n/a	9.04	
4	92.9	19.7	24.1	22.8	18.9	22.3	22	18.9	
5	48.5	24.5	23.4	20.1	19	17.1	15.6	15.6	
6	35.6	9.1	16.0	11.3	10.7	6.8	8.3	6.8	
7	n/a	n/a	n/a	n/a	n/a	n/a	n/a	n/a	
Mean	44.8	21.6	16.2	19.1	18.5	13.7	14.4	12.3	
σ	28.1	8.7	2.50	5.9	6.1	6.4	5.2	4.8	

A paired t-test of the d_{COM} and a signed Wilcoxon ranks tests were performed to compare the best marker analysis case to the rigid registration values and resulted in p-values of 0.03 and 0.06; thus, indicating significant improvement based off the t-test and that the null hypothesis cannot be rejected based off the Wilcoxon test. A paired t-test and a signed Wilcoxon ranks tests

of the d_{COM} 's were performed to compare the deformable case without marker analysis to rigid registration and resulted in p-values of 0.08 and 0.03, respectively. A paired t-test and a signed Wilcoxon ranks tests was performed on the d_{COM} values to compare the deformable case without marker analysis to the deformable case using marker analysis (best marker analysis cases). These tests resulted in p-values of 0.12 and 0.15; indicating that the null hypothesis cannot be rejected. However, for this case, it should be noted that the number of matched lesion improved from 4 to 6 within the specified bounds thus, showing improvement with using marker analysis with the deformable mapping method.

6.5.3 Elastic Modulus Sensitivity Analysis

A sensitivity analysis was performed on the deformable models without using marker analysis by varying the Young's Moduli using the base, maximum, and minimum values as described in Table 6.2. These values are used to calculate the registration d_{COM} 's for the DBT to ABUS sets, by varying the lesion material properties (benign or malignant), fat, and glandular tissues. These were performed for benign and malignant lesion material properties with variation in the Young's Moduli for adipose and glandular tissues for the DBT (CC view) mapped to ABUS using the deformable mapping method without marker analysis. The results (d_{COM}) using the variation of material properties for adipose, lesion (benign), and glandular tissues is shown in Figure 6.8 based on the base E values shown in Table 6.1 and the minimum and maximum E values shown in Table 6.2.

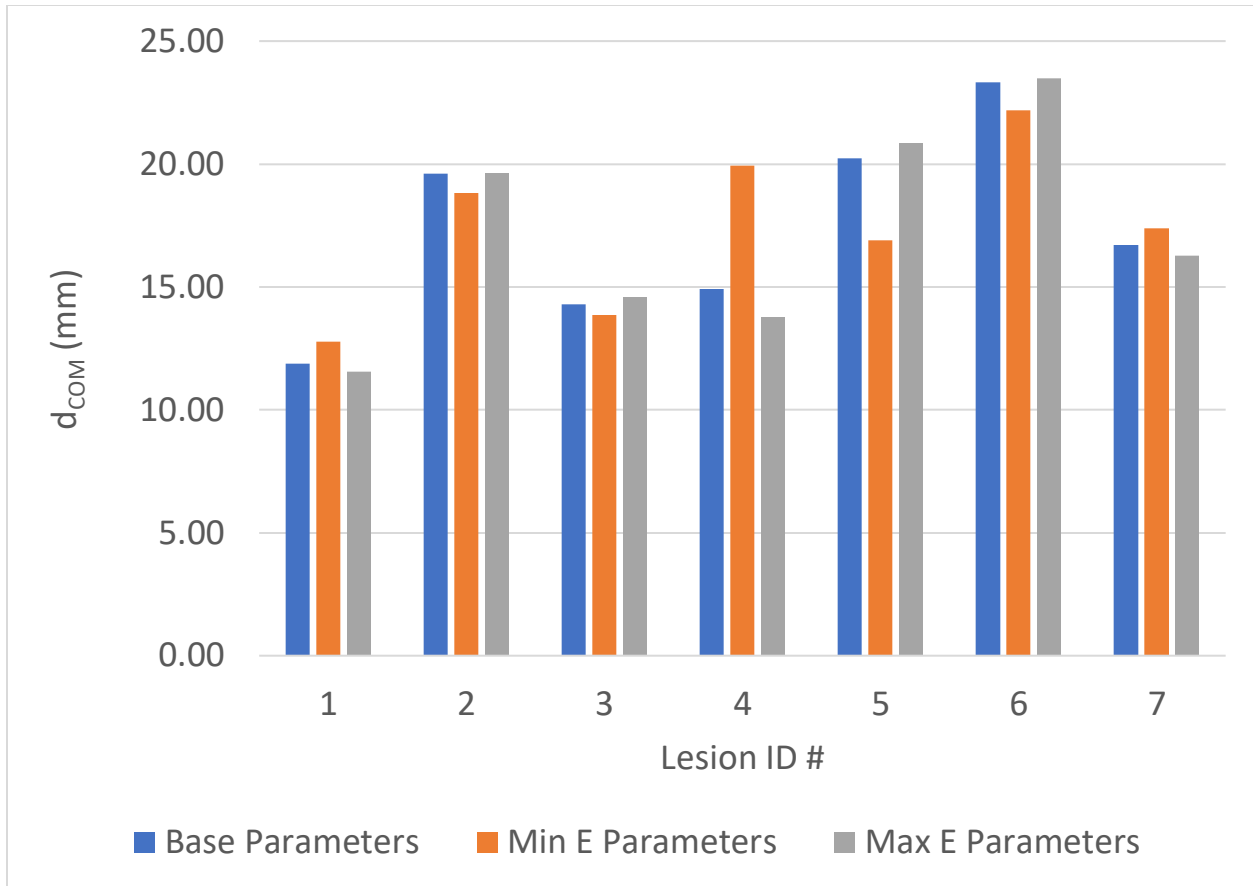


Figure 6.8: Sensitivity Analysis of variations in Young's Moduli, E , for registered d_{COM} for DBT (CC view) mapped to ABUS using the deformable mapping technique without marker analysis. Base values for E for lesion (benign), glandular tissue, and adipose tissue are shown in Table 6.1. The minimum and maximum E values for these tissues are shown in Table 6.2.

Assuming material properties of a malignant lesion, the results (d_{COM}) using the variation of material properties for adipose, lesion (malignant), and glandular tissues is shown in Figure 6.9 based on the base E values shown in Table 6.1 and the minimum and maximum E values shown in Table 6.2. For most lesions, there is not a significant difference in lesion d_{COM} as a result of the variation in material properties. However, Lesion ID's 4, 5, and 6 show d_{COM} differences up to 6 mm in the varied cases.

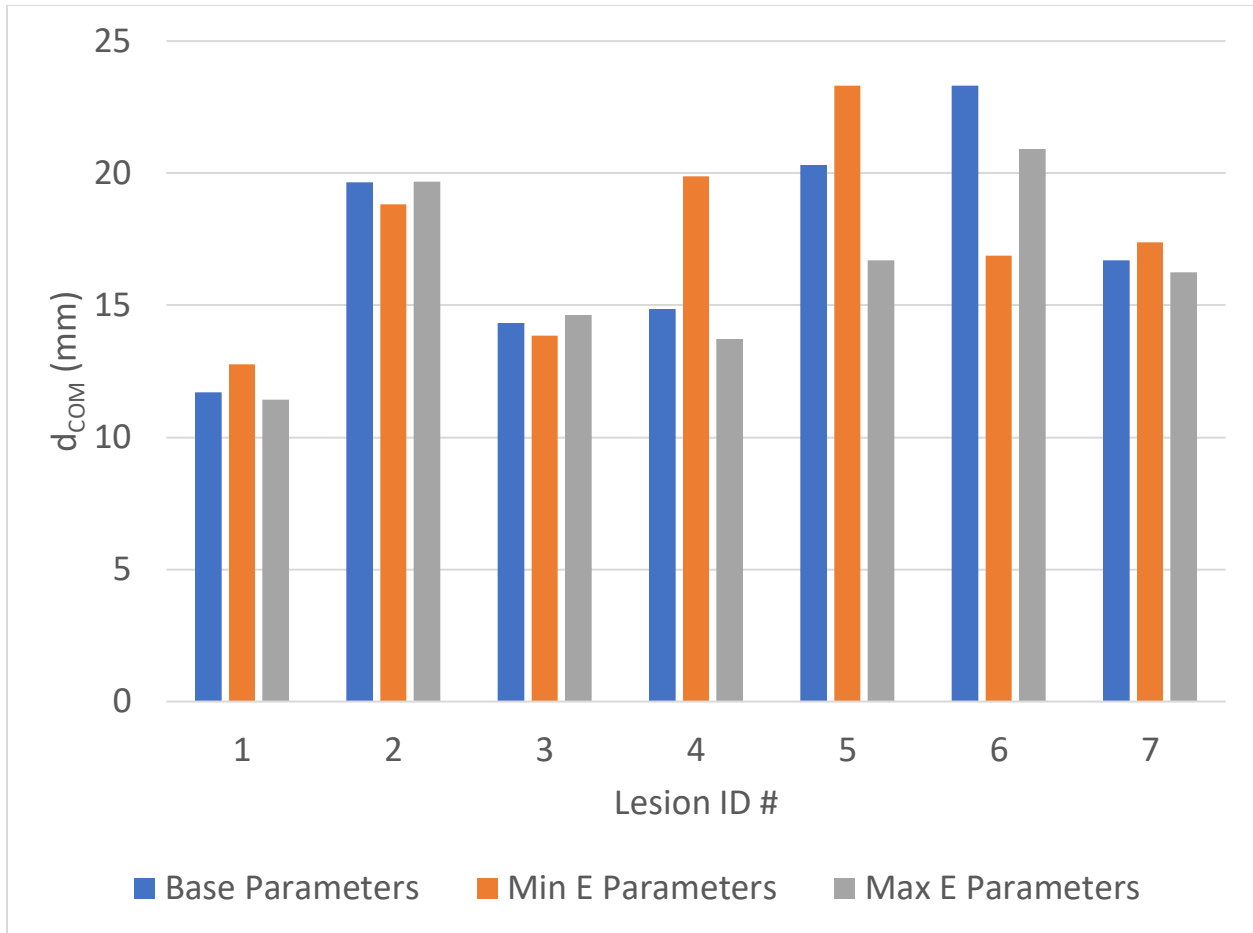


Figure 6.9: Sensitivity Analysis of variations in Young's Moduli, E , for registered d_{COM} for DBT (CC view) mapped to ABUS using the deformable mapping technique without marker analysis. Base values for E for lesion (malignant), glandular tissue, and adipose tissue are shown in Table 6.1. The minimum and maximum E values for these tissues are shown in Table 6.2.

6.5.4 Algorithm Optimization Study

An optimization study was performed on Subject ID #4 (see Table 6.4) to determine the effect on resulting d_{COM} and algorithm run time. The Subject ID #4 (Lesion ID #4) dataset was chosen because the subject had the largest breast volume which would cause for increased runtimes for the FEA within the algorithm. Two cases were tested to be compared against the base case to show differences in using the deformable mapping method without external marker analysis for DBT (CC view) to ABUS registration. Case 1 uses all the same parameters except uses a less discretized meshing scheme by using the HyperMesh function “divide by nearest

diagonals” instead of the default “divide midpoint to triangular”. Case 2 resamples the segmented DBT volumes to a 0.3 mm length, 0.3 mm depth, and 1 mm slice thickness rather than the default resampling of 0.2 mm length, 0.2 mm depth, and 1 mm slice thickness. Results (d_{COM}) are shown in Table 6.7. These results indicate no change in lesion d_{COM} and reduction in run time by a factor of 2, approximately.

Table 6.7: Variation in d_{COM} and FEA run time varying meshing parameters in Case 1 and resampling rates in Case 2 in comparison to the base values

Case	d_{COM} (mm)	FEA run time (minutes)
Base	14.7	25
1	14.9	15
2	14.7	14

6.6 Discussion

A novel deformable registration method has been described for providing a one-to-one correlation between corresponding lesions between two common DBT views (CC and MLO) to ABUS images based on 5 patient datasets and up to 7 lesions. For both analyzed cases there was a significant improvement in lesion d_{COM} in comparison to rigid registration using the deformable mapping method. This study extends upon our previous works by validating the algorithm to relate corresponding lesions on real patient datasets.

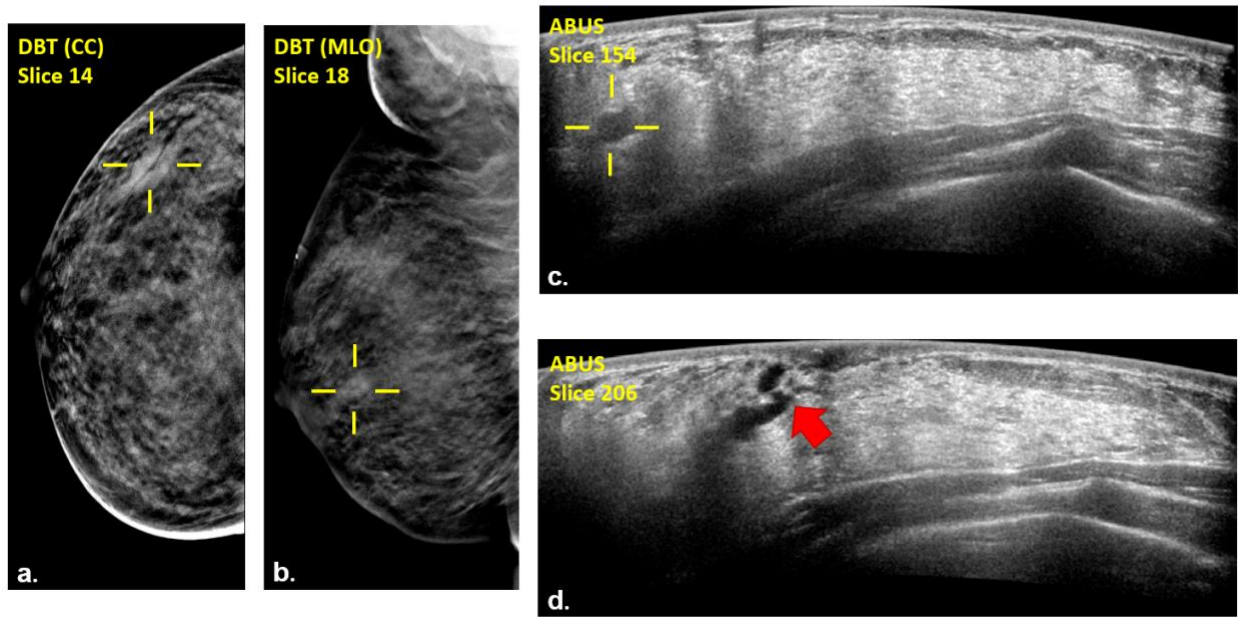


Figure 6.10: Registration results for Subject ID=2 Lesion ID=2 extremely dense breast tissue with presence of dilated ducts (a) registered lesion in DBT (CC view) (b) registered lesion in DBT (MLO view) (c) registered lesion in an ABUS image slice (d) presence of dilated ducts seen in a ABUS slice; These dilated ducts extended from ABUS Slices 180-215

We believe this method will be helpful for the one-to-one correlation of breast lesions and especially for women with dense breasts and multiple masses. Subject 2 of the study had very dense breast tissue and dilated ducts that can make it a more difficult case for a radiologist to find the corresponding mass between the DBT and ABUS modalities as shown in Figure 6.10. Additionally, since x-ray imaging has lower sensitivity for the imaging of dense breasts, ABUS imaging may find additional masses that are not seen in the DBT images as shown for Subject 1 (see Table 6.4). Therefore, this method would be especially helpful to ensure that a mass seen in DBT is registered to the correct lesion in ABUS.

Likewise, for the case with multiple masses (Subject ID=5), the deformable registration algorithm was able to register and differentiate 3 of the 4 total masses. The fourth mass was 4 mm in length in its widest dimension and could not be differentiated from other ultrasound structures and artifacts. However, 3 lesions were differentiated and matched using the

deformable mapping algorithm using the CC view as shown in Figure 6.11. Since the third lesion was superficial in-depth and located more anteriorly, the lack of compression anteriorly caused it to not be differentiable from other glandular structures in the DBT (MLO view).

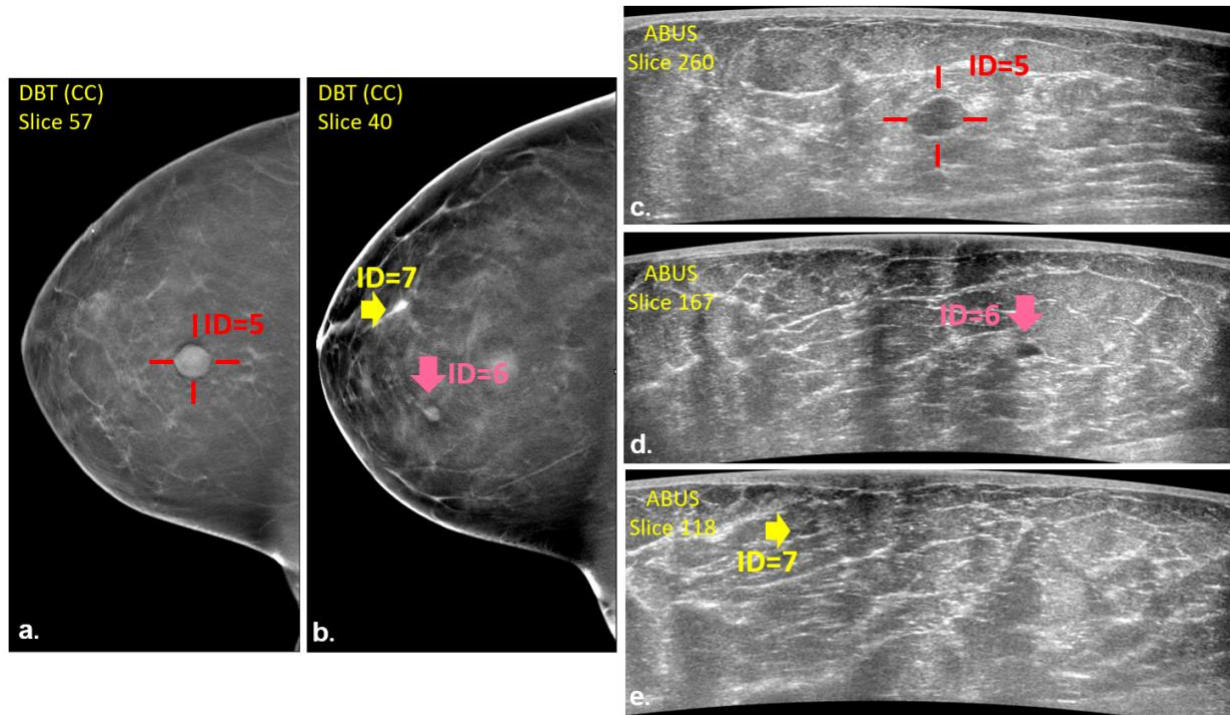


Figure 6.11: Corresponding lesions of multiple breast masses based on deformable registration results (a) a DBT (CC view) image slice showing Lesion ID=5 (b) a DBT (CC view) image slice showing Lesion ID=6 (red arrow) and Lesion ID=7 (yellow arrow) (c) the corresponding ABUS slice for Lesion ID=5 (d) the corresponding ABUS slice for Lesion ID=6 (e) the corresponding ABUS slice for Lesion ID=7

Based on the sensitivity analysis between material properties, the largest variation in d_{COM} values based on changes in Young's moduli are shown for Lesion ID's 4 and 5 using material properties of a benign lesion as shown in Figure 6.8. Both lesions are from subject's who have scattered breast densities where the masses are located mid-to-posterior in depth. Similarly, the largest variation in resulting d_{COM} based on changes in Young Moduli are shown for Lesion ID's 4,5, and 6 using the material properties for a malignant lesion as shown in Figure 6.9. Here we see that using the minimum E values as described in Table 6.2 have the largest variation increasing the d_{COM} for Lesion's 4 and 5 but the inverse effect for Lesion ID 6. This may indicate

that lesion depth can have an effect on the d_{COM} values. From these two figures, it can be observed that for the two cases of high breast density (Subjects ID's 1 and 2) that there was not much variation in resulting d_{COM} values with changes in material properties which may be attributed to the abundance of dense breast tissue.

This study uses two statistical metrics, paired t-test and signed Wilcoxon ranks tests, to determine if lesion d_{COM} was significantly improved using the deformable technique in comparison to a rigid registration. In our previous study³⁴, we only used t-tests to authenticate improvement of d_{COM} using the deformable case with and without external fiducial markers. However, we realize that due to the small sample size a normal distribution cannot be verified in order to use this test. Therefore, we decided to also include results from a non-parametric test (signed Wilcoxon ranks test) that is not based on a specific distribution in order to also evaluate the improvement in d_{COM} . There were several instances, when one statistical test indicated that there was significant improvement in d_{COM} ($p \leq 0.05$) and the other did not. This is caused due to underlying differences in how p-values are calculated between the two statistical tests based off their respective differences in methodology.

Various marker combinations are tested and their corresponding d_{COM} results are compared. Overall results from Table 6.5, show that for DBT (CC) to ABUS registration marker analysis is not needed in order for lesions to be within correlation bounds ($d_{COM} \leq 25$ mm). Corresponding, p-values based on both statistical tests show significant improvement using the deformable method with markers vs. without. Best marker results are shown for the use of 6 external markers. Using 1 external marker, was not performed for retroareolar breast masses. This is because the closest identifiable location is the nipple. A nipple correction is already being accounted for (if needed) by the algorithm. Therefore, modulating the next marker nearest to this

lesion will result in worse results since it is only correcting for that specific region in the breast. Using 1 marker for deformable analysis showed improved d_{COM} results for only Lesion ID 5. Similarly, for DBT (MLO) to ABUS registration as shown in Table 6.6, larger marker combinations (6 markers or greater) showed the largest improvement in d_{COM} results. Based on these results, we recommend that if marker analysis is being used, that at least 6 markers are needed to be placed at the indicated areas for the most optimal d_{COM} result.

Additionally, this methodology would work best if used adjunct to a computer-aided detection (CAD) program in order to detect breast masses and with a fully-automated segmentation program to segment those detected masses. In this study, masses were detected by the eye of a single viewer and segmented using semi-automated techniques. If the mass was not obvious, a radiologist was consulted in order to determine the lesion location and if the semi-automated program did not segment the masses sufficiently, manual segmentation was performed.

One limitation to this registration technique is the fact that it registers DBT images to ABUS images and cannot do the inverse of registering ABUS images to DBT (FEA to deform the ABUS image to DBT). The latter would be helpful in the cases where additional ABUS findings can potentially indicate where in the DBT volume a lesion may be present (e.g. Subject 1 who had two additional masses found in the ABUS images with high breast density). Another limitation is that this technique only registers to the AP ABUS volume. Since up to 3 sweeps of the breast (central, medial, and lateral margins with some overlap) are taken in a typical ABUS exam for women with larger breasts the single AP sweep may not be enough to ensure full breast coverage. In the case of large breasts, the fusion of the ABUS volumes could be useful and would allow the deformable method to register to the stitched ABUS view. M. Costa

demonstrated the stitching of ABUS volumes using a homographic transfer model to render a stitch panorama view for areas within the AP and lateral ABUS views¹⁶¹.

Another limitation to this study is that it was not tested on lesions within the axillary tail and some lesions within the areolar region can be missed in ABUS images due to shadowing caused inferior to the nipple. Providing sufficient coupling to the axillary region is difficult for the large ABUS transducer. Often times HHUS is used in addition to ABUS to ensure there is sufficient imaging of the axillary region. Nipple offset pads could be used to reduce artifacts caused by the nipple in ABUS images to decrease signal fall out so that that retroareolar masses can be seen.

Additionally, using the external markers can be troublesome when translated into the clinic, especially with the use of the ABUS camisole. This can be minimized by assisting the patient in putting on the camisole, ensuring that enough time (at least 5 minutes) has passed before putting on the camisole after markers are glued, and by indicating locations on the breast (e.g. by using a washable marker) to reapply the external fiducial markers in case the external marker position is compromised. Additionally, if ABUS images are segmented to separate fat and glandular tissues. These segmentations could be used to provide internal landmarks for the deformable mapping algorithm which could allow less reliance for the methodology on external marker locations.

Criteria for volunteers in this study was restricted to women with masses within the breast (excluding axillary region) and masses ≥ 5 mm in size. Therefore, the validity of this technique was not tested on smaller masses or masses located in the axillary regions. Additionally, the algorithm was tested on a small sample size (5 subjects). Therefore, more patients would need to be scanned using this method to increase statistics. A larger sample size would allow for a more in-depth analysis to be performed to determine which marker combination yields optimal registration results based on lesion location and potentially breast density. It could also allow for

the investigation of the effect of lesion depth and density in vary the material properties used in the deformable registration analysis. Although this algorithm was tested on a small sample size, it should be noted that other studies were published that have used FEM based registration techniques to register lesions from breast MRI to mammography (CC and/or MLO views) that used 4 to 6 cases ^{86,90,162}, 10 cases ^{85,163}, 14 cases ⁸⁷, and 79 cases ⁸⁸.

6.7 Conclusions

This work presents a validated deformable registration technique using FEM to register breast lesions between DBT and ABUS 3D image volumes. The results show 13 registrations between two common DBT views mapped to ABUS based on 5 patient datasets. This indicates this method could be a useful tool to aid in the detection and characterization of breast cancers and lesions between modalities. Our method is to our knowledge the first to show a direct correlation between DBT mapped to ABUS on patient datasets. The method uses nodal displacements in the FEA instead of simulating plate compressions which can be more expensive in computer run time. We assigned various material properties to the fibroglandular, adipose, and lesions to evaluate the differences in lesion accuracy and saw that in most cases there was no difference in the resulting d_{COM} . However, there were a few cases where there were larger differences in the resulting d_{COM} , which may be a result of breast density and lesion depth. Using the deformable mapping method, there is up to 5 times improvement in d_{COM} in comparison to a rigid registration and the use of external skin markers can aid in registration results. Future work will further validate this technique on a larger patient data set, where we can investigate which deformable analysis combination produces higher registration accuracy. We can also perform a more in depth analysis on dependence of the accuracy of the technique on breast density and lesion location. For the easy/obvious cases (e.g. one mass in a fatty breasts) this method would

only be beneficial in saving a radiologist time in navigating between the two 3D image volumes. However, for more difficult cases (e.g. multiple masses, dense breasts) this technique can be extremely useful in aiding a radiologist in determining corresponding lesion locations between DBT and ABUS images which can aid to the early detection of cancer masses.

6.8 Acknowledgements

This work was supported in-part by a research grant (15-PAF04328) from GE Global Research, the Glenn Knoll Fund from the University of Michigan Nuclear Engineering and Radiological Sciences department, and by a University of Michigan Rackham Research Grant. Crystal A. Green is supported by the Science, Mathematics and Research for Transformation (SMART) Scholarship for Service Program (HQ0034-16-C-0008). The authors would like to thank Taaron Foote and Darius Fadanelli of Altair for their assistance in FEA. Special thanks to the sonographers (Brittany Ramaut, Janelle Tucker, Rebekah Jacobson, Leila Barakat, Erica Tolkinen, and Poppy Cilibraise) for recruitment and sonography imaging of patient volunteers. Special thanks to supervisors Diane Martel and Terri Pirochta of the Breast Imaging Department at the University of Michigan for study oversight and guidance. Special thanks to the mammography technologists (Angie Pequet, Brittany Ramaut, Mary Brown, Carrie Farnung, Barbara Schaedler, Rachel Bonaminio, and Julie McClothin) in the Breast Imaging Department at the University of Michigan Medical Center for DBT imaging and study logistics. The authors would like to thank Mary Burton for maintaining all records of the IRB-approved patient study and consenting all volunteers. The authors would like to thank Ted Lynche for the TPE material used to create the external fiducial markers. The authors would also like to thank Susan Zalucha of Susan's Custom Sewing for camisole design and generation.

Chapter 7

Conclusions and Future Works

7.1 Summary of Contributions

The work presented in this dissertation has demonstrated the efficacy and the diagnostic potential of using novel deformable registration methods to relate breast masses between 3D x-ray (DBT and bCT) and 3D ultrasound (ABUS) breast modalities. For the phantom studies involved in this dissertation, this technique showed an improvement in lesion registration using external fiducial markers, including having more lesions within the specified correlation bounds (Chapter 3 and Chapter 5 ($d_{COM} \leq 15$ mm) and Chapter 4 ($d_{COM} \leq 25$ mm)). Based on the IRB-approved patient study, this technique shows an improvement in lesion registration with the use of external fiducial markers. However, external markers are not mandatory in order to establish whether lesions correspond within the specified correlation bounds ($d_{COM} \leq 25$ mm). Ultimately, the work in this dissertation demonstrates that this deformable mapping tool can be helpful for a radiologist by reducing the time spent navigating through 3D image volumes and provides a higher confidence between regions of interests between two modalities, especially for more difficult clinical cases, such as women with dense breasts or multiple lesions. Chapter 6 illustrates a validation study tested on clinical datasets for DBT and ABUS images using the deformable registration methodology. A similar IRB-approved study is needed to quantify the

effectiveness of this method for bCT to DBT and bCT to ABUS registration based on the deformable registration algorithm's preliminary phantom results described in Chapter 5.

7.2 Conclusions and Limitations

7.2.1 Efficacy of Deformable Mapping Technique to relate lesions between DBT and ABUS images (Phantom Study)

Compressible multi-modality breast phantoms were used for studies in Chapter 3 and Chapter 4 to provide the foundation of the deformable registration algorithm for DBT to ABUS lesion registration. In Chapter 3, two breast phantoms (A and B) with varying stiffness properties are used to show the relationship of breast lesions using the FEM for DBT (CC view) to ABUS registration. This technique applies nodal displacements to the compressed DBT model in order to deform the breast for registration to the ABUS model using FEA. Without using external markers for Phantom A, results showed a mean lesion d_{COM} of 6.8 ± 2.8 mm. Using external markers, the average d_{COM} improved to 4.9 ± 2.4 mm. For Phantom B without external markers, the average lesion d_{COM} of 9.7 ± 3.5 mm improved to 8.5 ± 4.0 mm using marker analysis. Additionally, this study had more restrictive correlation bounds than used in Chapter 4 and Chapter 6 (patient study) of 15 mm ($d_{COM} \leq 15$ mm) vs 25 mm ($d_{COM} \leq 25$ mm). To our knowledge, this was the first published work to show registration between lesions in DBT and ABUS breast images. This study shows an improvement in the overall lesions' correlation with the use of external fiducial markers during FEA.

The work presented in Chapter 4 performs deformable registration for the DBT (CC view) to ABUS view and incorporates deformable registration for the DBT (MLO view) for ABUS registration. The matching criterion was increased to 25 mm ($d_{COM} \leq 25$ mm) from the 15 mm ($d_{COM} \leq 15$ mm) used in Chapter 3 in order to account for translation of this technique to patients,

where the phantom is not representative of breast heterogeneity and complexity. For mapping of DBT (CC view) to ABUS without markers, the mean d_{COM} was 13.6 ± 6.3 mm. With markers the mean d_{COM} was 12.8 ± 6.0 mm. Without markers, 14 of 18 lesions were matched within correlation bounds and with markers this improved to 17 of 18 lesions matched. This resulted in a p-value of 0.04 (paired T-test) which shows a significant improvement in lesion registration. However, a p-value of 0.06 (Wilcoxon signed-rank test) indicated that not enough evidence is available to suggest that d_{COM} improves using external markers. For mapping of DBT (MLO view) to ABUS without markers, the mean d_{COM} was 9.3 ± 2.8 mm and which worsens to the mean d_{COM} was 12.3 ± 5.8 mm using external markers. Without markers, 8 of 18 lesions were matched which improved to 17 of 18 lesions matched. Based on these phantom studies, we see the largest improvement using external fiducial markers. A proof-of-concept study will need to be performed to validate this technique and specify its potential use to specific breast regions.

There are several limitations to these studies based on the fact that the phantoms are not anthropomorphic in that they used homogenous material and exhibit linear elastic behavior, whereas breasts are heterogeneous and exhibit non-linear elastic behavior. Additionally, the phantoms used in Chapter 3 and Chapter 4 do not contain an axillary attachment making it further difficult to resolve the implementation of this technique for lesions within the axillary region. Additionally, not having this axillary attachment may also contribute to the phantom's linear elastic behavior under compression.

7.2.2 Efficacy of Deformable Mapping Technique to relate corresponding lesions between bCT to ABUS and DBT images (Phantom Study)

Chapter 5 describes the deformable mapping methodology for relating simulated bCT phantom images to DBT and ABUS images. The same phantom was used for this study as in Chapter 4 that contained 20 lesions. Anterior-to-posterior plate compression is simulated on the bCT model using FEA to relate the compressed bCT model to ABUS image volume. Additionally, CC and MLO compression is simulated on the bCT model using FEA to relate the compressed bCT model to the DBT image volumes.

For bCT to ABUS registration, without markers, 13 out of 20 lesions were matched and the mean d_{COM} was 8.6 ± 3.0 mm. With markers, 20 lesions were matched and the mean d_{COM} improved to 4.8 ± 2.4 mm. This resulted in p-values of 0.01 (paired T-test) and 0.02 (Wilcoxon signed-rank test); thus, indicating a significant improvement using external markers within the analysis. For registration of bCT to DBT (CC view), without using markers, 9 out of the 18 lesions were matched and the mean d_{COM} was 11.6 ± 2.0 mm. With markers, all 18 lesions were matched and the mean d_{COM} was 5.0 ± 2.2 mm. This resulted in p-values of 0.00001 (paired T-test) and 0.004 (Wilcoxon signed-rank test); thus, indicating a significant improvement using external markers within the analysis. For registration of bCT to DBT (MLO view), without using markers, 9 out of the 18 lesions were matched and the mean d_{COM} was 8.2 ± 3.1 mm. With markers, all 18 lesions were matched and the mean d_{COM} was 4.7 ± 2.5 mm. This resulted in p-values of 0.002 (paired T-test) and 0.01 (Wilcoxon signed-rank test) thus indicating a significant improvement using external markers within the analysis.

Similar to Chapter's 3 and 4, a major limitation to the bCT studies described in Chapter 5 is that the breast phantom has numerous inconsistencies in comparison to a real breast as described

in the previous section. These results indicate that the methodologies could be of potential use after validation with patient volunteers. Therefore, this method still needs to be validated with an IRB-approved proof of concept study for bCT to DBT and bCT to ABUS registration. Additionally, plate compression involved in this method is highly taxing in terms of computational time which may not make using this method applicable for medical centers that do not have access to super-computing capabilities. The time it took to run bCT to ABUS registration is approximately 13 hours, for bCT to DBT (CC view) registration approximately 30 hours, and bCT to DBT (MLO view) registration approximately up to 45 hours. These high runtimes can be reduced by using parallel processors using super computers and larger graphics processing units.

Additionally, this method could be translated to uncompressed ultrasound CT for breast imaging provided by the Delphinus Medical Technologies (Novi, MI) for direct use to relate to DBT imaging. This will be discussed further within this chapter in Section 7.3.4 in Future Works.

7.2.3 Design and Implementation of ABUS Camisole to Restrict Breast Motion

In Chapter 2, information was provided about the development and implementation of using an ABUS camisole to restrict breast motion during ABUS imaging which acquires multiples views for a complete ABUS examination. The overall results of this camisole design ensured that there was not degradation to the ultrasound beam penetration depth and minimal distortion. Several fabrics were tested, and a stretchable nylon mesh fabric was found to be superior. The camisole was tested on ten normal volunteers and was found to be helpful in restricting breast motion during ABUS imaging. Clinical translation of this camisole was used in the IRB-approved study discussed in Chapter 6.

7.2.4 Implementation of Deformable Mapping Technique to relate corresponding lesions between DBT and ABUS images (Patient Study)

Chapter 6 discusses the results of the deformable mapping technique applied to clinical patient data sets and describes the minor modifications in the algorithm to relate corresponding lesions between DBT (CC and MLO views) to ABUS in clinical datasets. Up to 7 lesions were assessed from 5 patient datasets. This study compares the deformable registrations metrics (with and without using marker analysis) to a rigid registration and shows there was up to 5 times improvement using the deformable method over rigid registration.

For DBT (CC view) mapped to ABUS resulting p-values of 0.01 (paired T-test) and 0.02 (Wilcoxon signed-rank test); thus, indicating a significant improvement in d_{COM} using the deformable mapping algorithm in comparison to rigid registration. Further analysis showed that using marker analysis has an insignificant affect in the number of total matched lesions in comparison to using the deformable mapping method without using marker analysis for lesion registration improvements. Thus, showing that markers increase the efficacy of the registration for DBT to CC views, however markers are not needed to ensure matched lesions are within correlation bounds.

For DBT (MLO view) mapped to ABUS resulting p-values of 0.03 (paired T-test) and 0.06 (Wilcoxon signed-rank test) thus significant improvement based on the t-test using the deformable mapping algorithm in comparison to rigid registration. Improvements using the registration method ranged from 16% improvement over rigid registration to up to 5.2 times improvement. Further analysis showed that using marker analysis has a significant affect in the number of total matched lesions in comparison to using the deformable mapping method without using marker analysis for lesion registration improvements. Thus, showing that using marker

analysis is significant in improving lesion registration and the total number of matched lesions within correlation bounds based on the deformable mapping technique.

With such a small sample size, conclusive results on which breast regions the deformable registration has the most effect cannot be determined. However, based on the results presented, all breasts quadrants saw improvement using the deformable registration in comparison to a rigid registration. Lesions that had greater than twice the registration improvement included lesions in the retroareolar, medial, and upper outer breast regions for DBT (CC view) to ABUS registrations. For MLO view to ABUS registration, all breast mass locations except for one retroareolar case showed at least 2 times improvement over rigid registration.

Overall, it was mostly observed that when testing various ranges of material properties (i.e. Young's modulus) there was not a significant difference in resulting d_{COM} . This is advantageous as it shows the method is mostly independent of material parameters which can widely vary. However, as shown for Lesions ID's 4 and 5 further analysis into whether or not a lesion's depth and breast density may explain the variation in d_{COM} using the varied elastic properties. To our knowledge, there are not any other studies that register breast lesions between two compressed states as shown in this study. However, uncompressed breast studies imaging with MRI or bCT often simulate the breast compression of mammography using FEM's. A study by Hsu. et al. validated compression using a breast phantom by varying the relative Young's modulus for the glandular, fat, and skin tissues of a breast and found it had a significant impact on the deformation of the breast under mammographic plate compression, even more so for less dense breasts.¹⁴⁶ This may indicate why those lesions (Lesion ID's 4, 5 and 6) show high differences. However, since this study applies FEA using nodal displacements to deform the DBT to ABUS

and not simulating the plate compression/decompression of the DBT image volume we suspect that this may reduce the mechanical property dependence.

Among the patient data sets there were cases of high breast density and multiple lesions within a breast. These are cases for which the algorithm would have the most impact. This deformable registration algorithm is also useful in reducing the time needed for a radiologist to navigate between large 3D image volumes. These results demonstrate the potential of the utility of the deformable registration technique to relate lesions between DBT and ABUS image volumes. Another advantage to this technique is that the FEA runs off nodal displacements the run times are about 30-60 minutes depending on breast volume. Thus, making the technique feasible to translate into the clinic. Although commercial FEA solvers are used within this dissertation, the methods can be translated to in-house or open source FEM packages for implementation.

A limitation of this technique is the fact that the deformable mapping algorithm relates DBT images to ABUS and not relate ABUS images to DBT. The latter would be helpful in the cases where additional ABUS findings can potentially indicate where in the DBT volume a lesion may be present, especially for dense breasts. Another limitation is that this technique only registers to the AP ABUS volume. Since up to 3 sweeps of the breast (AP, medial, and lateral margins with some overlap) are taken in a typical ABUS exam for women with larger breasts, the single AP sweep is not enough to ensure full breast coverage. Stitching of the ABUS volumes could be useful for this case in which then this method could use to register to the stitched ABUS view. M. Costa showed stitching of ABUS volumes using a homographic transfer model to render a stitch panorama view for areas within the AP and LAT views.¹⁶¹ Additionally, Chang et al. used a simple sum of absolute block-mean difference based registration technique to stitch 3D

ultrasound for women in pendant positioning and using ultrasound CT acquisition and validated the algorithm on 25 experimental cases.¹⁶⁴ Nonetheless, stitching ABUS views would be very difficult due to the issues of alignment, a transducer tracking type of algorithm could be helpful in multi-view ABUS stitching to improve this alignment.

Criteria for volunteers in this study was restricted to women with masses within the breast (excludes axillary region) and masses (≥ 5 mm) in size. Therefore, the validity of this technique was not tested on smaller masses and masses located in the axillary regions. Additionally, the algorithm was tested on a small sample size (5 patient volunteers) therefore more patients would need to be scanned using this method to determine more accurate statistics. There was difficulty to recruit women to participate in the study due to the emotional distress associated with having a biopsy procedure and needing to come in before that procedure to receive additional imaging. We believe this software would be great to be used in adjunct to a computer aided diagnostic software in order to allow for automated detection of a breast lesion. Additionally, automated segmentation techniques would improve the pre-processing segmentation steps that can be directly fed into the algorithm for FE model generation.

7.3 Future Works

7.3.1 Extensive Proof-of-Concept study for DBT to ABUS Deformable Registration

As discussed previously, a more extensive study would be needed to gain proper statistics to determine the validity of this method with patient volunteers. With a more extensive study, we can more definitively quantify the improvement using marker analysis and determine which marker combination can provide optimal results based on lesion location/depth. The study results shown in Chapter 6 are based on up to 7 lesions from 5 clinical datasets. Although only 5 subjects were imaged to validate this technique, other groups who used FEM based methods for

lesion registration for breast MRI and mammography (CC and/or MLO views) also had small sample sizes between 4 to 6 subjects.^{86,90,162}.

With larger patient datasets some of the parameters that can be investigated are the quantity and location of the external fiducial markers and the effects on the deformable registration based on lesion location (breast quadrant), and depth. Additionally, more datasets will allow a more in depth analysis to determine if this technique improves a radiologist's ability to better characterize lesions in dense breasts.

7.3.2 Proof of Concept Study for bCT to DBT and bCT to ABUS Deformable Registration

Although promising results for bCT to DBT registration and bCT to ABUS registration are shown in Chapter 5, an IRB approved proof-of-concept study is still needed with patient volunteers to determine the validity of the technique. Within this study, investigations of quantity and location of fiducial markers can be assessed based on lesion location. Also, studies into the modeling the plate compression such as the friction coefficient can be analyzed along with a sensitivity analysis on the effects of using different material properties during the simulated plate compressions. A surprising finding within the patient study for DBT to ABUS registration showed that overall the lesion correlations (d_{COM}) are independent of changes in material properties (e.g. Young's Moduli). Since this study does not model the actual decompression and plate compression of the breast for the deformable registration. I would hypothesize that modeling these mechanics would allow for more substantial changes to be seen in registration using material properties. Therefore, for the deformable registration techniques described in Chapter 5 that do simulate actual plate compression on the bCT model to register to ABUS and DBT models, I would expect changes in material properties to have a more significant impact based on results shown by a study by Hsu et al. that varied the elastic modulus of breast tissues

in a phantom model and found it had significant impact on the deformation of the breast under mammographic plate compression.¹⁴⁶ Additionally, improved patient specific FE models can be generated with the isotropic spatial resolution provided in bCT imaging which can possibly show improvement in the deformable registration by accounting for breast heterogeneity.

7.3.3 Relating Multiple ABUS Views into Singular 3D Volume

As mentioned in Chapter 6, one limitation to the deformable mapping algorithm is the fact that the DBT volume can only be registered to the AP ABUS projection. For women with larger breasts, the AP ABUS view may not acquire complete coverage for the breast when imaged. In these cases, creating a singular 3D ABUS volume based on all the views would be helpful. The use of FEMs could be used to apply deformation to the views based on the nipple location and relating the external fiducial markers to one another. There would need to be a correction for the medial and lateral views since the transducer is angled and positioned in a different orientation. We believe the use of the ABUS camisole can help reduce the amount of correction due to these effects by restricting breast motion.

Modeling the different views to create a solitary image volume could be simulated in FEA by modeling plate compression or by applying nodal displacements based on the nipple and/or marker locations. Additionally, if a lesion or other internal breast structures are seen between views this could provide an additional landmark in order to stitch views into one image volume. This is advantageous as the markers are only located at the breast surface and depth information can better relate internal breast structures.

7.3.4 Deformable Registration to relate corresponding lesions from ABUS to DBT

As mention in Chapter 6, a limitation to the deformable registration algorithm described here is that it relates from DBT to ABUS and not ABUS to DBT. This can be especially limiting

for women with dense breasts. For dense breast cases where additional lesions are found in ABUS, the ability to map to a ROI within the original DBT location could be helpful to improve lesion characterization. The main reason this was not done is because ultrasound imaging can provide many artifacts and acoustic shadowing which makes it difficult to segment dense breast structures. Additionally, the breast surface is not as well defined as in DBT imaging and ultrasound has increased false positive findings^{13,14,165}. There are also limited publications in automated segmentation methods to segment the dense breast structures from 3D ultrasound systems. Complete breast segmentation of the ABUS volume is essential for FEA to perform on the ABUS model for registration to DBT. Improvements in ABUS segmentation could allow for this technique to be implemented for ABUS to DBT registration.

Likewise, 3D ultrasound CT ultrasound systems (e.g. Delphinus Medical Systems) like bCT also acquire breast images in the prone geometry (unlike the ABUS supine geometry). Acquiring ultrasound images in the pendant configuration can allow for direct 3D models to be created using FEM of the breast in an uncompressed state. Therefore, the deformable registration method described in Chapter 5 could be implemented to use FEM to simulate plate compression on the uncompressed 3D ultrasound CT model to register with a reference DBT volume; thus, directly correlating and characterizing a lesion from ultrasound CT to DBT. This would be beneficial as ultrasound can decipher between solid and cystic lesions and that these determine and display ultrasound attenuation and ultrasound speed of sound images in addition to ultrasound B-mode reflection images. The disadvantage of this technique is the markers used within this study cannot be used since the adhesive used to attach the markers to the breast is not waterproof. Additional work would need to be completed to find an acceptable marker to be used between the two image sets if external markers would like to be analyzed for improved registration.

7.4 Final Thoughts

This dissertation presents validated methodologies to investigate the accuracy and performance of a novel deformable registration technique to relate corresponding lesions between 3D (DBT and bCT) x-ray and 3D ultrasound images. The methods described can save a radiologist time in navigating 3D volumes and provide higher confidence in relating the corresponding masses between the image sets. Implementation of this methodology could improve a radiologist's characterizations of breast lesions, reduce negative biopsies, reduce patient callbacks and could be a useful tool for the early detection of breast cancers based on the direct localization of corresponding lesions between 3D x-ray and 3D ultrasound breast images.

Appendix

Clinical Protocol for ABUS Camisole Evaluation Study

1. Research assistant will setup ABUS Machine in designated area. Research assistant will input the anonymized patient identification information into Invenia workstation. This includes putting a new ABUS mesh panel on ABUS transducer.
2. The study coordinator, will consent the patient with the specified forms
3. Research assistant will fit the patient for their camisole based on taking a band measurement (under the breast). Patient will try on camisole to ensure fit
4. Research assist will denote fiducial marker areas on the patient's breast with a magic marker attach the external markers at those locations.
5. Ultrasound technologist will position patient and ensure that the ultrasound camisole is placed over the breast with the external markers underneath the camisole.
6. Ultrasound technologist will place ultrasound lotion over the camisole. Performs the first anterior to posterior, AP, scan for the left breast. If needed a second scan of the lateral margins of the breast will be performed. If needed a third scan of the medial portions of the breast will be performed. Additional scans can be added to ensure complete coverage.
7. Repeats Step 6 for the right side of the breast.
8. Research assistant or Ultrasound technologist helps patients remove excess gel/lotion and markers from breast with alcoholic wipes.

9. Research assistant will dispose of the used Invenia mesh panel, camisoles, and external markers from patient
10. Research assistant will save patient images on USB drive on Invenia, breakdown Invenia device, and perform any other cleaning involved with the room used for ABUS images.
11. Patient redresses and signs form for gift card for participation in research study.

Procedures for Developing External Fiducial Markers

1. Spread glass beads across a baking mini-cupcake baking sheet.
2. Place 2-4 glass beads in each baking compartment. (Note: Use sufficient spacing between each glass bead as they will need to be cut into separate squares for each marker)
3. Place the thermoplastic elastomer clear gel over glass beads in each baking compartment.
4. Cover the top of the baking sheet in aluminum foil. (Note: Do not fold over the sides so that air bubbles can escape)
5. Place in vacuum oven and heat to 130° C. (Note: Do NOT Preheat oven and then add sample tray. TPE must heat with oven to avoid voids within material.)
6. Once oven reaches set temperature point turn on vacuum to reduce oven pressure to 1.5-2 inHg.
7. Close vacuum once pressure point is reached. Allow to sit at set temperature and pressure point for one hour.
8. Turn off the oven temperature to allow it too cool down back to room temperature (Do Not release vacuum) this takes several hours to cool.
9. Release vacuum and take out samples.
10. Cut samples into square pieces with the glass bead as the center point.

Clinical Protocol for Proof-of Concept Study

1. ABUS Machine setup in Ultrasound Imaging Room. She will input the anonymized Patient identification information into Invenia workstation. This includes putting a new ABUS mesh panel on ABUS transducer.
2. Patient consented by study coordinator, or research assistant, and will verify which breast is being biopsied (right or left).
3. Research assistant will fit the patient for their camisole based on taking a band measurement (under the breast). Patient will try on camisole to ensure fit. The camisole will not be used for x-ray imaging.
4. Research assistant will use a washable magic marker to designate areas on the breast. Research assistant will attach the external fiducial markers to the breast at those locations using a commercial body adhesive. And place Tomospot sticker over each marker.
5. Patient volunteer will be given a gown/robe and will be escorted to mammography room to prepare for the DBT examination.
6. Research assistant will give mammography technologist the anonymized information for Patient study to input into the DBT machine.
7. Mammography technologist will image the patients' breast with DBT in the CC view and DBT in the MLO view. If attached markers come off during imaging they will be reattached before next image phase is performed.
8. Patient will robe and be escorted to the ABUS imaging room (Research room). External fiducial markers will remain attached to the breast.

9. Patient will put on the ultrasound camisole above her breasts while sitting up on the bed. The patient will then lay down and with assistance of the research assistant or the ultrasound technologist for the camisole to be lowered across the breast for ABUS imaging.
10. Ultrasound technologist will place ultrasound lotion over the camisole. The technologist will perform the first anterior to posterior, AP, scan of the indicated breast. A second scan of the lateral margins of the breast will be performed adding lotion if needed. Next, a third scan of the medial margins of the breast will be performed with added lotion if needed. Additional scans can be added to ensure complete coverage.
11. Research assistant will cut the camisole off the patient from behind. Research assistant or Ultrasound technologist will help patient remove excess gel/lotion and markers from breast with towels. The patient will wash her breast to remove the magic marker ink.
12. Research assistant will dispose of the used Invenia mesh panel, camisoles, and external markers from patient.
13. Research assistant will save patient's ultrasound images on an USB drive on the Invenia, shut down Invenia device, and perform any other cleaning involved with the room used for ABUS images.
14. Patient dresses and signs form for gift card for participation in research study.

Parameters used for MiViewer Program

Table A.1 shows the parameter settings used for Lesion segmentation using the MiViewer program. It was found that two combination of parameters were most helpful in using the software, shown for Run 1 and Run 2 in Table A.1. For use of this software please contact the University of Michigan CAD laboratory^y.

Table A.2: Parameter setting used to Run MiViewer program on DBT and ABUS images

	<i>Run 1</i>	<i>Run 2</i>
<i>Blur Kernel</i>	0.2	0.2
<i>Diffusion Conductance</i>	2	2
<i>Diffusion Timesteps</i>	8	8
<i>Sample Width</i>	3	3
<i>Ellipse Radius</i>	0.8	1
<i>Sample Radius</i>	-1	-1
<i>Level-Set 1 Timesteps</i>	150	150
<i>Level-Set 2 Timesteps</i>	4	4
<i>Level-Set 3 Timesteps</i>	10	10
<i>Level-Set 4 Timesteps</i>	5	5
<i>Main Propagation Scaling</i>	0.9	1.2
<i>Main Advection Scaling</i>	4	4
<i>2D Propagation Scaling</i>	0.9	1.2
<i>2D Advection Scaling</i>	4	4
<i>2D Time-Steps</i>	20	25
<i>curvscale</i>	-1	-1
<i>Zblur1</i>	0.2	0.2
<i>timestep</i>	0.045	0.045
<i>gradchopoff</i>	1200	1200
<i>gradblursigma</i>	0	0
<i>holerad1</i>	2	2
<i>holerad2</i>	2	2
<i>gradchop</i>	0.5	0.5
<i>gaussianthresh</i>	0.7	0.7
<i>priorsigma</i>	4.5	4.5
<i>printseg</i>	1	1
<i>printgrad</i>	0	0

^y <https://medicine.umich.edu/dept/radiology/research/basic-radiological-sciences-brs/cad-research-laboratory>

HyperMesh Scripting Optimization

Tcl/Tk scripting is used in order to create input files to run HyperMesh commands by a command prompt. Using HyperMesh the input files are generated to run for the specific FEA problem. For more information, on these built in commands for HyperMesh please see the following scripting documentation^z as this entire process was automated using a MATLAB script. The script is used to build the models and export the 3D parameters to be analyzed to compute things such as the center of mass (COM) based on the nodal information. Additionally, information on how to use HyperMesh to generate the input files needed for FEA for Optistruct and ABAQUS can be found in the HyperMesh Solver Interfaces documentation^{aa}.

Each segmentation should be housed in its own folder within the parent directory in order for the base FEM model file to be generated. An example of these directories are shown in Figure A.1. The original DICOM images should be in a separate folder within that directory (in Figure A.1 that folder is denoted as “Base_DCM”). Folder ‘1’ indicates the folder that contains the DICOM segmentation files for the lesion. If multiple lesions are used each lesion is separated (e.g. Folder “2” and Folder ‘3’). Mk1, Mk2, Mk3 etc. folders show the separate marker DICOM files. Folders for the segmented fat, glandular tissue, skin should also be housed as a separate folder in the directory.

^z

https://altairhyperworks.com/hwhelp/Altair/2017/help/hm_ref_guide/topics/chapter_heads/commands_and_functions_scripts_r.htm

^{aa} https://altairhyperworks.com/hwhelp/Altair/2017/help/hm/hmbat.htm?HyperMesh_solver_interfaces_tutorials.htm

Name	Date modified	Type	Size
1	10/25/2018 10:24 ...	File folder	
Base_DCM	11/5/2018 10:52 AM	File folder	
Fat_Segmented	10/25/2018 10:28 ...	File folder	
GlandularTissue_Segmented	10/25/2018 10:27 ...	File folder	
Mk1	10/25/2018 10:24 ...	File folder	
Mk2	10/25/2018 10:25 ...	File folder	
Mk3	10/25/2018 10:25 ...	File folder	
Mk4	10/25/2018 10:26 ...	File folder	
Mk5	10/25/2018 10:26 ...	File folder	
Mk6	10/25/2018 10:27 ...	File folder	
Mk7	10/25/2018 10:28 ...	File folder	
Skin_Segmented	10/22/2018 9:39 PM	File folder	

Figure A.1: Example of parent directory that houses all segmentation folders and base DICOM folder for base FE model generation

The Morfeus software is run on the segmented DICOM data to produce a resulting STL file. Therefore, all folders containing segmented data will have a Morfeus generated STL file. The STL file is the 3D object surface mesh based on the segmented DICOM information. These STL files are read into the HyperMesh program in order to mesh the base model. Base model generation can be described in the following pseudo-code for creating a BASE DBT file using HyperMesh shown in Figure A.2. The base templates contains the necessary components identifies and material properties for the run.

```

IMPORT Base template for Deformable Mapping Program
READ STLs of DBT Lesions
READ STLs for DBT Markers
READ STLs for Skin, Fat, and Glandular Tissues
Mesh DBT Lesions interior and assign Lesion material property
Mesh DBT Markers interior and assign Lesion material property
Determine if DBT Lesions and are inside or outside of glandular tissue or fatty tissue
Store location of DBT Lesions
Determine if DBT Markers and are inside or outside of skin or fatty tissue
Store location of DBT Markers
If DBT Lesion is inside glandular tissue
    Mesh Glandular internal glandular tissue and external DBT Lesion
    Assign Glandular material property
ELSE
    Mesh Glandular internal glandular tissue
    Assign Glandular material property
END IF
If DBT Lesion is inside fatty tissue
    IF DBT Markers are also within fatty tissue
        Mesh internal fatty tissue and external DBT Lesion(s), and DBT (markers)
        Assign Fatty material property
    END IF
ELSE DBT Lesion is not inside fatty tissue
    Mesh internal fatty tissue and external DBT (markers)
    Assign Fatty material property
END IF
If DBT Markers are interior to skin mesh but exterior to the Fat surface
    Mesh Skin internal tissue, External Fatty tissue, and external DBT Markers
    Assign Skin material property
ELSE
    Mesh Skin internal tissue and External Skin
    Assign Skin material property
END
EXPORT Base file model file in Home Directory

```

Figure A.2: Pseudo-code describing base FE model generation used within the deformable mapping algorithm

GUI Interface for relating corresponding lesions

A graphical user interface, GUI, was developed in order for a radiologist to view corresponding masses based on the deformable mapping registration results. The interface uses the slice information from the segmented DICOM files between modalities to determine lesion locations in the original DICOM images. It then takes the deformable mapping results to know which lesions are matched to the corresponding modality lesion. A user can pick from a drop down menu the Lesion ID number and the GUI will automatically change to the corresponding image slices for DBT and ABUS imaging.

First a user needs to indicate the specific parent folders that houses the base directory through a menu for each modality as shown in Figure A.3 for DBT and ABUS.

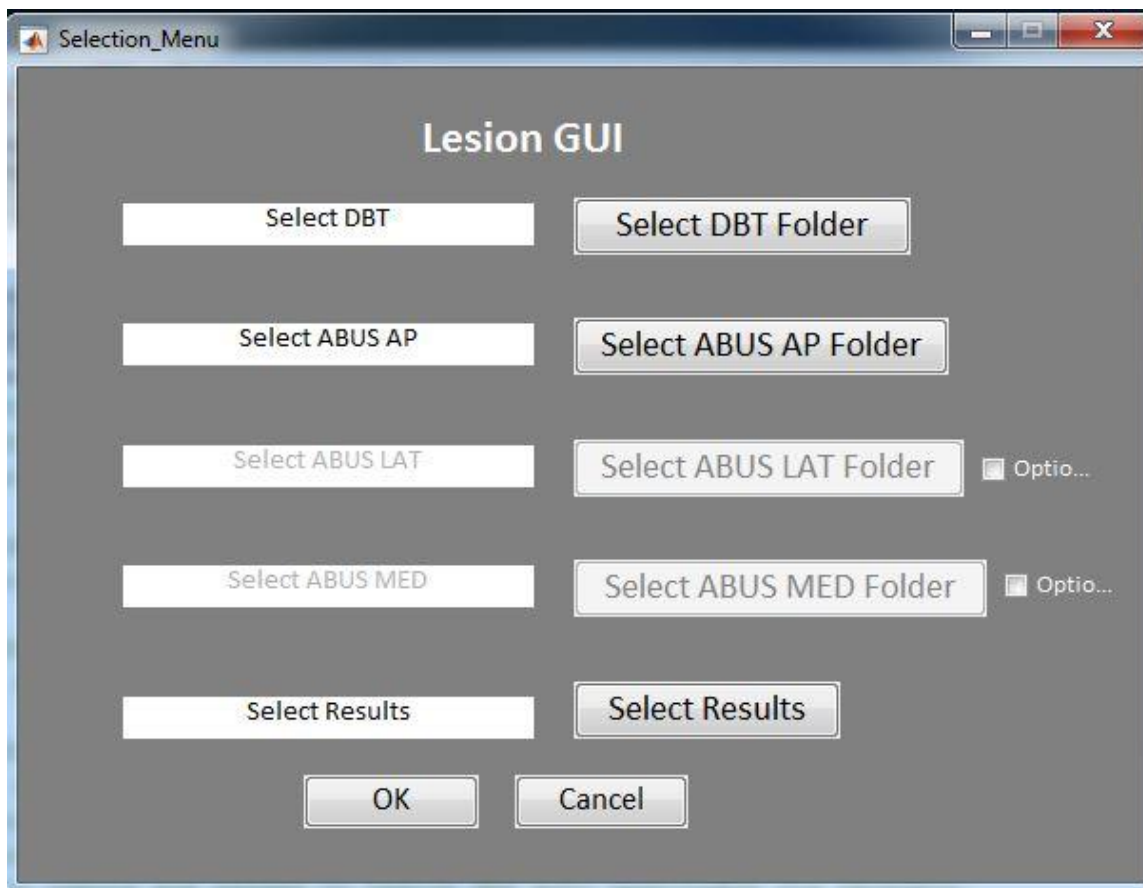


Figure A.3: Selection Menu for GUI interface

Additionally, the lateral (LAT) and medial (MED) ABUS views can also be shown. However, the deformable mapping program only registers to the ABUS AP view. Therefore, lesions will not be located to the LAT and MED views but can still be viewed as supplemental information. The resulting MATLAB file from the deformable mapping program will contain the folder information needed for the GUI to know which lesion segmentation folders to look in. This file also contains the `dcom` values based off the algorithm results.

If only one mass was seen in corresponding views the User must select Lesion ID 1. Once the Lesion is displayed from the drop down menu the corresponding results can be viewed as shown in Figure A.4. A red cross hair will be shown on the middle slice for the corresponding lesions between views.

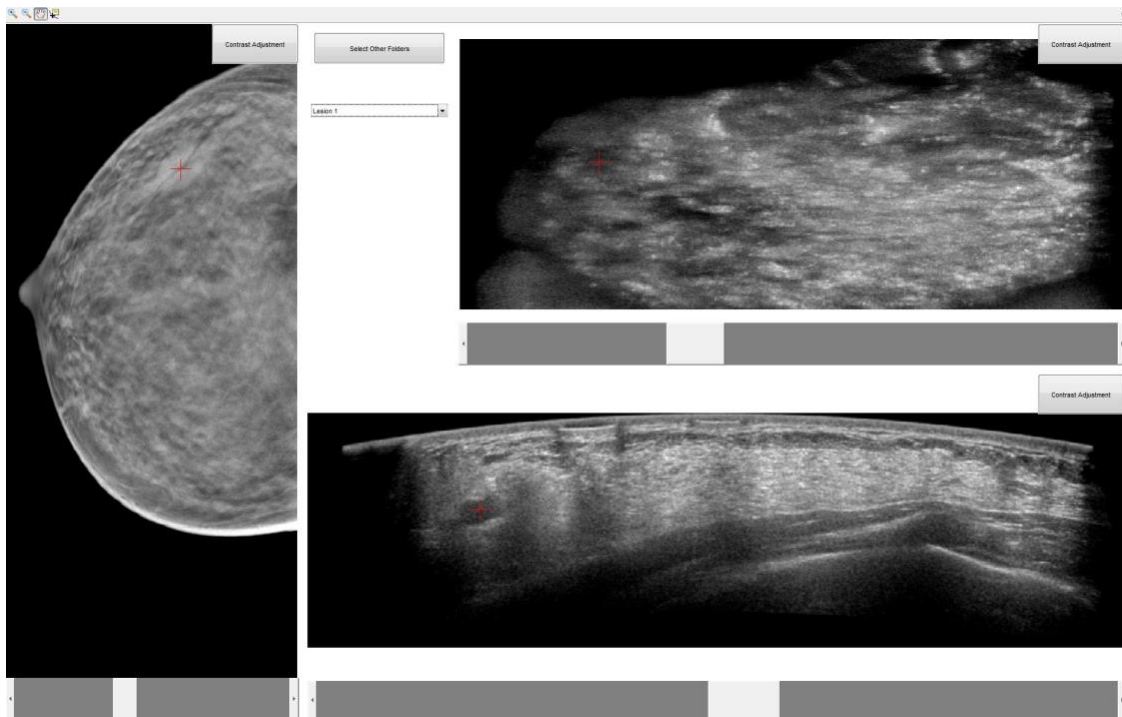


Figure A.4 GUI Viewer results for a corresponding mass between the DBT (CC view) and ABUS view indicated by the red cross hair.

The image window/level settings can be manually adjusted for the DBT and ABUS image views.

DBT/ABUS Study Radiologist Form

Patient

ID _____ Date _____

Radiologist Initials _____

	Yes	No	Additional Comments
DBT Image Quality			
Do the external fiducial markers affect the quality of DBT images?			
Can the lesion be clearly identified and is it sufficiently segmented?			
Are there any additional findings from the DBT images?			
ABUS Image Quality			
Do the external fiducial markers affect the quality of the ABUS images?			
Does the breast camisole affect the quality of the ABUS images?			
Can the lesion be clearly identified and is it sufficiently segmented?			
Are there any additional findings from the ABUS images?			
Comment on the image quality of the ABUS images in comparison to conventional ultrasound.			
Deformable Registration Algorithm	dCOM-CC=	dCOM-MLO=	
Does the algorithm correctly identify the corresponding lesion in the two modalities?			
Does the algorithm aid in lesion characterization between DBT and ABUS images?			

- 1) Do you have any recommendations for improving the display of the corresponding lesions in the ABUS and DBT images?
- 2) Is the distance between the corresponding lesions sufficient?
- 3) Do you have any suggestions for improving the interface for scrolling through the corresponding DBT and ABUS images?

Additional Comments:

ABUS Camisole Form

Patient ID _____

Date _____

Ultrasound Technologist/ Observer Initials _____

	Yes	No	Additional Comments
Were all external markers glued to breast before ABUS imaging?			
Did the glued external markers move when ultrasound gel/lotion is added over breast?			
Did the glued external markers move when patient puts on ABUS camisole?			
Was the camisole fitted to the breast?			
Does the camisole help restrict breast motion in comparison to if no camisole were not used?			
Do the external markers remain in the same position in between ABUS scans?			
Did the external fiducial markers have to be repositioned at any time during ABUS exam?			
Once breast camisole is removed were the external markers still in place?			

Additional Comments:

Bibliography

1. Siegel RL, Miller KD, Jemal A. Cancer statistics, 2018. *CA Cancer J Clin.* 2018;68(1):7-30. doi:10.3322/caac.21442.
2. Chlebowski RT, Kuller LH, Prentice RL, et al. Breast Cancer after Use of Estrogen plus Progestin in Postmenopausal Women. *N Engl J Med.* 2009;360(6):573-587. doi:10.1056/NEJMoa0807684.
3. Howlader N, Noone A, Krapcho M. SEER Cancer Statistics Review, 1975-2014. Table 4.13. https://seer.cancer.gov/archive/csr/1975_2014/. Accessed July 23, 2018.
4. Nelson HD, Fu R, Cantor A, Pappas M, Daeges M, Humphrey L. Effectiveness of breast cancer screening: Systematic review and meta-analysis to update the 2009 U.S. Preventive services task force recommendation. *Ann Intern Med.* 2016;164(4):244-255. doi:10.7326/M15-0969.
5. Siu AL. Screening for breast cancer: U.S. Preventive services task force recommendation statement. *Ann Intern Med.* 2016;164(4):279-296. doi:10.7326/M15-2886.
6. Gøtzsche PC, Nielsen M. Screening for breast cancer with mammography. *Cochrane Database Syst Rev.* 2009;(4). doi:10.1002/14651858.CD001877.pub3.
7. Buist DSM, Porter PL, Lehman C, Taplin SH, White E. Factors contributing to mammography failure in women aged 40-49 years. *J Natl Cancer Inst.* 2004;96(19):1432-1440. doi:10.1093/jnci/djh269.
8. Wilt TJ, Harris RP, Qaseem A, et al. Screening for cancer: Advice for high-value care from the American college of physicians. *Ann Intern Med.* 2015;162(10):718-725. doi:10.7326/M14-2326.
9. Bevers B, Anderson B, Bonaccio E, et al. Breast Cancer Screening and Diagnosis. *J Natl Compr Cancer Netw.* 2009;7(10):1060-1096. doi:10.1007/978-1-4939-1267-4.
10. Hendrick RE, Helvie MA. United States Preventive Services Task Force Screening Mammography Recommendations: Science Ignored. *Am J Roentgenol.* 2011;196(2):W112-W116. doi:10.2214/AJR.10.5609.
11. Kopans DB. Arguments against mammography screening continue to be based on faulty science. *Oncologist.* 2014;19(2):107-112. doi:10.1634/theoncologist.2013-0184.
12. Hendrick RE, Baker JA, Helvie MA. Breast cancer deaths averted over 3 decades. *Cancer.* February 2019. doi:10.1002/cncr.31954.
13. Berg WA. Rationale for a trial of screening breast ultrasound: American College of Radiology Imaging Network (ACRIN) 6666. *Am J Roentgenol.* 2003;180(5):1225-1228. doi:10.2214/ajr.180.5.1801225.
14. Kolb TM, Lichy J, Newhouse JH. Occult cancer in women with dense breasts: detection with screening US--diagnostic yield and tumor characteristics. *Radiology.* 1998;207(1):191-199. doi:10.1148/radiology.207.1.9530316.
15. Conway WF, Hayes CW, Brewer WH. Occult Breast Masses : Use of a Mammographic Localizing Grid for US Evaluation. *Radiology.* 1991;181(1):143-146. doi:10.1148/radiology.181.1.1653441.
16. Taylor KJW, Merritt C, Piccoli C, et al. Breast Examination to characterize breast masses. *Ultrasound Med Biol.* 2002;28(1):19-26. doi:10.1016/S0301-5629(01)00491-4.
17. Jackson V. The role of US in breast imaging. *Radiology.* 1990;177(2):305-311. doi:10.1148/radiology.177.2.2217759.
18. Ohuchi N, Suzuki A, Sobue T, et al. Sensitivity and specificity of mammography and

- adjunctive ultrasonography to screen for breast cancer in the Japan Strategic Anti-cancer Randomized Trial (J-START): A randomised controlled trial. *Lancet*. 2016;387(10016):341-348. doi:10.1016/S0140-6736(15)00774-6.
19. Wilczek B, Wilczek HE, Rasouliyan L, Leifland K. Adding 3D automated breast ultrasound to mammography screening in women with heterogeneously and extremely dense breasts: Report from a hospital-based, high-volume, single-center breast cancer screening program. *Eur J Radiol*. 2016;85(9):1554-1563. doi:10.1016/j.ejrad.2016.06.004.
 20. Giuliano V, Giuliano C. Improved breast cancer detection in asymptomatic women using 3D-automated breast ultrasound in mammographically dense breasts. *Clin Imaging*. 2013;37(3):480-486. doi:10.1016/J.CLINIMAG.2012.09.018.
 21. Sinha SP, Goodsitt MM, Roubidoux MA, et al. Automated Ultrasound Scanning on a Dual-Modality Breast Imaging System: Coverage and Motion Issues and Solutions. *J Ultrasound Med*. 2007;26(5):645-655. doi:10.7863/jum.2007.26.5.645.
 22. Sinha SP, Roubidoux MA, Helvie MA, et al. Multi-modality 3d breast imaging with X-ray tomosynthesis and automated ultrasound. In: *Proceedings of the 29th Annual International Conference of the IEEE EMBS*. ; 2007:1335-1338. doi:10.1109/IEMBS.2007.4352544.
 23. Emons J, Wunderle M, Hartmann A, et al. Initial clinical results with a fusion prototype for mammography and three-dimensional ultrasound with a standard mammography system and a standard ultrasound probe. *Acta radiol*. 2018;59(12):1406-1413. doi:10.1177/0284185118762249.
 24. Goodsitt MM, Chan HP, Hadjiiski L, LeCarpentier GL, Carson PL. Automated registration of volumes of interest for a combined X-ray tomosynthesis and ultrasound breast imaging system. *Lect Notes Comput Sci (including Subser Lect Notes Artif Intell Lect Notes Bioinformatics)*. 2008;5116 LNCS:463-468. doi:10.1007/978-3-540-70538-3_64.
 25. Kapur A, Carson PL, Eberhard J, et al. Combination of Digital Mammography with Semi-automated 3D Breast Ultrasound. *Technol Cancer Res Treat*. 2004;3(4):325-334. doi:10.1177/153303460400300402.
 26. Padilla F, Roubidoux MA, Paramagul C, et al. Breast Mass Characterization Using 3-Dimensional Automated Ultrasound as an Adjunct to Digital Breast. *Am Inst Ultrasound Med*. 2013;32(1):93-104. doi:10.7863/jum.2013.32.1.93.
 27. Lecarpentier GL, Goodsitt MM, Verweij S, Li J, Padilla F, Carson PL. Acoustic Performance of mesh compression paddles for a multimodality breast imaging system. *Ultrasound Med Biol*. 2014;40(7):1503-1511. doi:10.1016/j.ultrasmedbio.2013.03.014.
 28. Li J, Goodsitt MM, Padilla F, et al. Effect of a Gel Retainment Dam on Automated Ultrasound Coverage in a Dual-Modality Breast Imaging Ultrasound System. *J Ultrasound Med*. 2010;29(7):1075-1081. doi:10.7863/jum.2010.29.7.1075.
 29. Vaughan CL, Douglas TS, Said-Hartley Q, et al. Testing a dual-modality system that combines full-field digital mammography and automated breast ultrasound. *Clin Imaging*. 2016;40(3):498-505. doi:10.1016/j.clinimag.2015.11.024.
 30. Schulz-Wendtland R, Jud SM, Fasching PA, et al. A Standard Mammography Unit – Standard 3D Ultrasound Probe Fusion Prototype: First Results. *Geburtshilfe Frauenheilkd*. 2017:679-685. doi:10.1055/s-0043-107034.
 31. Suri J, Guo Y, Coad C, Danielson T, Elbakri I, Janer R. Image Quality Assessment via Segmentation of Breast Lesion in X-ray and Ultrasound Phantom Images from Fischer's

- Full Field Digital Mammography and Ultrasound (FFDMUS) System. *Technol Cancer Res Treat*. 2005;4(1):83-92. doi:10.1177/153303460500400111.
32. LeCarpentier GL, Goodsitt MM, Verweij S, Li J, Padilla FR, Carson PL. Acoustic performance of mesh compression paddles for a multimodality breast imaging system. *Ultrasound Med Biol*. 2014;40(7):1503-1511. doi:10.1016/j.ultrasmedbio.2013.03.014.
 33. Larson ED, Lee W-M, Roubidoux MA, et al. Automated Breast Ultrasound: Dual-Sided Compared with Single-Sided Imaging. *Ultrasound Med Biol*. 2016;42(9):2072-2082. doi:10.1016/j.ultrasmedbio.2016.05.001.
 34. Green CA, Goodsitt MM, Brock KK, et al. Deformable mapping technique to correlate lesions in digital breast tomosynthesis and automated breast ultrasound images. *Med Phys*. 2018;45(10):4402-4417. doi:10.1002/mp.13113.
 35. Green CA, Goodsitt MM, Lau JH, Brock KK, Davis CL, Carson PL. Evaluation of an Automated Deformable Mapping Technique with and Without External Fiducial Markers to Relate Corresponding Lesions in Digital Breast Tomosynthesis and Automated Breast Ultrasound Images. In: *Radiological Society of North America 2018 Scientific Assembly and Annual Meeting, November 25 - November 30, 2018, Chicago IL.* ; 2018. archive.rsna.org/2018/18005292.html.
 36. Green CA, Goodsitt MM, Lau JH, Brock KK, Davis CL, Carson PL. Deformable Mapping Method to Relate Lesions in Dedicated Breast CT Images to those in Automated Breast Ultrasound and Digital Breast Tomosynthesis Images. *Manuscr Submitt Publ*. 2019.
 37. Breast Cancer Resources | GE Healthcare Breast Density. GE Healthcare. <http://knowyourrisk.gehealthcare.com/en/resources>. Accessed April 2, 2019.
 38. All breasts are not the same. GE Healthcare. <https://www.gehealthcare.com/-/media/3bfa2856163e484096f8478ed7b533f9.pdf>. Published 2018. Accessed April 1, 2019.
 39. Sak MA, Littrup PJ, Duric N, Mullooly M, Sherman ME, Gierach GL. Current and Future Methods for Measuring Breast Density: A Brief Comparative Review. *Breast Cancer Manag*. 2015;4(4):209-221. doi:10.2217/bmt.15.13.
 40. D'Orsi C, Sickles E, Mendelson E, Morris E. ACR BI-RADS atlas, breast imaging reporting and data system. *Reston, VA Am Coll Radiol*. 2013.
 41. Boyd NF, Guo H, Martin LJ, et al. Mammographic Density and the Risk and Detection of Breast Cancer. *N Engl J Med*. 2007;356(3):227-236. doi:10.1056/NEJMoa062790.
 42. Yaghjian L, Colditz GA, Collins LC, et al. Mammographic breast density and subsequent risk of breast cancer in postmenopausal women according to tumor characteristics. *J Natl Cancer Inst*. 2011;103(15):1179-1189. doi:10.1093/jnci/djr225.
 43. Ho JM, Jafferjee N, Covarrubias GM, Ghesani M, Handler B. Dense breasts: A review of reporting legislation and available supplemental screening options. *Am J Roentgenol*. 2014;203(2):449-456. doi:10.2214/AJR.13.11969.
 44. Rodríguez-Ruiz A, Castillo M, Garayoa J, Chevalier M. Evaluation of the technical performance of three different commercial digital breast tomosynthesis systems in the clinical environment. *Phys Medica*. 2016;32(6):767-777. doi:10.1016/j.ejmp.2016.05.001.
 45. Rafferty EA, Park JM, Philpotts LE, Poplack SP, Sumkin JH. Digital Mammography and Breast Tomosynthesis Compared with Digital Mammography Alone : Results of a Multicenter, multireader trial. *Radiology*. 2013;266(1):104-113. doi:10.1148/radiol.12120674/-/DC1.

46. Friedewald SM, Rafferty EA, Rose SL. Breast cancer screening using tomosynthesis in combination with digital mammography. *JAMA*. 2014;311(24):2499-2507. doi:10.1001/jama.2014.6095.
47. Andersson I, Ikeda DM, Zackrisson S, et al. Breast tomosynthesis and digital mammography: A comparison of breast cancer visibility and BIRADS classification in a population of cancers with subtle mammographic findings. *Eur Radiol*. 2008;18(12):2817-2825. doi:10.1007/s00330-008-1076-9.
48. Destounis S V., Morgan R, Arieno A. Screening for dense breasts: Digital breast tomosynthesis. *Am J Roentgenol*. 2015;204(2):261-264. doi:10.2214/AJR.14.13554.
49. Lindfors KK, Boone JM, Nelson TR, Yang K, Kwan ALC, Miller DF. Dedicated Breast CT: Initial Clinical Experience. *Radiology*. 2008;246(3):725-733. doi:10.1148/radiol.2463070410.
50. Lindfors KK, H MP, Boone JM, et al. Dedicated Breast CT : The Optimal Cross Sectional Imaging Solution? *Radiol Clin North Am*. 2011;48(5):1043-1054. doi:10.1016/j.rcl.2010.06.001.
51. Kuzmiak C, Cole E, Zeng D, Tuttle L, Steed D, Pisano E. Dedicated Three-dimensional Breast Computed Tomography: Lesion Characteristic Perception by Radiologists. *J Clin Imaging Sci*. 2016;6(1):14. doi:10.4103/2156-7514.179428.
52. Nosratieh A, Yang K, Aminololama-Shakeri S, Boone JM. Comprehensive assessment of the slice sensitivity profiles in breast tomosynthesis and breast CT. *Med Phys*. 2012;39(12):7254-7261. doi:10.1118/1.4764908.
53. Kaphingst KA, Persky S, Lachance C. The potential role of dedicated 3D breast CT as a diagnostic tool: Review and early clinical examples Avic. *Breast J*. 2010;14(4):384-399. doi:10.1080/10810730902873927.Testing.
54. Leconte I, Feger C, Galant C, et al. Mammography and subsequent whole-breast sonography of nonpalpable breast cancers: The importance of radiologic breast density. *Am J Roentgenol*. 2003;180(6):1675-1679. doi:10.2214/ajr.180.6.1801675.
55. Mariscotti G, Houssami N, Durando M, et al. Accuracy of mammography, digital breast tomosynthesis, ultrasound and MR imaging in preoperative assessment of breast cancer. *Anticancer Res*. 2014;34(3):1219-1225.
56. Choudhery S, Axmacher J, Connors AL, Geske J, Brandt K. Masses in the era of screening tomosynthesis: Is diagnostic ultrasound sufficient? *Br J Radiol*. December 2018;20180801. doi:10.1259/bjr.20180801.
57. Giger ML, Inciardi MF, Edwards A, et al. Automated breast ultrasound in breast cancer screening of women with dense breasts: Reader study of mammography-negative and mammography-positive cancers. *Am J Roentgenol*. 2016;206(6):1341-1350. doi:10.2214/AJR.15.15367.
58. Brem RF, Tabár L, Duffy SW, et al. Assessing Improvement in Detection of Breast Cancer with Three-dimensional Automated Breast US in Women with Dense Breast Tissue: The SomoInsight Study. *Radiology*. 2015;274(3):663-673. doi:10.1148/radiol.14132832.
59. Rella R, Belli P, Giuliani M, et al. Automated Breast Ultrasonography (ABUS) in the Screening and Diagnostic Setting: Indications and Practical Use. *Acad Radiol*. 2018;25(11):1457-1470. doi:10.1016/J.ACRA.2018.02.014.
60. An YY, Kim SH, Kang BJ. The image quality and lesion characterization of breast using automated whole-breast ultrasound: A comparison with handheld ultrasound. *Eur J*

- Radiol.* 2015;84(7):1232-1235. doi:10.1016/J.EJRAD.2015.04.007.
61. Chang JM, Moon WK, Cho N, Park JS, Kim SJ. Radiologists' performance in the detection of benign and malignant masses with 3D automated breast ultrasound (ABUS). *Eur J Radiol.* 2011;78(1):99-103. doi:10.1016/J.EJRAD.2011.01.074.
 62. Jeh SK, Kim SH, Choi JJ, et al. Comparison of automated breast ultrasonography to handheld ultrasonography in detecting and diagnosing breast lesions. *Acta radiol.* 2016;57(2):162-169. doi:10.1177/0284185115574872.
 63. Padilla F, Roubidoux MA, Paramagul C, et al. Breast mass characterization using 3-dimensional automated ultrasound as an adjunct to digital breast tomosynthesis: a pilot study. *J Ultrasound Med.* 2013;32(1):93-104. doi:10.1097/MPG.0b013e31824d256f.Pediatric.
 64. Choi WJ, Cha JH, Kim HH, et al. Comparison of Automated Breast Volume Scanning and Hand- Held Ultrasound in the Detection of Breast Cancer : an Analysis of 5, 566 Patient Evaluations. *Asian pacific J Cancer Prev.* 2014;15(21):9101-9105. doi:10.7314/APJCP.2014.15.21.9101.
 65. Kim YW, Kim SK, Youn HJ, Choi EJ, Jung SH. The clinical utility of automated breast volume scanner: A pilot study of 139 cases. *J Breast Cancer.* 2013;16(3):329-334. doi:10.4048/jbc.2013.16.3.329.
 66. Invenia ABUS - ABUS Breast Imaging - Ultrasound - Products. General Electric Company. http://www3.gehealthcare.com/en/products/categories/ultrasound/somo_v_abus_breast_imaging/invenia_abus. Published 2018. Accessed May 25, 2018.
 67. Gorny KR, Tradup DJ, Hangiandreou NJ. Implementation and validation of three automated methods for measuring ultrasound maximum depth of penetration: Application to ultrasound quality control. *Med Phys.* 2005;32(8):2615-2628. doi:10.1118/1.1951095.
 68. Standard I. *Ultrasonics - Pulse-Echo Scanners -- Part 2 : Measurement of Maximum Depth of Penetration and Local Dynamic Range (IEC 61391-2 : 2010 (EQV))*; 2010.
 69. Krol A, Unlu MZ, Baum KG, et al. MRI / PET Nonrigid Breast-Image Registration Using Skin Fiducial Markers. *Phys Medica.* 2006;21(1):39-43. doi:10.1016/S1120-1797(06)80022-0.
 70. Unlu MZ, Krol A, Magri A, et al. Computerized method for nonrigid MR-to-PET breast-image registration. *Comput Biol Med.* 2010;40(1):37-53. doi:10.1016/j.compbio.2009.10.010.
 71. Han L, Hipwell JH, Tanner C, et al. Development of patient-specific biomechanical models. *Phys Med Biol.* 2012;57:455-472. doi:10.1088/0031-9155/57/2/455.
 72. Kucukkaya F, Aribal E, Tureli D, Altas H, Kaya H. Use of a volume navigation technique for combining real-time ultrasound and contrast-enhanced MRI: Accuracy and feasibility of a novel technique for locating breast lesions fikret kucukkaya1. *Am J Roentgenol.* 2016;206(1):217-225. doi:10.2214/AJR.14.14101.
 73. Cloutier G, Soulez G, Qanadli SD, et al. A multimodality vascular imaging phantom with fiducial markers visible in DSA, CTA, MRA, and ultrasound. *Med Phys.* 2004;31(6):1424-1433. doi:10.1118/1.1739300.
 74. Maurel W, Thalmann D, Wu Y, Thalmann NM. *Biomechanical Models for Soft Tissue Simulation.*; 1998. doi:10.1007/978-3-662-03589-4.
 75. Erdemir A, Guess TM, Halloran J, Tadepalli SC, Morrison TM. Considerations for reporting finite element analysis studies in biomechanics. *J Biomech.* 2012;45(4):625-633.

- doi:10.1016/j.jbiomech.2011.11.038.
76. Samani A, Bishop J, Yaffe MJ, Plewes DB. Biomechanical 3-D Finite Element Modeling of the Human Breast Using MRI Data. *IEEE Trans Med Imaging*. 2001;20(4):271-279.
 77. Azar FS, Metaxas DN, Schnall MD. A Deformable Finite Element Model of the Breast for Predicting Mechanical Deformations under External Perturbations. *Acad Radiol*. 2001;8(10):965-975. doi:10.1016/S1076-6332(03)80640-2.
 78. Azar FS, Metaxas DN, Schnall MD. Methods for modeling and predicting mechanical deformations of the breast under external perturbations. *Med Image Anal*. 2002;6(1):1-27. doi:10.1016/S1361-8415(01)00053-6.
 79. Ramião NG, Martins PS, Rynkevic R, Fernandes AA, Barroso M, Santos DC. Biomechanical properties of breast tissue, a state-of-the-art review. *Biomech Model Mechanobiol*. 2016;15(5):1307-1323. doi:10.1007/s10237-016-0763-8.
 80. Sinkus R, Tanter M, Catheline S, et al. Imaging anisotropic and viscous properties of breast tissue by magnetic resonance-elastography. *Magn Reson Med*. 2005;53(2):372-387. doi:10.1002/mrm.20355.
 81. García E, Diez Y, Diaz O, et al. A step-by-step review on patient-specific biomechanical finite element models for breast MRI to x-ray mammography registration. *Med Phys*. 2018;45(1):e6-e31. doi:10.1002/mp.12673.
 82. Gefen A, Dilmony B. Mechanics of the normal woman's breast. *Technol Health Care*. 2007;15(4):259-271.
 83. Kruse SA, Smith JA, Lawrence AJ, et al. Tissue characterization using magnetic resonance elastography: preliminary results. *Phys Med Biol*. 2000;45(6):1579-1590. doi:10.1088/0031-9155/45/6/313.
 84. Tanner C, Guarino S, Hall-craggs MA, Hawkes DJ. Large breast compressions : Observations and evaluation of simulations. *Med Phys*. 2011;38(2). doi:10.1118/1.3525837.
 85. Mertzaniidou T, Hipwell J, Johnsen S, et al. MRI to X-ray mammography intensity-based registration with simultaneous optimisation of pose and biomechanical transformation parameters. *Med Image Anal*. 2014;18(4):674-683. doi:10.1016/j.media.2014.03.003.
 86. Lee AWC, Rajagopal V, Babarenda Gamage TP, Doyle AJ, Nielsen PMF, Nash MP. Breast lesion co-localisation between X-ray and MR images using finite element modelling. *Med Image Anal*. 2013;17(8):1256-1264. doi:10.1016/j.media.2013.05.011.
 87. Solves-Llorens JA, Rupérez MJ, Monserrat C. A complete software application for automatic registration of x-ray mammography and magnetic resonance images. *Med Phys*. 2014;41(8):081903. doi:10.1118/1.4885957.
 88. Hopp T, Dietzel M, Baltzer PA, et al. Automatic multimodal 2D / 3D breast image registration using biomechanical FEM models and intensity-based optimization. *Med Image Anal*. 2013;17(2):209-218. doi:10.1016/j.media.2012.10.003.
 89. Hipwell JH, Vavourakis V, Han L, Mertzaniidou T, Eiben B, Hawkes DJ. A review of biomechanically informed breast image registration. *Phys Med Biol*. 2016;61(2):R1-R31. doi:10.1088/0031-9155/61/2/R1.
 90. Ruiters N V, Stotzka R, Müller T, Gemmeke H, Reichenbach JR, Kaiser WA. Model-Based Registration of X-Ray Mammograms and MR Images of the Female Breast. In: *IEEE Transactions on Nuclear Science*. Vol 53. ; 2006:204-211.
 91. Han L, Hipwell JH, Eiben B, et al. A nonlinear biomechanical model based registration method for aligning prone and supine mr breast images. *IEEE Trans Med Imaging*.

- 2014;33(3):682-694. doi:10.1109/TMI.2013.2294539.
92. Hipwell JH, Vavourakis V, Han L, Mertzaniidou T, Eiben B, Hawkes DJ. A review of biomechanically informed breast image registration. *Phys Med Biol*. 2016;61:R1-R31. doi:10.1088/0031-9155/61/2/R1.
 93. Lee A, Rajagopal V, Bier P, Nielsen PMF, Nash MP. Correlation of breast image alignment using biomechanical modeling. In: *Proceedings of SPIE- The International Society for Optical Engineering*. Vol 7262. ; 2009:1-9. doi:10.1117/12.811789.
 94. Sinkus R, Tanter M, Xydeas T, Catheline S, Bercoff J, Fink M. Viscoelastic shear properties of in vivo breast lesions measured by MR elastography. In: *Magnetic Resonance Imaging*. Vol 23. Elsevier; 2005:159-165. doi:10.1016/j.mri.2004.11.060.
 95. McKnight AL, Kugel JL, Rossman PJ, Manduca A, Hartmann LC, Ehman RL. MR Elastography of Breast Cancer: Preliminary Results. *Am J Roentgenol*. 2002;178(6):1411-1417. doi:10.2214/ajr.178.6.1781411.
 96. Athanasiou A, Tardivon A, Tanter M, et al. Breast Lesions: Quantitative Elastography with Supersonic Shear Imaging—Preliminary Results. *Radiology*. 2010;256(1):297-303. doi:10.1148/radiol.10090385.
 97. Kellner AL, Nelson TR, Cervino LI, Boone JM. Simulation of Mechanical Compression of Breast Tissue. *IEEE Trans Biomed Eng*. 2007;54(10):1885-1891. doi:10.1109/TBME.2007.893493.
 98. Alonzo-Proulx O, Packard N, Boone JM, et al. Validation of a method for measuring the volumetric breast density from digital mammograms. *Phys Med Biol*. 2010;55(11):3027-3044. doi:10.1088/0031-9155/55/11/003.
 99. Altair Engineering Inc. Linear Static Analysis. In: *Optistruct User Guide*. ; 2017. https://altairhyperworks.com/hwhelp/Altair/2017/help/os/topics/solvers/analysis_linear_static_c.htm#analysis_linear_static_c. Accessed January 15, 2019.
 100. Altair Engineering Inc. Nonlinear Solution Method. In: *Optistruct User Guide*. Troy, MI; 2017. https://altairhyperworks.com/hwhelp/Altair/2017/help/os/topics/solvers/analysis_nonlinear_solution_method_r.htm. Accessed January 15, 2019.
 101. Altair Engineering Inc. Nonlinear Quasi-Static Analysis. https://altairhyperworks.com/hwhelp/Altair/2017/help/os/topics/solvers/analysis_nonlinear_quasi_static_c.htm?hl=quasi-static. Accessed January 15, 2019.
 102. Dassault Systèmes Simulia Corp. *Abaqus Theory Manual*. Providence, RI; 2010. <https://www.sharcnet.ca/Software/Abaqus610/Documentation/docs/v6.10/books/stm/default.htm>.
 103. Broyden CG. A Class of Methods for Solving Nonlinear Simultaneous Equations. *Math Comput*. 1965;19(92):577-593. doi:https://doi.org/10.1090/S0025-5718-1965-0198670-6.
 104. Davidson WC. Variable metric method for minimization (revised), Technical Report ANL-5990. *Argonne Natl Lab*. 1959.
 105. BROYDEN CG. The Convergence of a Class of Double-rank Minimization Algorithms 1. General Considerations. *IMA J Appl Math*. 1970;6(1):76-90. doi:10.1093/imamat/6.1.76.
 106. Matthies H, Strang G. The solution of nonlinear finite element equations. *Int J Numer Methods Eng*. 1979;14(11):1613-1626. doi:10.1002/nme.1620141104.
 107. Hopp T, Duric N, Ruiter N V. Image fusion of Ultrasound Computer Tomography volumes with X-ray mammograms using a biomechanical model based 2D/3D registration. *Comput Med Imaging Graph*. 2015;40:170-181.

- doi:10.1016/j.compmedimag.2014.10.005.
108. Tanner C, Schnabel JA, Hill DLG, Hawkes DJ, Leach MO, Hose DR. Factors influencing the accuracy of biomechanical breast models. *Med Phys*. 2006;33(6Part1):1758-1769. doi:10.1118/1.2198315.
 109. Hakim CM, Chough DM, Ganott MA, et al. Digital Breast Tomosynthesis in the Diagnostic Environment : A Subjective Side-by-Side Review. *Am J Roentgenol*. 2010;195(2):W172-W176. doi:10.2214/AJR.09.3244.
 110. Kim SA, Chang JM, Cho N, Yi A, Moon WK. Characterization of Breast Lesions : Comparison of Digital Breast Tomosynthesis and Ultrasonography. *Korean J Radiol*. 2015;6(2):229-238. doi:10.3348/kjr.2015.16.2.229.
 111. Larson ED, Lee W-M, Roubidoux MA, et al. Automated Breast Ultrasound: Dual-Sided compared with single-sided imaging. *Ultrasound Med Biol*. 2016;42(9):2072-2082. doi:10.1016/j.ultrasmedbio.2016.05.001.
 112. Georgii J, Zöhrer F, Hahn HK. Model-based position correlation between breast images. In: *Proceedings Volume 8670, Medical Imaging 2013: Computer-Aided Diagnosis*. Vol 8670. ; 2013:1-7. doi:10.1117/12.2007472.
 113. Telegrafo M, Rella L, Stabile Ianora AA, Angelelli G, Moschetta M. Supine breast US: How to correlate breast lesions from prone MRI. *Br J Radiol*. 2016;89(1059). doi:10.1259/bjr.20150497.
 114. Narayanasamy G, LeCarpentier GL, Roubidoux M, Fowlkes JB, Schott AF, Carson PL. Spatial registration of temporally separated whole breast 3D ultrasound images. *Med Phys*. 2009;36(9):4288. doi:10.1118/1.3193678.
 115. Hungr N, Long JA, Beix V, Troccaz J. A realistic deformable prostate phantom for multimodal imaging and needle-insertion procedures. *Med Phys*. 2012;39(4):2031-2041. doi:10.1118/1.3692179.
 116. Negron L a, Viola F, Black EP, Toth C a, Walker WF. Development and Characterization of a Radiation Force Imaging. 2002;49(11):1543-1551.
 117. Howard S, Yuen J, Wegner P, Zanelli CI. Characterization and FEA simulation for a HIFU phantom material. *IEEE Symp Ultrason 2003*. 2003;2(c):1270-1273. doi:10.1109/ULTSYM.2003.1293134.
 118. Adam Cunha J, Hsu IC, Pouliot J, et al. Toward adaptive stereotactic robotic brachytherapy for prostate cancer: Demonstration of an adaptive workflow incorporating inverse planning and an MR stealth robot. *Minim Invasive Ther Allied Technol*. 2010;19(4):189-202. doi:10.3109/13645706.2010.497000.
 119. Munding A. 3D Supine Automated Ultrasound (SAUS, ABUS, ABVS) for Supplemental Screening Women with Dense Breasts. *J Breast Heal*. 2016;12(2):52-55. doi:10.5152/tjbh.2016.2940.
 120. Stavros AT, Rapp CL, Parker SH. *Breast Ultrasound*. Philadelphia, Pennsylvania: Lippincott Williams & Wilkins; 2004.
 121. Fedorov A, Beichel R, Kalpathy-cramer J, et al. 3D Slicer as an image computing platform for the Quantitative Imaging Network. *Magn Reson Imaging*. 2012;30(9):1323-1341. doi:10.1016/j.mri.2012.05.001.
 122. Dice LR. Measures of the Amount of Ecologic Association Between Species. *Ecology*. 1945;26(3):297-302. doi:10.2307/1932409.
 123. Boverman G, Davis CEL, Geimer SD, Meaney PM. Image Registration for Microwave Tomography of the Breast Using Priors from Non-Simultaneous Previous Magnetic

- Resonance Images. In: *2017 First IEEE MTT-S International Microwave Bio Conference (IMBIOC)*. Vol 7249. IEEE; 2017:1-4. doi:10.1109/JERM.2017.2786025.
124. Gu P, Lee W-M, Roubidoux MA, Yuan J, Wang X, Carson PL. Automated 3D ultrasound image segmentation to aid breast cancer image interpretation. *Ultrasonics*. 2016;65(11):51-58. doi:10.1016/j.ultras.2015.10.023.
 125. Kelly KM, Richwald GA. Automated Whole-Breast Ultrasound: Advancing the Performance of Breast Cancer Screening. *Semin Ultrasound, CT MRI*. 2011;32(4):273-280. doi:10.1053/j.sult.2011.02.004.
 126. Rummel S. Tumour location within the breast: Does tumour site have prognostic ability? *Ecancermedicalscience*. 2015;9:1-10. doi:10.3332/ecancer.2015.552.
 127. Cha KH, Hadjiiski L, Samala RK, Chan H-P, Caoili EM, Cohan RH. Urinary bladder segmentation in CT urography using deep-learning convolutional neural network and level sets. *Med Phys*. 2016;43(4):1882-1896. doi:10.1118/1.4944498.
 128. Elawady M, Sadek I, Shabayek AER, Pons G, Ganau S. Automatic nonlinear filtering and segmentation for breast ultrasound images. In: *Lecture Notes in Computer Science (Including Subseries Lecture Notes in Artificial Intelligence and Lecture Notes in Bioinformatics)*. Vol 9730. Springer, Cham; 2016:206-213. doi:10.1007/978-3-319-41501-7_24.
 129. Rafferty EA, Durand MA, Conant EF, et al. Breast Cancer Screening Using Tomosynthesis and Digital Mammography in Dense and Nondense Breasts. *Jama*. 2016;315(16):1784. doi:10.1001/jama.2016.1708.
 130. O'Connell A, Karellas A, Vedantham S. The potential role of dedicated 3D breast CT as a diagnostic tool: Review and early clinical examples. *Breast J*. 2014;20(6):247-253. doi:10.1111/tbj.12327.
 131. Alonzo-Proulx O, Mainprize JG, Packard NJ, et al. Development of a peripheral thickness estimation method for volumetric breast density measurements in mammography using a 3D finite element breast model. *Lect Notes Comput Sci (including Subser Lect Notes Artif Intell Lect Notes Bioinformatics)*. 2010;6136 LNCS:467-473. doi:10.1007/978-3-642-13666-5_63.
 132. Sturgeon GM, Kiarashi N, Lo JY, Samei E, Segars WP. Finite-element modeling of compression and gravity on a population of breast phantoms for multimodality imaging simulation. *Med Phys*. 2016;43(5):2207-2217. doi:10.1118/1.4945275.
 133. Santos J, Chaudhari AJ, Joshi AA, et al. Non-rigid registration of serial dedicated breast CT, longitudinal dedicated breast CT and PET/CT images using the diffeomorphic demons method. *Phys Medica*. 2014;30(6):713-717. doi:10.1016/j.ejmp.2014.06.040.
 134. Tanner C, Schnabel JA, Hill DLG, et al. Quantitative evaluation of free-form deformation registration for dynamic contrast-enhanced MR mammography. *Med Phys*. 2007;34(4):1221-1233. doi:10.1118/1.2712040.
 135. Hill A, Mehnert A, Crozier S, McMahon K. Evaluating the accuracy and impact of registration in dynamic contrast-enhanced breast MRI. *Concepts Magn Reson Part B Magn Reson Eng*. 2009;35B(2):106-120. doi:10.1002/cmr.b.20133.
 136. Dmitriev ID, Loo CE, Vogel W V, Pengel KE, Gilhuijs KGA. Fully automated deformable registration of breast DCE-MRI and PET/CT. *Phys Med Biol*. 2013;58(4):1221-1233. doi:10.1088/0031-9155/58/4/1221.
 137. Shih T, Chen J, Liu D, et al. Computational Simulation of Breast Compression Based on Segmented Breast and Fibroglandular Tissues on Magnetic Resonance Images. *Phys Med*

- Biol.* 2010;55(14):4153-4168. doi:10.1088/0031-9155/55/14/013.Computational.
138. *Multi-Modality Breast Biopsy and Sonographic Trainer.*; 2014. [http://www.cirsinc.com/file/Products/073/073_DS_110617\(3\).pdf](http://www.cirsinc.com/file/Products/073/073_DS_110617(3).pdf). Accessed January 3, 2019.
 139. Samala RK, Chan H-P, Hadjiiski L, Helvie MA, Wei J, Cha K. Mass detection in digital breast tomosynthesis: Deep convolutional neural network with transfer learning from mammography. *Med Phys.* 2016;43(12):6654-6666. doi:10.1118/1.4967345.
 140. Street E, Hadjiiski L, Sahiner B, et al. Automated volume analysis of head and neck lesions on CT scans using 3D level set segmentation. *Med Phys.* 2007;34(11):4399-4408. doi:10.1118/1.2794174.
 141. Hadjiiski L, Chan H-P, Caoili EM, Cohan RH, Wei J, Zhou C. Auto-Initialized Cascaded Level Set (AI-CALS) Segmentation of Bladder Lesions on Multidetector Row CT Urography. *Acad Radiol.* 2013;20(2):148-155. doi:10.1016/J.ACRA.2012.08.012.
 142. Fedorov A, Beichel R, Kalphaty-Cramer J, et al. 3D slicers as an image computing platform for thw quantitative imaging network. *Magn Reson Imaging.* 2012. doi:10.1016/j.mri.2012.05.001.3D.
 143. Brock KK, Sharpe MB, Dawson L a, Kim SM, Jaffray D a. Accuracy of finite element model-based multi-organ deformable image registration. *Med Phys.* 2005;32(6):1647-1659. doi:10.1118/1.1915012.
 144. Pathmanathan P, Gavaghan DJ, Whiteley JP, Chapman SJ, Brady JM. Predicting Tumor Location by Modeling the Deformation of the Breast. *IEEE Trans Biomed Eng.* 2008;55(10):2471-2480. doi:10.1109/TBME.2008.925714.
 145. Yin HM, Sun LZ, Wang G, Yamada T, Wang J, Vannier MW. ImageParser: a tool for finite element generation from three-dimensional medical images. *Biomed Eng Online.* 2004;3(1):31. doi:10.1186/1475-925X-3-31.
 146. Hsu CML, Palmeri ML, Segars WP, Veress AI, Dobbins JT. An analysis of the mechanical parameters used for finite element compression of a high-resolution 3D breast phantom. *Med Phys.* 2011;38(10):5756-5770. doi:10.1118/1.3637500.
 147. Eiben B, Vavourakis V, Hipwell J, et al. *Breast Deformation Modelling: Comparison of Methods to Obtain a Patient Specific Unloaded Configuration.* Vol 9036.; 2014. doi:10.1117/12.2043607.
 148. Vavourakis V, Hipwell JH, Hawkes DJ. An Inverse Finite Element u/p-Formulation to Predict the Unloaded State of In Vivo Biological Soft Tissues. *Ann Biomed Eng.* 2016;44(1):187-201. doi:10.1007/s10439-015-1405-5.
 149. Eiben B, Vavourakis V, Hipwell JH, et al. Symmetric Biomechanically Guided Prone-to-Supine Breast Image Registration. *Ann Biomed Eng.* 2016;44(1):154-173. doi:10.1007/s10439-015-1496-z.
 150. O'Hagan JJ, Samani A. Measurement of the hyperelastic properties of tissue slices with tumour inclusion. *Phys Med Biol.* 2008;53(24):7087-7106. doi:10.1088/0031-9155/53/24/006.
 151. O'Hagan JJ, Samani A. Measurement of the hyperelastic properties of 44 pathological ex vivo breast tissue samples. *Phys Med Biol.* 2009;54(8):2557-2569. doi:10.1088/0031-9155/54/8/020.
 152. Chung JH, Rajagopal V, Laursen TA, Nielsen PMF, Nash MP. Frictional contact mechanics methods for soft materials: Application to tracking breast cancers. *J Biomech.* 2008;41(1):69-77. doi:10.1016/j.jbiomech.2007.07.016.

153. Taylor ZA, Cheng M, Ourselin S. High-Speed Nonlinear Finite Element Analysis for Surgical Simulation Using Graphics Processing Units. *IEEE Trans Med Imaging*. 2008;27(5):650-663. doi:10.1109/TMI.2007.913112.
154. Han L, Hipwell J, Taylor Z, Tanner C, Ourselin S, Hawkes DJ. Fast Deformation Simulation of Breasts Using GPU-Based Dynamic Explicit Finite Element Method. In: Martí J, Oliver A, Freixenet J, Martí R, eds. *Digital Mammography*. Berlin, Heidelberg: Springer Berlin Heidelberg; 2010:728-735.
155. Drukteinis JS, Mooney BP, Flowers CI, Gatenby RA. Beyond mammography: new frontiers in breast cancer screening. *Am J Med*. 2013;126(6):472-479. doi:10.1016/j.amjmed.2012.11.025.
156. Keller BM, Nathan DL, Wang Y, et al. Estimation of breast percent density in raw and processed full field digital mammography images via adaptive fuzzy c-means clustering and support vector machine segmentation. *Med Phys*. 2012;39(8):4903-4917. doi:10.1118/1.4736530.
157. Huang S-Y, Boone JM, Yang K, Kwan ALC, Packard NJ. The effect of skin thickness determined using breast CT on mammographic dosimetry. *Med Phys*. 2008;35(4):1199-1206. doi:10.1118/1.2841938.
158. Kellner AL, Nelson TR, Cervino LI, Boone JM. Simulation of Mechanical Compression of Breast Tissue. *IEEE Trans Biomed Eng*. 2007;54(10):1885-1891. doi:10.1109/TBME.2007.893493.
159. Alonzo-Proulx O, Packard N. Validation of a method for measuring the volumetric breast density from digital mammograms. *Phys Med ...* 2010;55(11):3027-3044. doi:10.1088/0031-9155/55/11/003.Validation.
160. Tozaki M, Fukuma E. Pattern classification of ShearWaveTM Elastography images for differential diagnosis between benign and malignant solid breast masses. *Acta radiol*. 2011;52(10):1069-1075. doi:10.1258/ar.2011.110276.
161. Costa M. Automated Deformable Registration of Breast Images: towards a software-assisted multimodal breast image reading. March 2016.
162. Mertzaniidou T, Hipwell J, HAN L, Huisman H, Karssemajjer N, Hawkes D. MRI to X-ray mammography registration using an ellipsoidal breast model and biomechanically simulated compressions. *MICCAI Work Breast Image Anal*. 2011:161-168.
163. García E, Oliver A, Diaz O, et al. Mapping 3D breast lesions from full-field digital mammograms using subject-specific finite element models. In: *Proc.SPIE*. Vol 10135. ; 2017. <https://doi.org/10.1117/12.2255957>.
164. Chang R-F, Chang-Chien K-C, Takada E, et al. Rapid image stitching and computer-aided detection for multipass automated breast ultrasound. *Med Phys*. 2010;37(5):2063-2073. doi:10.1118/1.3377775.
165. Berg WA, Zhang Z, Lehrer D, et al. Detection of breast cancer with addition of annual screening ultrasound or a single screening MRI to mammography in women with elevated breast cancer risk. *JAMA*. 2012;307(13):1394-1404. doi:10.1001/jama.2012.388.